BERGISCHE UNIVERSITÄT WUPPERTAL

ADAPTIVE MULTIMODAL PUSHOVER ANALYSIS OF BRIDGES CONSIDERING MULTIDIRECTIONAL EARTHQUAKE EXCITATIONS

DOMINIK MATTHIAS KÄMPER, M. SC.

Dissertation

accepted by the
School of Architecture and Civil Engineering
at the **University of Wuppertal**

in partial fulfillment of the requirements
for the degree of Dr.-Ing.

Wuppertal 2025

Danksagungen / Acknowledgements

Zudem wäre die Promotion auch nicht denkbar gewesen ohne die fortwährende Unterstützung meiner Familie sowie meiner besten Freunde, insbesondere in schwierigen Phasen der Dissertation. Danke euch für jede Form der Förderung, Ablenkung und Aufmunterung.

Wuppertal, im Juli 2025   *Dominik Matthias Kämper*

Abstract

The design of bridge structures for earthquake loads is a challenge in civil engineering. On the one hand, this is caused by the poor detectability of the stochastic process and, on the other hand, by the occurrence of sometimes severe damage in the event of an earthquake, which – if it occurs in a controlled manner – is in some cases entirely desirable, since the earthquake stress is dissipated in the rest of the structure by ductile load-bearing behavior. In addition, the seismic design of bridges is of great importance. In areas of high seismicity, a design that is on the unsafe side can lead to devastating uncontrolled damage or even bridge collapse. Besides the fact that in such cases there is usually a high number of fatalities, many bridges represent a central component of the transport infrastructure that is particularly necessary in the event of an earthquake. In areas of low seismicity, on the other hand, the calculation should also not be overconservative due to strong simplifications to the extent that the load case earthquake becomes relevant for the design and can result in an extremely uneconomical design. A costly seismic analysis can therefore eventually be justified regardless of the earthquake level.

For the seismic analysis of structures, numerous concepts with different complexity are available. In general, the structural responses due to earthquake can be determined both linearly or nonlinearly and, in the second case, statically or dynamically. Due to various advantages, nonlinear-static pushover calculations increasingly come to the fore and are becoming more and more normatively anchored. In addition to initial monomodal approaches by assuming almost unchanged mode shapes, numerous extended concepts including higher modal contributions and the adaption of mode proportional load patterns have been developed in the last decades. However, in most cases even these methods are based on considerable simplifications, such as constant damping, modal scaling based on elastic spectral accelerations or the widespread subsequent combination of individual modal contributions, so that damage accumulation effects of these remain unconsidered in the course of the nonlinear calculation.

Therefore, on the basis of a comprehensive literature review, an optimal concept according to the current state of science, the *Adaptive Multimodal Interaction Analysis* (*AMI*) by NORDA (2012), is optimized and extended to remedy the still existing deficits. Key aspects

of these adaptions include damage accumulation of different modal components while considering a realistic correlation as well as a reasonable combination of multidirectional earthquake excitations. While the introduction of correlation factors leads to a substantial improvement of the overall results, a comprehensive parameter study shows that the previous multidirectional combination of the *AMI* at load level is unreliable. This approach is therefore replaced by a posterior superposition concept, separately for orthogonal and collinear response components, developed in the present work. Furthermore, the procedure is adjusted in such a way that individual adaption steps are always related to the occurrence of new relevant plastic effects, whereby the required number of steps and thus the numerical effort can be considerably reduced.

Another essential part of this doctoral thesis is the computational algorithm developed for the automated application of this method. More specifically, it is a wrapper programmed in *MATLAB*, which uses the computational kernel of the software program *SAP2000*, widely used in earthquake engineering, and enables a fully automated adaptive pushover calculation. Difficulties of the program development lie in the identification of mode interchanges, i.e. the swapping of numbers for certain modes due to changes in the natural frequencies as a result of nonlinear load-bearing behavior, whereby the natural mode shapes themselves change qualitatively. Furthermore, ensuring constant directions of mode proportional load distributions as well as determining reasonable numbers of pushover steps in the respective adaption steps is an algorithmic challenge.

Comparisons of the optimized *AMI* method with other linear and, in particular, nonlinear methods widely used in practice and research show that, in the course of monodirectional and, above all, multidirectional investigations, significantly better approximations to the results of nonlinear time history calculations can be achieved, especially for complex load-bearing behavior. Finally, this work is concluded by the successful validation of the method on a horizontally curved bridge with irregular stiffness distribution as well as on a cable-stayed bridge by renewed comparison with nonlinear time history calculations under bi- or three-directional seismic excitation, respectively. However, it should also be mentioned that in case of systems with a huge number of degrees of freedom, such as the investigated cable-stayed bridge, the algorithm in its current form reaches its limits.

Overall, the developed modified *AMI* (*mAMI*), including the comprehensive and comparative investigations, thus represents an added scientific value. The method is able to consider several modal contributions under realistic mapping of their correlation. Furthermore, with the occurrence of relevant plastic effects, the modal load distributions and maximum modal spectral accelerations are selectively updated, with a reasonable number of such updates in most cases. It is important to note that all bridge piers that may become plastic have to be activated by

an appropriate reference mode, since companion modes lead to much lower stresses due to an only partial correlation. Thus, if the base mode exhibits almost no deformation components at a particular bridge pier, a further calculation should be performed in which this pier is more strongly stressed by an alternative reference mode. Under these conditions, deformations, internal forces and normal stresses can be calculated very accurately in most cases and otherwise at least with larger deviations on the safe side. Only the normal stresses in the piers of the cable-stayed bridge investigated could not be correctly estimated with the current version of the *mAMI*. This can mainly be attributed to the stress level in the area of the material strengths, which means that the subsequent *SRSS* combination of the stress components due to orthogonal seismic excitations is not valid. In addition to the aspect that self-induced vertical modes due to horizontal excitations, which cannot yet be mapped, could have additionally worsened the results, this is the only application limit of the *mAMI* that could be identified in this PhD dissertation.

In general, it is worth mentioning that the quality of the results strongly depends on the modeling of the inelastic load-bearing behavior. It was found that only fiber hinges in *SAP2000* are capable of representing the realistic development of natural modes due to nonlinear behavior. In many cases, these exhibit vertical vibration components in previously exclusively horizontal mode shapes due to the decrease in tangent axial stiffness, which cannot be captured by plastic hinge models. With regard to the calculation effort for the applications of the modified *AMI* carried out within the scope of this PhD dissertation, it should also be emphasized in conclusion that the consideration of two or three modal load combinations (with varying base modes or modal signs) was sufficient in each case to determine the respective structural responses accurately enough and on the safe side. However, if more load combinations become necessary in certain cases, this method may become less attractive due to the significant increase in computational effort.

Contents

List of Symbols and Abbreviations

Small Roman letters

Symbol	Description
$\mathbf{a}$	Acceleration vector in the α *operator splitting scheme*
a_g	Ground acceleration
a_n	Matrix scaling factor
c	Scalar damping
c_{crit}	Critical damping
$\mathbf{d}$	Displacement vector in the α *operator splitting scheme*
f	Natural frequency
$\mathbf{f}$	Force vector in the α *operator splitting scheme*
f_c	Characteristic unconfined concrete compressive strength
f_{cm}	Mean compressive strength of concrete
f_{ctm}	Concrete mean tensile strength
f_u	Ultimate stress of reinforcement steel
f_{uk}	Characteristic tensile strength of reinforcement steel
f_y	Yield stress of reinforcement steel
g	Earth gravitational acceleration ($= 9.81$ m/s^2)
j	FE node index
k	Load combination index or
	Correlation factor
$\tilde{k}$	Modal stiffness
k_0	Initial gradient of the capacity spectrum
$k_0^{(i)}$	Initial gradient of the i-th segment of the capacity spectrum
m	System mass
$\tilde{m}$	Modal mass
$m_{eff,n}^{(i)}$	Effective modal mass of mode n in step i

m_j	Nodal mass (of node j)
p	Pushover point
q	Behavior factor (acc. to EC 8)
r	Natural frequency ratio (for two modes) or
	Response quantity (e.g. bending moment)
$\mathbf{r}$	Static restoring force vector in the α *operator splitting scheme*
$\overline{r}_n$	Modal response quantity for a unit displacement increment
$\mathbf{r}_d$	Vector, connecting the degrees of freedom and the accelerogram direction d
s_{glob}	Ratio between the p-th and the first slope in the i-th segment of the pushover curve
s_{loc}	Ratio of two neighboring slopes in the i-th segment of the pushover curve
$sl^{(i),(p)}$	Slope of the p-th internal pushover segment for the i-th adaption step
t	Time variable
$\mathbf{v}$	Velocity vector in the α *operator splitting scheme*
$v_{target}^{(i)}$	Target displacement at the pier head within the scope of *PSD* tests
$\ddot{v}$	Nodal acceleration

Capital Roman letters

Symbol	Description
A_c	Cross-sectional area
B	Base mode index
$\mathbf{C}$	System damping matrix
E	General response component or
	Elastic modulus
$E_{ed,X/Y}$	Response component resulting from seismic excitation in X or Y direction
E_{cm}	Elastic modulus of concrete
E_D	Hysteresis energy
E_n	Response contribution of mode n
E_{So}	Maximum elastic energy
E_{st}	Elastic modulus of reinforcement steel
$F^{(i)}$	Scaling factor of the displacement increment in the *IRSA*
F_b	Base shear
$\Delta F_{b,n}^{(i)}$	Base shear increment of mode n
$\Delta F_{b,loc/glob}^{(i,p)}$	Target base shear in the i-th *mAMI* step based on the $k_{loc/glob}$ criterion
$\Delta F_{b,target}^{(i,p)}$	Decisive target base shear in the i-th *mAMI* step

F_j	Load component at joint j
ΔF_b	Base shear increment
$\Delta F_{b,CQC}$	CQC-combined base shear increments
$\mathbf{F}_n$	Seismic load vector for mode n
I_{jj}	Moment of inertia of the section about the j-axis
$\mathbf{K}$	System stiffness matrix
$\mathbf{K}_T^{(i)}$	Tangent stiffness matrix
L^e	Length of finite element
$\mathbf{M}$	System mass matrix
$M_{2/3}$	Moment about the 2- or 3-axis
$M_{j,y}$	Yield moment at node j
$\mathbf{P}$	Load vector
$\Delta\mathbf{P}$	Incremental load vector
R_μ	Reduction factors used to determine the inelastic acceleration response spectra
S	Soil parameter (acc. to EC 8)
S_a	Spectral acceleration
$\Delta S_{a,n}^{(i)}$	i-th spectral acceleration increment of mode n
$S_{a,n,max}^{(i)}$	i-th maximum spectral acceleration of mode n
$S_{a,p}^{(i)}$	i-th estimate for the spectral performance acceleration
$S_{a,y}^{(i)}$	Effective spectral yield acceleration in iteration step i
S_d	Spectral displacement
$\Delta S_{d,n}^{(i)}$	i-th spectral displacement increment of mode n
$S_{d,n,max}^{(i)}$	i-th maximum spectral displacement of mode n
$S_{d,p}^{(i)}$	i-th estimate for the spectral performance displacement
$S_{d,y}^{(i)}$	Effective spectral yield displacement in iteration step i
$\mathbf{S}_n$	Restoring forces (n-th modal contribution)
SF_m	Scaling factor for correcting A_c concidering the reinforcement
SF_{pb}	Scaling factor for correcting I_{yy} concidering the reinforcement
SR_a	Reduction factor (of the CSM) to reduce the spectral accelerations
SR_d	Reduction factor (of the CSM) to reduce the spectral displacements
T_n	Eigenperiod of mode n
$T_{B/C/D}$	Control periods of the RS (acc. to EC 8)
$\mathbf{V}$	Vector of nodal displacements
$\overline{\mathbf{V}}^{(i)}$	Vector of nodal displacements for a unit displacement increment
$\ddot{\mathbf{V}}$	Vector of nodal accelerations

Greek symbols

Symbol	Description
α	Parameter of the *Newmark's Method* or
	the α *operator splitting scheme*
$\alpha_{c/o}$	Percentage factor for collinear (c) or orthogonal (o) response components
$\alpha_n^{(k)}$	Modal sign for load combination k of the original *AMI* or
	Intermodal correlation factor for load combination k of the *mAMI*
α_M, α_K	Rayleigh parameters
α_1, α_2	Parameters of the *Pivot Hysteresis Model*
β	Parameter of the *Newmark's Method* or the α *operator splitting scheme* or
	Ratio between the peak unidirectional responses caused by $a_{g,X}$ and $a_{g,Y}$
β_n	Modal participation factor
β_1, β_2	Parameters of the *Pivot Hysteresis Model*
$\tilde{\beta}_n$	Modal seismic mass
$\Gamma^{(i)}$	Load correction factor in the i-th step of the *mAMI*
γ	Parameter of the α *operator splitting scheme* or
	Combination factor of the *BPA*
$\Delta\gamma$	Rotation angle of the local pier coordinate system
Δ	User-defined increment of the iteration tolerance in the *CAAP* tool
Δ_{mp}	Displacement of the monitoring point
$\Delta_{nm}^{(i)}$	Mean difference in the nodal displacements of modes n and m
Δ_y	Yield displacement of a specific node
ε	Uniaxial strain
ε_u	Ultimate strain of reinforcement steel
η	Parameter of the *Pivot Hysteresis Model*
$\ddot{\eta}_n/\dot{\eta}_n/\eta_n$	Acceleration/Velocity/Displacement of the modal SDOF system
θ	Seismic incident angle
κ	Correction factor of the equivalent damping or
	curvature
$\kappa_{tot/pl}$	Total or plastic curvature
λ	Mass reduction factor or
	Reduction factor of the behavior factor q
$\lambda_n^{(i)}$	Intermodal scaling factor in the *IRSA* and *AMI*

μ	Ductility factor
$\mu_{eff,d}$	Effective modal mass participation in the direction d
ξ_0	Basic damping ratio
ξ_{eff}	Effective damping ratio
ξ_{eq}	Basic viscous damping ratio
ξ_{hyst}	Hysteretic damping ratio
ξ_n	Modal damping ratio
π	Circle constant
ρ_c	Concrete density
ρ_{nm}	Correlation coefficient of modes n and m
ρ_{st}	Density of reinforcement steel
σ	Uniaxial normal stress
$\boldsymbol{\Phi}_n$	Eigenvector of mode n
φ_n	Phase of mode n
$\varphi(\omega)$	Coherency function between $a_{g,X}$ and $a_{g,Y}$
ψ	Combination factor in the first multidirectional $mAMI$ approach
ω_g	Predominant circular frequency of the ground motion
ω_n	Natural circular frequency of mode n
$\omega_{n,eff,inel.}$	Effective natural circular frequency of mode n

Abbreviations

Abbreviation	Description
AEPOA	*Adaptive Energy-based Pushover Analysis*
AMC	*Adaptive Modal Combination*
AMI	*Adaptive Multimodal Interaction Analysis*
APA	*Adaptive Pushover Analysis*
AsPP	*Adaptive spectra-based Pushover Procedure*
B/BM	Base mode n
BPA	*Bidirectional Pushover Analysis*
CAAM	*Constant Average Acceleration Method*
CAAP	*Complete Automated Adaptive Pushover*
CNSP	*Coupled Nonlinear Static Pushover*
CQC	*Complete Quadratic Combination*

CS	Capacity spectrum or
	Cross-section
CSM	*Capacity Spectrum Method*
DAP	*Displacement Based Adaptive Pushover Procedure*
DOF	Degree of freedom
EC	Eurocode
ELSA	*European Laboratory for Structural Assessment* in Ispra (Italy)
FAP	*Force-Based Adaptive Pushover Algorithm*
fc	Full correlation
FE	Finite elements
FFT	*Fast FOURIER Transformation*
FH	Fiber hinge
IMPAβ	*Incremental Modal Pushover Analysis for Bridges*
IRI	*Irregularity Index*
IRSA	*Incremental Response Spectrum Analysis*
LAM	*Linear Acceleration Method*
LC	Load combination
MDOF	Multi degree-of-freedom (system)
MMP	*Multi-modal Pushover Procedure*
mAMI	*modified Adaptive Multimodal Interaction Analysis*
mp	Monitoring point
MPA	*Modal Pushover Analysis*
NSM	*Nonlinear Static Methods*
NLTHA	*Nonlinear Time History Analysis*
pc	Partial correlation
pd	Primary direction
PGA	Peak ground acceleration
PH	Plastic hinge
pr	Percentage rule
PRC	*Pushover Results Combination*
PSD	*Pseudo-dynamic* (testing)
RC	Reinforced concrete
RS	Response spectrum
RSM	*Response Spectrum Method*
sd	Secondary direction
SDOF	Single degree-of-freedom (system)

sia	Seismic incident angle
SIMQKE	Tool for generation of artificial earthquake records
SRSS	*Square root of the sum of the squares*
SSI	Soil-structure interaction
VI	*Variation Index*
VMPA-A	*Adaptive Version of Modal Pushover Analysis*

List of Figures

List of Tables

1 Introduction

1.1 Motivation

Seismic design of bridges is a challenge in civil engineering. One main reason is the poor ascertainability of the seismic excitation. Like wind loading, an earthquake represents a random process, but unlike steady state aerodynamic loading, it is transient and difficult to predict because of its relatively infrequent occurrence. The second main difficulty lies in the development of (sometimes severe) damage during earthquake action, which – if it occurs in a controlled manner – is permitted, even desirable, as ductile seismic behavior reduces the seismic stresses in the rest of the structure. Furthermore, the seismic design of bridges is of particular importance. Firstly, in areas of high seismicity, a design that is on the unsafe side can lead to devastating uncontrolled damages or even a complete bridge collapse (see Fig. 1.1). Apart from the fact that this would result in a high number of fatalities, many bridges represent a central part of the transport infrastructure for the rescue of injured people and the supply with relief goods, which is especially necessary in a disaster situation like an earthquake. Secondly, in areas of low seismicity, strong simplifications in the seismic calculation should also not result in the earthquake load case becoming decisive for the design and thus potentially leading to an uneconomical design. In both cases, a relatively costly seismic analysis may be justified or even required.

In particular, a sufficiently accurate calculation of inelastic effects is crucial for a realistic representation of the load-bearing behavior in the event of an earthquake. Depending on the structure and intensity of the earthquake, a change in the stiffness distribution resulting from plastic effects can lead to a completely different load-bearing behavior compared to the linear-elastic initial system. However, it is precisely this consideration that proves to be highly demanding. On the one hand, localized yield zones can form abruptly. On the other hand, plastic areas may also form successively, extending over several meters. The latter occurs in particular with compact reinforced concrete cross-sections due to increasing cracking in the concrete and possible subsequent flowing of the reinforcement. Both effects should therefore be able to be represented by the numerical model. Another crucial aspect is the consideration of different excitation components

1

Figure 1.1: *Pier failure of a road bridge, Earthquake Kobe 1995* [1]

and directions, since an earthquake is not a monodirectional excitation with a predetermined incident angle.

With regard to the calculation concepts available in standards and in the literature, there is currently a need for research (see section 2.3) to map precisely these effects more accurately without increasing the calculation effort to an unacceptably high level. Within the scope of the dissertation, a specific calculation concept is therefore optimized with regard to this objective (see Chapter 3).

1.2   Seismic design concepts

For the seismic analysis of structures, different concepts with different complexity are available. In general, the structural responses due to earthquakes can be determined both linearly and nonlinearly. Furthermore, the calculation methods can be divided into static and dynamic methods. In this chapter, the widely used linear-static *Response Spectrum Method* (*RSM*) as well as the *Nonlinear Time History Analysis* (*NLTHA*) are first presented before different nonlinear-static concepts are discussed in subsequent Sections 1.2.3, 1.3 and Chapter 2.

---

[1] `https://www.ibtimes.co.uk/kobe-earthquake-20th-anniversary-facts-about-devastating-1995-great-hanshin-earthquake-1483786`, call: 10/2023

1.2.1 Response Spectrum Method (RSM)

The representative of the linear-static concept is the *Response Spectrum Method* (*RSM*), which is widespread in engineering practice. Starting point of this method are linear SDOF systems with a specific damping but different natural periods, for which the structural response (acceleration, velocity or displacement of the SDOF system) to a specific earthquake is calculated in the time domain. If the maximum structural responses of the SDOF systems are plotted over their corresponding natural periods, a so-called response spectrum is obtained. The core idea of the *RSM* is now to use this once generated spectrum in order to derive the response without the need of renewed calculations in the time domain. If the evaluation variable under consideration is acceleration, for example, an inertia force can be determined for a static calculation by multiplying it by the mass:

$$F = S_a(T,\xi) \cdot m \ . \tag{1.1}$$

This concept can even be applied on multi-degree-of-freedom (MDOF) systems, if the response is significantly dominated by a base mode *B*. For this application, the MDOF system simply needs to be reduced to the relevant modal SDOF by a modal transformation:

$$\tilde{m}_B \cdot \ddot{\eta}_B(t) + 2 \cdot \xi_B \cdot \tilde{m}_B \cdot \omega_B \cdot \dot{\eta}_B(t) + \tilde{k}_B \cdot \eta_B(t) = -\mathbf{\Phi}_B^T \cdot \mathbf{M} \cdot \mathbf{r}_d \cdot a_g(t) \ , \tag{1.2}$$

$$\text{with } \mathbf{\Phi}_B^T \cdot \mathbf{M} \cdot \mathbf{r}_d = \tilde{\beta}_B \ , \tag{1.3}$$

$\mathbf{r}_d$ connecting the degrees of freedom of the structure and the imposed accelerogram direction d. In this equation, not the actual mass $\tilde{m}_B$ of the modal SDOF system, but the so-called modal seismic mass $\tilde{\beta}_B$ is multiplied by the ground acceleration on the right side. For this reason, the result S_a from the response spectrum must subsequently be multiplied by the modal participation factor

$$\beta_B = \frac{\tilde{\beta}_B}{\tilde{m}_B} \ , \tag{1.4}$$

so that the following equation for the static equivalent loads is obtained:

$$\mathbf{F} = \mathbf{M} \cdot \mathbf{\Phi}_B \cdot S_a(T_B, \xi_B) \cdot \beta_B \ . \tag{1.5}$$

According to the European standard (EUROCODE 8 - PART 1 , 2010), this procedure can be applied in a simplified way for common building structures under certain conditions with regard to the regularity of the structure, assuming that the structure vibrates almost exclusively in its respective fundamental mode in a certain horizontal direction. With the associated natural period and damping, a single spectral acceleration S_a is read from the normative response spectrum and the total earthquake force F_b is determined via the following product:

$$F = S_a(T_1, \xi_1) \cdot m \cdot \lambda \ . \tag{1.6}$$

Here, m describes the system mass and λ a normatively defined reduction factor taking into account that not the entire system mass is excited to vibrations by the natural mode. This resulting horizontal earthquake force must then be distributed over the height in a manner proportional to the mass and mode shape for the static calculation, whereby the modal shape can even be approximated by a distribution that increases linearly with the height.

However, if the structural response of an MDOF system is not based on one fundamental modal contribution, the *RSM* must be carried out with additional consideration of relevant higher modes. According to the European standard this case occurs if the conditions for the applicability of the aforementioned simplified approach are not given or if a bridge structure is investigated (EUROCODE 8 - PART 1 , 2010; EUROCODE 8 - PART 2 , 2011). Eurocode 8 then requires the consideration of all modes n that have an effective modal mass of at least 5% of the total effective mass, or until the applied masses add up to 90%. On the basis of Eqs. 1.2 to 1.4, evaluated for all relevant modes n, the following equation for the static equivalent loads of the n-th modal contribution is obtained:

$$\mathbf{F}_n = \mathbf{M} \cdot \mathbf{\Phi}_n \cdot S_a(T_n, \xi_n) \cdot \beta_n \ . \tag{1.7}$$

Multiplying this load vector scalarly by the already mentioned vector $\mathbf{r}_d$ leads to the sum of forces of this mode, the so-called base shear F_b:

$$F_{b,n} = \tilde{\beta}_n \cdot \beta_n \cdot S_{a,n} \ . \tag{1.8}$$

Furthermore, this equation yields the definition of the above mentioned effective modal mass of mode n:

$$m_{eff,n} = \tilde{\beta}_n \cdot \beta_n \ . \tag{1.9}$$

If the equivalent static loads are applied separately for each modal component and a corresponding static calculation is performed, independent response quantities E_n are obtained for each mode n. In many cases, these can then be superimposed using the so-called *SRSS* method (*square root of the sum of the squares*, NEWMARK & ROSENBLUETH (1971)):

$$E = \sqrt{\sum E_n^2} \ . \tag{1.10}$$

Alternatively, in the case of similar natural periods, this combination can or even should be performed by means of the *CQC* rule (*complete quadratic combination*), assuming a stronger correlation (WILSON ET AL , 1981):

$$E = \sqrt{\sum_n \sum_m E_n \cdot \rho_{nm} \cdot E_m} \ , \tag{1.11}$$

ρ_{nm} being the modal correlation coefficient:

$$\rho_{nm} = \frac{8 \cdot \sqrt{\xi_n \cdot \xi_m} \cdot (\xi_n + r \cdot \xi_m) \cdot r^{3/2}}{(1 - r^2)^2 + 4 \cdot \xi_n \cdot \xi_m \cdot r \cdot (1 + r^2) + 4\left(\xi_n^2 + \xi_m^2\right) \cdot r^2} \ , \tag{1.12}$$

$$\text{with } r = \frac{min(\omega_n, \omega_m)}{max(\omega_n, \omega_m)} \ . \tag{1.13}$$

This superposition rule leads to a sum of the absolute values of both modal contributions in case of a full correlation, whereas it corresponds to the *SRSS* rule when the modes are fully decorrelated.

Another aspect that has a decisive influence on the results is the question of whether inelastic load-bearing behavior is present or not. In many cases, seismic excitation leads to plastic effects that cannot be neglected. In particular, these are even desirable to a certain extent, as ductile behavior reduces the seismic loads. In case of the *RSM* all inelastic effects are reduced to a single factor q, which is used to scale the response spectrum. This approach, however, is not able to represent the real distribution of ductility in the system and thus cannot accurately capture the real nonlinear seismic behavior.

The main advantage of the *Response Spectrum Method* is its simple applicability in engineering practice, which allows an easy estimation of the demand quantities to be expected in the event of an earthquake at a given location. However, since this method bundles all energy dissipation effects in order to define the design response spectrum into a single ductility factor to be estimated in advance, it can be rated as the most unprecise approach. Furthermore, following the calculation, it must be proven within the framework of a capacity design that the ductility, assumed for the selection of the q factor, actually occurs under the calculated seismic demand. If this is not the case, the entire calculation must be repeated with a new, adjusted ductility factor.

1.2.2 Nonlinear Time History Analysis (NLTHA)

As a nonlinear and dynamic approach the nonlinear time history calculation is the most advanced but also most realistic procedure in earthquake engineering. It is based on the direct time integration of the coupled nonlinear differential equation system for a given set of possibly scaled real accelerograms, or artificially generated ground motion inputs corresponding to normative spectra. Various integration methods are available for this purpose, such as the well-known *CAAM* (*Constant Average Acceleration Method*) or the *LAM* (*Linear Acceleration Method*). In the literature, the nonlinear time history calculation is generally considered to be the most accurate method for determining realistic structural responses due to earthquakes, since it directly accounts for all interaction effects of different modal and directional components

together with dead loads, cyclic stiffness degradation as well as hysteretic dissipation. However, it is also characterized by a number of drawbacks, which are listed below:

Handling and calculation effort

- The calculation itself is demanding, since the hysteresis behavior and damping values for the governing natural modes have to be estimated realistically, which is especially demanding if soil-structure interactions (*SSI*) are to be considered (PINKAWA , 2022), and a sufficient number of earthquake time histories have to be selected according to standards or generated artificially.

- Rayleigh damping can only accurately map two modal damping ratios.

- In case of high relevant modes, it can be challenging to define a suitable time step size that leads to accurate results whilst ensuring an acceptable computing time.

- Furthermore, nonlinear time history calculations are generally time and memory intensive (PARASKEVA ET AL , 2006; KAPPOS ET AL , 2011; PETRONIJEVIC ET AL , 2018; ANTONIOU & PINHO , 2004a; ISAKOVIC & FISCHINGER , 2014).

Result evaluation and interpretation

- Postprocessing is very time-consuming in case of a sufficiant number of ground motion inputs, since all desired results are determined separately by averaging the maxima and are not readily available from the output of the dynamic analysis. In many cases, an external automated evaluation must be programmed for this purpose.

- The evaluation of damage in the cross-sections on the basis of the nonlinear normal stress distribution, including the observation of cracked concrete areas with tensile stresses that have dropped to zero, can only be analyzed for specific time history calculations at specific time steps. Thus, no overall impression can be gained of how the inelastic seismic behavior develops as a whole in order to evaluate the earthquake-compatible structural design.

- In particular, this method does not allow an assessment with regard to the magnitude of the plastification of the system on the one hand and the still existing inelastic reserve capacity on the other hand. It is not possible to assess directly whether the structure still has a significantly higher capacity than required or whether the system has even remained linear-elastic throughout. For the latter point, the hinge results would have to be evaluated in all relevant structural areas for all time history calculations. However, for the static nonlinear methods considered below this is readily identifiable by the pushover curve.

Due to the above-mentioned disadvantages and limitations, the *NLTHA* is therefore mainly used as a reference method in science, while it usually exceeds the affordable effort in practice (ISAKOVIC ET AL , 2003). The German national annex of Eurocode 8, Part 1 (EUROCODE 8 (G.N.A.) - PART 1 , 2021), for example, also permits its (sole) use only in exceptional cases.

1.2.3 Nonlinear Static Methods: Performance-based approach

In principle, linear calculation methods are not able to describe the failure behavior of seismically excited structures, including bridges, with sufficient accuracy. Since cracks often form in the concrete of reinforced concrete structures even in case of relatively low seismic intensity, there is almost no significant linear-elastic behavior in such cases (MESKOURIS ET AL , 2011). According to MESKOURIS ET AL , nonlinearities are particularly influential at higher earthquake intensities and long earthquake durations, which cause stronger dissipation effects as well as a larger stiffness degradation due to the higher number of load cycles. As an alternative to a nonlinear time history calculation with the above-mentioned disadvantages, it is possible to consider nonlinear seismic behavior and, in particular, the associated redistribution effects also in the course of static calculations. This constitutes an advantageous option for practical applications.

General concept of performance-based design

Basically, deformation-based nonlinear static calculations in earthquake engineering are to be distinguished from pure force-based static calculation methods, such as the *Response Spectrum Method*. In the latter, spectral accelerations due to the design earthquake are determined only as a function of the respective natural frequency and damping. Despite, they are externally impressed in the form of resulting forces. Structural deformations, however, are only determined as secondary quantities, without these having any influence on the applied accelerations or inertia forces. In deformation-based nonlinear static calculations, on the other hand, the nonlinear deformation capacity of the structure is directly included in the determination of the specific seismic demand. This turns the pure verification of an equilibrium state with the inclusion of internal forces and stresses into an additional direct verification that the expected relative deformations due to the design earthquake do not exceed the nonlinear deformation capacity of the structure. In addition to the fact that this design concept does much better justice to the interaction between deformability and inertia forces that exists in reality, another advantage is the possibility of directly incorporating specifications concerning serviceability limits. Due to the direct inclusion of the structural deformations, such methods are also referred to as 'performance-based design methods'.

Developement of various performance-based approaches

Since the 1980s, various performance-based methods have been developed worldwide on the basis of this general concept and also applied to common continuous bridges (CALVI & KINGSLEY , 1995; KOWALSKY , 2002; DWAIRI & KOWALSKY , 2006; CALVI & PRIESTLEY , 2007; SUAREZ & KOWALSKY , 2011; CALVI ET AL , 2013; KAPPOS , 2015; ASSARZADEH , 2016) as well as on long span (ADHIKARI ET AL , 2008, 2010), skewed (CATACOLI , 2014) and even arch bridges (KHAN ET AL , 2014).

Particularly noteworthy are the *Displacement Coefficient Method* (*DCM*), described in the FEMA 356 (2000) guideline, the *Direct Displacement-Based Design* (*DDBD*) by PRIESTLEY & CALVI (2003), the *Capacity Spectrum Method* (*CSM*) according to FREEMAN (1998) (basic idea already mentioned in FREEMAN ET AL (1975)) that is described in ATC-40 (1996) and the *N2 method* by FAJFAR (2000), contained in the informative Annex B of EUROCODE 8 - PART 1 (2010).

However, the most widely used and most discussed methods in the literature are certainly the *CSM* and *N2 method*, which belong to the so-called 'pushover' methods. While the *CSM* is based on reduced elastic response spectra, the *N2 method* uses inelastic response spectra according to VIDIC ET AL (1994), determined via statistical evaluations of time history calculations. Another central difference between these two methods is the idealized pushover curve by two linear segments in the *N2 method*. In addition to this central simplification, however, the *N2 method* is characterized by further limitations, such as the restriction to structures that can be investigated as planar systems, or the prerequisite of stable hysteresis loops and medium to high natural periods. Against this background, the *CSM*, which is more precise and can be usefully applied to significantly more cases, is regarded as the main pushover method according to the current state of research. Therefore, this procedure will be described in more detail below, with particular emphasis on the definitions and assumptions to be made in the individual steps. Due to the central importance of the pushover concept for this dissertation, it is presented in a separate chapter.

1.3 Pushover method

The pushover concept offers the possibility of representing the nonlinear seismic behavior much more accurately than the *Response Spectrum Method*. The basis for this enhancement is the consideration of geometric nonlinearity, usually in the form of P-Delta effects, and material nonlinearity, for which the distributed plasticity is represented by an inelastic numerical model. In most cases, the latter is based on the arrangement of local or over certain areas distributed plastic hinges, where the cracking and yielding is expected to occur. This captures, on the one hand, redistribution effects resulting from the emergence of local plastic effects and, on the other hand, the deformation-dependent influence on the seismic demand itself. Since the seismic impact thus interacts with the structural response, an iterative procedure is required.

The widespread international use of pushover methods is reflected, inter alia, in their anchoring in numerous sets of standards, such as FEMA 356 (2000) in the USA or EUROCODE 8 - PART 1 (2010) and EUROCODE 8 - PART 2 (2011) in Europe. Since the publication of the basic concept almost 50 years ago, a wide range of further development of this deformation-dependent approach has emerged, differing strongly in complexity. These methods can be categorized in terms of their simultaneous consideration of higher modes (single- and multi-mode methods), the possible adaption of mode proportional load patterns (non-adaptive and adaptive methods), and in terms of their handling of orthogonal earthquake components. In this chapter, however, the general pushover concept and the earthquake design based on the single-mode, non-adaptive as well as the monodirectional *Capacity Spectrum Method* (*CSM*) are presented first, before more complex further developments are discussed in Chapter 2.

Pushover analysis

The basis for the pushover analysis is the so-called pushover curve, a load-deformation curve representing the building capacity (see Fig. 1.2). This curve plots the resulting base shear, and thus the total earthquake force, against the displacement of a characteristic point of the structure, referred to as monitoring point (*mp*). For multi-storey buildings, a point at roof level is usually chosen as the *mp*, since deformations are greatest at the top of a building. For bridge structures, however, the choice of a suitable representative system node is highly controversial (PARASKEVA ET AL , 2006; PARASKEVA & KAPPOS , 2010; ISAKOVIC & FISCHINGER , 2011; KAPPOS ET AL , 2011; PETRONIJEVIC ET AL , 2018). Frequent suggestions include choosing the center of mass of the bridge deck, the (varying) location of maximum deck deformations or the head of the longest bridge pier.
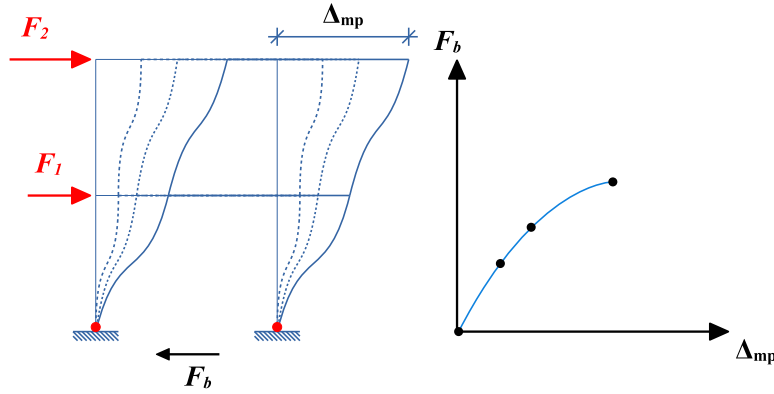
Figure 1.2: *Pushover analysis of a two-storey structure*

The pushover curve is determined under monotonically increasing horizontal loads, while the existing vertical loads are kept constant and, as a rule, P-Delta effects are considered. This analysis is performed either up to a certain defined maximum displacement or up to the collapse of the structure. The applied horizontal loads are intended to represent the inertial forces that arise during an earthquake excitation. Basically, a load pattern proportional to the mass and mode shape (see Eq. 1.14 with $B = \mathbf{B}$ase mode) represents them best (ATC-40 , 1996):

$$F_j = \frac{m_j \cdot \mathbf{\Phi}_B(j)}{\sum_k m_k \cdot \mathbf{\Phi}_B(k)} \cdot F_b \ . \tag{1.14}$$

However, if the mode shape changes significantly due to nonlinear load-bearing behavior, the load pattern would need to be updated in terms of an adaptive approach. Therefore, in non-adaptive methods, a mass proportional distribution is often chosen for multi-storey buildings, which better fits the displacements after the formation of a soft ground floor (NORDA , 2012). Alternatively, a purely height proportional distribution can be applied in a simplifying manner for multi-storey structures. In case of bridge structures, however, constant or mode (and mass) proportional load patterns are commonly used.

Transformation of the pushover curve

For the subsequent determination of the equilibrium state, the pushover curve must first be converted into a so-called capacity spectrum, which is described by the spectral deformation on the abscissa and the spectral acceleration on the ordinate axis.

The multimodal *RSM* provides the starting point for the transformation of the abscissa values:

$$\mathbf{V}_{max} = \sum_n \mathbf{V}_{n,max} = \sum_n \mathbf{\Phi}_n \cdot \beta_{n,d} \cdot S_{d,n,max} \quad (\beta_{n,d} \text{ corresp. to direction } d). \tag{1.15}$$

In this equation, $\mathbf{V}_{n,max}$ is the maximum displacement vector of the structure due to the n-th modal contribution and $S_{d,n,max}$ the spectral displacement of mode n. Equation 1.15 implies perfect positive correlation of all modes. This assumption, however, is unrealistic, c. f. Section 1.2.1. Under the assumption that the structural response depends significantly on only one base mode B, the sum can be reduced to this contribution and the correlation problem disappears. If the equation is evaluated specifically for the selected monitoring point (mp), the nodal displacement Δ_{mp} can be written as

$$\Delta_{mp} = \mathbf{V}(mp) \approx \mathbf{\Phi}_B(mp) \cdot \beta_{B,d} \cdot S_{d,B} \ . \tag{1.16}$$

Solving Equation 1.16 for the spectral displacement yields the following transformation function for the abscissa values:

$$S_d \approx \frac{\Delta_{mp}}{\mathbf{\Phi}_B(mp) \cdot \beta_{B,d}} \ . \tag{1.17}$$

The initial equation for the transformation of the base shear is obtained in a similar way by reducing Eq. 1.8 (with Eq. 1.9) to the base mode contribution:

$$F_b \approx m_{eff,B,d} \cdot S_{a,B} \ . \tag{1.18}$$

The spectral accelerations are thus given as

$$S_a \approx \frac{F_b}{m_{B,eff,d}} \ . \tag{1.19}$$

Equations 1.17 and 1.19 can now be used to transform the pushover curve into an 'S_a-S_d' spectrum.

Capacity Spectrum Method (CSM)

To determine the maximum displacement under earthquake loading, the capacity spectrum is superimposed with an analogous 'S_a-S_d' representation of the response spectrum (see Fig. 1.6). If there is an intersection of the two curves, which is also referred to as the 'performance point', the seismic capacity is sufficient. The performance point indicates the maximum displacement of the equivalent SDOF model, from which the maximum displacement of the monitoring point under the given earthquake load can be determined by applying a back-transformation. The following section first explains the transformation of the response spectrum and then the iterative design process according to the *CSM*.

The starting point of the *CSM* is not a design spectrum, but an elastic response spectrum with a basic damping ξ_0 of usually 5%. The ordinates are already available as spectral accelerations, so that only the abscissa values need to be converted into spectral displacements. For this, the well-known pseudo-spectra relationship and the relationship between the natural frequency and period ($\omega = 2\pi/T$) can be used:

$$S_d = \frac{1}{\omega^2} \cdot S_a = \frac{T^2}{4\pi^2} \cdot S_a \ . \tag{1.20}$$

An essential component of the *CSM* is that energy dissipation is taken into account by an effective damping ξ_{eff}. This is determined in each step i by adding an updated weighted equivalent viscous damping $\xi_{eq}^{(i)}$ to the constant basic damping:

$$\xi_{eff}^{(i)} = \xi_0 + \xi_{eq}^{(i)} \cdot \kappa \ , \tag{1.21}$$

whereby the basic viscous damping ratio $\xi_{eq}^{(i)}$, depending on the actual (i-th) displacement state, is given as

$$\xi_{eq}^{(i)} = \frac{1}{4\pi} \cdot \frac{E_D^{(i)}}{E_{So}^{(i)}} \ . \tag{1.22}$$

In this equation, E_{So} corresponds to the maximum strain energy and E_D to the hysteresis energy, representing the area enclosed by the hysteresis loop (cf. Fig. 1.5). E_{So} can be determined as the triangular area of the right-angled triangle whose hypotenuse is bounded by the coordinate origin and the current iteration point $(S_{d,p}^{(i)}, S_{a,p}^{(i)})$ (cf. Fig. 1.3):

$$E_{So}^{(i)} = \frac{S_{d,p}^{(i)} \cdot S_{a,p}^{(i)}}{2} \ . \tag{1.23}$$
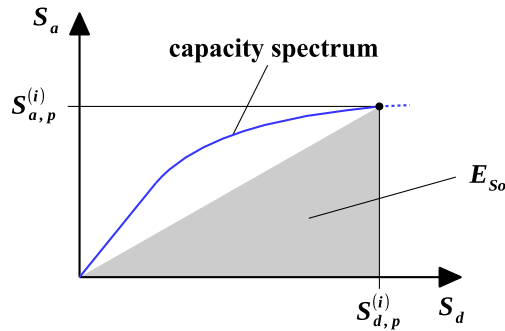
Figure 1.3: *Maximum strain energy in the capacity spectrum*

In order to determine the hysteresis energy, the capacity spectrum is approximated by two linear segments between the coordinate origin and the currently estimated performance point $(S_{d,p}^{(i)}, S_{a,p}^{(i)})$ in method A according to ATC-40 (1996). In addition to the condition that the hysteresis curve idealized in this way is also limited by those two points, the determination is based on an equal initial gradient k_0 and the requirement of an energy equivalence in this area, which mathematically requires an equal area of the surface enclosed by both curves. For

this purpose, a straight line with the gradient k_0 is first laid through the origin and a second straight line through the point $(S_{d,p}^{(i)}, S_{a,p}^{(i)})$ in such a way that the areas of A_1 and A_2 are identical according to Figure 1.4. This allows the effective yield point $(S_{d,y}^{(i)}, S_{a,y}^{(i)})$ to be determined as the intersection of these two straight lines and the idealized capacity spectrum to be described unambiguously.
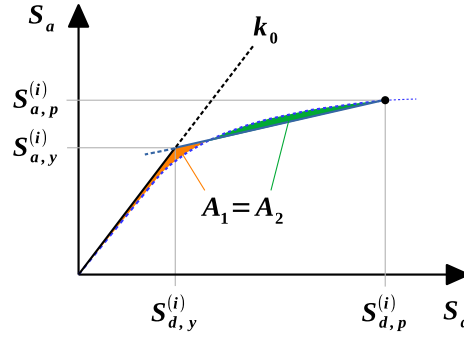
Figure 1.4: *Idealization of the capacity spectrum according to ATC-40 (1996) (method A)*

With the hysteresis loop adapted to this idealization, which corresponds to a parallelogram according to Figure 1.5, the hysteresis energy is obtained as

$$E_D^{(i)} = 4 \cdot \left(S_{a,y}^{(i)} \cdot S_{d,p}^{(i)} - S_{d,y}^{(i)} \cdot S_{a,p}^{(i)} \right) \ . \tag{1.24}$$
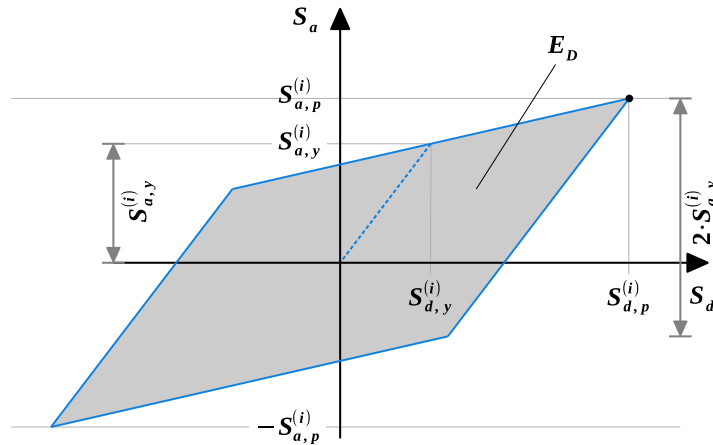
Figure 1.5: *Idealized hysteresis loop*

However, as the actual hysteresis curve does not correspond to the idealized one (cf. Fig. 1.5), the equivalent damping $\xi_{eq}^{(i)}$ must be reduced by a correction factor κ according to ATC-40 (1996). This reduction factor describes the ratio of the actual area enclosed by the real hysteresis loop to that resulting from the linear idealization. Depending on the equivalent damping ξ_{eq} and the type of hysteretic behavior, the following equations for determining the correction factor κ are given in ATC-40 (1996):

Table 1.1: *Correction factor κ and SR_{min} values according to ATC-40 (1996)*

Hysteresis loops	ξ_{eq} [%]	κ [-]	$SR_{a,min}$	$SR_{d,min}$
stable	≤ 16.25	1.000	0.33	0.50
	> 16.25	$1.130 - 0.510 \cdot \frac{S_{a,y} \cdot S_{d,p} - S_{d,y} \cdot S_{a,p}}{S_{a,p} \cdot S_{d,p}}$		
relatively low constricted	≤ 25.00	0.670	0.44	0.56
	> 25.00	$0.845 - 0.446 \cdot \frac{S_{a,y} \cdot S_{d,p} - S_{d,y} \cdot S_{a,p}}{S_{a,p} \cdot S_{d,p}}$		
strongly constricted	any value	0.330	0.56	0.67

The effective damping ratio ξ_{eff}, calculated according to Equation 1.21, can then be used to determine the following factors in order to reduce the transformed response spectrum for the current iteration step i:

$$S_{a,red} = S_a \cdot SR_a \tag{1.25}$$

$$S_{d,red} = S_d \cdot SR_d \ . \tag{1.26}$$

These reduction factors are defined in ATC-40 (1996) as:

$$SR_a = \frac{3.21 - 0.68 \cdot ln(\xi_{eff})}{2.12} \geq SR_{a,min} \tag{1.27}$$

$$SR_d = \frac{2.31 - 0.41 \cdot ln(\xi_{eff})}{1.65} \geq SR_{d,min} \ , \tag{1.28}$$

where $SR_{a,min}$ and $SR_{d,min}$ are the minimum values to be complied with according to Table 1.1.

Now, the intersection point $(S_{d,ip}^{(i)}, S_{a,ip}^{(i)})$ of the two curves, the capacity spectrum and the reduced response spectrum, can be determined (cf. Fig. 1.6). However, as the reduced response spectrum is based on the test performance point $(S_{d,p}^{(i)}, S_{a,p}^{(i)})$, it is now necessary to check whether the intersection point is close enough to the estimated point according to the following limiting criterion (ATC-40 , 1996):

$$0.95 \cdot S_{d,p}^{(i)} \leq S_{d,ip}^{(i)} \leq 1.05 \cdot S_{d,p}^{(i)} \ . \tag{1.29}$$

If this is the case, the intersection point can be regarded as the actual performance point. However, if the deviation is too large, the effective damping must be updated in a new iteration step based on a new estimator for the performance point and the response spectrum must be reduced again. This procedure is repeated until the specified criterion (Eq. 1.29) is met. The intersection point of the previous iteration step can be used as the respective estimator.
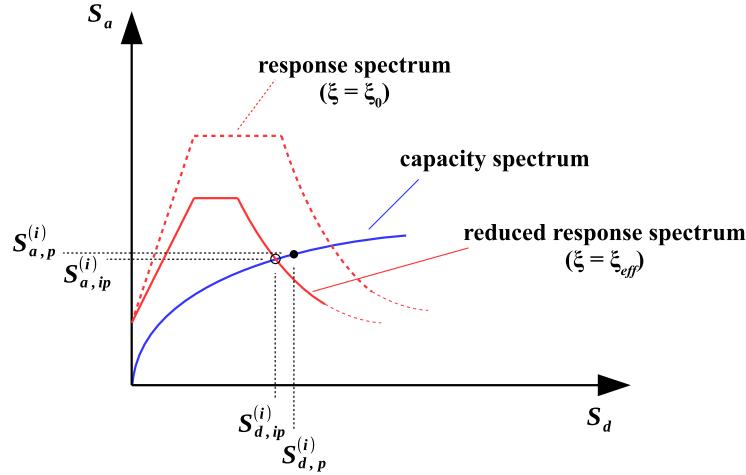
Figure 1.6: *Iterative determination of the performance point*

Assessment of the *CSM*

In principle, a pushover calculation maps the distributed plasticity and thus the structural ductility much better than the *RSM*. This also enables the explicit detection of plastic deformations or damaged cross-sections (KRAWINKLER & SENEVIRATNA , 1998), so that the inelastic load-bearing behavior in the event of an earthquake can be better assessed and the system can be adapted accordingly if necessary. The resulting advantage of a generally more economical design is supplemented by the further advantage that the plastic reserves (still available for a specific earthquake level) can be estimated. In particular, however, a pushover calculation not only covers the verification of the inelastic capacity, but also ensures that the deformation limits described by the capacity curve are complied with. Nevertheless, the basic concept of the pushover method is based on some significant simplifications. In this respect, the assumption that the structural response is approximately based only on one single mode should be mentioned in particular. This relates to the horizontal loads on the one hand and the transformation of the pushover curve on the other. Furthermore, there are various (bridge) structures, where the assumption of constant mode shapes, i.e. independent of the earthquake intensity, leads to an incorrect representation of the inelastic dynamic behavior. These limitations have led to numerous further developments of the pushover concept in recent decades, which are discussed in Chapter 2.

2 Multi-mode and adaptive pushover concepts – state of research

2.1 Overview of widespread procedures

As explained in the previous chapter, single-mode non-adaptive pushover methods are based on the assumptions that, on the one hand, the dynamic structural response to an earthquake results from a single modal contribution and, on the other hand, that its modal shape changes only insignificantly due to inelastic load-bearing behavior. However, according to Kappos et al (2012) (Table 5.1), these two assumptions are only permissible for bridge structures in the case of short bridges on moderately stiff to stiff soil which are pinned at the abutments and either not supported by very short columns or by short side and long central columns. If, on the other hand, one or even several of the boundary conditions mentioned are not given, higher modes contribute significantly to the overall structural response. Due to plastic effects, the contributing mode shapes may also change to such an extent that this must be considered in the course of the calculation. For structures with such complex seismic behavior, either multi-storey buildings or bridges, numerous pushover methods have been developed, which can take several modal contributions into account or the change in mode shapes by adapting the mode proportional load patterns, or even both effects. This section provides a brief chronological overview of the most common concepts found in the literature, followed by a presentation of some outstanding approaches that are considered particularly suitable. Here, extensions with regard to the consideration of multidirectional earthquake excitations are deliberately excluded and later examined separately in Chapter 7.

Non-adaptive multi-mode concepts

The first multimodal pushover approach, the so-called *Multi-modal Pushover Procedure* (*MMP*), was developed by Paret et al (1996) and is based on a separate determination of pushover curves resulting from different modal load patterns and a subsequent separate application of the *CSM*. However, this method only allows qualitative conclusions to be drawn regarding the

relevance of certain modes, while it does not provide a specific quantitative determination of the overall structural response (ANTONIOU & PINHO , 2004a; HOLTSCHOPPEN , 2009). According to PARET ET AL (1996), the aim here is rather to detect the most critical modes and most probable damage locations. Six years later, CHOPRA & GOEL (2002) published the *Modal Pushover Analysis* (*MPA*), by far the most widespread multimodal non-adaptive pushover method. This procedure also includes separate modal analyses with subsequent determination of the associated performance points. Afterwards, the structural responses in the respective performance states are superimposed using the *SRSS* combination rule. The main limitations of this concept are, however, that it is based only on the modal properties determined for the elastic structure and that the subsequent *SRSS* combination does not capture any mutual influence of the nonlinear effects in the sense of damage accumulation (KALKAN & KUNNATH , 2004; PARASKEVA ET AL , 2006; WEI ET AL , 2011). At about the same time, MOGHADAM & TSO (2002) published the *Pushover Results Combination* (*PRC*), a method based on the *MMP* with subsequent combination of the modal contributions by a sum of the components weighted with the respective modal participation factors. The limitation of the *MPA*, however, is largely also valid to this method. Furthermore, there are procedures based on the combination of fundamental modes in different directions, such as the *Coupled Nonlinear Static Pushover* (*CNSP*) concept by CAMARA (2011), which, as already mentioned, are dealt with in Chapter 7.

Adaptive single-mode concepts

The earliest well-known concept of adapting incremental loads goes back to BRACCI ET AL (1997) with the *Adaptive Pushover Analysis* (*APA*). However, due to the single-mode approach, this concept is again very limited and can only utilize the advantage of load adaptions in a few cases. According to ANTONIOU & PINHO (2004a), even the extension by LEFORT (2000) to include force scaling to take account of higher mode effects does not provide satisfactory results. The *Adaptive Energy-based Pushover Analysis* (*AEPOA*) by ALBANESI ET AL (2002), published a little later, is based on the principle of energy equivalence with regard to the kinetic energy of a certain mode under earthquake excitation. However, ANTONIOU & PINHO (2004a) show that this method can sometimes lead to a considerable underestimation of the structural responses. Furthermore, this concept is not widely mentioned in the literature.

Adaptive multi-mode concepts

By far the largest number of advanced pushover procedures can be classified as adaptive and multi-mode approaches. The first notable advance in this area was made by GUPTA & KUNNATH (2000) with the so-called *Adaptive spectra-based Pushover Procedure* (*AsPP*), which was later further developed by KALKAN & KUNNATH (2006) with the *Adaptive Modal Combination*

(*AMC*). In this procedure, which is only suitable for conventional multi-storey buildings, modal storey loads are determined in each load step from the product of the modal participation factor, the eigenvector normalized to the modal mass, the storey mass and the spectral superelevation factor. Individual pushover analyses are carried out for each modal contribution within a load step and the total values are determined by an *SRSS* combination. The system stiffness is then updated followed by an eigenvalue analysis in order to renew modal load patterns of the next load step. However, Aydinoglu (2003) criticizes that the modal scaling is based on elastic spectral accelerations, which cannot correctly reflect the actual inelastic behavior. Furthermore, Antoniou & Pinho (2004a) and Themelis (2008) emphasize that the *SRSS* combination leads to the theoretical inconsistency that there is no equilibrium at the end of each load step. Moreover, it should be critically noted that even with the *AMC*, the eigenvectors are updated, but not the damping. A publication by Requena & Ayala (2000) also contains an early but much less widespread procedure, the so-called '*Two variations of adaptive pushover*'. While the method '2A' is based on *SRSS*-combined modal load components, in method '2B' the mode shapes themselves are superposed by means of the *SRSS* rule and a load vector corresponding to this fictitious, effective natural mode is formulated. For this load vector, equilibrium is satisfied in the subsequent performance state. However, any changing signs are eliminated by the squaring at load level according to the *SRSS* rule in both concepts ('2A' and '2B').

Another common method is the *Incremental Response Spectrum Analysis* (*IRSA*) by Aydinoglu (2003). Here, the modal incremental load vectors are weighted with so-called 'intermodal scaling factors' in order to ensure that the maximum modal spectral displacements are achieved in the same adaption step. After each incremental step, which leads to the occurrence of a new plastic effect, these factors – as well as the mode shapes themselves – are updated. However, a central point of criticism is again the subsequent *SRSS* combination of separately determined modal contributions to the structural response, which does not capture the intermodal damage accumulation. It is precisely this problem that has been solved in the further development of the *IRSA*, published by Norda (2012). This concept, the *Adaptive Multimodal Interaction Analysis* (*AMI*), is based on a linear combination of modal load vectors with varying signs in different load combinations. It retains, however, the main advantage of the *IRSA* by adapting the load distributions after each incremental step.

The *Force-Based Adaptive Pushover Algorithm* (*FAP*) by Antoniou & Pinho (2004a) and the *Displacement Based Adaptive Pushover Procedure* (*DAP*) by Antoniou & Pinho (2004b) should also be mentioned as further representatives of known multi-mode adaptive procedures. However, with regard to the first method itself, the authors state that the *SRSS* or *CQC* combination of modal load components is error-prone and does not necessarily represent the actual

characteristics of the dynamic system response in a satisfactory manner and therefore propose a weighted vectorial addition. The results of Pinho et al (2005) show some considerable deviations from the comparative results of nonlinear time history calculations. However, the results of the *DAP* in Pinho et al (2005) also show similarly large deviations in some cases, so that this concept, contrary to the authors' claims, does not appear to be fully suitable either. The so-called *Adaptive Version of Modal Pushover Analysis* (*VMPA-A*) by Sürmeli & Yüksel (2015), as well as the bidirectional extension of this procedure (Sürmeli & Yüksel , 2018), is far less widespread. This method also involves a subsequent *SRSS* combination of separately determined modal structural responses. However, the subsequent manual consideration of the interaction between bending moments and normal forces represents a rather cumbersome process. Finally, the relatively recent *Incremental Modal Pushover Analysis for Bridges* (IMPAβ) by Bergami et al (2020) should be mentioned, which is based on the *SRSS* combination of modal performance points. By additionally varying the earthquake level, a kind of multimodal capacity curve is gradually built up. This elaborate procedure, however, has not been validated as a perceptible improved approach compared to other existing concepts.

In the following section, special procedures that play a particular role in this dissertation are presented in more detail.

2.2   Presentation of selected procedures

Modal Pushover Analysis (*MPA*)

The *Modal Pushover Analysis* (*MPA*) by Chopra & Goel (2002) is based on separate analyses of different modes, whereby the procedure is similar to the linear *RSM* method. However, the *MPA* uses inelastic or reduced elastic response spectra resulting from empirical investigations. In a first publication (Chopra & Goel , 2002), this method was initially presented for two-dimensional systems and then extended to spatial investigations in a further publication (Chopra & Goel , 2004) in order to enable the consideration of several earthquake directions. In this chapter, only the two-dimensional basic concept is presented. Chapter 7 then deals with the extension to a multidirectional approach.

In the *MPA*, for each mode considered a separate pushover analysis with a load pattern proportional to the mass and corresponding mode shape is performed. The maximum displacement of the monitoring point, up to which the structure is pushed, is very important, as the pushover curves are then approximated linearly by two segments, strongly depending on the end point of the pushover curve. Ideally, the pushover analysis should be carried out until the true deformation state of the inelastic system under earthquake loading is reached. However, since this value

is unknown, an estimate of the maximum displacement must first be made. CHOPRA & GOEL were able to use the results of a previous time history calculation for this estimation, although these are generally not available. Therefore, the maximum displacement of the *mp* on the basis of an elastic response spectrum can be used as an initial estimate. This is obtained for each mode n under consideration by

$$\Delta_{mp,max,n,el.} = \beta_n \cdot \Phi_n(mp) \cdot S_{d,n,max}(T_{n,el.}, \xi_0) \tag{2.1}$$

and will generally be greater than the maximum displacement determined later using the *MPA*, since the maximum spectral response $(S_{d,n,max})$ is reduced due to plastic effects. It is not explained how the idealization of the pushover curves is actually carried out, but reference is made in both publications to the graphical representation (a) below.

(a) Idealized pushover curve   (b) Idealized capacity spectrum
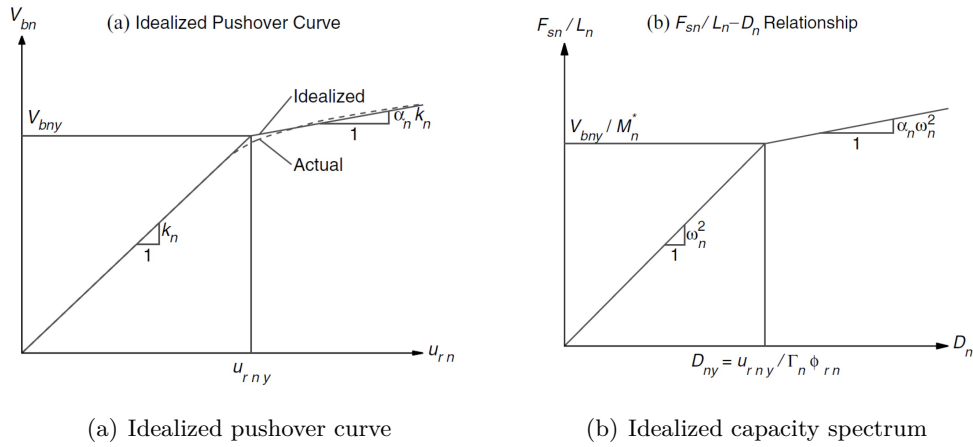
Figure 2.1: *Idealizations of the MPA (CHOPRA & GOEL , 2002)*

This suggests that the linearization is probably analogous to the *CSM*, where the initial slope of the pushover curve, the end point of the pushover curve and the requirement of an equal area represent the boundary conditions of the idealization. In contrast to the *CSM*, only the effective yield point then needs to be converted into an 'S_d-S_a' representation:

$$S_{d,y,n} = \frac{\Delta_{mp,y,n}}{\Phi_n(mp) \cdot \beta_n} \; , \tag{2.2}$$

$$S_{a,y,n} = \frac{F_{b,y,n}}{m_{eff,n}} \; . \tag{2.3}$$

This point can be used to determine the slope of the first branch of the linearized capacity spectrum, which should correspond to the squared effective natural circular frequency $(\omega_{n,eff,inel.})^2$ of mode n (cf. Fig. 2.1 (b)). However, if the actual initial stiffness is always adopted for the first linear segment in accordance with the above explanations, the effective yield point always

lies on a straight line with the same gradient, in the spectral representation namely the square of the elastic natural circular frequency. Since it is therefore not possible to determine $\omega_{n,eff}$ in a meaningful way, the idealization of the pushover curve should be carried out as in the *IRSA* (AYDINOGLU , 2003), which is considered below. Within the scope of this procedure, the tangential slope is prescribed at the end point of the pushover curve, while the initial slope is variable, again based on equal areas A_1 and A_2 (cf. Fig. 1.4). With this effective initial slope $(\omega_{n,eff,inel.})^2$, the effective inelastic natural period can then be determined as follows:

$$T_{n,eff,inel.} = 2\pi \cdot \sqrt{\frac{S_{d,y,n}}{S_{a,y,n}}} \ . \tag{2.4}$$

For this effective natural period, which is the central result of the modal pushover analysis, the maximum spectral displacement $S_{d,max,n,inel.}$ can now be looked up for each mode from an inelastic or damped elastic response spectrum and then transformed back accordingly:

$$\Delta_{mp,max,n,inel.} = \Phi_n(mp) \cdot \beta_n \cdot S_{d,n,max,inel.}(T_{n,eff,inel.}, \xi_{n,eff}) \ . \tag{2.5}$$

Alternatively, the maximum inelastic displacement can be calculated on the basis of a dynamic time history calculation on a modal inelastic SDOF model with a natural period of $T_{n,eff,inel.}$ and a corresponding damping. However, CHOPRA & GOEL (2002) do not formulate any specifications for this. In the final step, the structure is pushed again up to this inelastic target displacement, after which the required structural results are looked up. The overall results due to all modal contributions considered are then calculated using the *SRSS* or the *CQC* rule.

Incremental Response Spectrum Analysis (IRSA)

The *Incremental Response Spectrum Analysis (IRSA)* by AYDINOGLU (2003) is, as the name suggests, an incremental procedure based on the modal response spectrum method. Here, spectral displacement increments are applied for all modes under consideration. These are not chosen to be constant, but are determined in each incremental step in such a way that they lead to the emergence of a new plastic hinge. Furthermore, the spectral increments of the so-called accompanying modes are determined by a special scaling of the respective increment of the base mode, thus ensuring a parallel development and thereby achievement of the maximum spectral displacements of all modes. In contrast to many other methods, such as the *Adaptive spectra-based Pushover Procedure (AsPP)* by GUPTA & KUNNATH (2000), this intermodal scaling is based on inelastic spectral displacements corresponding to the current system properties. The individual steps that take place within an incremental step in the course of the *IRSA* are described below.

At the beginning of the *i*-th increment step, a modal analysis is performed on the basis of the current tangent stiffness matrix modified at the end of the last step. This provides the

natural frequencies and eigenvectors as well as the participation factors for all modes under consideration.

The maximum modal displacements $S_{d,n,max}^{(i)}$ are then determined for each mode n taken into account. For this purpose, the respective modal capacity spectrum up to the last known point is approximated by two linear segments. This idealization is defined, on the one hand, by a straight line through the end point with the current tangential gradient and, on the other hand, by a second straight line through the origin of the spectrum, so that the intersection of these two lines leads to equally large areas under the actual and the piecewise linearized capacity spectrum up to the current development point. This point of intersection then marks the next effective modal yield point $(S_{d,n,y}^{(i)}, S_{a,n,y}^{(i)})$ and defines the square of the corresponding effective natural circular frequency $\omega_{n,eff}^{(i)}$ by the slope of the first section (cf. Fig. 2.2 (a)). With this effective natural frequency of the current modal SDOF system, the associated maximum modal displacement $S_{d,n,max}^{(i)}$ can now be determined, according to AYDINOGLU (2003), either via a nonlinear time history calculation of an inelastic SDOF system with $\omega = \omega_{n,eff}^{(i)}$ or from a smooth elastic response spectrum using the effective period $T_{n,eff}^{(i)} = 2\pi/\omega_{n,eff}^{(i)}$.

(a) Idealized capacity spectrum

(b) Spectral displacement increment
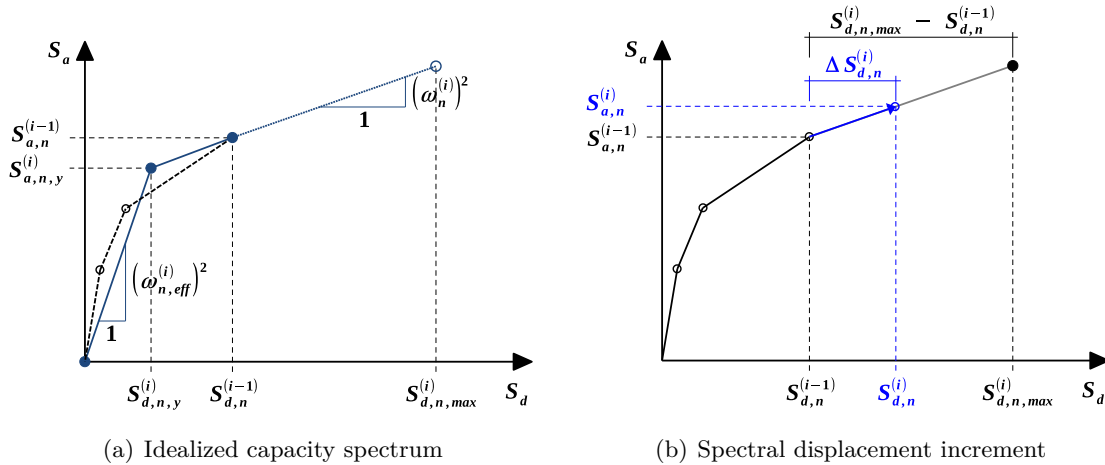
Figure 2.2: *Idealizations of the IRSA acc. to* AYDINOGLU *(2003)*

Based on the relationship between spectral displacements and accelerations according to Equation 1.20, a straight line with the gradient $(\omega_n^{(i)})^2$ could be drawn up to the initially fictitious end point $(S_{d,n,max}^{(i)}, S_{a,n,max}^{(i)})$, starting from the last known point $(S_{d,n}^{(i-1)}, S_{a,n}^{(i-1)})$ of the previously developed modal capacity spectrum (see Fig. 2.2 (b)). This intermediate solution would correspond to the case where the plastic hinge emerged in the previous step (*i-1*) is the last one that occurs in the entire structure. However, since this is generally not the case, except in the last step, the fictitious straight line starting from the point $(S_{d,n}^{(i-1)}, S_{a,n}^{(i-1)})$ must be scaled in such a

way that the new actual segment with the displacement increment $\Delta S_{d,n}^{(i)}$ only reflects the area up to the formation of the next yield point (cf. Fig. 2.2 (b)), so that the capacity spectrum in this section is linear. The initially unknown scaling factor $F^{(i)}$ for determining the actual modal displacement increments is defined as follows in accordance with the previous explanation:

$$\Delta S_{d,n}^{(i)} = F^{(i)} \cdot \left(S_{d,n,max}^{(i)} - S_{d,n}^{(i-1)} \right) \ . \tag{2.6}$$

However, instead of calculating this i-th, mode-independent scaling factor $F^{(i)}$ using the above definition and thus directly calculate all current modal displacement increments, AYDINOGLU chooses the already mentioned intermodal scaling, which refers to the base mode B:

$$\lambda_n^{(i)} = \frac{S_{d,n}^{(i)}}{S_{d,B}^{(i)}} = \frac{\left(S_{d,n,max}^{(i)} - S_{d,n}^{(i-1)} \right) \cdot F^{(i)}}{\left(S_{d,B,max}^{(i)} - S_{d,B}^{(i-1)} \right) \cdot F^{(i)}} = \frac{\left(S_{d,n,max}^{(i)} - S_{d,n}^{(i-1)} \right)}{\left(S_{d,B,max}^{(i)} - S_{d,B}^{(i-1)} \right)} \ . \tag{2.7}$$

This results in the following n-th modal displacement increment:

$$\Delta S_{d,n}^{(i)} = \lambda_n^{(i)} \cdot \Delta S_{d,B}^{(i)} \ . \tag{2.8}$$

It is worth mentioning at this point that the intermodal scaling factor $\lambda_n^{(i)}$ can be calculated directly, as all variables contained in the last (shortened) quotient of Equation 2.7 are known at this point. The question, however, is how large the new unknown $\Delta S_{d,B}^{(i)}$ in Equation 2.8 (instead of $F^{(i)}$ according to Eq. 2.6) must be in order to cause the next plastic hinge to occur as a result of all modal contributions.

The starting point for the determination is the following reverse transformation relationship based on intermodal scaling:

$$\Delta \mathbf{V}_n^{(i)} = \mathbf{\Phi}_n^{(i)} \cdot \beta_n^{(i)} \cdot \Delta S_{d,n}(i) = \mathbf{\Phi}_n^{(i)} \cdot \beta_n^{(i)} \cdot \lambda_n(i) \cdot \Delta S_{d,B}(i) \ , \tag{2.9}$$

$$\text{with } \mathbf{\Phi}_n^{(i)} \cdot \beta_n^{(i)} = \overline{\mathbf{V}}_n^{(i)} \left(\Delta S_{d,n} = 1 \right) \ . \tag{2.10}$$

Furthermore, the total increment of any response quantity r due to the modal increments $\overline{r}_n(i)$ for a modal unit displacement increment $\Delta S_{d,n} = 1$ and the known relationship between $\Delta S_{d,n}^{(i)}$ and $\Delta S_{d,B}^{(i)}$ is given as:

$$\Delta r_{tot}^{(i)} = \sqrt{\sum \left(\overline{r}_n(i) \cdot \Delta S_{d,n}(i) \right)^2} = \sqrt{\sum \left(\overline{r}_n(i) \cdot \lambda_n(i) \right)^2} \cdot \Delta S_{d,B}^{(i)} \ . \tag{2.11}$$

If the displacement state $\overline{\mathbf{V}}_n^{(i)}$ corresponding to this unit modal displacement increment is now applied to the current (i-th) FE model and the resulting bending moments $\overline{M}_{j,n}^{(i)}$ are calculated in each potentially relevant point j, the resulting total unit moment can be determined as follows:

$$\overline{M}_{j,tot}^{(i)} \left(\Delta S_{d,B} = 1 \right) = \sqrt{\sum \left(\overline{M}_{j,n}^{(i)} \left(\Delta S_{d,B} = 1 \right) \cdot \lambda_n^{(i)} \right)^2} \ . \tag{2.12}$$

The following relationship now applies to the formation of the next plastic hinge at a potential location j, whereby the additional influence of the normal force on the achievement of the yield moment $M_{j,y}$ is neglected:

$$M_{j,tot}^{(i-1)} + \Delta M_{j,tot}^{(i)} \stackrel{!}{=} M_{j,y} \; , \tag{2.13}$$

$$\text{with } \Delta M_{j,tot}^{(i)} = \overline{M}_{j,tot}^{(i)} \left(\Delta S_{d,B} = 1 \right) \cdot \Delta S_{d,B}^{(i)} \; . \tag{2.14}$$

Since the displacement increment of the reference mode is included linearly in this equation, it can be solved for as follows:

$$\Delta S_{d,B}^{(i)} = min \left(\frac{M_{j,y} - M_{j,tot}^{(i-1)}}{\overline{M}_{j,tot}^{(i)}} \right)_j \; . \tag{2.15}$$

With the now known modal displacement increment $\Delta S_{d,B}^{(i)}$ of the base mode and the likewise known relative modal scaling factors $\lambda_n^{(i)}$, the new points for all modal capacity spectra are obtained as

$$S_{d,n}^{(i)} = S_{d,n}^{(i-1)} + \lambda_n^{(i)} \cdot \Delta S_{d,B}^{(i)} \tag{2.16}$$

$$\text{and } S_{a,n}^{(i)} = S_{a,n}^{(i-1)} + \lambda_n^{(i)} \cdot \left(\omega_n^{(i)} \right)^2 \cdot \Delta S_{d,B}^{(i)} \; . \tag{2.17}$$

Now, it can be checked whether the spectral displacement $S_{d,B}^{(i)}$ of the reference mode has reached or even exceeded its current maximum value $S_{d,n,max}^{(i)}$, which would then be the case for all modes simultaneously due to the intermodal scaling. All structural responses of interest can then be calculated on the basis of the increments according to Equation 2.11 and the calculation is complete. If this is not yet the case, the stiffness matrix is updated with regard to the newly created plastic hinge and the next incremental step is started.

Adaptive Multimodal Interaction Analysis (AMI)

The *AMI* described below was developed by NORDA (2012) for the seismic calculation of masonry structures, but can in principle be applied to all types of structures. Overall, the *AMI* can be described as an extension of the previously presented *IRSA* by AYDINOGLU (2003). However, the special feature of this method is that all potentially relevant combinations k of the various signed modal components and earthquake directions are defined after an initial modal analysis of the elastic system. Also with regard to this method, the consideration of orthogonal ground motion excitations is neglected at this moment, as this will be dealt with in Chapter 7.

In a higher-level loop over these modal load combinations k, in each adaption step i after the update of all modal variables, such as $\boldsymbol{\Phi}_n^{(i)}$, $\beta_n^{(i)}$ and $S_{d,n,max}(i)$, a system calculation is performed

based on an incremental deformation vector $\mathbf{\Delta V}^{(i)}$ resulting from all modal contributions taken into account. Thus, the different mode components are considered simultaneously, so that the determination of the current tangent stiffness matrix $\mathbf{K}_T^{(i)}$ is based on all damage-relevant contributions or plasticization effects. In comparison to various other multimodal pushover methods, the subsequent modal superposition using the *SRSS* or *CQC* rule is thus avoided, which means that combinations with specific modal signs are possible. The relevant state variables (deformations and internal forces) can then be determined at the very end by means of an 'envelope' analysis of the individual calculation results for the respective combinations *k*. Analogous to the previously discussed *IRSA*, the detailed procedure in each adaption step is also presented with regard to the *AMI*.

The very first step, a modal analysis of the system based on the current stiffness distribution, and the subsequent calculation of effective modal yield points $(S_{d,n,y}^{(i)}, S_{a,n,y}^{(i)})$ and effective natural frequencies $\omega_{n,eff}^{(i)}$, are completely identical to *IRSA*. NORDA (2012) also deliberately uses the same two-segmented linearization of the modal capacity spectra according to AYDINOGLU (2003). Next, the maximum modal displacements $S_{d,n,max}^{(i)}$ are also determined as in the *IRSA* by using the effective natural period $T_{n,eff}^{(i)}(\omega_{n,eff}^{(i)})$. However, NORDA proposes the use of response spectra damped with $\xi_{n,eff}^{(i)}$. For the effective modal damping the following equation according to PRIESTLEY ET AL (2007) is used in the *AMI*:

$$\xi_{n,eff}^{(i)} = \xi_0 + \xi_{hyst} = 0.05 + 0.519 \cdot \frac{\mu - 1}{\mu \cdot \pi} \ . \tag{2.18}$$

It remains unclear, however, how the ductility factor μ should be calculated here. While it is described in the aforementioned original source by PRIESTLEY ET AL as the ratio Δ_d/Δ_y, i.e. the relation of the displacement of a representative node to an associated yield displacement, NORDA only states that μ results from the respective modal capacity spectrum. This would be given by the following relationship, whereby it is uncertain whether the formula of PRIESTLEY ET AL can also be applied to spectral quantities without further ado:

$$\mu = \frac{S_{d,n}^{(i-1)}}{S_{d,n,y}^{(i-1)}} \ . \tag{2.19}$$

The maximum modal displacements $S_{d,n}^{(i)}$ are then used to calculate the intermodal scaling factors according to AYDINOGLU (2003). But, in contrast to the *IRSA*, the displacement increment $\Delta S_{d,B}^{(i)}$ of the base mode is not determined in such a way that it leads to the formation of a new plastic hinge, but is set to a user-defined, constant value. All other modal increments $\Delta S_{d,n}^{(i)}$ or $\Delta S_{a,n}^{(i)}$ can then be calculated according to Equations 2.16 and 2.17.

The main difference between *IRSA* and *AMI*, however, is that the structural responses are not determined separately for each mode being subsequently combined, but the following signed linear combination is already formed during the formulation of the input vector for the FE calculation. In this case, it is an incremental displacement vector:

$$\Delta \mathbf{V}^{(i,k)} = \sum_n \alpha_n^{(k)} \cdot \beta_n^{(i)} \cdot \mathbf{\Phi}_n^{(i)} \cdot \Delta S_{d,n}^{(i)} \, , \tag{2.20}$$

with:

- $\alpha_n^{(k)} = -1 \vee 1$

- $\Delta S_{d,n}^{(i)} = \lambda_n^{(i)} \cdot \Delta S_{d,B}^{(i)}$ acc. to Eq. 2.8 .

It is worth noting that the modal displacement increments are based on intermodal scaling, which ensures simultaneous heading for the respective maximum values. However, the modal contributions themselves are not scaled any further, which means that in the performance state all modes would have to show their maximum response at the same time. In other words, this corresponds to the assumption of a perfect correlation of all modes, which will generally lead to a significant overestimation of the structural responses. NORDA herself also notes precisely this overestimation, although she does not attribute it to correlation effects. To overcome this problem, she therefore introduces the following mass reduction factor, the theoretical basis of which, however, is not readily apparent:

$$\frac{m_{eff,n}^{(i)}}{m_{tot}} \, . \tag{2.21}$$

As the above Equation 2.20 already includes the participation factor β_n, an additional scaling with a mass participation factor should at least be questioned.

For the pushover analysis, the vector of incremental deformations according to Equation 2.20 can then be used to determine an incremental load vector by multiplication with the current tangent stiffness matrix:

$$\Delta \mathbf{P}^{(i,k)} = \mathbf{K}_T^{(i,k)} \cdot \Delta \mathbf{V}^{(i,k)} \, . \tag{2.22}$$

After the subsequent FE calculation with this incremental load vector, starting from the last state (i-1), it is now checked whether a structural failure has occured. If so, the earthquake design proof has failed. However, if this is not the case, the next step is to check whether the modal spectral displacements have reached or exceeded their maximum, so that the performance state has been found and the next load combination can be investigated. If not, adaption step (i+1) follows.

2.3   Evaluation of existing calculation concepts

In principle, multimodal and adaptive pushover methods represent an improvement of the basic concept, as they are able to map higher mode effects or the change of mode shapes due to nonlinear seismic behavior. However, the multimodal methods differ in terms of whether the modal system properties are determined on the elastic or the current inelastic system and whether an overall structural response is determined as a result of all modal contributions and, if so, in which way. In most cases, a subsequent *SRSS* combination of the individual results takes place, which does not take into account any mutual influence of the nonlinear effects in the sense of damage accumulation. This aspect, however, is critical for complex structures and high earthquake intensities, where higher mode effects play a particularly important role. With regard to adaptive methods, it can also be noted that they differ mainly in whether equilibrium exists in the performance state and whether only the eigenvectors and mode proportional load patterns themselves are updated or also the modal damping. Another differentiation criterion refers to the question whether intermodal scaling is based on current inelastic system properties.

In view of this range of multimodal adaptive pushover concepts, the *IRSA* by AYDINOGLU (2003) and, in particular, the further developed *AMI* by NORDA (2012) stand out particularly positively. Both methods are based on the same approach of intermodal scaling factors in order to ensure a simultaneous achieving of the respective performance state of all modes, whereby these factors refer to the current inelastic spectral displacements. Concerning the determination of the latter AYDINOGLU and NORDA both propose a practical approach based on smooth response spectra, which is much less cumbersome than using time history calculations on nonlinear modal SDOF models. However, both procedures calculate the maximum spectral displacement $S_{d,n,max}^{(i)}$ on the basis of the effective natural period $T_{n,eff}^{(i)}$, which results from the slope $\left(\omega_{n,eff}^{(i)}\right)^2$ of the elastic branch in the idealized capacity spectrum. According to the well-known *equal displacement rule* it is assumed that spectral displacement of the (effective) elastic and the inelastic system are practically equal to each other. Thus, the corresponding spectral acceleration can be estimated by projecting the intersection point of the extrapolated effective linear elastic branch with the response spectrum onto the capacity spectrum (see Fig. 2.3). This assumption, however, does not appear to be necessary, as the intersection of the modal capacity spectrum itself with the response spectrum can be used analogously to the *CSM* without additional effort. As the capacity curve is only built up step by step, it must be extrapolated from the last point (*i-1*) with the current tangential gradient $\left(\omega_{n,eff}^{(i)}\right)^2$ (see turquoise line in Fig. 2.3). The error resulting from this extrapolation, however, decreases as the performance state is approached and finally almost disappears completely. Hence, this alternative approach is used in the specially *modified AMI* (*mAMI*) (see. Sec. 3.1.1).
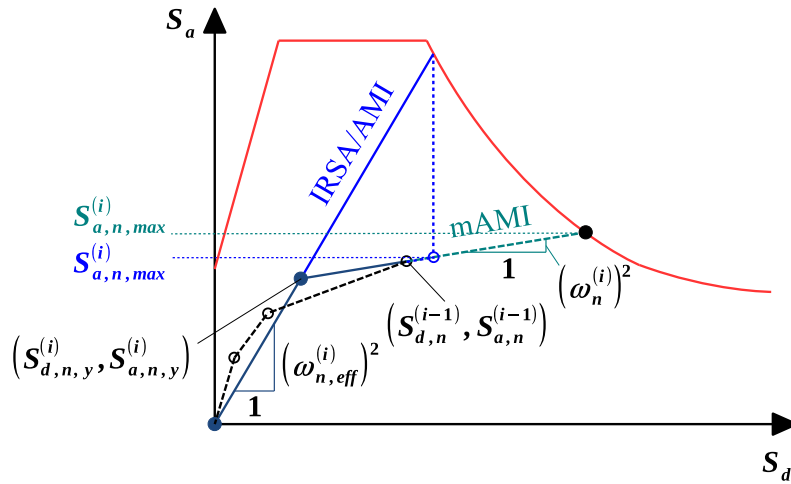
Figure 2.3: *Comparison of the $S^{(i)}_{a,n,max}$ determination for the IRSA, AMI and mAMI*

The subsequent calculation of the displacement increment for the base mode also appears to be relatively complex in the *IRSA*, as the formation of the next plastic hinge must be evaluated separately for all potentially relevant points. Furthermore, this procedure is obviously oriented towards plane frame systems without large vertical loads, since no interaction effects are taken into account in the corresponding formula and a successive development of distributed plastic zones cannot be reproduced. The approach of an arbitrarily selectable constant increment $\Delta S_{d,B}$ in the *AMI*, on the other hand, is much easier to implement. However, it could be difficult in practical applications to define a reasonable value in advance that captures critical areas accurately enough without leading to an excessive total number of adaption steps and thus an unacceptable calculation time. Particularly in case of a large initial linear-elastic branch, which could theoretically be represented by a single increment, many unnecessary adaption steps could be avoided. In addition, the general determination of the incremental load vector has two disadvantages:

1. Spectral displacements must first be determined from the normative acceleration spectra via the pseudo-spectra relationship.

2. The tangent stiffness matrix must be re-evaluated in each incremental step or read out from the FE software used to determine $\Delta\mathbf{P}(\Delta\mathbf{V})$.

The calculation of the final structural responses in the *IRSA* is based on an *SRSS* combination, taking place, however, only at the end of each adaption step. The separate modal investigations in the next step are thereby based on the previous nonlinear effects of all modes. The modal superposition in the form of a linear combination at load level in the course of the *AMI* has the advantage that combinations of the considered modes with varying signs are possible. However,

since the respective maximum modal responses do not occur simultaneously in reality, the correlation of different modes must be taken into account. The mass participation factor applied by NORDA admittedly is not an adequate solution for this. Furthermore, the *AMI* concept could lead to a large number of load combinations to be calculated if many modes are relevant, which could make it unattractive to use. This aspect should be kept critically in mind during application.

Finally, it should also be noted that neither method provides for an initial calculation of the dead loads considering P-Delta effects, which can, however, play a major role in the case of large normal compressive forces and significant horizontal displacements. Both aspects are potentially present in bridge piers, so that gravitational loads in combination with second order effects should generally be taken into account in the course of nonlinear seismic analyses of bridges (cf. EUROCODE 8 - PART 2 (2011), Sec. 4.2.4.1 & 4.2.5). Furthermore, it should be emphasized that the separate modal capacity spectra considered in both methods (*IRSA* & *AMI*), as well as in the *MPA*, are based on the pseudo-spectra relationship. This assumes, on the one hand, that the respective modal structural response is harmonic and, on the other hand, that the relative system deformations are significantly larger than the ground movements (so that $v_{rel} \approx v_{tot}$). However, both aspects are reasonable in case of the broadband excitation of an earthquake with resonant amplification of the respective natural frequency, regarding separate modal SDOF systems. Nevertheless, the spectral displacements $S_{d,n}$ are not geometrically interpretable before the reverse transformation and only refer to the fictitious modal SDOF systems. It is also worth mentioning that incremental methods such as *IRSA* or *AMI* assume piecewise linear behavior between the relevant plastic effects in the modal capacity spectra. This is the only way to justify an adapted modal decomposition on the basis of updated inelastic SDOF systems.

According to the current state of science, the basic aspects of the *AMI*, in particular due to the modal combination at load level, are considered to constitute the most accurate static approach with the greatest potential to determine realistic seismic responses even for complex bridges. Nevertheless, some theoretical weaknesses and points of criticism with regard to practical application were identified in this chapter, the elimination of which forms a central part of this dissertation.

2.4   Scope of the dissertation

Even the best rated sophisticated static nonlinear calculation method in the previous chapter, the *AMI* by NORDA (2012), is generally not able to represent the inelastic seismic load-bearing behavior of complex bridges with sufficient accuracy. Therefore, within the scope of this doctoral thesis, the currently still existing deficits of this procedure are eliminated by comprehensive

optimizations and extensions. The main focus lies on the consideration of a damage accumulation of different modal contributions and in applying a realistic correlation as well as a reasonable representation of multidirectional excitations. Thus, the method has the potential to provide a better agreement with the results of nonlinear time history calculations than other existing methods, especially for complex bridge structures. This is to be worked out within the scope of the present doctoral thesis. In addition, the basis for a practical application is to be created by further algorithmic optimizations with respect to the restriction to necessary adaption steps, so that the computing time can be considerably reduced.

The following chapter 3 first contains a comprehensive explanation of the aforementioned theoretical optimizations and extensions of the *AMI*.

3 Modification and further development of the *AMI*

3.1 Explanation of the individual optimizations and extensions

3.1.1 Overview

The main part of the dissertation is the modification and further development of the *AMI*, which is referred to as *modified AMI*, or *mAMI* for short. The respective optimizations and extensions of the *AMI* that were made in order to eliminate the weaknesses identified in Chapter 2 are listed below:

1. For the dead loads, an initial nonlinear static calculation taking into account P-Delta effects is performed, which is followed by the first modal analysis.

2. In order to avoid the determination of the incremental load vector via the relationship $\mathbf{K}_T \cdot \Delta \mathbf{V}$, the load pattern is determined with inertial forces, as it is the custom in static earthquake methods. The corresponding load vector is thus proportional to mass and mode shape, potentially including load components in all three Cartesian coordinate directions.

3. Norda (2012) applies the ductility factor μ from Priestley et al (2007), which was actually derived for node displacements v_j, to spectral displacements S_d in order to calculate $\xi_{n,eff}(i)$, without justifying this in more detail. The *modified AMI* determines the effective damping as in the *CSM* according to ATC-40 (1996) (cf. Section 1.3 of this thesis, Eqs. 1.21 to 1.24 and Tab. 1.1).

4. The estimation of the maximum spectral acceleration $S_{a,n,max}^{(i)}$ is based on an extrapolation of the corresponding modal capacity spectrum with the tangent slope of the latter in the last point $(i\text{-}1)$ instead of using $T_{n,eff}^{(i)}$ and the *equal displacement rule* (cf. Fig. 2.3).

5. A correlation factor α_n is introduced which, unlike the mass participation factor proposed by Norda , captures actual correlation effects for all modal contributions beyond the base mode.

6. In addition, instead of using a constant spectral increment for the reference mode, a determination of optimized increments is implemented. In contrast to the *IRSA*, however, these do not have to lead to the explicit formation of a new plastic hinge. Instead, in order to be able to capture the successive formation and development of distributed plastic zones, the determination is based on both a local and a global investigation of the pushover curve. The local examination detects kink points, while the global one identifies specific deviations between the initial slope of the current segment and the slopes of the further points. The second check in particular ensures that even continuous developments of plastic zones can be detected.

Points 2, 5 and 6 require detailed derivations, which are given in detail below.

3.1.2   Revised determination of the incremental load vector

As already mentioned, the incremental load vector should no longer be based on the expression '$\mathbf{K}_T \cdot \Delta\mathbf{V}$', as proposed by Norda , but on inertia forces via '$\mathbf{M} \cdot \Delta\ddot{\mathbf{V}}$'. As a result, the load vector is independent of the vector $\Delta\mathbf{V}$, which frequently results from pseudo-spectral displacements S_d, and of the tangent stiffness matrix $\mathbf{K}_T$.

The alternative calculation now is based on the requirement that both approaches can be converted to the other and thus cause the same reaction forces in a structure subjected to an equal seismic input. This is shown below for a fictitious modal contribution n with linear-elastic seismic behavior (according to Meskouris et al (2011), Section 3.1). The restoring forces of an elastic system under earthquake loading can initially be calculated from the spectral displacement of the n-th mode as follows:

$$\mathbf{S}_n = \mathbf{K} \cdot \mathbf{V}_n = \mathbf{K} \cdot \mathbf{\Phi}_n \cdot \beta_n \cdot S_{d,n} \ . \tag{3.1}$$

As the n-th eigenvector $\mathbf{\Phi}_n$ results from the generalized eigenvalue problem $(\mathbf{K} - a_n \cdot \mathbf{M}) \cdot \mathbf{\Phi_n} = \mathbf{0}$, the following applies to the matrices $\mathbf{M}$ and $\mathbf{K}$:

$$\mathbf{K} \cdot \mathbf{\Phi}_n = a_n \cdot \mathbf{M} \cdot \mathbf{\Phi}_n \ , \tag{3.2}$$

whereby $a_n = \omega_n^2$. This relationship (Eq. 3.2) can be used to substitute the product $\mathbf{K} \cdot \mathbf{\Phi}_n$ in Equation 3.1:

$$\mathbf{S}_n = \left(\omega_n^2 \cdot \mathbf{M} \cdot \mathbf{\Phi}_n \right) \cdot \beta_n \cdot S_{d,n} = \mathbf{M} \cdot \left(\mathbf{\Phi}_n \cdot \beta_n \cdot \omega_n^2 \cdot S_{d,n} \right) \ . \tag{3.3}$$

Using the pseudo-spectra relationship $S_{a,n} = \omega_n^2 \cdot S_{d,n}$, Equation 3.3 can be converted into the following form, which corresponds to the static equivalent load vector for the modal contribution n based on inertia forces:

$$\mathbf{S}_n = \mathbf{M} \cdot (\mathbf{\Phi}_n \cdot \beta_n \cdot S_{a,n}) = \mathbf{M} \cdot \ddot{\mathbf{V}}_n = \mathbf{P}_n \ . \tag{3.4}$$

It was thus shown that the internal reaction force components for the modal contribution n can be determined from the product of the stiffness matrix and the displacement vector on the one hand and, on the other hand, equally via the product of the mass matrix and the vector of the nodal accelerations. In order to be able to use this in the nonlinear *mAMI* calculation, the above relationship must be related to the tangent stiffness matrix and the corresponding eigenvectors in i-th step of the incremental approach.

For this purpose, a sum of all modal contributions scaled with the sign factor α_n according to NORDA (2012) is introduced. By substituting $\mathbf{K}_T^{(i,k)} \cdot \Delta\mathbf{V}^{(i,k)}$ (in Eqs. 2.20 and 2.22 of the original *AMI*) for $\mathbf{M} \cdot \Delta\ddot{\mathbf{V}}^{(i,k)}$ and neglecting the already questioned mass participation factor proposed by NORDA , the following equation is obtained for the new incremental load vector of the k-th load combination in step i:

$$\Delta\mathbf{P}^{(i,k)} = \mathbf{K}_T^{(i,k)} \cdot \Delta\mathbf{V}^{(i,k)} \Leftrightarrow \Delta\mathbf{P}^{(i,k)} = \mathbf{M} \cdot \Delta\ddot{\mathbf{V}}^{(i,k)} \tag{3.5}$$

$$\Delta\mathbf{P}^{(i,k)} = \mathbf{K}_T^{(i,k)} \cdot \sum_n \alpha_n^{(k)} \cdot \mathbf{\Phi}_n^{(i)} \cdot \beta_n^{(i)} \cdot \Delta S_{d,n}^{(i)} \Leftrightarrow \Delta\mathbf{P}^{(i,k)} = \mathbf{M} \cdot \sum_n \alpha_n^{(k)} \cdot \mathbf{\Phi}_n^{(i)} \cdot \beta_n^{(i)} \cdot \Delta S_{a,n}^{(i)} \ . \tag{3.6}$$

The right-hand side of the above Equation 3.6 is now reshaped so that the sum contains the incremental load vector of each modal contribution. In addition, each modal load vector is related to the acceleration increment of the base mode B via the relationship $\Delta S_{a,n}^{(i)} = \lambda_n^{(i)} \cdot \Delta S_{a,B}^{(i)}$ (following Eq. 2.8, with $\lambda_n^{(i)}$ = intermodal scaling factor of the *IRSA*, cf. Sec. 2.2):

$$\Delta\mathbf{P}^{(i,k)} = \sum_n \alpha_n^{(i,k)} \cdot \mathbf{M} \cdot \mathbf{\Phi}_n^{(i)} \cdot \beta_n^{(i)} \cdot \lambda_n^{(i)} \cdot \Delta S_{a,B}^{(i)} \ . \tag{3.7}$$

In this Equation 3.7 for the incremental load vector of the *mAMI*, the factor $\alpha_n^{(i,k)}$ is no longer a pure modal sign factor ($-1 \vee 1$), which only depends on the current load combination k. In the *mAMI* it also captures the intermodal correlation. Its derivation can be found in Section 3.1.3. Overall, this factor in the *mAMI* therefore contains the modal sign of the mode n in the current combination k (acc. to NORDA) as well as the current (i-th) scaling factor refering to the intermodal correlation.

In addition, it is worth mentioning that Equation 3.7 refers to a specific investigated earthquake direction, since the simultaneous consideration of several excitation components is only discussed in Chapter 7. Nevertheless, the load vector may include components in all three orthogonal coordinate directions if there are relevant spatial mode shapes, as is typical, for example, due to the coupling by the cables for cable-stayed bridges (see Fig. 3.1), or also for horizontally curved bridges. This should be emphasized explicitly, as the following notation (Eq. 3.8) is commonly used, both in the literature and in numerous standards, for the force component of node j and

mode n for load distributions proportional to mass and mode shape:

$$F_{n,j} = F_b \cdot \frac{m_j \Phi_{n,j}}{\sum_n m_j \Phi_{n,j}} \ . \tag{3.8}$$

Both the base shear F_b and the eigenvector component $\Phi_{n,j}$ of the node j tacitly refer to a specific earthquake direction. Thus, the conclusion can be drawn that Equation 3.8 assumes the sole occurrence of eigenvector or load components in the direction of ground motion under consideration. Formulation 3.7, however, does not make this assumption. Nevertheless, Appendix A contains a derivation of how the widely used load approach according to the above Equation 3.8 can be converted into a spatial formulation.
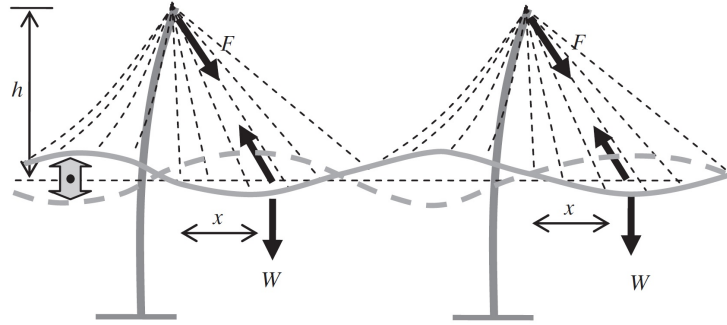
Figure 3.1: *Coupled longitudinal and vertical mode of a cable-stayed bridge (CALVI ET AL , 2013)*

3.1.3   Modal combination based on a partial correlation

As already explained, the summation of the modal components when determining the incremental load vector (acc. to Eq. 3.7) should include the intermodal correlation. Although the eigenmodes themselves are linearly independent, modal responses can be more or less strongly correlated depending on the frequency and damping ratio. The *CQC* rule is therefore generally more suitable but numerically not more expensive than the *SRSS* superposition ($\hat{=}$ *CQC* rule for $\rho_{nm} = 0$) which is only valid for decorrelated modes (WILSON ET AL , 1981). In principle, it would be conceivable to perform a *CQC* superposition of all modal contributions for each load component P_j. However, this would cause all the signs of the individual forces to be eliminated by squaring. Therefore, this procedure would only lead to sensible results if all modes n had positive displacement components at all nodes. Since this is not the case in reality, an alternative approach must be chosen in order to take account of the actual qualitative load distributions of the respective modes, maintaining the corresponding sign changes.

Against this background, the only option is to sum up the modal load vectors via a linear combination, where a corresponding reduction factor can be applied to each vector. However,

in order to bundle the intermodal correlation effects of each mode into a single scaling factor, a simplification must be made. It is hence assumed that the fundamental mode dominates the structural response to such an extent that it is sufficient to only consider the correlation of each additional mode with this fundamental mode. The correlation of two accompanying modes, on the other hand, must be neglected. As a consequence of this simplification, the correlation with the reference mode can now be considered separately for each accompanying mode n and a corresponding reduction factor can be determined. The load vector of the reference mode is therefore always scaled by a factor of 1.0. For determining the n-th reduction factor, an equation must now be found that describes the intermodal correlation between the modes B and n in relation to a representative variable. Since the factor later scales the n-th incremental load pattern, the resultant of this vector is used as the representative variable, i.e. the respective base shear increment. The basic concept of the determination is now that the linear combination of the two base shear increments $\Delta F_{b,B}^{(i)}$ and $\Delta F_{b,n}^{(i)}$, in which the base mode also enters 1.0-fold, should correspond to the actual *CQC* superposition of both increments:

$$1.0 \cdot |\Delta F_{b,B}^{(i)}| + \alpha_n^{(i)} \cdot |\Delta F_{b,n}^{(i)}| \stackrel{!}{=} \Delta F_{b,CQC,B-n}^{(i)} \ , \tag{3.9}$$

$$\text{whereby } \Delta F_{b,CQC,B-n}^{(i)} = \sqrt{ \left[|\Delta F_{b,B}^{(i)}| \quad |\Delta F_{b,n}^{(i)}| \right] \cdot \begin{bmatrix} \rho_{BB}^{(i)} & \rho_{Bn}^{(i)} \\ \rho_{nB}^{(i)} & \rho_{nn}^{(i)} \end{bmatrix} \cdot \begin{bmatrix} |\Delta F_{b,B}^{(i)}| \\ |\Delta F_{b,n}^{(i)}| \end{bmatrix} } \ . \tag{3.10}$$

The *CQC* factors ρ depend on the eigenfrequencies and the modal damping. For the latter, the effective modal damping $\xi_{n,eff}^{(i)}$ based on the respective hysteresis energy according to ATC-40 (1996) (cf. Section 1.3 of this thesis, Eqs. 1.21 to 1.24) is considered. By solving Equation 3.9 for $\alpha_n^{(i)}$, the following equation for determining the correlation factor $\alpha_n^{(i)}$ is finally obtained:

$$\alpha_n^{(i)} = \frac{\Delta F_{b,CQC,B-n}^{(i)} - |\Delta F_{b,B}^{(i)}|}{|\Delta F_{b,n}^{(i)}|} \ . \tag{3.11}$$

Overall, this concept of correlation factors assumes that the decisive fundamental mode reaches its maximum impact and the accompanying modes n are reduced according to their correlation with the reference mode. Since the result of Equation 3.11 is always positive due to the deliberately used absolute values, the factor $\alpha_n^{(i)}$ can still cover the original sign of mode n in combination k provided by NORDA (2012) in the course of determining $\Delta \mathbf{P}^{(i,k)}$. In other words, the factor $\alpha_n^{(i)}$ later is both a sign and a correlation factor. The influence of considering the linear correlation approach presented is examined in Section 6.3.

3.1.4   Approach of optimized adaption steps

The last central extension of the *AMI* pursues the goal of reducing the number of adaption steps to a minimum without neglecting relevant system changes. This can only be achieved by adapting the spectral acceleration increments of the base mode to the occurrence of relevant plastic effects. In contrast to the *IRSA*, however, no analytical determination of the optimized step sizes is implemented here, as this is considered too complex and it is reduced to a binary consideration of emerged or inactive plastic hinges. Since the aim of the *modified AMI* is to be able to also depict successive formations of plastic zones, a different approach must therefore be pursued. The implementation in the *mAMI* is thus based on the assumption that relevant system changes due to nonlinear seismic behavior can be detected by means of a sudden or a successive change in the slope of the pushover curve. The specific procedure for identifying relevant plastic effects is explained in detail below.

Detection of relevant nonlinear effects

The nonlinear pushover curves are computed by an incremental-iterative path-tracing algorithm; in this work the *Newton-Raphson* method has been used. Nonlinearity is introduced by geometrically nonlinear effects, i.e. the second-order P-Delta effect, and physical nonlinearities caused by cracking of concrete or yielding of reinforcement. The modelling of inelastic effects is addressed in Chapter 4.

One of the constituting, name-giving properties of the *mAMI* is its adaptiveness: eigenfrequencies and eigenmodes are continually updated as the system siffness is degraded due to the growing nonlinear effects. Theoretically, such an update should occur at each step. Steps, however, may be small to achieve good path-tracing properties so that continuous updates are unnecessary. A re-calculation of modes is only necessary if the incremental stiffness degradation surpasses a suitable threshold. Degrading of stiffness manifests in two ways, c.f. Figure 3.2:

- A concentrated plastic zone, commonly denoted as plastic hinge, is activated. This leads to a sudden decrease in stiffness which becomes visible by a kink in the load-displacement curve. The stiffness degradation is then a local phenomenon that occurs at the specific point in the pushover curve where the hinge opens. For its detection a local criterion will be developed in the following.

- Nonlinearities develop smoothly by the formation of distributed plastic zones which grow continually over the cross-section and along the beam lenght. Locally the pushover curve remains smooth – the stiffness degradation is a global accumulative effect that can only be detected by analyzing a whole segment of the curve.
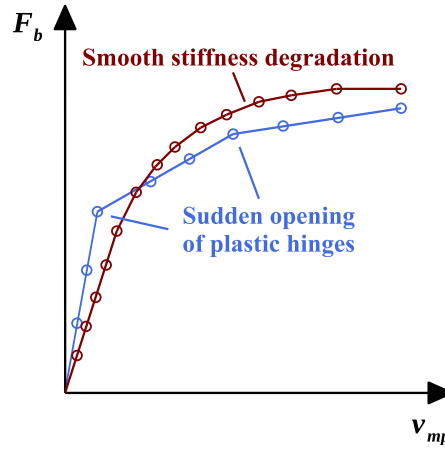
Figure 3.2: *Different types of stiffness degradation*

A suitable measure for the siffness degradation is the slope of the pushover curve that plots the total base shear F_b over the displacement of the monitoring point mp. The slope is approximated by the linear interpolation between two neighboring ('pushover') points p and $p + 1$:

$$sl^{(i),(p)} = \frac{F_b^{(i),(p+1)} - F_b^{(i),(p)}}{v_{mp}^{(i),(p+1)} - v_{mp}^{(i),(p)}} \ , \tag{3.12}$$

where the index i denotes the i-th adaption step and p is the index of the load step within the i-th adaption step. Thus, p is also an internal index for all points of the i-th segment of the pushover curve. According to Equation 3.12 $sl^{(i),(p)}$ describes the 'forward' slope relevant when progressing from point p to $p + 1$. The point p itself, however, does not have a specific gradient due to the non-continuous derivative of the piecewise linear pushover curve at this point.

(a) Case 1: Local analysis

(b) Case 2: Global analysis
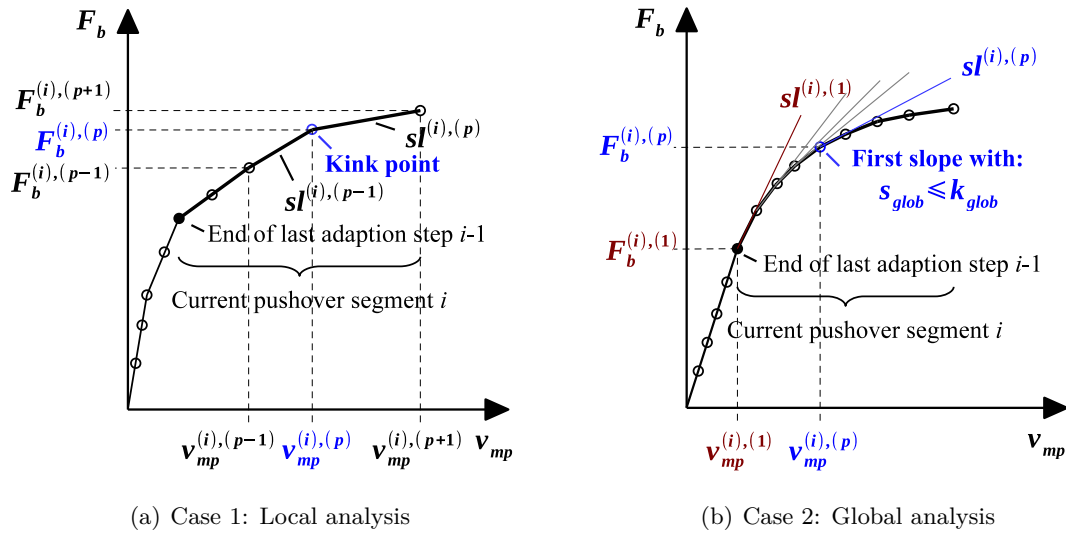
Figure 3.3: *Local and global analysis of the pushover curve in the mAMI*

Case 1: Detection of kinks

A point p is analyzed by calculating the slopes between p and its two neighboring points $p-1$ and $p+1$ according to Equation 3.12 (see Figure 3.3 (a)). A suitable stiffness degradation measure s_{loc} is given by the ratio between the smaller slope and the larger slope:

$$s_{loc} = \frac{min(sl^{(i),(p-1)}, sl^{(i),(p)})}{max(sl^{(i),(p-1)}, sl^{(i),(p)})} \leq k_{loc} . \tag{3.13}$$

A kink occurs if s_{loc} is smaller than some threshold value k_{loc}. The threshold value must be chosen by the user who can thereby control accuracy and computational effort of the *mAMI*.

Case 2: Detection of a continuous stiffness degradation

The check of the continuous stiffness degradation encompasses a whole segment of the pushover curve, starting from the point where the last adaption occurred, i.e. the first point $p = 1$ of the current (i-th) segment of the pushover curve (see Figure 3.3 (b)). The initial slope $sl^{(i),(1)}$ between points 1 and 2 is computed via Equation 3.12. Then the slopes of subsequent segments p are computed analogously and compared to the initial slope to define the global stiffness degradation s_{glob} between the internal segments 1 and p of the i-th overall segment of the pushover curve:

$$s_{glob} = \frac{min(sl^{(i),(1)}, sl^{(i),(p)})}{max(sl^{(i),(1)}, sl^{(i),(p)})} \leq k_{glob} . \tag{3.14}$$

The analysis stops once s_{glob} falls below a threshold value k_{glob} whose value is once again set by the user.

The above discourse tacitly assumed a monotonically decreasing stiffness of the pushover curve; therforce the consistent use of the term 'degradation'. This, however, need not necessarily be the case. In contrast to the graphical representations frequently used in literature, a pushover curve can also experience a re-stiffening. This at first glance surprising behavior can be caused by redistribution effects and activation of tensile reinforcement in areas of cracked concrete. Against this background, the minimum of the respective slopes must be set in relation to the maximum for both criteria, instead of simply dividing the later slope by the previous one. The following Figure 3.4 visualizes the fulfilment of various k_{loc} and k_{glob} criteria between 0 and 1 for ficticious idealized pushover curves.

(a) k_{loc} (b) k_{glob}
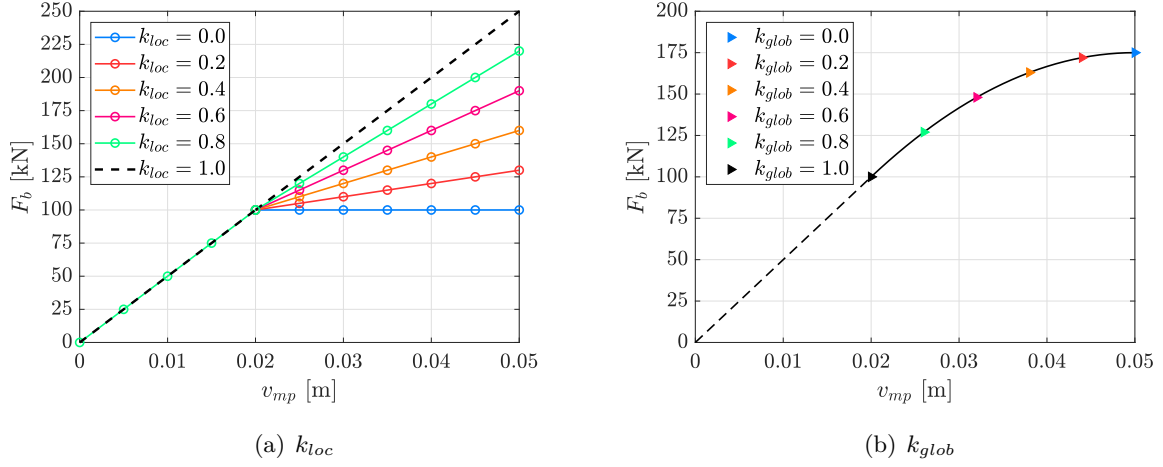
Figure 3.4: *Visualization of various k_{loc} & k_{glob} criteria for the mAMI*

Realization of the automated step control within the *mAMI*

Now that it has been explained in detail how suddenly occurring and continuously increasing plastic effects are identified, the embedding of these analyses in the overall *mAMI* calculation process must be considered. According to Equation 3.7, the only control parameter in terms of automated step control is the size of the spectral increment $\Delta S_{a,B}^{(i)}$, i.e. the increment of the spectral acceleration of the base mode B. Against this background, the question arises as to how the identification of relevant plastic effects is related to the determination of this spectral increment and which calculations are required in advance and afterwards.

In the first *mAMI* step, $\Delta S_{a,B}^{(1)}$ is set to $S_{a,B,max}^{(1)}$ so that the reference mode and thus also all accompanying modes reach the respective maximum acceleration $S_{a,n,max}^{(1)}$. In this step, $S_{a,n,max}$ can be determined analogously to the *RSM* without taking nonlinear effects into account. The corresponding load increment vector $\Delta \mathbf{P}_{max}^{(1)}(\Delta S_{a,n,max}^{(1)})$ is then used to perform an initial nonlinear static calculation, later referred to as 'Max computation', whose pushover curve is analyzed afterwards. This analysis is now used to determine the point up to which the initial (elastic) system properties are valid. The point at which the pushover curve deviates too much from the initial linear branch is to be defined as the first limiting point. As a new calculation in the applied FE program *SAP2000* can only be continued from the end of a calculation that has already been completed, a correction calculation must now be carried out up to this limiting point. This static calculation is followed by a renewed modal analysis. With the updated modal properties the load distribution as well as the effective modal damping values $\xi_{n,eff}^{(2)}$ and the maximum modal accelerations $S_{a,n,max}^{(2)}$ can be recalculated. As already noted in Section 2.3,

the latter is achieved by a superposition of the response spectrum for a modal damping ratio of $\xi_{n,eff}^{(2)}$, and the extrapolated modal capacity spectrum (cf. Fig. 2.3).

Starting from the final state of the correction calculation, a new calculation is then performed with $\Delta\mathbf{P}_{max}^{(2)}(\Delta S_{a,n,max}^{(2)})$, whereby $\Delta S_{a,n,max}^{(2)}$ describes the difference between $S_{a,n,max}^{(2)}$ and the last existing value $S_{a,n,end}^{(1)}$ of the previous step 1. Following this calculation, it must then be checked at which point within the new segment of the pushover curve a relevant plastic effect can be detected. This entire procedure is repeated until the pushover curve resulting from the *i*-th 'Max computation' no longer requires a new correction step.

The previously explained limiting criteria (cf. Eqs. 3.13 & 3.14) generally lead to different points $(v_{mp}, F_b)_{lim,loc}^{(i)}$ and $(v_{mp}, F_b)_{lim,glob}^{(i)}$. Hence, the point that occurs first is the target point $(v_{mp}, F_b)_{target}^{(i)}$. The base shear $F_{b,target}^{(i)}$ corresponding to this point is then used to calculate a new target increment:

$$\Delta F_{b,target}^{(i)} = F_{b,target}^{(i)} - F_{b,end}^{(i-1)} \ . \tag{3.15}$$

With this increment and the existing increment of the current 'Max computation', a corresponding correction factor $\Gamma^{(i)}$ can finally be calculated:

$$\Delta F_{b,target}^{(i)} = \sum_j \Delta P_{j,target}^{(i)} \overset{!}{=} \sum_j \Delta P_{j,max}^{(i)} \cdot \Gamma^{(i)} \tag{3.16}$$

$$\Leftrightarrow \Gamma^{(i)} = \frac{\Delta F_{b,target}^{(i)}}{\sum_j \Delta P_{j,max}^{(i)}} \ . \tag{3.17}$$

Due to the linear relationship between load pattern and base shear, the load increment vector $\Delta\mathbf{P}^{(i)}$ is scaled accordingly based on this factor so that the correction calculation can be carried out. It should be noted that $\sum_j \Delta P_{j,max}^{(i)}$ should be used instead of the theoretical value $\Delta F_{b,max}^{(i)}$ ($= |\Delta\mathbf{P}_{max}^{(i)}|$) in Equation 3.17, as in some cases the system may not be able to fully absorb the applied loads $\Delta\mathbf{P}_{max}^{(i)}$ and $\sum_j \Delta P_{j,max}^{(i)}$ can thus significantly fall below $\Delta F_{b,max}^{(i)}$.

In addition, a corresponding capacity spectrum must be built up successively for each mode, which is used to determine the effective modal damping $\xi_{n,eff}^{(i)}$ and the maximum acceleration $S_{a,n,max}^{(i)}$. For this purpose, $\Delta S_{a,n}^{(i)}$ and $\Delta S_{d,n}^{(i)}$ are calculated as follows in each correction step:

$$\Delta S_{a,n}^{(i)} = \Gamma^{(i)} \cdot \Delta S_{a,n,max}^{(i)} \text{ and} \tag{3.18}$$

$$\Delta S_{d,n}^{(i)} = \frac{\Delta S_{a,n}^{(i)}}{\left(\omega_n^{(i)}\right)^2} \ . \tag{3.19}$$

This results in the new points of the modal capacity spectra for all modes considered:

$$\left(S_{d,n}^{(i)}, S_{a,n}^{(i)}\right) = \left(S_{d,n}^{(i-1)} + \Delta S_{d,n}^{(i)}, S_{a,n}^{(i-1)} + \Delta S_{a,n}^{(i)}\right) \ . \tag{3.20}$$

This separate determination of the corrected acceleration increments $\Delta S_{a,n}^{(i)}$ is possible because the correction factor $\Gamma^{(i)}$ related to the total load vector scales all modal summands equally.

Finally, it should be noted that the determination of the maximum acceleration increments $\Delta S_{a,n,max}^{(i)} = S_{a,n,max}^{(i)} - S_{a,n}^{(i-1)}$ can be negative for certain modes towards the end of the *mAMI* calculation. The reason for this is that the maximum spectral accelerations $S_{a,n,max}^{(i)}$ normally decrease significantly, while the existing modal accelerations $S_{a,n}^{(i-1)}$ increase continuously. As the *mAMI* is a nonlinear static procedure, a calculation that goes too far and then steps backwards should be avoided. Instead, in such a case, the performance state should be approached starting from the previous step (i-1) with a small constant step size $\Delta S_{a,B}$ or even the last step can be considered approximately as the performance state.

3.2 Process workflow of the *modified AMI* (*mAMI*)

Based on a manually performed nonlinear analysis for dead loads with a subsequent modal analysis, the user has to specify which modes are taken into account and with which sign combinations k. The starting point of the automated *mAMI* itself is again a nonlinear static calculation for dead loads. Both nonlinear analyses of the dead weight, the manual pre-calculation as well as the first automated calculation, take physical nonlinearity and P-Delta effects into account.

The subsequent procedure for each load combination k per adaption step i is listed step by step below:

1. Modal analysis based on the current system stiffness $\mathbf{K}_T^{(i-1)}$ to determine $\omega_n^{(i)}$, $\boldsymbol{\Phi}_n^{(i)}$ and $\beta_n^{(i)}$.

2. Calculation of the effective modal yield points $(S_{d,n,y}^{(i)}, S_{a,n,y}^{(i)})$ according to AYDINOGLU (2003) by means of a two-segmented linearization of the respective capacity spectra up to the end point of the last correction step with equal areas and a gradient of $\left(\omega_n^{(i)}\right)^2$ in the second branch (cf. Section 2.2, following formulas are derived in Appendix B):

$$S_{a,n,y}^{(i)} = \frac{2 \cdot A_n^{(i-1)} - \left(\frac{S_{a,n}^{(i-1)}}{\omega_n^{(i)}}\right)^2}{S_{d,n}^{(i-1)} - \frac{S_{a,n}^{(i-1)}}{\left(\omega_n^{(i)}\right)^2}} \tag{3.21}$$

$$\text{and } S_{d,n,y}^{(i)} = S_{d,n}^{(i-1)} - \frac{S_{a,n}^{(i-1)} - S_{a,n,y}^{(i)}}{\left(\omega_n^{(i)}\right)^2} \ , \tag{3.22}$$

where $A_n^{(i-1)}$ is the area below the n-th modal capacity spectrum up to the last point $(S_{d,n}^{(i-1)}, S_{a,n}^{(i-1)})$.

3. Calculation of the effective modal damping ratios $\xi_{n,eff}^{(i)}$ based on the respective hysteresis energy according to ATC-40 (1996) (cf. Section 1.3 of this thesis, Eqs. 1.21 to 1.24).

4. Determination of each modal acceleration $S_{a,n,max}^{(i)}$ by superimposing the response spectrum based on $\xi_{n,eff}^{(i)}$ and the extrapolated modal capacity spectrum (cf. Fig. 2.3).

5. Calculation of the corresponding maximum acceleration increments $\Delta S_{a,n,max}^{(i)}$:

$$\Delta S_{a,n,max}^{(i)} = S_{a,n,max}^{(i)} - S_{a,n}^{(i-1)} \ . \tag{3.23}$$

Due to the fact that the maximum spectral acceleration increments $\Delta S_{a,n,max}^{(i)}$ for each mode are applied directly to the load vector (cf. Eq. 3.24), this approach indirectly includes the intermodal scaling factors $\lambda_n^{(i)}$ by AYDINOGLU (2003) (acc. to Eq. 2.7).

6. Adaption of the maximum incremental load vector $\Delta \mathbf{P}_{max}^{(i,k)}$ corresponding to the current load combination k:

$$\Delta \mathbf{P}_{max}^{(i,k)} = \sum_n \alpha_n^{(i,k)} \cdot \beta_n^{(i)} \cdot \mathbf{M} \cdot \mathbf{\Phi}_n^{(i)} \cdot \Delta S_{a,n,max}^{(i)} \ , \tag{3.24}$$

with:

- $\alpha_n^{(i,k)}$ = correlation factor according to Eq. 3.11, which also contains the modal sign for the current combination k,

- $\beta_n^{(i)}$ = modal participation factor (cf. Eq. 1.4),

- $\mathbf{M}$ = system mass matrix,

- $\mathbf{\Phi}_n^{(i)}$ = currently updated n-th eigenvector and

- $\Delta S_{a,n,max}^{(i)}$ = maximum spectral acceleration increment.

7. Nonlinear static FE calculation based on an incremental load application of $\Delta \mathbf{P}_{max}^{(i,k)}$ in several pushover steps p: $\Rightarrow \mathbf{V}^{(i,p,k)}$.

   In addition: storing of the resulting pushover curve corresponding to the previously selected monitoring point (mp).

8. Analysis of the current (i-th) segment of the pushover curve in order to detect relevant system changes:

- Local analysis: Identification of sudden changes in stiffness that lead to kink points in the pushover curve. The comparison of the slopes between all neighboring pairs of pushover points is carried out according to Equation 3.13 (cf. Fig. 3.4 (a)).

- Global analysis: Identification of excessive, continuously developed deviations from the initial slope of the current (i-th) overall segment of the pushover curve (cf. Fig. 3.4 (b)), according to Equation 3.14.

Possible results of this investigation:

- No limiting point has been detected, meaning that no further adaption step is necessary. Thus, the results of the current 'Max computation' based on $\Delta \mathbf{P}_{max}^{(i,k)}$ represent the performance state. A check, however, whether the last FE computation was successful has to be performed. If so, the earthquake design proof is done and the next load combination k can be investigated. If the last computation was not successful, the inelastic capacity of the structure is not sufficient to withstand the investigated earthquake.

- Only one of the two criteria yields a limiting point p. Then the target base shear is given as $F_{b,target}^{(i)} = F_b^{(i),(p)}$. Continue with process stage 9 (explained below).

- Both criteria yield (different) limiting points p. Then the target state is defined by the point that occurs first: $F_{b,target}^{(i)} = min\left(F_{b,loc}^{(i),(p)}, F_{b,glob}^{(i),(p)}\right)$. Continue with process stage 9 (explained below).

9. Calculation of a correction factor $\Gamma^{(i)}$ in order to reduce all modal increments $\Delta S_{a,n,max}^{(i)}$ and the incremental load pattern $\Delta \mathbf{P}_{max}^{(i,k)}$ according to Equation 3.17.

10. Determination of new points for all modal capacity spectra based on corrected spectral increments (cf. Eqs. 3.18-3.20):
$$\Rightarrow \left(S_{d,n}^{(i)}, S_{a,n}^{(i)}\right) = \left(S_{d,n}^{(i-1)} + \Delta S_{d,n}^{(i)}, S_{a,n}^{(i-1)} + \Delta S_{a,n}^{(i)}\right).$$

11. Corrective FE computation with a reduced load increment vector $\Delta \mathbf{P}_{red}^{(i,k)} = \Gamma^{(i)} \cdot \Delta \mathbf{P}_{max}^{(i,k)}$, yielding the corresponding reduced displacements $\mathbf{V}_{red}^{(i,p,k)}$.

12. Continue with adaption step i+1.

3.3 Interim theoretical conclusion

The modifications and extensions presented improve the original *mAMI*. The theoretical weaknesses, discussed in Chapter 2, have been adressed and mainly eliminated. Furthermore, the *mAMI* is based on optimized spectral increments in order to significantly reduce the numerical effort and thus especially computing times. Both aspects are examined in more detail later in this dissertation. In contrast to the original version of the *AMI* presented by NORDA (2012),

the user does not have to specify a constant spectral increment of the reference mode, but instead the two limit values k_{loc} and k_{glob} for the analysis of the pushover curve. In addition, this analysis requires the selection of a monitoring point. However, as the latter only affects the size of the respective adaption steps and not directly the determination of the performance state, it has a much smaller influence overall than in the case of other pushover methods. Later analyses will show that it is even almost negligible.

The finite element software *SAP2000* (COMPUTERS & STRUCTURES, INC., 2016), which is widely used in earthquake engineering and is also established in practice, is chosen for the application of this method. One reason for this is that the software already contains a number of calculation options as standard, which are required for a wide range of static and dynamic earthquake calculations. On the other hand, different variants of plastic or fiber hinges can be modeled and P-Delta effects can be taken into account. However, two extensive work steps are necessary before the *mAMI* can be used in practice:

1. Even though there are numerous publications that document and advocate the modeling of physically nonlinear reinforced concrete beams and columns in general or bridge piers in particular using concentrated plastic hinges (KAPPOS ET AL , 2005; CHIOU ET AL , 2008; CARVALHO ET AL , 2013; ZHOU , 2016; MARJANOVIC & PETRONIJEVIC , 2018; BERGAMI ET AL , 2020), CHIOREAN (2003) criticizes this approach for investigations of reinforced concrete structures. Since the plasticity effects cannot be limited to a local point or area, he strongly recommends the use of models with distributed plasticity. In addition to the question of which zone the plastic behavior is limited to, there is also the question of how the inelastic behavior of massive reinforced concrete cross-sections can be represented by plastic hinge models if the cross-section dimensions become very large, as in the case of bridge piers. Against this background, the modeling of a physically nonlinear behavior of bridge piers using plastic or fiber hinges in *SAP2000* has to be validated using the results of so-called *pseudo dynamic tests* on real reinforced concrete bridge piers. These post-experimental studies are documented in the following Chapter 4.

2. Furthermore, the *mAMI* method presented cannot be easily implemented with commercial software. The automated implementation of this multimodal adaptive pushover method requires the development of an algorithm that implements the steps described in Section 3.2 using an existing FE calculation kernel, in this case from *SAP2000*. For this reason, an automated algorithm, or more precisely a wrapper, was developed as part of this dissertation that fulfills the previously documented requirements. The main features of this algorithm are explained in Chapter 5.

4 Validation of the inelastic model

4.1 Introductory remarks

In bridge structures, plastic zones may normally only occur in the piers. The appropriate approach of an elastic superstructure and inelastic piers can be found uniformly in all common seismic standards and in the literature, with the only exception being separate seismic isolation systems (KAPPOS , 2015). The inelastic modeling can be divided into (1) lumped and (2) distributed plasticity models, whose properties and areas of application are discussed in FISCHINGER & ISAKOVIC (2003), NGO-HUU & KIM (2012), CARVALHO ET AL (2013) and SALIHOVIC & ADEMOVIC (2017), among others. On the other hand, it can be categorized according to the level from which the inelastic behavior is described. In this context, a distinction can be made between (a) macro (plastic hinges) and (b) micro models (fiber hinges or elements) (CHIOREAN , 2003). In the former, the plastification of the cross-sections is accounted for by smooth M-κ curves for bending and N-ε curves for axial loading effects. An interaction between normal force and bending moment and between bidirectional moments by means of (N-M_x-M_y) yield surfaces is additionally taken into account in many cases. In micro models, on the other hand, the cross-section is not viewed from the outside, but subdivided into numerous fibers, all fibers being under a uniaxial state of stress. Each fiber can be assigned to a specific material and thus to an associated σ-ε diagram and only has certain coordinates and a specific surface area as other information. By integrating the nonlinear fiber stress distribution in each calculation step, the internal forces in the cross-section can be determined on a macro level. An (N-M_x-M_y) interaction is therefore automatically mapped via the normal stresses. This approach is much more accurate and therefore more realistic, but requires significantly more computational effort.

Furthermore, it is crucial for nonlinear dynamic calculations to map the hysteretic behavior correctly. While in case of macro models the hysteresis energy must also be described at cross-section level, corresponding hysteresis models of micro models can be defined at material level and assigned separately to the individual fibers.

As already discussed in Section 3.3, the question arises especially for bridge piers,

a) with regard to which spatial extent plastic deformations occur and thus, whether distributed plasticity must be considered and

b) whether the macro model using plastic hinges, which is undoubtedly oriented towards beam elements, is sufficient for compact pier cross-sections with sometimes very large dimensions in order to represent the inelastic load-bearing behavior realistically.

In addition, for bridge piers, as for all other structures, the adequate mapping of hysteresis behavior plays a central role in nonlinear seismic analyses.

The provided numerical model should therefore be validated using test data in view of the three aspects mentioned. Especially for large systems, such as bridge structures, so-called *pseudo-dynamic tests* (*PSD* tests) are commonly used for this purpose (Pegon & Pinto , 2000; Dhakal et al , 2007; Paolacci et al , 2013), which also enable a realistic earthquake testing for such systems at a reasonable cost. On the one hand it is neither possible nor desirable to excite existing bridge structures in such a way that plastic structural reserves are activated by the formation of a significant damage in order to be measured. On the other hand, it is also impossible to completely reconstruct a whole bridge in the laboratory and subject it to shaking table tests. The basis of the *PSD* tests is therefore a so-called 'numerical-experimental substructering technique', in which large parts of the system are only modeled and calculated numerically, while certain substructures relevant for the inelastic behavior, such as specific piers, are tested in parallel in the laboratory. The input for this test procedure is a discrete real or artificially generated earthquake time history $a_g(t^{(n)})$ with equidistant time points $t^{(n)}$. In the *ELSA* (*European Laboratory for Structural Assessment*) laboratory of the European *Joint Reasearch Centre* in Ispra (Italy), the so-called α *operator splitting scheme* (Hilber et al , 1977) is used to calculate the system responses of the FE model for each time step and to simultaneously carry out measurements on the respective piers. The corresponding measurement results are then returned to a higher-level algorithm, thus having an influence on the further FE calculation. For each point in time this procedure essentially consists of the four steps listed below, which can only be briefly described here, but are set out in more detail in Appendix C.1:

1. Compute estimates for the current displacements and velocities (prediction phase).

2. Apply the estimated displacements of all FE nodes to the numerical model and the displacements at the top of the tested piers to the latter (control phase) in order to get the static restoring forces (measuring phase).

3. Calculate the corresponding current accelerations (calculating phase).

4. Compute the actual displacements and velocities for the current state (correction phase).

It is worth mentioning that the displacements are applied to the pier heads in the laboratory by increasing a corresponding horizontal point load until the respective target displacement is reached. As this is done statically, the measured force required is in fact a purely static restoring force. For this reason, the procedure is referred to as *pseudo-dynamic* testing, as no real dynamic tests are carried out, even though the higher-level system of equations of motion, which is solved step by step, is dynamic.

The results of such *PSD* tests on realistic bridge piers at a scale of 1:2.5, which were carried out at the *ELSA* (PINTO ET AL , 2001, 2002), were kindly provided by the *Joint Research Center* for the dissertation project. These can thus be used to validate the nonlinear numerical model in *SAP2000* with particular consideration of the three previously mentioned key aspects (concentrated vs. distributed plasticity, macro vs. micro model & hysteresis behavior).

4.2 Post-experimental study of *Pseudo Dynamic Tests*

The test data used are taken from the *PSD* tests (PINTO ET AL , 2002) carried out at *ELSA* on a large-scale model of the *Talübergang Warth Bridge*, a highway bridge of the A2 in Austria between Vienna and Graz (see Fig. 4.1).
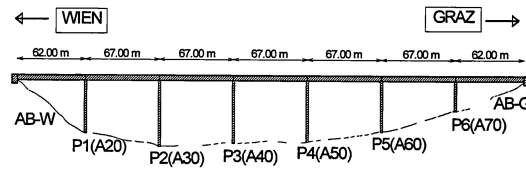
Figure 4.1: *Talübergang Warth Bridge in Austria (PINTO ET AL , 2001)*

To validate the nonlinear numerical model, a post-test calculation of the laboratory test *v22* on the model of the bridge pier A40 ('tested structure') at a scale of 1:2.5 is carried out. Analogous to the laboratory tests, the current target displacement $v_{target}^{(i)}$ is implemented step by step in *SAP2000* by applying a successively adapted horizontal top load until the target displacement is reached. The required force measured and returned to the *PSD* algorithm in the laboratory can then be compared with the inelastic restoring force in *SAP2000* for each point in time. Since the data set of this experiment relates to 1242 points in time, for each of which a separate load case has to be defined in *SAP2000*, the calculation must be automated. This is realized by a tool programmed in *MATLAB*, which generates a nonlinear static load case for each of the 1242 data points, whose concentrated horizontal load at the pier top is increased in a certain number of steps until the displacement increment $\Delta v_{target}^{(i)} = v_{target}^{(i)} - v_{target}^{(i-1)}$ is reached. This incremental approach is necessary because, although the test results are available as absolute

displacements, the individual load cases in *SAP2000* build on each other in order to represent the entire nonlinear load-deformation path. It should be noted that no negative target displacements can be specified in *SAP2000*, so that in case of negative displacement increments the amount of these must be applied in combination with a 'load scale factor' of -1.

In addition, the approximately constant normal compressive force of -3300 kN of pier A40 is also applied using the previously mentioned tool.

4.2.1 Modeling aspects

Pier A40 is a 14 m high reinforced concrete pier, consisting of a box girder cross section with external dimensions of 2.74 and 1.02 m and wall thicknesses of 21 and 17 cm. At *ELSA*, the pier was integrated into a foundation block measuring (W x H x D) 5.5 x 1.2 x 2.5 m. A total of 16 vertical prestressed anchors (see Fig. 4.2 (a)) ensured an approximate surface tension- and compression-resistant connection between the foundation block and the rigid laboratory floor. Due to the finite rotational stiffness of the pier restraint by the foundation, the pier was not assumed to be fixed in the FE model of the post-test calculation, but was modeled together with the foundation block (see Fig. 4.2 (b)). Since the anchors do not represent completely deformation-free fixed supports for the foundation despite the prestressing, they were applied as springs with a very high spring stiffness (of $2 \cdot 10^5$ kN/m). In addition to these springs relevant for the global rotational spring stiffness of the foundation, a fixed vertical support was applied in the central node, ensuring the direct transfer of the compression normal force from the pier into the load-bearing base due to contact pressure without any bending of the foundation block.

(a) Foto (Pinto et al , 2002)   (b) FE model
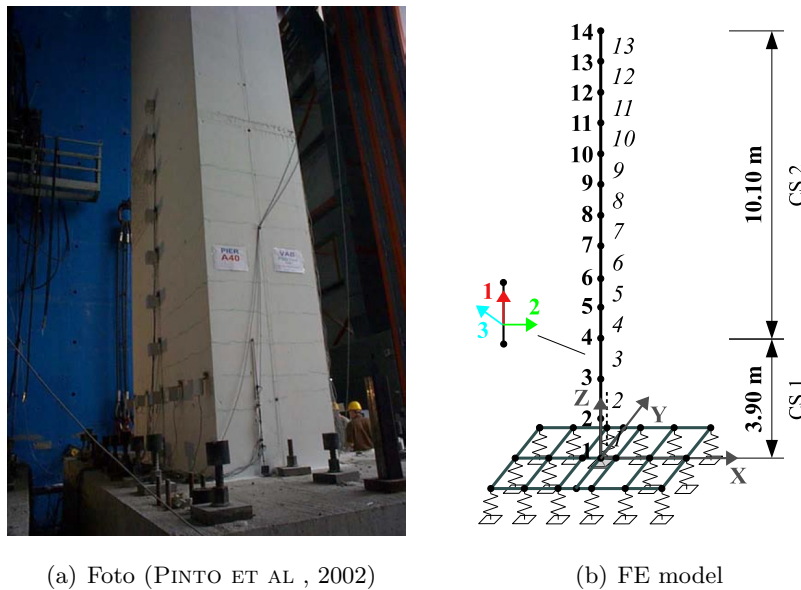
Figure 4.2: Pier A40 with foundation block (ELSA, test v22)

The pier consists of C35/45 concrete and B500A reinforcing steel. Both materials were subjected to material tests in the *ELSA* laboratory, from which certain material parameters were derived, documented in PINTO ET AL (2002). These were applied in the course of the post-experimental study in order to achieve the most realistic possible representation of the tested pier. For the parameters not covered by this, the usual normative values for C35/45 and B500A are used. Table C.1 in Appendix C contains all the material parameters applied. The longitudinal reinforcement of pier A40 is reduced to almost half from about 3.5 m above the foundation. Against this background, two differently reinforced pier cross-sections were considered in the modeling: a cross-section 1 with 76 Ø 12 = 85.95 cm² and another cross-section 2 with only 40 Ø 12 = 45.25 cm² longitudinal reinforcement. The specific arrangement of the individual longitudinal bars is shown in Figures C.1 to C.3 in Appendix C.

Due to the fact that the pier is embedded in the reinforced concrete foundation, the effective pier height is 14.0 m instead of 13.25 m from the top of the footing (cf. PINTO ET AL (2002), Sec. 2.1). Thus, the lower part of the pier with the cross-section 1 was set at a length of 3.90 m (see Fig. 4.2 (b)), consisting of three beam elements of length 1.30 m. The remaining pier (with cross-section 2) was modeled with ten beam elements of length 1.01 m thus leading to a total length of 10.10 m. In addition, the foundation block was mapped with 12 *Shell Thick* elements with a cross-section of 1.20 m in height. The longitudinal reinforcement of a total of 20 Ø 12/12.5 cm in the load direction (global *X* direction acc. to Fig. 4.2 (b)) was taken into account with regard to the resulting increased stiffness in contrast to unreinforced concrete via corresponding stiffness modifiers. The derivation of the two scaling factors SF_m for the membrane and SF_{pb} for the plate bending effects can be found in Appendix C.4.

A total of ten potential plastic or fiber hinges were defined along the pier for all beam elements, each with a plastic length of 10% of the element length. The plastic or fiber hinges were then distributed over the respective element to the relative locations of 5%, 15%, 25%, ... 95% of the element length. Accordingly, 30 hinges were defined on the first 3.9 m, whose *M-κ* curve or fiber division is based on the reinforcement of cross-section 1 (see Fig. C.2, App. C). On the remaining 10.10 m, a total of 100 additional hinges were arranged based on the reinforcement of cross-section 2 (according to Fig. C.3, App. C). Figure C.4 in Appendix C illustrates the described hinge configuration along the bridge pier.

For the plastic hinges, *INCA2*[2], developed at the *Hamburg University of Technology (TUHH, Germany)*, was used to generate *M-κ* curves for the constant normal force of -3303 kN, separately for cross-sections 1 and 2, which must be reduced to 5 points each for use in *SAP2000*. In addition, the plastic curvatures are applied there according to $\kappa_{pl} = \kappa_{tot} - M/EI$. The M-$\kappa_{tot}$

---

[2] `http://www.u-pfeiffer.de/inca2/inca2-09.html`, call: 05/2020; see also: PFEIFFER (2006)

curves are depicted in Figure 4.3. It can be seen there that the moment drops drastically in each case due to the rupture of the concrete tension zone until the reinforcement is activated and finally leads to a further increase in the inelastic moment capacity.

(a) Cross-section 1
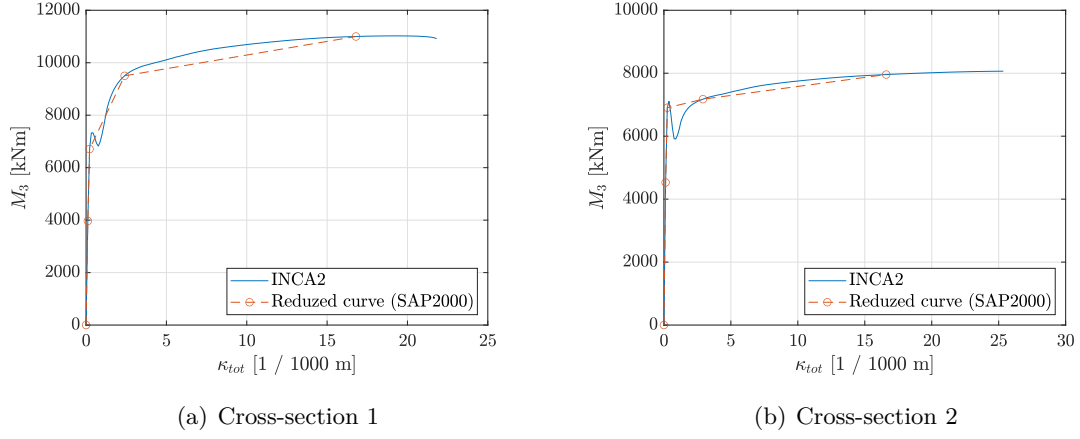
(b) Cross-section 2

Figure 4.3: *M-κ curves for both cross-sections of pier A40*

(a) Cross-section 1
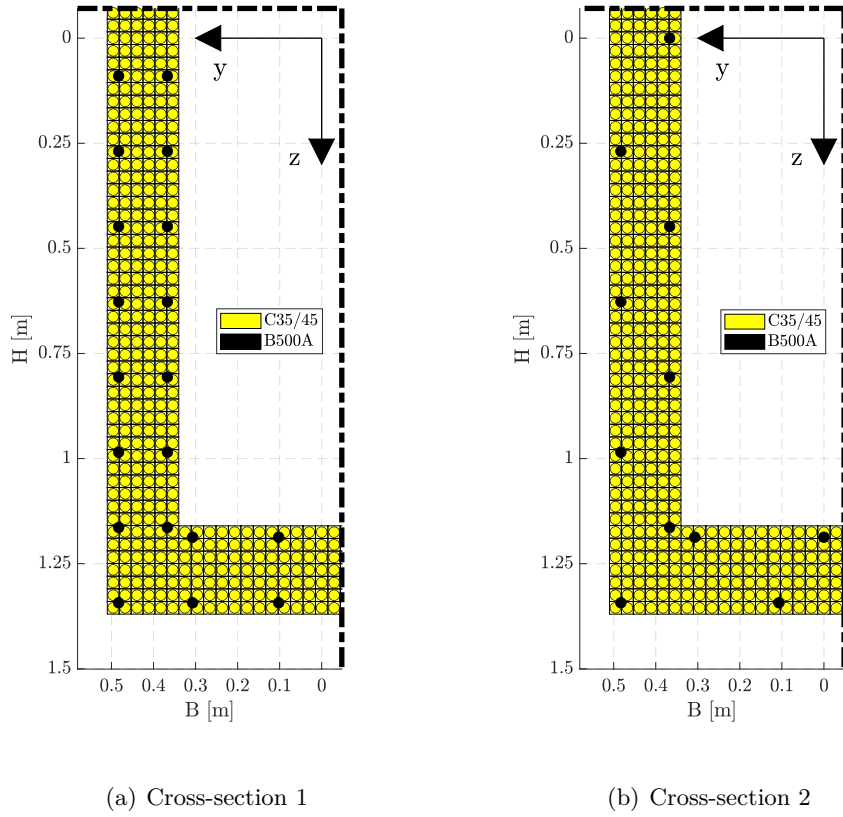
(b) Cross-section 2

Figure 4.4: *Subdivision of cross-sections 1 & 2 of pier A40 into fibers*

Finally, Figure 4.4 shows the subdivision of both cross-sections into material-related fibers for the fiber hinges. These consist of 1490 and 1454 fibers, respectively, which were also automatically divided by a self-developed tool in *MATLAB* on the basis of a specified maximum cell size of 3 x 3 cm. In addition to other finer and coarser fiber meshes, the ones previously shown were selected as they ensure sufficient accuracy with regard to the calculation results while still requiring a reasonable computational effort.

4.2.2   Results for the plastic hinge model

First, a calculation is carried out, in which deliberately no plastic or fiber hinges are applied in order to force a linear-elastic behavior. The results of the corresponding horizontal load development P(t) compared with the test data (see. Fig. 4.5 (a)) show an expected clear overestimation of the required restoring forces except in the initial, actually linear-elastic range. This calculation only serves to estimate the influence of the inelastic load-bearing behavior. In addition, Fig. C.5 in Appendix C shows the comparison of the pier head displacements as a plausibility check.

The subsequent calculation is now based on a deliberate overestimation of the hardening by selecting the *Kinematic Hysteresis Model*, which is actually only suitable for pure steel cross-sections. Figure 4.5 (b) clearly shows that after one complete loading and unloading cycle, i.e. with the onset of hysteretic behavior, this leads to a partly significant overestimation of the forces and thus of the hardening behavior.
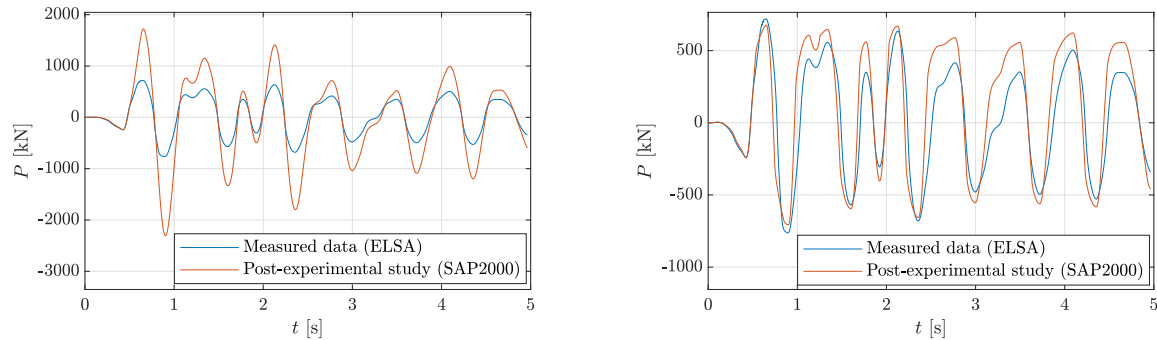
(a) Linear-elastic calculation   (b) Inelastic calculation with 'wrong' hysteresis model

Figure 4.5: *Comparison of elastic and 'wrong' inelastic restoring forces $P(t)$*

By choosing the appropriate *Pivot Hysteresis Model* (DOWELL ET AL , 1998) for the RC cross-section a satisfactory agreement with the test results can be observed (see Fig. 4.6 (a)). While this calculation is based on the default parameters of the *Pivot* model in *SAP2000* ($\alpha_1 = \alpha_2 =$

10.0, $\beta_1 = \beta_2 = 0.7$, $\eta = 0$), the next step is the attempt to obtain an even better match with the test data by varying these parameters as a calibration of the hysteresis model. Here it can be stated that a different choice of $\beta_{1/2} = 1.0$ (instead of 0.7) causes a slight improvement in the results (cf. Fig. 4.6 (b)), while the other parameters do not show any significant influence on the final results. Figure 4.7 schematically visualizes the influence of $\alpha_{1/2}$ and $\beta_{1/2}$. Accordingly, α_1 and α_2 influence the slope of the unloading path in the positive and negative value range, respectively, and $\beta_{1/2}$ the slope of the respective reloading path. Furthermore, η, with $0 \leq \eta \leq 1$, determines the amount of degradation of the elastic slopes after plastic deformation.
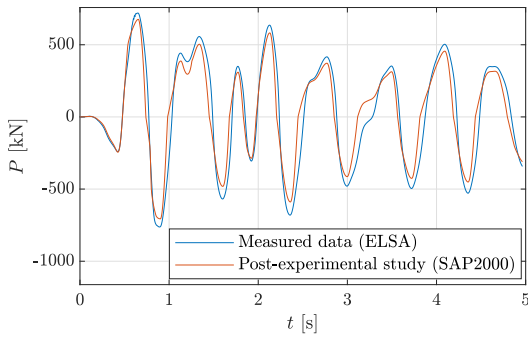
(a) *Pivot Hysteresis Model* with default values
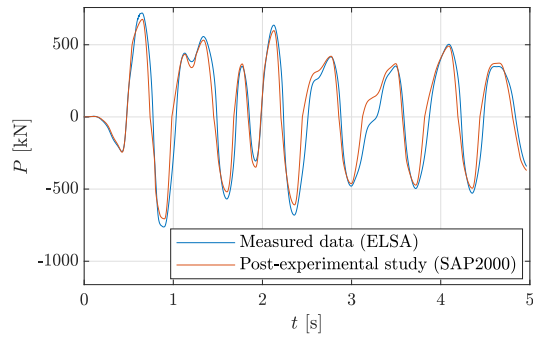
(b) *Pivot Hysteresis Model* with $\beta_{1/2} = 1.0$

Figure 4.6: *Comparison of restoring forces for varying parameters in the* Pivot Hysteresis Model
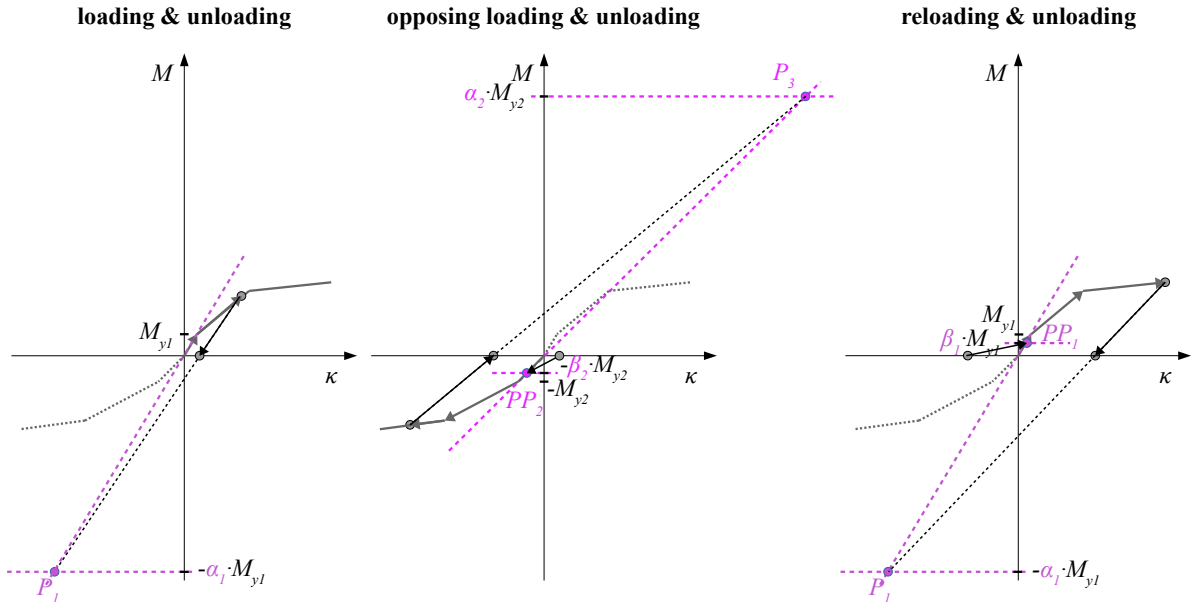
Figure 4.7: *Pivot Hysteresis Model - Schematic diagram (acc. to* Dowell et al *(1998))*

Finally, it should be noted that in the last calculation, plastic deformations occurred on approximately the lower 7 meters (cf. Fig. C.6 in Appendix C). This confirms that there is no alternative to modeling distributed plasticity.

4.2.3 Results for the fiber hinge model

The micro model, based on the material-specific *Concrete* and *Kinematic Hysteresis Model* for concrete and steel fibers, respectively, first leads to a calculation crash (cf. Fig. 4.8 (a)). By varying different parameters of the nonlinear equation solver, numerical problems occur in completely different *PSD* steps. The only common feature is that there is a sudden drop in the pushover curve in each case. However, in view of the hinge results, this cannot be attributed to a mechanical system failure. In all probability, this is a numerical problem with the mapping of sometimes extremely small load increments in comparison to the overall load level already present in each case. Apparently, *SAP2000* has greater difficulties in mapping these with the numerically more complex fiber hinges than with the previously examined plastic hinges. The only possible solution here is a significant local increase in the iteration convergence tolerance, which, however, does not lead to any globally noticeable error due to the very small load increments mentioned, as can be seen in the following Figure 4.8 (b).

(a) Crashed computation

(b) Successful computation
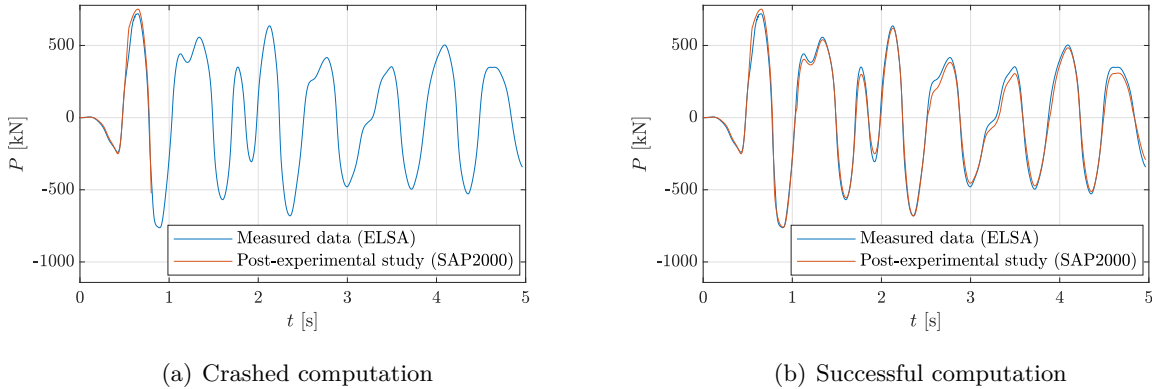
Figure 4.8: *Restoring forces for the fiber hinge model*

4.3 Conclusion

Overall, the fiber hinge model shows equally good results as the plastic hinge model with optimized hysteresis parameters. While the calibration of the hysteresis model for plastic hinges requires additional effort, which is difficult in practice without available test data, the previously outlined numerical problems of the micro model can certainly be solved more easily in such cases.

In principle, however, both the micro and macro model show an unexpected good agreement with the test data against the background that both models cannot reproduce local effects, such as buckling of vertical reinforcement bars, wich occured in the test *v22* at *ELSA* (see Fig. 4.9).

Figure 4.9: *Pier A40: Buckling of longitudinal reinforcement at 3.5 m (Pinto et al , 2002)*

However, if interaction effects due to a variable normal force or double bending have to be taken into account, the modeling of plastic hinges is much more complex. Even in the former case, an interaction yield surface as well as a set of different M-κ curves for varying normal forces must be defined. In *SAP2000*, a corresponding M-κ curve is then interpolated for the normal force when the yield surface is first reached (cf. yield point in Fig. 4.10 (a)). If this is carried out in version 20.0 of *SAP2000* used here, however, it is found that precisely this interpolation is incorrect and the actual hinge results show an underestimation of the bending moment (see Fig. 4.10 (b)). This error was confirmed by *Computers and Structures, Inc.* in a corresponding support request (in August 2020), but was not corrected, at least in this version, so that plastic hinges in version 20.0 of *SAP2000* should only be used for pure *M3* plastic hinges with a constant normal force. In case of any variable interaction effects, however, fiber hinges that directly map an interaction via the normal stresses should always be used against this background (cf. Sec. 6.5 & Chap. 7).

(a) Interaction yield surface

(b) Wrong plastic hinge results
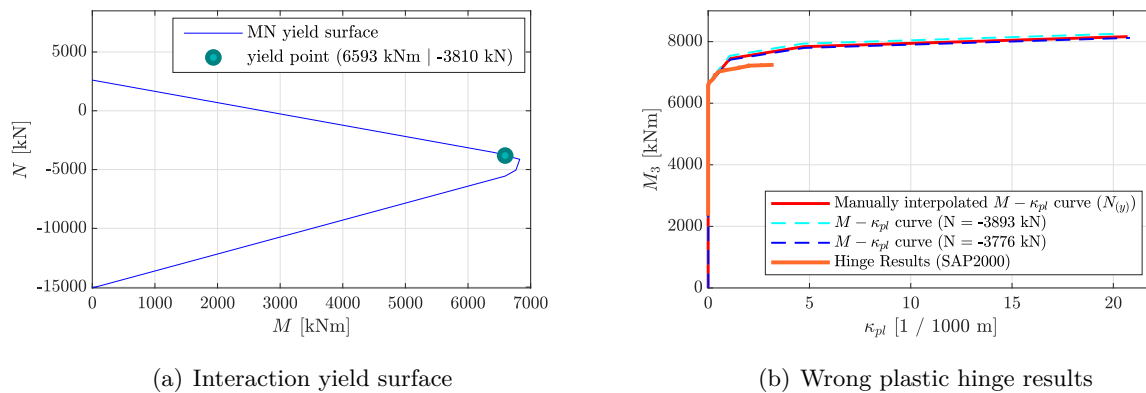
Figure 4.10: *Incorrect behavior of Interaction Plastic Hinges in SAP2000 (V20.0)*

5 Development of an automated adaptive pushover algorithm

5.1 General concept and program flow

As already explained in Chapter 3, the *modified AMI* (*mAMI*) procedure presented can only be applied with a corresponding, self-developed algorithm that covers all the steps described in Section 3.2. Against this background, within the scope of this PhD dissertation the so-called *CAAP* tool (***C**omplete **a**utomated **a**daptive **p**ushover*) was programmed as a wrapper in *MATLAB*, which uses the *SAP2000* calculation kernel and is otherwise autonomous. It is freely available as open source code[3] (KÄMPER & OSTERKAMP , 2024). When applying the *CAAP* tool, the user essentially has to perform two steps before starting the automated calculation:

1. development of a nonlinear numerical model of the structure in *SAP2000* and preliminary modal analysis to identify relevant modes,

2. creation of a *MATLAB* script to define all relevant calculation parameters.

These two steps are explained in more detail below.

Numerical modeling in *SAP2000*

First, the structure must be numerically modeled, including the potential plastic zones. Although the *CAAP* algorithm can process both line (beams and cables) and area (shell and plane) elements, the consideration of plastic zones via plastic or fiber hinges is limited to beam elements. Three load cases must then be created: a load case for the dead loads as a nonlinear static load case, a load case for the modal analysis and a pushover load case, the last two based on the stiffness distribution and structural responses at the end of the dead load case. Both static load cases have to be defined as 'full load' calculations under consideration of P-Delta effects. In case of the pushover load case, the (primary) earthquake direction must be selected

---

[3] `https://github.com/DMKaemper/CAAP-Complete-Automated-Adaptive-Pushover-`

for the monitored displacement, whereby a node that exhibits relatively large deformations in the earthquake direction concerning the base mode should generally be selected as the monitoring point (mp). However, the latter aspect can only be assessed more precisely on the basis of an eigenvalue analysis and may therefore need to be adjusted accordingly. An initial modal analysis can then be carried out manually on the basis of the system properties at the end of the nonlinear calculation for the dead loads. From the results of this preliminary modal analysis, a first impression can already be gained concerning

- which natural modes should be considered in which earthquake direction, being assessed on the basis of the effective modal masses, and

- which node is suitable as mp for the primary direction of seismic excitation in combination with the relevant modes.

Creation of a *MATLAB* script with all relevant calculation parameters

A *MATLAB* script must be created for each calculation with the *CAAP* tool, in which all essential specifications for the calculation are first defined. These definitions are followed by the function call of the main routine 'MAIN CAAP', which may be carried out in a loop over all load combinations to be analyzed with different input parameters. Appendix D contains an example of such a script. The main specifications for a *mAMI* calculation are explained below.

The first block contains the general information stored under 'arg.info'. This includes the relevant paths of the *SAP2000* (.exe) and the model file as well as the names of the load cases to be analyzed. In addition, the extent to which the algorithm informs the user about the calculation progress and possible problems (from console outputs and acoustic signals to e-mail notifications) can be specified. The subsequent block with information on specific calculation parameters is more important in terms of content. Here, the user can define the minimum and maximum number of load increment steps p to be used within a specific pushover calculation (per adaption step). Furthermore, the limit values k_{loc} and k_{glob} described in Section 3.1 can be defined, as well as a constant spectral acceleration increment $\Delta S_{a,B}$ for the case also described in Section 3.1 in which a change is made to constant increments of the reference mode at the end of the *mAMI* calculation. In particular, the earthquake direction, the modes to be considered and the type of load distribution must also be specified at this point, whereby the latter should generally be proportional to the mass and mode shape. The initial modal damping and the hysteresis type (A, B or C acc. to column 1 of Tab. 1.1) must also be defined. In the last section, the user has to compile all information required to define the response spectrum. In addition to the standard to be used, whereby currently only the main part (EUROCODE 8 - PART 1 , 2010) and the German National Annex (EUROCODE 8 (G.N.A.) - PART 1 , 2021) of EC 8 are available,

this includes the associated values a_g and possibly a_{vg} (for vertical excitations) and the soil parameter S as well as the control periods T_B to T_D and the resolution of the time axis (T_{min}, T_{max} and ΔT).

Program flow

The following figure contains a program flow chart of the *CAAP* tool. While most of it should be immediately understandable on the basis of Section 3.2, the steps 'Check eigenmodes' and 'Optimize pushover steps' as well as other detailed aspects require a separate explanation. This is provided in the following Section 5.2.
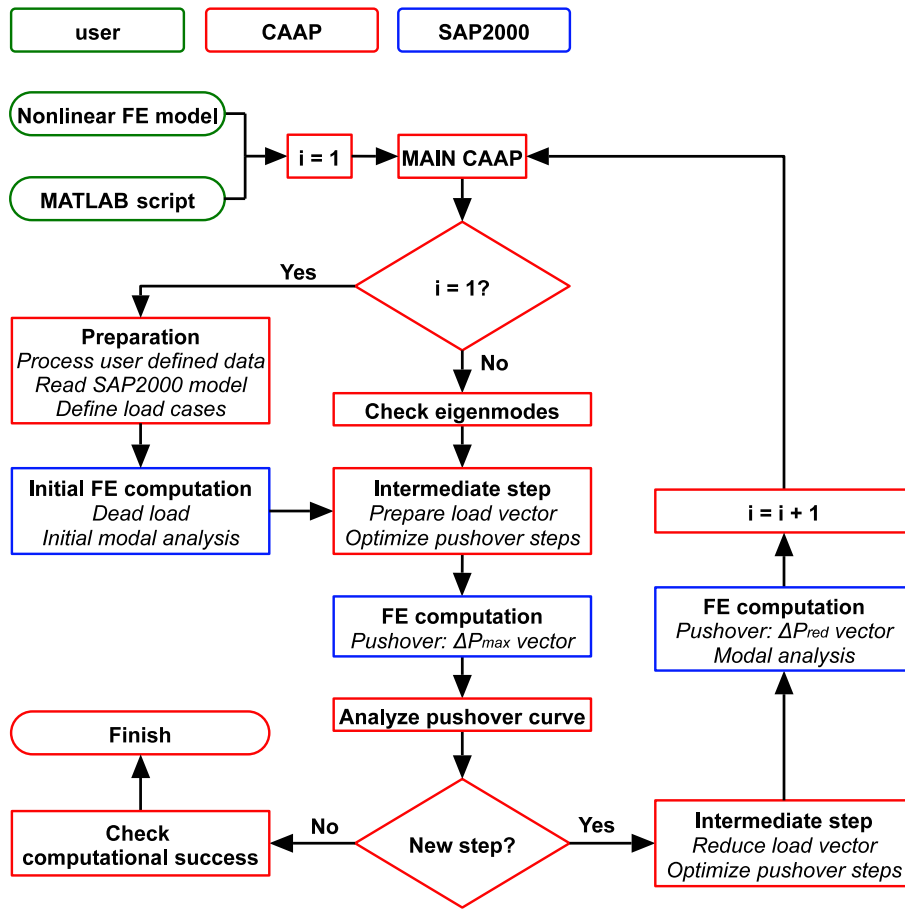
Figure 5.1: *Program flow chart of the CAAP algorithm*

5.2   Specific algorithmic aspects

The updates of the natural modes at the end of each adaption step allow a much more accurate representation of the inelastic dynamic system properties for the respective load level. However, they also lead to the following two central algorithmic challenges:

1. The mode shapes will generally change qualitatively in each step. Also the natural frequencies will change, but to very different degrees. For example, a certain mode n, which is very strongly influenced by the formation of a specific plastic zone, can suddenly exhibit a much lower natural frequency, whereas a neighboring mode n-1 may remain unchanged. A typical example of this is the softening of a bridge pier, which leads to a sudden decrease in the natural frequencies of all horizontal modes in which this pier exhibits large deformations. Vertical modes, in which the bridge piers hardly deform at all, but act like vertical fixed supports, would accordingly not change either qualitatively or with regard to the natural frequencies. If the reduced natural frequency $f_n^{(i)}$ then falls below the unchanged frequency $f_{n-1}^{(i)}$ of the neighboring mode n-1, there is an interchange between the two modes, as these are always numbered chronologically based on their natural frequencies. Such a mode interchange is shown in the following Figure 5.2 as an example.

(a) Mode 6 ($mAMI$ step 2)   (b) Mode 5 ($mAMI$ step 3)
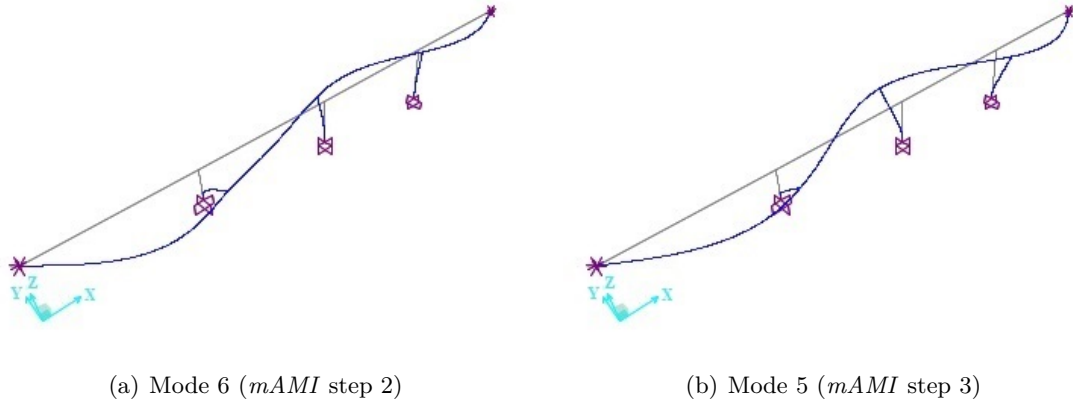
Figure 5.2: *Example of a mode interchange*

In case of a fully automated adaptive calculation, such mode interchanges must be identified automatically by the algorithm. The solution to this problem in the *CAAP* tool is explained in the following Section 5.2.1.

2. In addition, the signs of the mode shapes are determined randomly in many eigenvalue solvers or in a way that is not accessible to the user, as is the case in *SAP2000*. As a result, a certain mode shape in steps i-1 and i can possibly be mirrored due to a changed sign, either exactly or approximately in case of minor qualitative changes (see Fig. 5.3 below).

(a) Mode 6 ($mAMI$ step 2)   (b) Mode 6 ($mAMI$ step 3)
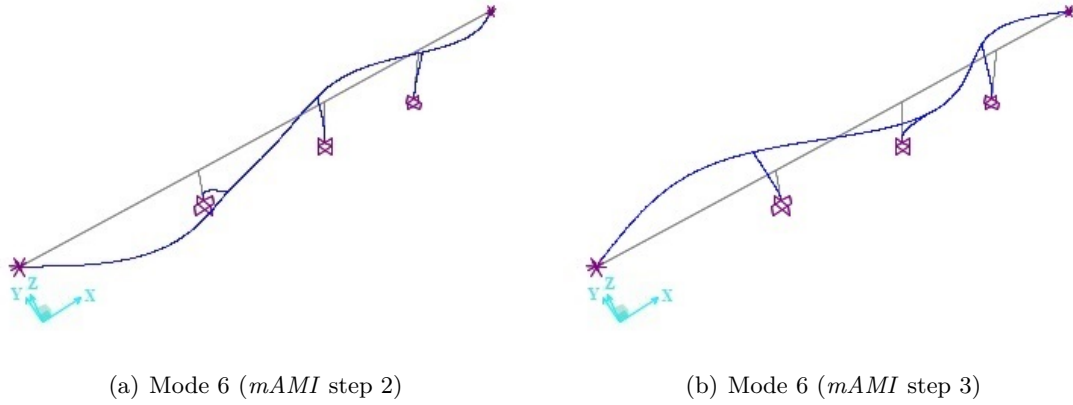
Figure 5.3: *Example of an approximately mirrored mode shape*

This must also be reliably recognized by the algorithm and corrected accordingly, which is discussed in more detail in relation to the *CAAP* algorithm in Section 5.2.2.

5.2.1 Identification of natural modes

The problem of mode interchanges in an automated adaptive pushover calculation by changing of the natural frequencies between two adaption steps, as previously described, was taken into account in the *CAAP* tool. In general, a fixed number of eigenmodes are determined in the course of each modal analysis. After the initial modal analysis, the user selects the relevant modes for the *mAMI* calculation, for example modes 1, 4 and 7. The algorithm must then reliably identify these modes in each step based on their characteristic features. Due to the formation of plastic zones, the relevant mode 7, for example, may become mode 6 at some point when its natural frequency decreases while that of the former mode 6 remains the same. As already mentioned, this often occurs when neighboring modes are influenced to different degrees by the formation of certain plastic effects (e.g. in a certain bridge pier). The algorithm should automatically recognize such an interchange, so that in the above example the new mode 6 is taken into account in the current adaption step instead of the current mode 7. This automated mode identification is implemented in the *CAAP* tool with a two-stage system, which is explained in detail below.

In the current step i, the modes of the previous step $i-1$ are considered one after the other ('reference mode') and a new 'partner' is searched for in each case. This involves a comparison of a specific reference mode $n^{(i-1)}$ with the current mode $n^{(i)}$ (i.e. with an identical number) and its up to four neighbors on both sides ($m^{(i)} = [n^{(i-1)} - 4, n^{(i-1)} - 3, ...n^{(i-1)} + 4]$). The latter means that mode 1 of the last step would be compared with modes 1 to 5 of the current step, while the former mode 7 would be compared with the current modes 3 to 11.

Stage 1: Identification based on the effective modal masses

The first check, which is generally simpler and more reliable than the check of stage 2, attempts a clear assignment via the effective modal masses. Here, the effective modal masses are only analyzed with regard to those directions d in which the reference mode $n^{(i-1)}$ has an effective mass of more than 2%. The check of effective modal masses now covers the following steps for each reference mode $n^{(i-1)}$ to be considered:

- Reading out the values $\mu_{eff,n,(d)}^{(i-1)}$ and $\mu_{eff,m,(d)}^{(i)}$ (with fixed n and $m = [n-4, n-3, ...n+4]$) for all relevant directions d (with $\mu_{eff,n,(d)}^{(i-1)} > 2\%$) from the results of the last modal analysis

- For each relevant direction d: Identification of the closest value $\mu_{eff,m,(d)}^{(i)}$ to $\mu_{eff,n,(d)}^{(i-1)}$

- Check 1 for each relevant direction d: Is the difference between $\mu_{eff,m,(d)}^{(i)}$ (potential new partner) and $\mu_{eff,n,(d)}^{(i-1)}$ (reference mode) at most half the difference to the second closest effective modal mass $\mu_{eff,k,(d)}^{(i)}$, but the latter in turn is at least 4%?

$$\left| \mu_{eff,n,(d)}^{(i-1)} - \mu_{eff,k,(d)}^{(i)} \right| \geq max \left(2 \cdot \left| \mu_{eff,n,(d)}^{(i-1)} - \mu_{eff,m,(d)}^{(i)} \right|, 4\% \right) \tag{5.1}$$

This check is intended to ensure that no automated assignment based on the effective modal masses should take place if, for example, $\mu_{eff,n,(d)}^{(i-1)} = 75\%$, $\mu_{eff,m,(d)}^{(i)} = 65\%$ and $\mu_{eff,k,(d)}^{(i)} = 64\%$. In this case, the differences $75-65 = 10$ and $75-64 = 11$ would be too similar to classify the assignment as reliable. However, if this check (acc. to Eq. 5.1) is fulfilled, the other directions d are investigated and, in case of renewed success, check 2 follows.

- Check 2: Do all analyzed directions d provide the same number m for the new 'partner' of reference mode $n^{(i-1)}$? This check could be denoted as 'plausibility check'. In case of its fulfillment, two further checks are carried out in order to ensure a reliable assignment.

- Check 3: If $\mu_{eff,n,(d)}^{(i-1)}$ is assigned to $\mu_{eff,m,(d)}^{(i)}$, is the effective modal mass $\mu_{eff,m,(d)}^{(i-1)}$ in turn most similar to another mass than $\mu_{eff,m,(d)}^{(i)}$? This check is intended to detect if, when assigning the previous mode 7 to the current mode 6 for example, the previous mode 6 would also be assigned to the current mode 6 and thus to itself. This would refer to an unplausible assignment.

- Check 4: Finally, if checks 1 to 3 are fulfilled, there is an additional requirement that the eigenperiods of both, the reference mode $n^{(i-1)}$ and the new 'partner mode' $m^{(i)}$, should not deviate too far from each other. Specifically, the deviation between $T_n^{(i-1)}$ and $T_m^{(i)}$ should be less than 30%.

Whith every check (of the previous checks 1-4) a non-fulfillment leads to the fact that the first stage of checking on the basis of effective modal masses would be aborted by the algorithm, going on with stage 2.

Stage 2: Identification based on the mode shapes

If the mode assignment via the effective modal masses fails, the second stage of the identification process is entered, which is based on analyses of the relevant mode shapes. For each reference mode $n^{(i-1)}$ to be analyzed, it mainly consists of two steps, which are explained below:

1. Check, whether the mode shape $\mathbf{\Phi}_n^{(i-1)}$ has noticeably changed compared to $\mathbf{\Phi}_n^{(i)}$. The background to this preliminary investigation is that an almost identical qualitative shape leads to a self-assignment and a more complex comparison of different mode shapes can be avoided.

2. If there is, however, a larger deviation of the two mode shapes, the reference mode $n^{(i-1)}$ has to be compared to its up to four 'neighbors per side' (i.e. $[n-4, n-3, ...n+4]$). This concept is analogous the previous investigation of effective modal masses, now applied to the analysis of mode shapes.

Check 1 with regard to a possible self-assignment

As mentioned above, the natural mode shape $\mathbf{\Phi}_n^{(i-1)}$ from the previous modal analysis is at first compared with the current mode shape with the same number n. Specifically, this comparison of mode shapes includes the mean difference in the node displacements (i.e. the sum of the absolute nodal displacement differences, divided by the number of nodes), which is determined separately for different global directions d:

$$\Delta_{nn,(d)}^{(i)} = \frac{\sum_j \left| \mathbf{\Phi}_{n,(d)}^{(i-1)}(j) - \mathbf{\Phi}_{n,(d)}^{(i)}(j) \right|}{max(j)} \ . \tag{5.2}$$

Both mode shapes are normalized to the largest translation across all directions so that the largest overall displacement is exactly 1.0. Based on this boundary condition a self-assignment is carried out if $\Delta_{nn}^{(i)}$ is less than 0.05 for all directions d. However, it is worth mentioning that these differences are only considered with regard to those directions in which both mode shapes exhibit significant deformations. The latter is taken as given if the absolute value of the largest displacement in the respective direction is greater than 0.01 after normalization to the largest overall displacement. Eventhough this limit value that is also used for the second check of mode interchanges appears very low at first glance, the dissertation has revealed that even very small deformation components in a 'secondary' direction can be helpful in the assignment of modes. An example for this is shown in the following figures, where the transversal displacements are marked in color.

(a) Mode 1   (b) Mode 2
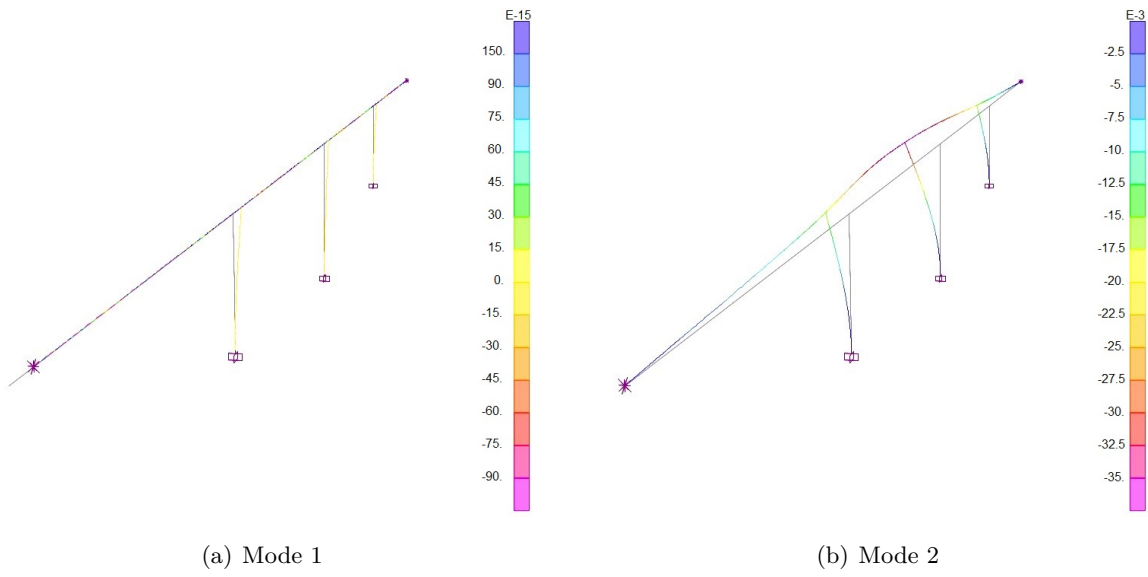
Figure 5.4: *Initial Step 1: Clearly separable longitudinal and transversal mode*

(a) Mode 1   (b) Mode 2
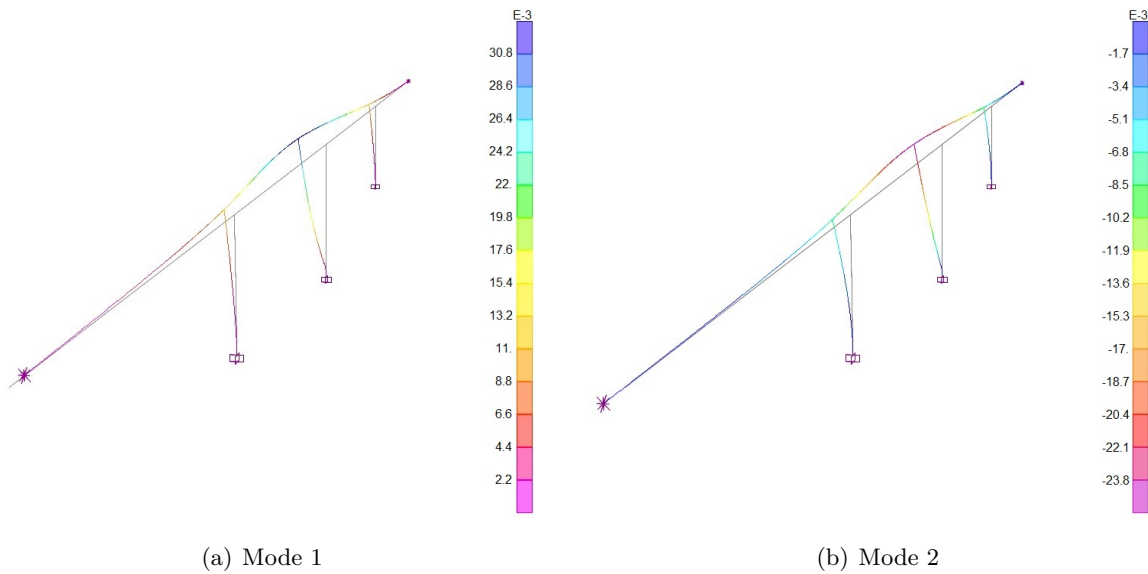
Figure 5.5: *Initial Step 5: Similar spatial modes*

In this example, the initially purely longitudinal mode 1 and the transversal mode 2 have increasingly converged towards step 5. Due to the normalization to the maximum total displacement of both mode shapes in the transverse direction, they were hardly distinguishable optically in this step and therefore also for the automated identification. The main differentiation criterion for the algorithm was therefore the sign of the longitudinal displacements (in global X direction), which was positive for mode 1 and negative for mode 2, albeit much smaller, in the case of posi-

tive transverse displacement (in global Y direction). This distinction was only possible because the algorithm also considered the X displacement of mode 2, which amounted to about 2% of the Y displacement. The formation of again distinctive longitudinal and transversal modes in the next step 6 shows that the assignment made in step 5 was obviously correct.

(a) Mode 1   (b) Mode 2
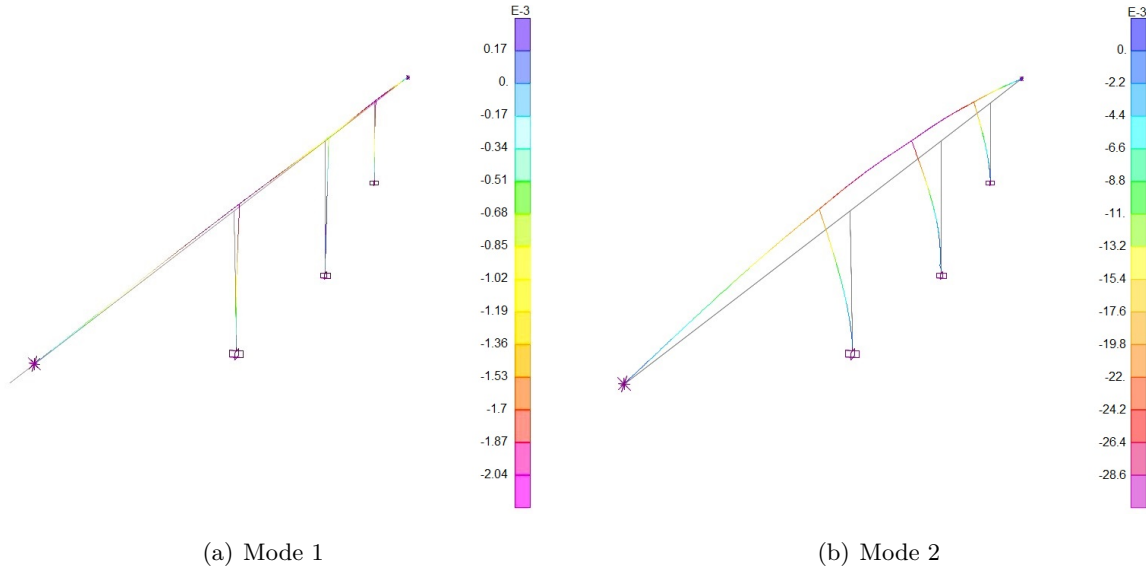
Figure 5.6: *Step 6: Clearly separable longitudinal and transversal mode*

Check 2 with regard to possible mode interchanges

If the self-assignment has not taken place in the previous check, it is now necessary to examine which other mode $m^{(i)}$ can be assigned to the reference mode $n^{(i-1)}$ of the previous step. For this assignment, the above Equation 5.2 is now applied to mode $n^{(i-1)}$ and $m^{(i)}$ ($m^{(i)} = [n^{(i-1)} - 4, n^{(i-1)} - 3, ...n^{(i-1)} + 4]$) with the same normalization and limitation to relevant directions d as before:

$$\Delta_{nm,(d)}^{(i)} = \frac{\sum_j \left| \mathbf{\Phi}_{n,(d)}^{(i-1)}(j) - \mathbf{\Phi}_{m,(d)}^{(i)}(j) \right|}{max(j)} \; . \tag{5.3}$$

The fact that a current comparison mode now corresponds to the modification of the previous reference mode under consideration is identified by the smallest difference sum. It is worth mentioning that a self-assignment is also possible in this second check if $\mathbf{\Phi}_n^{(i-1)}$ is most similar to $\mathbf{\Phi}_n^{(i)}$ eventhough it has significantly changed (i.e. check 1 failed).

Concluding it should be noted that, as already mentioned, the modal sign is randomly determined by the eigenvalue solver in *SAP2000*, but the identification or correction of this (according to Sec. 5.2.2) can only take place after the mode identification. For this reason, the 'old' mode shape $\mathbf{\Phi}_n^{(i-1)}$ is given a specific sign and the respective current comparison modes are applied in both directions (i.e. $\pm\mathbf{\Phi}_m^{(i)}$).

As an alternative to Equation 5.3, the widely used *Modal Assurance Criterion* (*MAC*) according to Equation 5.4 (ALLEMANG & BROWN , 1982), which is used in particular for comparisons of modes of an FEM calculation and a measurements that refer to the same (usually elastic) system, was also applied as a test.

$$MAC_{(d)}(n,m) = \frac{\left| \boldsymbol{\Phi}_{n,(d)}^{T} \boldsymbol{\Phi}_{m,(d)} \right|}{\left(\boldsymbol{\Phi}_{n,(d)}^{T} \boldsymbol{\Phi}_{n,(d)} \right) \left(\boldsymbol{\Phi}_{m,(d)}^{T} \boldsymbol{\Phi}_{m,(d)} \right)} \tag{5.4}$$

The following Figure 5.7 shows three simple examples of visualized *MAC* matrices for the cases: a) Pure self-assignments, b) Interchange 1-2 & 2-1, c) Interchange 1-2, 2-3 & 3-1. Here it can be seen that a clear assignment is characterized by the fact that each mode from step $i-1$ (x axis) is assigned exactly one bar, so that the corresponding new number can be read from the y axis ('Modes (i)'). A self-assignment is therefore synonymous with a single bar on the main diagonal.

(a) *MAC* for complete self-assignments

(b) *MAC* for interchanges 1-2 & 2-1

(c) *MAC* for interchanges 1-2 & 2-3 & 3-1
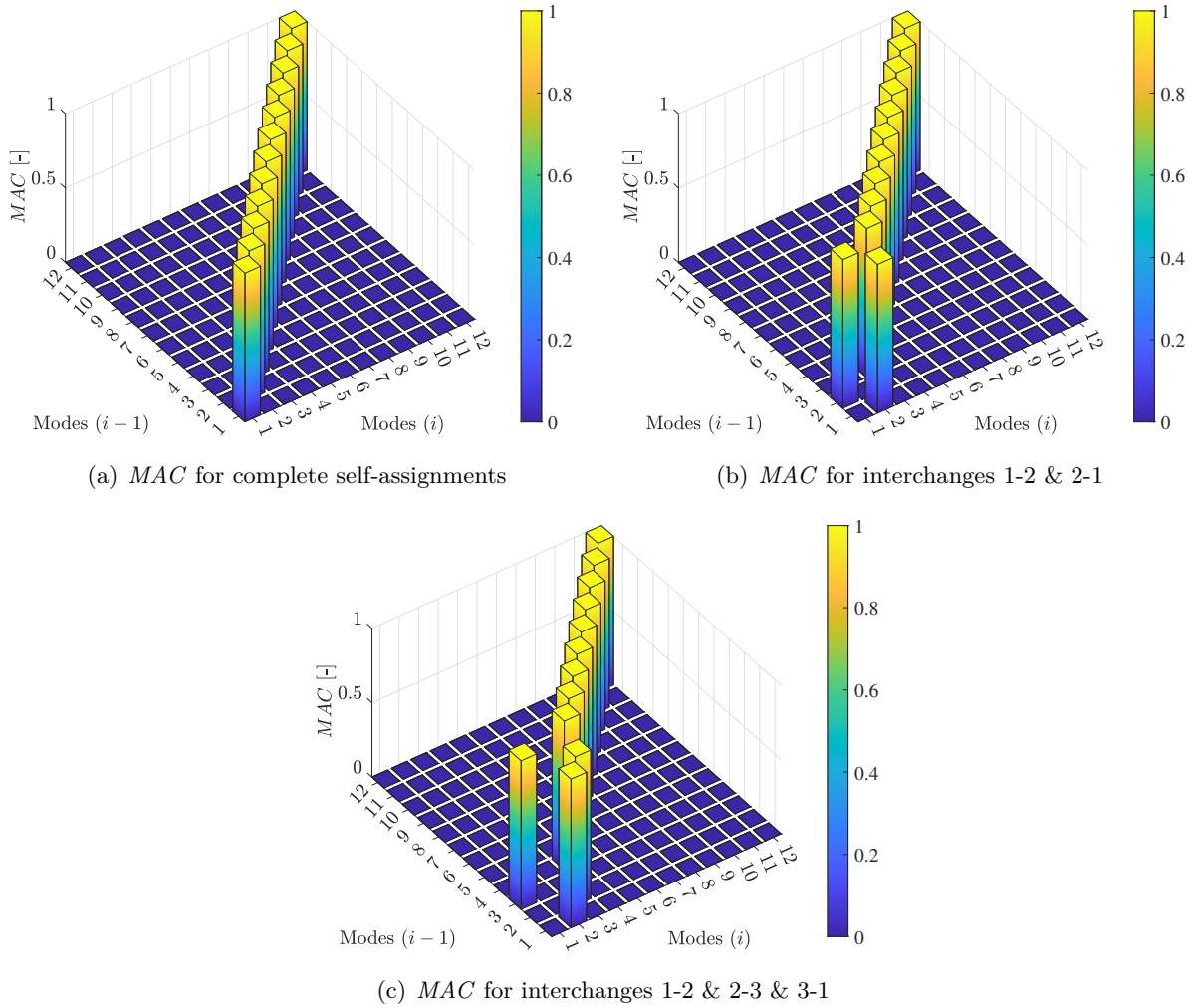
Figure 5.7: *Three exemplary visualizations of MAC matrices*

However, when applied to two numerical analyses concerning different inelastic states within the *mAMI* application, where two formerly distinctive mode shapes have become increasingly similar (on the system documented in Section 7.5.1), this approach provided less accurate assignments than the self-developed approach (acc. to Eqs. 5.2 & 5.3). Figure 5.8 visualizes the resulting *MAC* matrices for the eigenvector components in the X and Y directions, respectively. Here, for modes 4 and 5 as well as for modes 9 and 10, there are four columns of similar height at the main and the secondary diagonal. Furthermore, there are different columns with a measurable height assigned to almost each mode from step $i-1$. In view of this worse performance, the approach according to Equation 5.3 is used in the *CAAP* tool.

(a) *MAC* corresp. to the X direction   (b) *MAC* corresp. to the Y direction
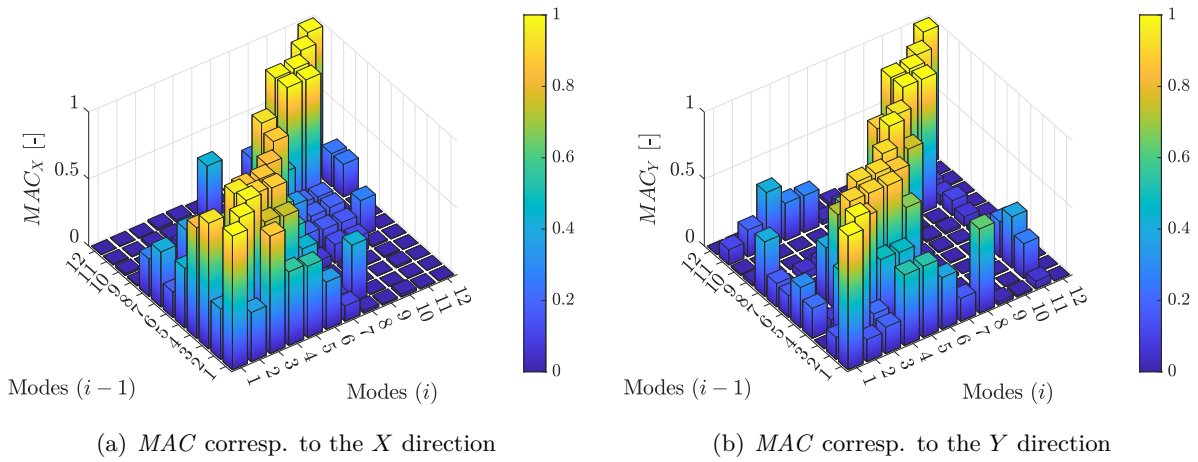
Figure 5.8: *Examples of two directional MAC matrices in certain steps of an application in the mAMI*

Algorithmic handling of mode interchanges

In order to ensure that all relevant modes can be clearly assigned when mode interchanges occur, a matrix with three columns and a varying number of rows is created (see Eq. 5.5). In this matrix, each row refers to a specific mode change. The first column contains the original mode number from the initial step, while the second and third columns contain the mode numbers of the preceding and current step, respectively.

$$arg.comp.modes.changes = \begin{pmatrix} n_I^{(1)} & n_I^{(i-1)} & n_I^{(i)} \\ n_{II}^{(1)} & n_{II}^{(i-1)} & n_{II}^{(i)} \\ \vdots & \vdots & \vdots \end{pmatrix} . \tag{5.5}$$

The background to this is that the modal capacity spectra and all associated variables (such as the effective yield points, effective natural frequencies, etc.) are always stored relating to the initial number. The last point of the respective capacity spectrum, e.g., is therefore accessed via the value in the first column of *arg.comp.modes.changes*. Current modal results from

SAP2000, such as modal participation factors or natural frequencies, however, are accessed via the current mode number $n^{(i)}$. The respective link then provides the additional third column of *arg.comp.modes.changes*. The indices *I, II (etc.)* in Equation 5.5 are related to the internal ascending numbering of the relevant modes affected by changes.

If a mode change occurs, the following four cases are basically possible:

1. A certain mode changes its number for the first time, e.g. the initial mode 2 becomes mode 1. Then the corresponding row in the above matrix would be: [2 2 1].

2. A mode that changed its number in the preceding step now changes back to its original number. Following on from the previous example, this would generate the following row in the matrix above: [2 1 2].

3. A mode changes its number again and is assigned a different number than before. Following on from the first case, for example: [2 1 3].

4. And finally, a mode that changed its number in the previous step may now keep this number. Again as an example, taking case 1 as the starting point: [2 1 1]. Here, only the second entry has to be updated, as the mode retains its initial and its current number. This row remains unchanched in the following steps until the mode changes again.

If a mode returns to its initial number and does not change it in the next step, a row with three identical entries is created. In the example above, this would be: [2 2 2]. This kind of row is eliminated by the algorithm as it can be seen as 'no active change'. This is therefore the only way in which a mode can leave the above matrix according to Equation 5.5. The complete change history, however, is not required and therefore not stored.

At the end of the mode identification an automated plausibility check is carried out. Here, the algorithm searches for the following two inadmissible mode changes, which are shown as examples in Figure 5.9 below:

1. Two different modes $n^{(i-1)}$ and $k^{(i-1)}$ of the previous modal analysis are assigned to the same current mode $m^{(i)}$. The number $m^{(i)}$ thus occurs twice in the third column of *arg.comp.modes.changes* (cf. blue arrows in Fig. 5.9).

2. Mode $n^{(i-1)}$ (e.g. 4, cf. orange arrows in Fig. 5.9) of the previous step was assigned to a new, current mode $m^{(i)}$ (e.g. 5) which has already been considered, but without this mode (here: 5) being assigned to a new mode (e.g. 4). Due to this self-assignment the number $m^{(i)}$ (e.g. 5) only appears in the third but not in the second column of *arg.comp.modes.changes*.
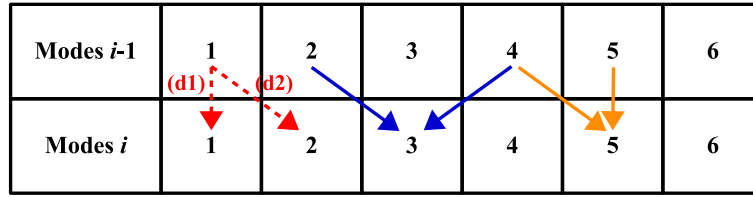
***Figure 5.9:** Visualization of unclear or invalid mode assignments*

In addition, it is also possible that a certain reference mode $n^{(i-1)}$ cannot be assigned to any new mode at all. This occurs when stage 1 as well as check 1 of stage 2 fail and the separate, direction-related differences $\Delta_{nm,(d)}^{(i)}$ have their minima corresponding to different current modes (in check 2). Figure 5.9 shows as an example (see red dashed arrows) that the first direction examined (d1) would lead to a self-assignment (1-1), while the second direction (d2) would result in a mode change 1-2.

If either an inadmissible assignment occurs (plausibility check) or no assignment is possible at all (at stage 2) for a particular reference mode, the automated mode identification failed. A corresponding warning is issued and the program sequence is not continued until the user has made a manual assignment by means of a console entry after examining the relevant modes in *SAP2000*. In this case the user is also given the opportunity to enter further changes, which he has identified, until the algorithm continues. Vice versa, if the algorithm has identified a change that does not occur in reality, the user can enter the 'old' number for the new assignment in order to undo the error.

In addition to these central processes, the *CAAP* tool also contains numerous smaller additional or intermediate checks as well as plausibility checks, which are either intended to ensure a reasonable self-assignment of modes if the above checks fail, or to prevent incorrect assignments. However, as the documentation of all checks would go beyond the scope of this chapter, the reader is referred to the *CAAP* manual (KÄMPER & OSTERKAMP , 2024).

5.2.2 Ensuring constant directions of modal load patterns

The problem has already been described that the sign of an eigenvector in *SAP2000*, as in other eigenvalue solvers, is chosen randomly. This means that even unchanged modes can be mirrored between two adaption steps, or can be approximately mirrored if the mode shape changes by a certain amount. Both cases must be recognized equally reliably by the algorithm so that a load distribution does not have a counteracting and thus unloading effect in certain adaption steps. In the *CAAP* tool, this is implemented using a two-stage method again:

1. Preliminary evaluation in step *i-1*: Here, for all modes n considered the displacements with the largest magnitude are read out across all three directions. The corresponding dominant direction d_{dom}, the node label j_{dom} and the sign of this decisive displacement are stored.

2. Main check in step *i*: In the next step, it can then be checked for each relevant mode n whether the new deformation component of the eigenvector $\mathbf{\Phi}_n^{(i)}$ in the previously saved node j_{dom} has the same sign in the direction d_{dom} as in the previous step. Based on this check, a respective sign correction factor is reset to either 1 or -1 in each *mAMI* step.

Finally, it should be noted that the modal participation factor $\beta_n^{(i)}$ in *SAP2000* also has varying signs, although these are independent of any changes in the sign of the corresponding mode shapes themselves. For this reason, the absolute value of $\beta_n^{(i)}$ is always included in the total load vector according to Equation 3.24 in order to maintain a constant direction of the respective modal load patterns.

5.2.3   Determination of optimized spectral increments and reasonable numbers of pushover steps

A further algorithmic difficulty lies in determining the optimized spectral acceleration increments $\Delta S_{a,B}^{(i)}$ and, adapted to it, an appropriate number of load steps for the respective pushover calculation. As already explained in Section 3.1.4, optimized $\Delta S_{a,B}^{(i)}$, in contrast to constant spectral increments of the base mode acceleration, serve to significantly reduce the total number of adaption steps and thus the computing time. This is achieved by targeting relevant plastic effects. Since in each adaption step the algorithm not only adapts the incremental load vector according to Equation 3.24, but also updates the effective modal damping values $\xi_{n,eff}^{(i)}$ and, above all, the maximum modal spectral accelerations $S_{a,n,max}^{(i)}$, it is crucial to recognize all system changes that have a significant effect on one of the variables mentioned. Figure 5.10 below shows an example of poorly optimized spectral increments, which led to a much too coarse mapping of the final range of the pushover calculation. Due to the fact that very few adaption steps took place in this range, the significant decrease in the first natural frequency, visible in Figure 5.10 (a), was obviously not adequately represented compared to the much more accurate calculation with constant spectral increments $\Delta S_{a,B}^{(i)} = 0.01$ m/s². This led to a significant overestimation of $S_{a,1,max}^{(end)}$ (1.12 > 0.96 m/s², cf. Fig. 5.10 (b), capacity spectrum of mode 1 (CS1)). In this specific case, the excessive spectral increments resulted from the fact that the analyzed pushover curve in the segment of the sixth 'Max computation' has an extremely low initial slope (cf. Fig. 5.11). In the first version of the *CAAP* algorithm, an initial slope of less than 10% of the global initial slope was regarded as an indicator for the end of the

calculation, since with very low gradients certain percentage deviations, which still lead to a fall below the constant values k_{loc} and k_{glob}, would eventually correspond to absolute differences of almost 0. As a result, no further adaption step was carried out in this case. A revision of this check now refers to the secant slope of a new pushover curve segment, which in this specific case (according to Fig. 5.11) is considerably greater than 10% of the initial slope (see 'Corr. comp. 1' in Fig. 5.11).

(a) Development of f_1

(b) First modal CS of the *mAMI* compared to the *CSM* result
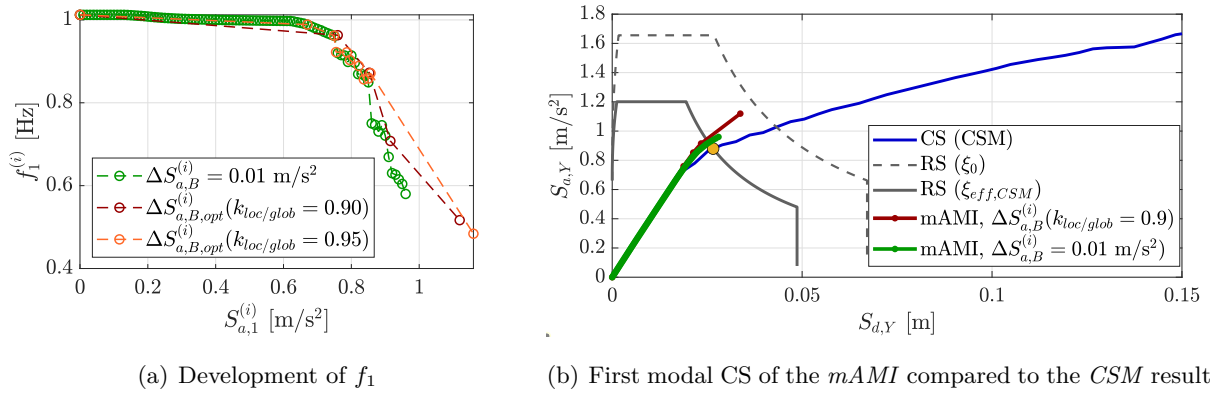
Figure 5.10: *Comparison of poorly optimized and fine constant acceleration increments $\Delta S_{a,B}^{(i)}$*
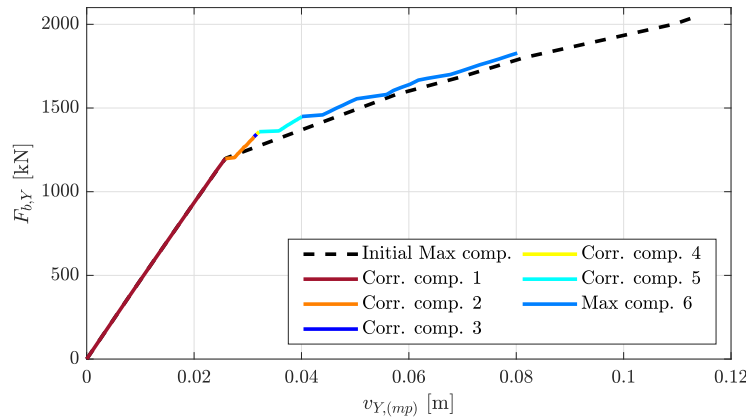
Figure 5.11: *mAMI calculation with an insufficient number of adaption steps*

Apart from this problem, which has now been solved, the key determinants for a sufficiently fine division into adaption steps are, on the one hand, the two limiting values k_{loc} and k_{glob} and, on the other hand, the resolution of the respective pushover curve segments in the individual 'Max computations'. While the first point is immediately obvious based on the explanations in Section 3.1.4, the second point can be explained by the fact that more and therefore shorter paths in the pushover curve lead to more potential kink points and general stiffness changes.

This results in significantly more points that may fulfill one of the two limiting criteria (cf. Eqs. 3.13 & 3.14), so that the limiting point is generally reached earlier.

However, even with a sufficiently accurate 'Max computation', it is important that the subsequent correction calculation is also precise enough so that the target base shear $F_{b,target}^{(i)}$ is also achieved as accurately as possible. Sample calculations in an early phase of the algorithm optimization showed that if this target value was exceeded too much, it was again identified as the next limiting value in the subsequent 'Max computation', so that a superfluous adaption step was carried out. Numerous parameter studies have shown that the first correction calculation with a mostly very long linear-elastic branch should be carried out with about 20 steps and the subsequent correction calculations with at least 5 steps in order to avoid the problem described before. Tightening the error tolerance, on the other hand, had no comparable effect.

Finally, however, the question arises as to how many pushover steps the other 'Max computations' should consist of. It is immediately obvious that the respective pushover curve segment must not be too imprecise for the subsequent analysis. On the other hand, however, it should not have a too high resolution in order to avoid generating an unnecessarily large number of adaption steps. Especially towards the end of the calculation with ever smaller acceleration increments $\Delta S_{a,B,max}^{(i)}$, which are due to continuously increasing values $S_{a,B}^{(i-1)}$ and generally decreasing maximum values $S_{a,B,max}^{(i)}$, this would become a problem with a constant number of pushover steps per 'Max computation'. The increasingly finer mapping of the adaption steps would lead to a drastic decrease in the acceleration increments per correction calculation and thus to more and more adaption steps, which is illustrated in the following Figure 5.12 (where each adaption step is represented by a different color in the overall pushover curve).
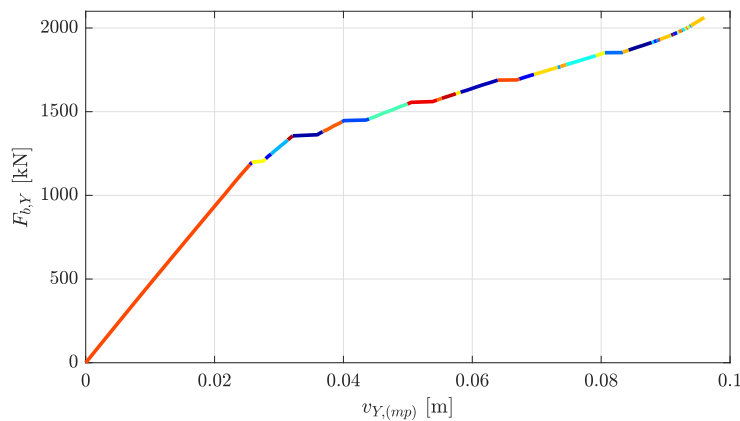
Figure 5.12: *mAMI calculation with unnecessarily decreasing spectral increments*

Thus, the idea is that the number of load increments per adaption step, defined in *SAP2000* as 'nonlinear steps' of the i-th pushover load case, should be based on the length of the upcoming path of the pushover curve. This would ensure that the length of the respective load-deformation segments would be approximately constant over the entire *mAMI* calculation. However, as the branch of the next 'Max computation' is not known beforehand, the corresponding length must be estimated on the basis of the previous one. To do this, the new maximum base shear $F_{b,max}^{(i)}$ is first calculated from the last existing value added to the sum of all current load increments:

$$F_{b,max}^{(i)} = F_{b,red}^{(i-1)} + \sum_j \Delta \mathbf{P}_{max}^{(i)}(j) \ . \tag{5.6}$$

Then all data points p of the previous 'Max computation' are counted for which the following applies:

$$F_{b,red}^{(i-1)} \leq F_b^{(i-1)(p)} \leq F_{b,max}^{(i)} \ . \tag{5.7}$$

This provides the best possible estimator for a sensible number of pushover steps for the upcoming 'Max computation' and is therefore used as a reasonable optimized number of pushover steps. Only in the very first step this approach is not possible. Thus, a basic value specified by the user is used here, which should be set relatively high (e.g. > 150), especially for systems with many smaller system changes expected.

The effectiveness of the optimizations described in this Section 5.2.3 with regard to reducing the computing time while maintaining a comparable quality of results is examined in Section 6.4.

5.2.4 Identification of the performance state and alternative termination criteria

If the analysis of the pushover curve does not require a new adaption step, the current maximum spectral accelerations $S_{a,n,max}^{(i)}$ correspond to the performance state. Since the last i-th 'Max computation' has headed exactly for this state, all structural responses in the performance state are already available. However, this is only the case if the last FE calculation was successful, which means that the last incremental load vector $\Delta \mathbf{P}_{max}^{(i)}$ could be fully absorbed. To verify this, the LOG file of the last calculation is therefore checked in order to see whether there were problems concerning the equilibrium iteration that led to the calculation being aborted. In the event of such a premature termination, an attempt is first made to enable a completely successful calculation by tripling the permissible number of failed iteration steps, in *SAP2000* referred to as 'null steps'. If this measure also fails, the error tolerance is increased in up to three stages by a specific, user-defined Δ and a new calculation attempt is made in each case. If this is also unsuccessful, the earthquake design check has failed and the *mAMI* calculation is aborted.

An analogous check is also carried out after each correction calculation. A failed correction calculation cannot be caused by exceeding the ultimate limit state because higher loads were already included in the previous 'Max computation'. However, in such a case, problems may occur within the equilibrium iteration if the load increments are very small compared to the existing load level. In such cases, the number of pushover steps in the correction calculation is reduced accordingly and the procedure described above is only carried out if this measure does not lead to a successful calculation.

5.3   Concluding remarks

An examination whether the FE computation for a given incremental load vector was completely successful, as described above, is not necessary for the 'Max computations' before the performance state is reached. Nevertheless, it makes sense to check whether the value $F_{b,max}^{(1)}$ was actually reached in case of the initial 'Max computation' or how large the maximum base shear $F_{b,max,exist}^{(1)}$, which the structure could accommodate, in fact was. On the one hand, this value can then be used as an upper limit in subsequent 'Max computations' if a smaller value $F_{b,max}^{(pp)}$ can be achieved in the final calculation. Thereby time-consuming iteration problems can be avoided, which would result from repeated attempts to exceed $F_{b,max,exist}^{(1)}$ in each $mAMI$ step. On the other hand, this upper limit should be taken into account when determining the optimized numbers of pushover steps according to Equation 5.7 in order to relate them to the actual pushover path to be expected.

Finally, it should also be noted that the $CAAP$ algorithm monitors two further critical mode developments. On the one hand, after each new modal analysis, it warns the user if there are modes that have not yet been taken into account and have an effective modal mass participation of at least 5% in the earthquake direction for the first time. On the other hand, the algorithm identifies when certain modes considered form significant displacement components in a previously at least almost deformation-free direction. Such a significant deviation of a mode shape is also output as a warning, even if the mode identification was successful, so that the user can assess after the calculation whether the assignment was indeed correct against this background.

6 Application of the *mAMI* procedure in the context of monodirectional earthquake investigations

6.1 Introduction

Overview of the comparative studies

Now that the chosen nonlinear numerical model in *SAP2000* has been validated and an algorithm for the automated execution of the *mAMI* has been developed, the latter can be applied and evaluated for the first time in conjunction with the *CAAP* tool. However, it is important to first examine certain procedural or algorithmic aspects individually in order to be able to draw reliable conclusions. Against this background, certain adjustments and extensions explained in Section 3.1, such as the correlation factors or the optimized spectral acceleration increments, are considered individually in separate analyses in order to better understand and specifically assess their influence on the calculation results. Furthermore, a monodirectional earthquake excitation is investigated first as the results are easier to interpret than in the bidirectional case. On the basis of the monodirectional earthquake and the constant normal force due to gravity loads, plastic hinges can be used at first to simplify the representation of the material nonlinearity.

The following investigations are carried out within this framework:

1. Evaluation of the *mAMI* procedure in general and the correlation factors in particular by comparing the results of a calculation with and without consideration of the partial correlation with those of a single-mode *CSM* calculation, a multi-mode *MPA* and *RSM* calculation as well as a *Nonlinear Time History Analysis* (*NLTHA*). In order to deliberately eliminate the influence of the optimized acceleration increments considered below, the latter are set to be constant with sufficiently fine step sizes.

2. Comparison of constant and optimized spectral acceleration increments $\Delta S_{a,B}^{(i)}$ of the reference mode to evaluate the optimization approach with regard to the result quality on the one hand and the reduction of the computational effort on the other hand.

3. General performance assessment of the *mAMI* on different bridge structures with varying complexity in the nonlinear seismic behavior. For this purpose, a parameter study is carried out using 11 bridge models with an increasingly asymmetric stiffness distribution. In addition, two different mass-stiffness ratios of the bridge deck are considered in order to significantly vary the influence of higher mode effects. This study serves to narrow down a reasonable range of application of the *mAMI* based on realistic structural simulations for a wide variety of bridge systems. For this reason, in contrast to the first two algorithmic or process-oriented studies, it is essential to capture all possible dynamical effects that could arise in reality. This includes the development of three-dimensional mode shapes, which only have vibration components in one direction for the initial elastic system. In case of bridge structures, this can occur due to a decrease of axial stiffness in the piers, where previously exclusively horizontal modes also form vertical vibration components. In order to be able to map this and other similar effects, fiber hinges are used for this analysis, as, according to Section 4.3, *Interaction Plastic Hinges* are faulty in the *SAP2000* version used and cannot capture a decreasing axial stiffness with varying bending moments anyway.

Earthquake loading

All calculations are based on an earthquake according to the elastic response spectrum of Eurocode 8 - Part 1 (2010) with a horizontal ground acceleration of $a_g = 0.1g$ and $\xi = 5\%$. The S value and the control periods correspond to ground category D and response spectrum type 1 ($S = 1.35$, $[T_B, T_C, T_D] = [0.2\text{ s}, 0.8\text{ s}, 2.0\text{ s}]$). For the time history calculations, response spectrum-compatible artificial acceleration records were generated using the *SIMQKE* tool[4] whose back-transformed values show a good approximation of the normative response spectrum (cf. Fig 6.1). This ensures comparability between static and dynamic calculations.

(a) Earthquake record in time domain   (b) Retransformed spectrum
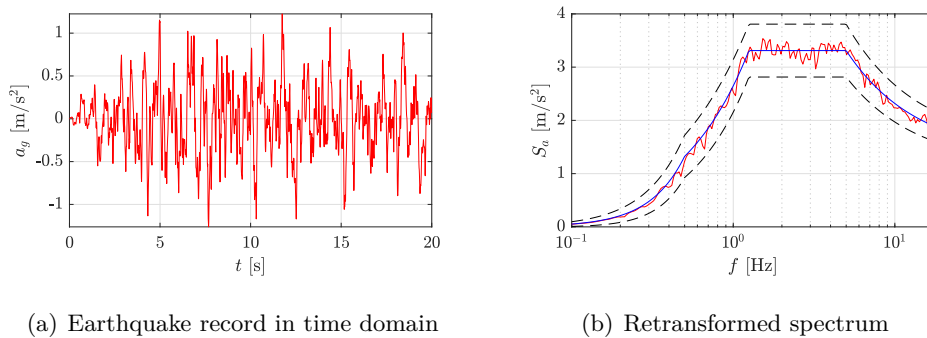
Figure 6.1: *Example of an artificial earthquake record*

---

[4] *SIMQKE*, version 1.1, 9.04 developed by Pierino Lestuzzi - CH-1015 Lausanne(Switzerland) acc. to Gasparini & Vanmarcke (1976)

6.2   Description of the investigated bridge structures

KAPPOS ET AL (2012) have dealt intensively with the assessment and categorization of various bridge systems concerning their inelastic seismic behavior (cf. KAPPOS ET AL (2012), Chap. 4 & Tab. 5.1). Depending on the abutment restraints and the ratio of the pier lengths and the associated stiffness distribution, there are systems whose dynamic behavior depends almost exclusively on one single predominant mode, which changes only insignificantly even at higher seismic intensity. On the other hand, there are bridges for which neither of these aspects apply.

In the following, the multimodal adaptive *mAMI* is to be compared with other less complex methods. Since the *mAMI* should demonstrate its advantages especially with complex seismic behavior, two bridge structures with very different load-bearing behaviors are investigated:

- A four-span bridge (model A, cf. Fig. 6.2 (a)) with a symmetric stiffness distribution based on the 'V232P' model investigated by KAPPOS ET AL (2012), which they classify as 'regular' so that it can be calculated using non-adaptive single- or multi-mode methods.

- A four-span bridge (model B, cf. Fig. 6.2 (b)) with a continuous increase in pier lengths and thus with a significantly asymmetric stiffness distribution based on model 'V123P' by KAPPOS ET AL (2012), which they classify as 'irregular', leading to the fact that at least a multi-modal and preferably also adaptive calculation concept is required.

In addition, transverse restraints at the abutments and pinned pier-deck connections are assumed as well as a fixed end-support of the bridge piers in the surrounding soil, whereby a soil-structure interaction (*SSI*) is neglected. In both models, the bridge piers are labeled P1 - P3, ascending in global *X* direction (cf. Appendix E, Figs. E.5 & E.6).

(a) Model A   (b) Model B
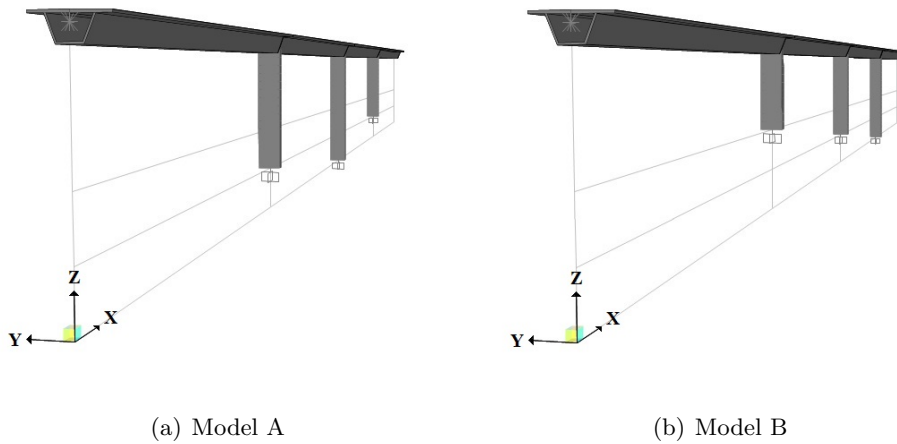
Figure 6.2: *Investigated bridge models A & B*

Both models are reinforced concrete bridges with four spans of 50 m in length. The piers each have a reinforced concrete box girder cross-section and lengths of 15, 20 and 15 m in model A and 10, 15 and 20 m in model B.

While an unreinforced box girder cross-section is modeled for the bridge deck and the rein-forcement is considered by increasing the cross-sectional area and the two moments of inertia by a factor of 1.2, the piers are modeled taking into account their specific reinforcement. For the piers, the cross-section 1 considered in Chapter 4 is applied, so that the definition of the plastic and fiber hinges is analogous to this. The M-κ curves for the plastic hinge models, which depend on the normal force due to the dead weight of the respective pier, are depicted in full in Appendix E.1, while Figure 6.3 (a) below contains an examplary presentation of the curve for edge pier P1 of model B. To simplify matters, the compressive force at the respective pier base points was taken into account, as this point is decisive for the first formation of a plastic zone. The idealizations of the M-κ curves, reduced to four sections for the definition in *SAP2000*, deliberately do not represent the relatively flat ending area up to the full utilization of the bending capacity, but end at about 98% of the maximum moment of plasticity. Since a cross-sectional utilization of 100% should not be aimed for anyway, the relevant initial area can thus be mapped more accurately. For the fiber hinges, the same fine fiber division was initially used as in Chapter 4 (cross-section 1 with 1490 fibers, cf. Fig. 4.4 (a)). Due to the expected high computing times for nonlinear time history and complex adaptive pushover calculations, a significantly rougher subdivision with only 212 fibers was also modeled (cf. Fig. 6.3 (b)). A preliminary pushover study provided practically identical base moments for both models with a deviation of less than 0.1%, so that this rough fiber division is used as the basis for the following micro models. However, the material parameters differ from those considered in Chapter 4. In contrast to the post-experimental study of the *ELSA* tests, only normative material parameters of the concrete (C35/45) and the reinforcing steel (B500A) are used in the following. These are listed in detail in Appendix E.1.

In view of the end restraint conditions of the piers, plastic zones are only expected to form at the base of the piers. Based on the findings from the model validation (with the same cross-section and a pier length of 15 m) the potential plastic or fiber hinges are arranged on the lowest 10 meters of each pier (cf. Figs. E.5 & E.6, App. E). Also based on the results documented in Chapter 4, the *Pivot Hysteresis Model* with $\alpha_{1/2} = 10.0$ and $\beta_{1/2} = 1.0$ was chosen for the reinforced concrete plastic hinge as well as the *Concrete* and the *Kinematic* model for the concrete and steel fibers of the fiber hinge, respectively, to describe the hysteretic behavior. Figures 6.4 to 6.6 show the relevant transversal mode shapes of models A and B.

(a) Examplary M-κ curve for P1 of Model B

(b) Rough fiber subdivision
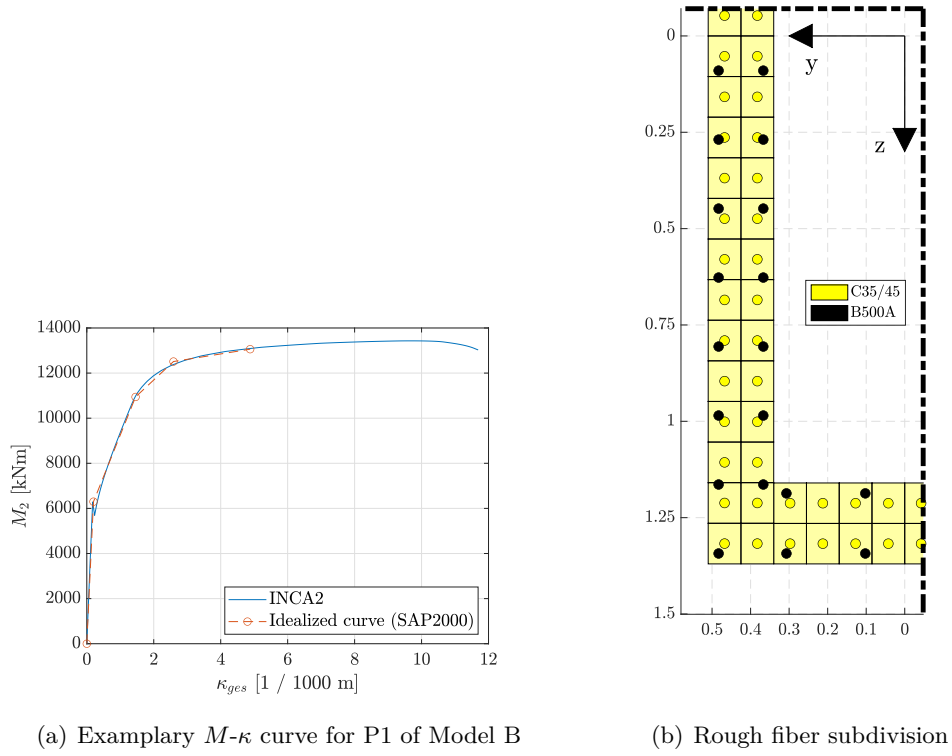
Figure 6.3: *Examplary M-κ curve for plastic hinges and used fiber division for fiber hinges*

(a) Mode 1 ($f_1 = 0.99$ Hz, $\mu_{eff,Y} = 69.7\%$)

(b) Mode 5 ($f_5 = 1.82$ Hz, $\mu_{eff,Y} = 20.2\%$)
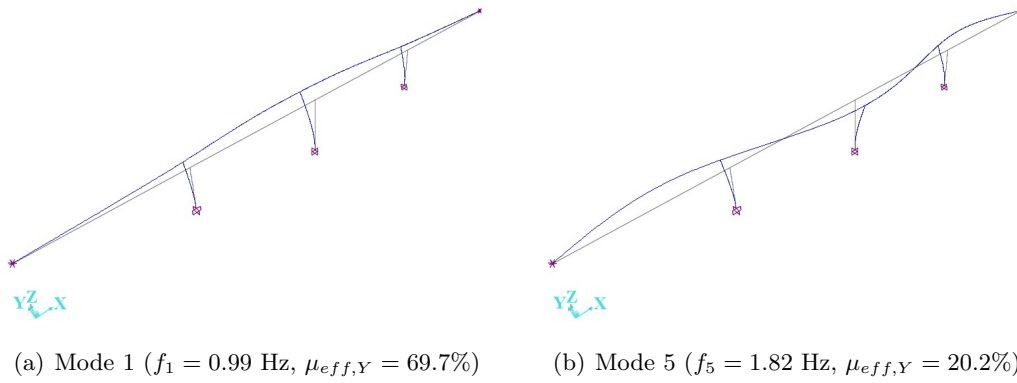
Figure 6.4: *Relevant transversal modes 1 & 5 of model A*

(a) Mode 1 ($f_1 = 1.01$ Hz, $\mu_{eff,Y} = 53.0\%$)   (b) Mode 4 ($f_4 = 1.63$ Hz, $\mu_{eff,Y} = 8.9\%$)
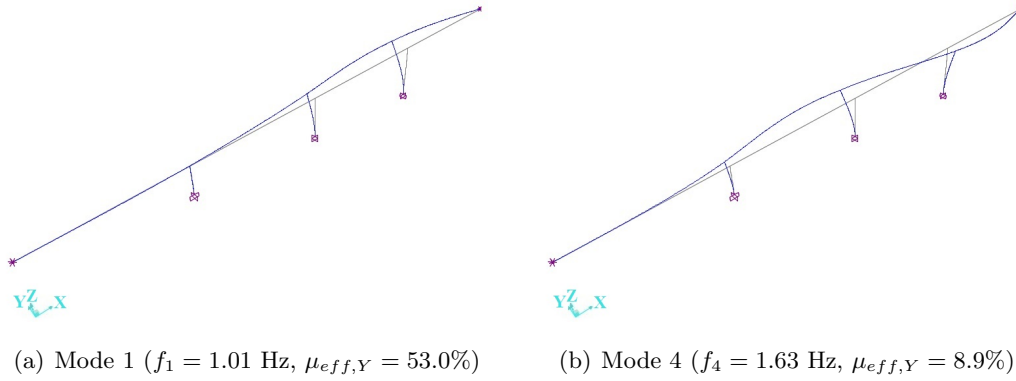
Figure 6.5: *Relevant transversal modes 1 & 4 of model B*
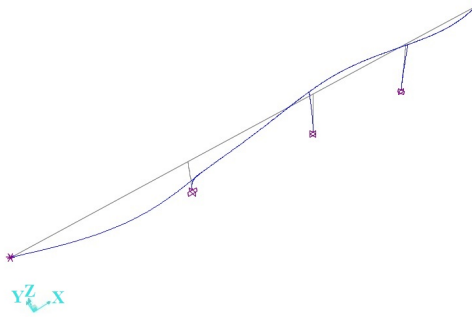
Figure 6.6: *Relevant transversal mode 6 of model B ($f_6 = 2.25$ Hz, $\mu_{eff,Y} = 29.0\%$)*

6.3 Evaluation of the *mAMI* procedure in general and the correlation factors in particular

6.3.1 Realization of the individual calculations

As already explained in Section 6.1, bridge model B exhibits an irregular seismic behavior. Hence, the application of a complex static method such as *mAMI*, including higher modes and continuous updates of the modal system properties, is advisable if not necessary. Therefore, this structure is selected for the following initial investigations of the *mAMI* before the bridge model A and a total of nine 'intermediate models' (between A and B) with interpolated pier lengths are also considered in the exploration of a reasonable range of application in Section 6.5.

In addition, these initial analyses on model B are deliberately kept simple with an exclusive seismic excitation in the transverse direction, taking into account the relevant modes 1, 4 and 6 (cf. Figs. 6.5 & 6.6). In the following, the essential analysis parameters of all applied methods are briefly presented.

Nonlinear Time History Analysis (*NLTHA*)

For the *Nonlinear Time History Analysis*, which as a dynamic calculation is generally regarded as the most realistic reference method, first the usual 7 (acc. to EC 8) and then, for a significantly higher accuracy of this scientific investigation, a total of 50 artificially generated earthquake time histories are examined. Furthermore, a Rayleigh damping based on the initial stiffness matrix is considered in *SAP2000*, where the coefficients α_M and α_K are determined on the basis of the usual system damping of 5% in earthquake engineering and the frequencies of the two most relevant natural modes with the largest effective modal mass in the Y direction (here: modes 1 & 6). The selected time increment $\Delta T = 0.0025$ s falls below the generally recognized criterion of $T/20$, even if T is the 28th eigenperiod (with $\mu_{eff,Y,28} \approx 1\%$). Since a comparative calculation with an even smaller step size of 0.002 s shows a deviation of less than 0.5% with regard to representative calculation results, the chosen ΔT of 0.0025 s is adequate. For the assumed earthquake duration of 20 s, this results in a total of 8000 time points to be examined.

Multi-mode *Response Spectrum Method* (*RSM*)

The *Response Spectrum Method* commonly used in practice is included in the method comparison as a reference procedure due to its central role in earthquake engineering. To create the design response spectrum, the parameters for the spectrum as described in Section 6.1 and a system damping of 5% are applied. The main focus is therefore on the difficult choice of the ductility factor q, which is briefly discussed below. Three different behavior factors are used in this academic study, in which, unlike in practice, no definitive single value has to be determined:

- $q = 1.0$ (highly conservative approach of structure without any energy dissipation effects)

- $q = 1.5$ (estimate for limited ductile behavior, cf. EUROCODE 8 - PART 2 (2011))

- $q = 3.5$ (upper estimate of the maximum ductility to be expected), whereby this value was determined according to EUROCODE 8 - PART 2 (2011), Table 4.1 as follows regarding the shortest pier (with the 'highest proportion of earthquake resistance'):

$$L_s = \frac{5}{6} \cdot 10 \text{ m} = 8.33 \text{ m} , \tag{6.1}$$

with: L_s = distance between the moment zero point, here at the pier top, and 'the plastic hinge', here: assumption of the 'effective center of the plastic zone' in the middle of a plastic zone of length 1/3 H. With the cross-section hight of $h = 2.74$ m follows:

$$\alpha_s = \frac{L_s}{h} = 3.04 \Rightarrow \lambda(\alpha_s \geq 3.0) = 1.0 \tag{6.2}$$

$$\rightsquigarrow q_{max} = 3.5\lambda(\alpha_s) = 3.5 \text{ (assumption of 'ductile' component behavior).} \tag{6.3}$$

The individual modal contributions are superimposed in each case using the *CQC* rule.

'Standard' pushover calculation based on the *Capacity Spectrum Method* (*CSM*)

The *CSM*, as a representative of the basic pushover concept, is carried out on the basis of mode 1 with a load distribution proportional to mass and mode shape that best takes into account inertia effects. Node 4 at the top of edge pier P3 (calculation A) and in a further calculation (B) node 3 at the head of center pier P2 are considered as respective monitoring points.

The transformation of the pushover curve and the subsequent determination of the performance point are outsourced to *MATLAB*. The reason for this, as was discovered in extensive studies, is that in *SAP2000* only components of the eigenvector in the monitored direction are taken into account in the transformation (acc. to Eqs. 1.17 and 1.19). However, this may lead to errors in case of spatial modes that become relevant later. In addition, the eigenvector is approximated by the deflection line from the pushover analysis in *SAP2000*, which is proposed in ATC-40 (1996) (Sec. 8.5.5.1) as an approximate solution in the absence of modal results.

Modal Pushover Analysis (*MPA*)

The application of the most common multi-mode pushover procedure, the *MPA* (*Modal Pushover Analysis*) by CHOPRA & GOEL (2002), is also carried out with a load distribution proportional to mass and mode shape. The following steps and assumptions are taken into account:

- Estimation of the target displacement $\Delta_{mp,max,n,el.}$ for each mode n considered based on the elastic *RSM* ($\xi_0 = 5\%$).

- Pushover analyses for all modes n until $\Delta_{mp,max,n,el.}$ is reached and two-segmented linearization of the pushover curve. Since the latter is not clearly defined by CHOPRA & GOEL (2002), the linearization according to AYDINOGLU (2003) is chosen, yielding $T_{eff,n,inel.}$.

- Determination of $S_{d,n,max,inel.}$ using the inelastic response spectrum reduced by $\xi_{eff,n}$ (acc. to ATC-40 (1996)) for $T = T_{eff,n,inel.}$ and subsequent reverse transformation. This yields the maximum inelastic monitoring displacement $\Delta_{mp,max,n,inel.}$.

- Push until the respective modal performance state (with $\Delta_{mp} = \Delta_{mp,max,n,inel.}$).

- *CQC* combination of relevant structural responses.

A first calculation is based on the monitoring point 4 (head of P3) and the second on 'optimized monitoring points' ('*o*') 4, 2 (head of P1) and again 2 for the modes 1, 4 and 6, respectively.

Modified *AMI* procedure (*mAMI*)

For the application of the *mAMI*, only half of the total of eight possible sign combinations of the three modes considered need to be analyzed due to the symmetry of the bridge structure with respect to the *X-Z* plane: {1 4 6}, {1 -4 6}, {1 4 -6} and {1 -4 -6} (LC 1-4).

As already mentioned, the constant spectral increments provided by NORDA (2012), here in the form of spectral accelerations, are first applied refering to the base mode. Initially, a constant acceleration increment of $0.05 \ \text{m/s}^2$ is applied and, in addition, values of $0.03 \ \text{m/s}^2$ and $0.01 \ \text{m/s}^2$ in the sense of a convergence study.

In order to be able to explicitly assess the influence of the correlation factors, all *mAMI* calculations are carried out both without and with consideration of the partial correlation. In the latter case, mode 1 is initially selected as the reference mode to determine the α_n factors, while the additional consideration of an alternative reference mode is carried out later.

6.3.2   Comparison of the lateral deck deflection lines

First, the lateral displacements along the bridge deck are evaluated, giving a good impression of the magnitude and qualitative distribution of the seismic loads. The statically determined deflection lines are mirrored in order to compare them with the averaged maximum and minimum displacements of the *NLHTA*. Since the latter do not all occur at the same time, it would be more appropriate to speak of pseudo-deflection lines, which will be omitted in the following for the sake of simplicity. For better orientation, the bridge piers are marked with point symbols.

Nonlinear Time History Analyses (NLTHAs)
First, the averaged maximum and minimum transversal deflections along the bridge deck are compared for nonlinear time history calculations based on 7 and 50 accelerograms.
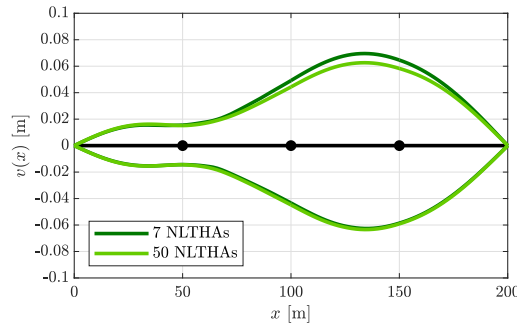
Figure 6.7: *Deck deflections of NLTHAs with 7 and 50 accelerograms*

While the curves of the averaged minima according to Figure 6.7 are approximately congruent, the two deflection lines of the averaged maxima show recognizable differences, especially in the third bridge span between the middle (P2) and the right edge pier (P3). The percentage difference between the two maximum deck displacements here is about 11%. For this reason, all subsequent comparisons are based on the averaged extremes of the 50 *NLTHAs*, as these are the reference results of a scientific study.

Multi-mode *Response Spectrum Method* (*RSM*)

Figure 6.8 compares the deformations of the bridge deck for the three *RSM* calculations with the averaged maxima and minima of the 50 nonlinear time history calculations.
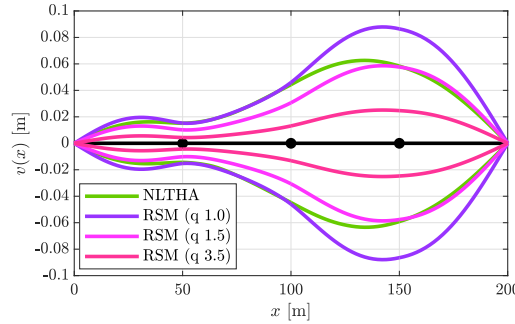
Figure 6.8: *Deck deflections of RSM calculations with varying q factors*

Here it becomes clear that the *RSM* cannot satisfactorily reproduce the actual transversal deformations with any q factor. Even though the ductility factor of 1.0 shows good agreement with the time history solution in the left half of the bridge (i.e. $0 \leq x \leq 100$ m), this leads to a clear overestimation of the deformations in the right half. On the other hand, the customary value of 1.5 leads to a considerable underestimation of the deformations in the center fields of up to 45%, where the normative maximum factor q of 3.5 even shows an underestimation of about 200%. Overall, the lateral displacements of this bridge structure are inadequately represented by the *RSM*, both qualitatively and quantitatively.

'Standard' pushover calculation based on the *Capacity Spectrum Method* (*CSM*)

Next, the lateral displacements of the bridge deck in the performance state of the two 'standard' pushover calculations with varying monitoring points are compared with the time history solution. On the one hand, this shows that the *CSM* calculation also inadequately depicts the deck deformations, especially in the left half of the bridge (see Fig. 6.9 (a)). In addition to the significant quantitative deviation, a clear qualitative difference in the respective deflection lines is also recognizable. This is obviously due to the fact that the mass and mode proportional load pattern used in the pushover calculation is only based on the contribution of the first mode, which shows only very small deck displacements in the Y direction near column P1.

On the other hand, there is a considerable dependence of the results in the performance state on the selected monitoring point (see also Fig. 6.9 (b) and 6.10). Overall, the calculation with *mp* 4 corresponding to the larger pier top displacement shows a slightly better agreement with the results of the *NLTHA* (cf. Fig. 6.9 (a)).

(a) Lateral deflection lines
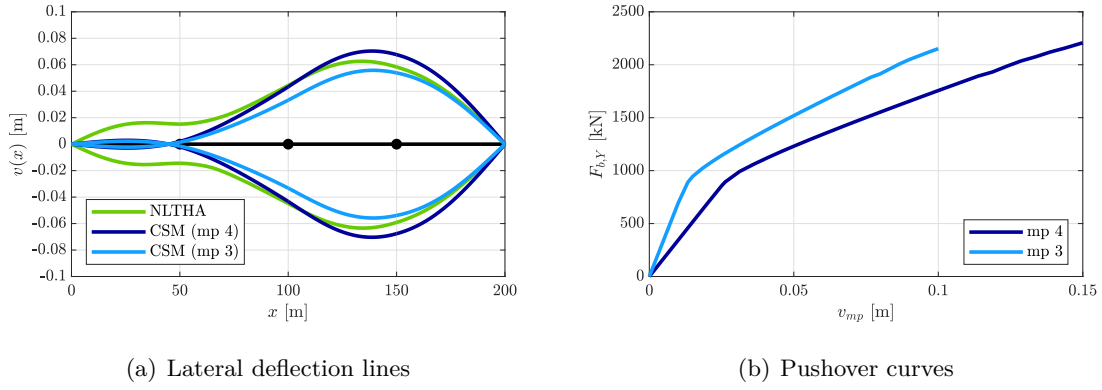
(b) Pushover curves

Figure 6.9: *Deck deflections and pushover curves of CSM calculations with varying mp*

(a) Monitoring point 4

(b) Monitoring point 3
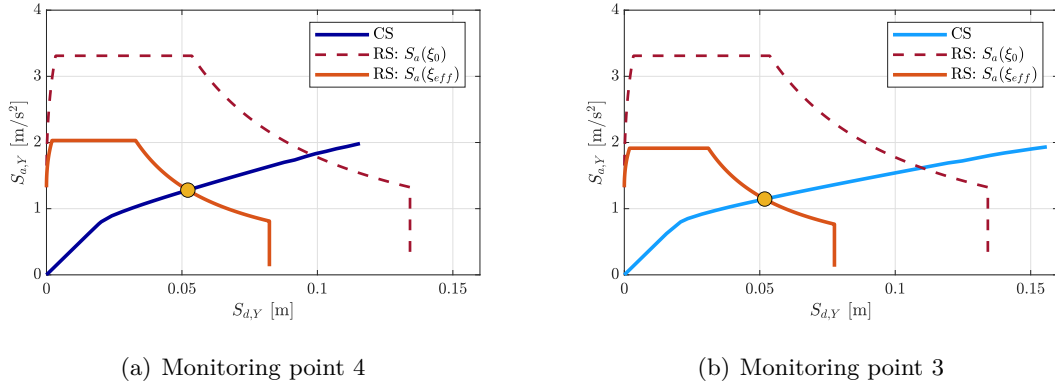
Figure 6.10: S_a-S_d *diagram of CSM calculations with varying mp*

The target displacements of the pushover analyses were deliberately set to 15 and 10 cm, respectively, so that they correspond to almost the same base shear (cf. Fig. 6.9 (b)). The end points of the two pushover curves are therefore plausible. However, the two curves are qualitatively different and thus lead to different effective damping values in the performance state after the transformation into the respective capacity spectrum, which can be recognized by the varying response spectra. This in turn results in the following different performance points:

$$(S_{d(mp4)}^{(PP)}, S_{a(mp4)}^{(PP)}) = (0.0522 \text{ m}, 1.28 \text{ m/s}^2) \ \& \ (S_{d(mp3)}^{(PP)}, S_{a(mp3)}^{(PP)}) = (0.0518 \text{ m}, 1.15 \text{ m/s}^2) \ .$$

The selection of the monitoring point is a central problem in the application of the *CSM* for such asymmetric bridge structures (cf. Paraskeva et al (2006), Paraskeva & Kappos (2010) and Isakovic & Fischinger (2014), among others). The literature cited contains studies on various approaches to the choice of the *mp* in bridge structures, including the deck mass centre or the top of the nearest to it pier, the location of the resultant of the modal load pattern, a

variable location of the respective (load step-related) maximum deck displacement and the head point of the pier with the maximum top displacement or most critical plastic rotation.

However, the core statement in most publications is not a specific recommendation for the selection of the monitoring point in pushover analyses of bridge structures, but rather a reference to the critical dependence of the calculation results on this choice. PARASKEVA ET AL (2006) and PARASKEVA & KAPPOS (2010) point out that the location of the *mp* only influences the inelastic part of the pushover curve. However, in view of the fact that pushover analyses have their greatest effect especially in the case of a pronounced nonlinear seismic behavior, this aspect is not a significant alleviation of the illustrated problem.

Since in the *AMI* by NORDA (2012) the pushover curve itself and the *mp* displacement in particular only represent secondary results that do not influence the determination of the structural responses in the performance state, the aforementioned problem can be completely avoided with this method when using a constant $\Delta S_{a,B}^{(i)}$ and at least almost avoided when using the optimized increments examined later (see Sec. 6.4).

Modal Pushover Analysis (MPA)

Following up the 'standard' pushover calculation, the *Modal Pushover Analysis* by CHOPRA & GOEL (2002) is evaluated below for the two *mp* approaches. Figure 6.11 depicts that the *MPA* can reproduce the deck deformations quantitatively much better than the single-mode *CSM* and in particular leads to satisfactory qualitative deflection lines in all bridge spans. In addition, the quality of the results is almost independent of the monitoring point. Overall, only a slight underestimation of the deformations is recognizable, which amounts to just under 15% in the third span. This is certainly due to the fact that the intermodal damage accumulation, which cannot be taken into account in the course of the *MPA* due to the subsequent modal combination, represents an overestimated stiffness. Although this generally leads to greater seismic loads due to the lower ductility, as is confirmed by the force variables investigated later, it also leads to significantly lower deformations under the same load.
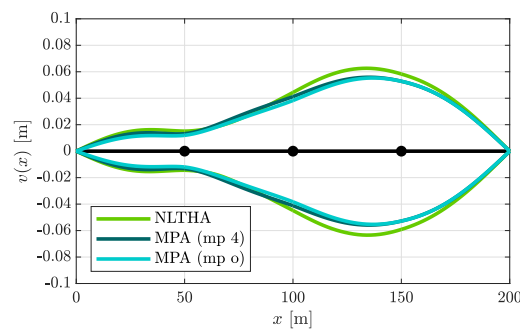
Figure 6.11: *Deck deflections of MPA calculations with varying mp*

Modified AMI procedure (*mAMI*)

Next, the *mAMI* calculations with and without linear combination factors are analyzed separately for all four load combinations investigated. Preliminary investigations showed that a successive reduction of the constant spectral acceleration increment $\Delta S_{a,B}$, starting from 0.05 m/s^2, leads to negligibly small differences in the calculation without correlation factors. However, in case of the more realistic approach of a partial correlation, there is only convergence of the results at a step size of about 0.01 m/s^2. Here, the design-relevant internal forces show a total difference of up to 7% compared to those based on the initial increment. The results of the latter calculation are therefore referred to the smallest acceleration increment of 0.01 m/s^2 below.

Against this background, the deflection lines shown in Figures 6.12 and 6.13 refer to the *mAMI* calculations without correlation coefficients, thus assuming a full correlation (fc), with $\Delta S_{a,B} = 0.05 \text{ m/s}^2$ and to those corresponding to a partial correlation (pc) with 0.01 m/s^2, whereby the results for the larger step size (pc*) are also illustrated as dashed lines for comparison.

(a) LC 1: {1 4 6}

(b) LC 2: {1 -4 6}
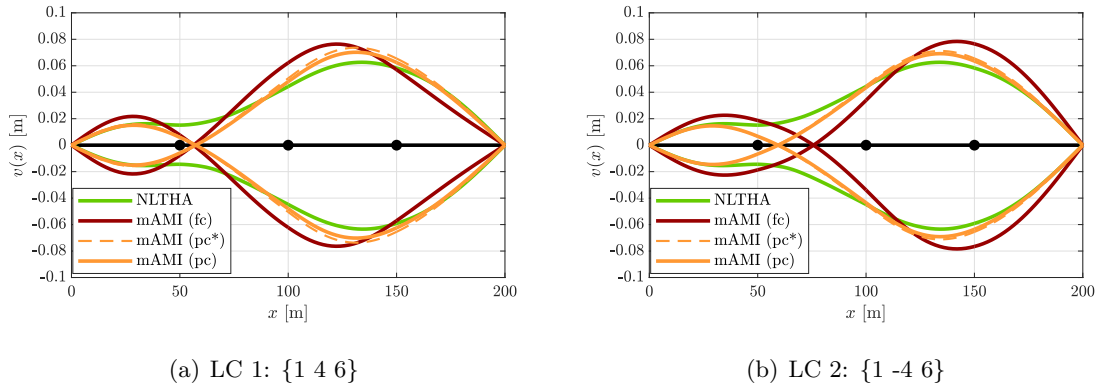
Figure 6.12: *Deck deflections of mAMI calculations with varying modal signs (LC 1 & 2)*

(a) LC 3: {1 4 -6}

(b) LC 4: {1 -4 -6}
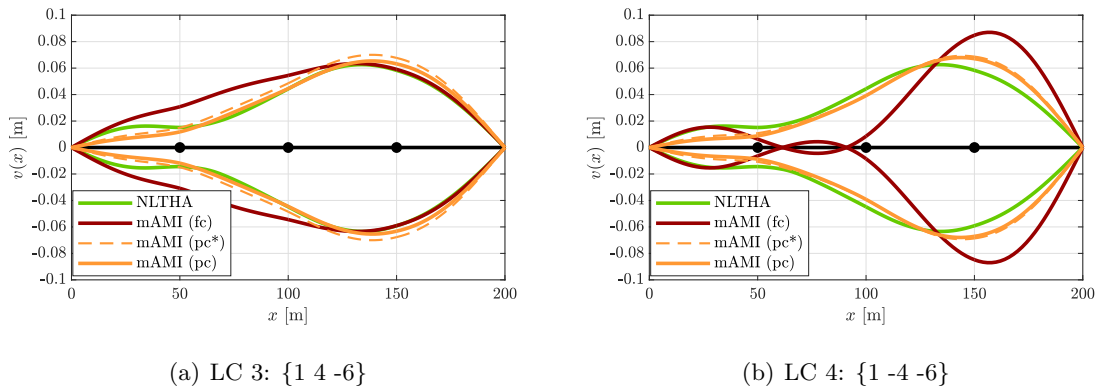
Figure 6.13: *Deck deflections of mAMI calculations with varying modal signs (LC 3 & 4)*

Looking at the results of load combinations 1 and 2 (cf. Fig. 6.12), it becomes clear that the deflection lines of the *mAMI* calculations in the performance state all consist of two unequal half-waves, so that one part of the bridge deck shows displacements in the positive Y direction and the remaining part in the opposite direction. However, even the envelope of the two mirrored deflection lines (for seismic excitation in positive or negative Y direction) of each *mAMI* calculation would deviate considerably from the time domain solution in certain areas. In Figure 6.13 it is noticeable that the *mAMI* calculation with correlation coefficients of load combinations 3 and 4 shows an overall satisfactory agreement with the averaged envelope of the deformations from the time history investigations, whereby the results of LC 3 are even better. This load combination corresponds to a load pattern in which the resultants of all modal contributions act in the same direction. With regard to the *mAMI* under the assumption of a full correlation, a sufficient representation of the real load-bearing behavior can only be attested for the right half of the deck in case of LC 3. In particular, due to the interplay of the sign combination of the modes and the generally stronger weighting of the two higher modal contributions, a completely different deformation curve with some changes in sign is also qualitatively mapped here (fc), compared to the time history calculation. Although the latter is only represented by an averaged envelope, vibration animations of the *NLTHAs* have shown that the bridge deck moves completely in one direction at most times and only rarely forms two opposing half-waves for a short time, but with significantly lower amplitudes.

Conclusion

Overall, the comparison of the lateral deck displacements leads to the conclusion that the multimode *MPA* together with the *mAMI* taking into account the correlation factors for the load combination 3 show by far the best approximations of the *NLTHA* results. However, the single-mode *CSM*, as well as the *mAMI* without correlation factors and thereby with a significant overestimation of higher mode effects, only provide realistic results in the right half of the bridge, which is primarily dominated by mode 1. Furthermore, the *RSM* as well as the *mAMI* calculations of load combinations 1, 2 and 4 with different signs of the total modal resultants lead to unusable overall results, especially if the higher modal contributions are overestimated by assuming a full correlation in the *mAMI*.

6.3.3   Comparison of representative force quantities

For a more precise assessment of the internal stresses, the results for the base shear and the base moments of all bridge piers are evaluated as representative force quantities (see Figs. 6.14 to 6.17). In *NLHTAs* as well as in static calculations, the base shear corresponds to the resultant of the inertia forces and thus to the total sum of the support reactions.
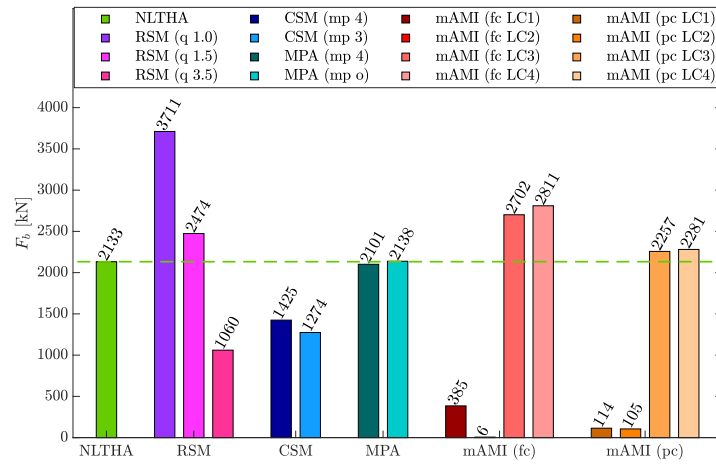
Figure 6.14: *Comparison of the base shear F_b*
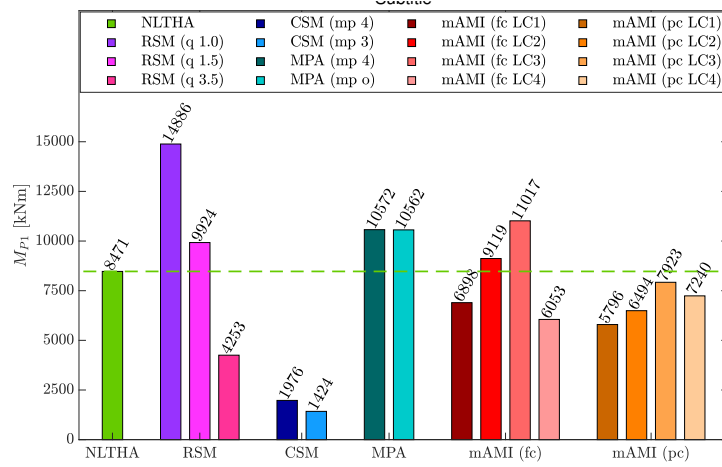
Figure 6.15: *Comparison of the base moment M_{P1}*
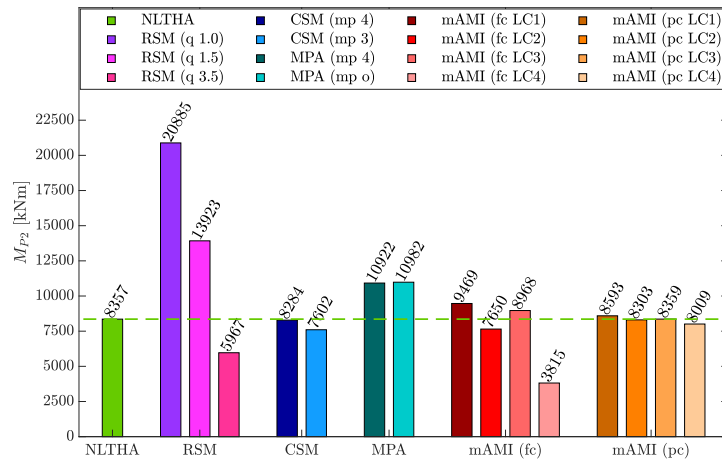
Figure 6.16: *Comparison of the base moment M_{P2}*
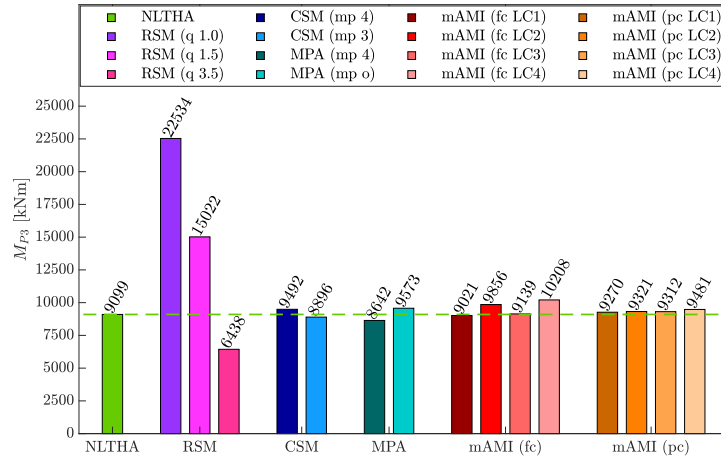
Figure 6.17: *Comparison of the base moment M_{P3}*

It should be noted that in the course of evaluating the *NLTHAs*, both the 50 maxima and minima are to be averaged separately and then the larger absolute value of these is to be used. The *RSM* results are still *CQC*-superimposed final values of the respective modal contributions, while all pushover analyses already deliver final results in the respective performance state. With regard to the *mAMI*, only the results for $\Delta S_{a,B} = 0.05$ m/s^2 of the calculations without and for 0.01 m/s^2 with correlation factors are considered, respectively.

The results essentially underpin the findings already obtained from the previously investigated deflections. On the one hand, it can be seen again that the *RSM* with different ductility factors provides an enormous scattering of the final results, which represents a central problem of this calculation method against the background of the difficult q factor estimation. Furthermore, the three calculations do not show any convergence towards the *NLTHA* solution that would indicate a possible behavior factor with overall satisfactory results. For example, while the calculation with a factor q of 1.5 leads to the smallest deviation from the time history calculation for the base shear, there is a significantly greater deviation with regard to the restraining moment in the central column P2 than with a factor of 3.5. This supports the finding that the different behavior factors lead to completely different result qualities in the individual structural areas.

With regard to the single-mode *CSM* it can be stated that it seriously underestimates the base shear and in particular the base moment of edge pier P1, as the base mode 1 does not show any deformations there. The other two base moments, on the other hand, are very well met. Furthermore, the multimodal *MPA* shows very good agreement with the time history results for F_b and M_{P3}, while it significantly overestimates the moments M_{P1} and M_{P2}. The latter could result from the fact that a seismic impact-reducing damage accumulation of the modal contributions is not taken into account.

In addition, it is also shown that the *mAMI* taking into account an only partial correlation represents a significant improvement in the results compared to the calculation assuming a full intermodal correlation and thus leading to considerably smaller deviations from the *NLTHA* results than the overall good performing *MPA*. For the maximum bending stress of a certain pier with regard to the *mAMI*, the modal sign combination in which the deformation components of the considered mode shapes in the respective pier point in the same direction (and thus also the corresponding inertia forces) is always decisive. Regarding mode shapes 1, 4 and 6 according to Figures 6.5 and 6.6, the modal load combination in which modes 4 and 6 are applied with different signs is therefore, as expected, decisive for the base moment of pier P1, whereby mode 1 and thus the associated sign is of no significant importance. This is the case for LC 2 and LC 3 according to the load combinations investigated (here: LC 3 decisive). Analogously, LC 1 (1, 4, 6) is decisive for the loading of the center column and LC 4 (1, -4, -6) for the edge column P3. It is noteworthy, however, that the differences between LC 3 and the respective governing load combination for the base moments of P2 and P3 are of a minor magnitude concerning the optimized *mAMI* (pc). Thus, load combination 3, in which all resultants of the modal load distributions act in the positive Y direction, leads to good overall results in this case.

While the results of the *mAMI* assuming a full correlation of the modal contributions provide very accurate moments at the base of pier P2 and P3, they significantly overestimate the base shear and the base moment in pier P1. By applying the correlation factors, the already well-captured bending moments M_{P2} and M_{P3}, i.e. in the area very strongly dominated by the first mode, change only to a negligible extent. However, the base moment of P1 at least shows a considerably smaller deviation of 6.9% from the averaged maxima of the time history results than the *mAMI* calculation with the assumption of fully correlated modes. For comparison only: the latter leads to an overestimation of M_{P1} of about 30%.

The fact that the *mAMI* calculation with correlation factors shows the largest deviation (of 6.9%) in pier P1 in the form of an underestimation of the reference *NLTHA* result is probably caused by the selection of the first mode as the reference mode, which, however, practically induces no bending in pier P1. It could therefore be that the choice of mode 6 as the base mode, which has the largest deformations in precisely this structural area, would have been more suitable for the approximation quality of the bending moments in pier P1.

Generally speaking, it is therefore reasonable to assume that for all structural members relevant to the inelastic seismic behavior and not being sufficiently excited by the fundamental mode, a corresponding mode with large deformation components in the respective member should be selected as the reference mode in a separate calculation. The background to this is that only the reference mode is applied to 100% whereas the accompanying modes are reduced by

the correlation factors $\alpha_n^{(i)}$ (< 1). The envelope of these different *mAMI* calculations with varying reference modes should then provide a realistic design value for each response quantity of interest. This procedure is comparable to the concept of 'leading and accompanying actions' for load combinations of independent variable loads according to EUROCODE 0 (2010), Eq. (6.10).

A new *mAMI* calculation is therefore carried out, taking into account the α_n factors as well as the sign combination of the previous LC 3, but now with varying base modes (BM) 1 and 6: {1 4 -6} and {-6 1 4}. Thus, the best *mAMI* calculation to date can be compared with the calculation that is presumably optimal for the investigation of pier P1. The *mAMI* assuming a complete correlation, on the other hand, is almost not influenced at all by the choice of the base mode. This results from the non-existent correlation factors and since refering to the intermodal scaling (acc. to AYDINOGLU (2003)) the reference mode only controls, which modal contribution is actually increased with the selected spectral acceleration increment, so that merely the actual step sizes of the modes are slightly influenced. The following evaluation therefore only contains the results of the previous *mAMI* calculation without α_n factors based on reference mode 1 for comparison. Figure 6.18 depicts the results for the base shear and the base moments of the three piers with regard to the *mAMI* only for the LC 3, on the one hand, without correlation coefficients and, on the other, with correlation factors α_n and varying base modes. The correlation factors in the calculation with reference mode 1 (orange bars) were on average 0.15 for mode 4 and 0.40 for mode 6 (with standard deviations of 0.07 and 0.14 respectively). In the calculation with base mode 6 (yellow bars), they averaged 0.59 and 0.32 for modes 1 and 4 (with standard deviations of 0.11 and 0.15).
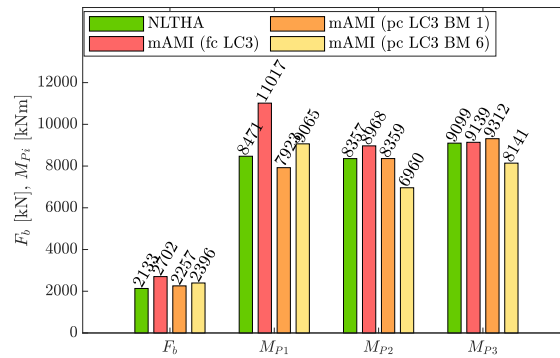

Figure 6.18: *Effect of a varying base mode*

It is noticeable that, as expected, the new calculation with base mode 6 does not produce any larger and thus decisive internal forces with regard to the moments M_{P2} and M_{P3}, which were already well represented by the selection of reference mode 1. In relation to the edge pier P1,

however, the base moment increases significantly due to the larger deformation components in this pier of the new fundamental mode 6. Although the deviation from the maximum moment M_{P1} of the nonlinear time history calculations is again around 7%, the design value of the *mAMI* calculation is now at least on the safe and no longer on the uncertain side.

6.3.4   Interim conclusion

In principle, it is possible to examine all 2^n sign combinations of the n modes considered and to subsequently evaluate the corresponding maximum for each structural response of interest. In most cases however, it is sufficient to limit the analysis to half of the corresponding combinations due to the symmetry with respect to the *X-Z* plane of the bridge structure. From the remaining load combinations, those can be selected that lead to decisive stresses in the relevant structural areas. This aspect has been confirmed by the previous evaluations of the pier base moments. In the special case that all structural areas are excited separately by certain modes alone, this could theoretically even lead to the fact that different sign combinations of the modal contributions have no significant influence at all. Apart from this special case, however, the number of investigated load combinations can at least be reduced to the potentially relevant ones in most cases. This is particularly important if a large number of modes are taken into account and the computational effort should nevertheless be limited to an acceptable level.

On the other hand, however, the results have also shown that certain structural members, which play a relevant role with regard to the inelastic seismic behavior, may not be sufficiently excited by the fundamental mode with the largest effective modal mass, so that the correlation factors ($\ll 1$) of the accompanying modes can lead to a significant underestimation of the corresponding internal forces. Against this background, it is recommended to check in advance whether the fundamental mode has only small deformation components in a structural member with a potential yield zone. If this is the case, an alternative reference mode with larger displacements in this member should be used in a further *mAMI* calculation.

Nevertheless, care must be taken to ensure that the alternative base mode does not have a too small effective modal mass compared to the 'actual' fundamental mode (with $m_{eff,max}$). Due to the proportional relationship between modal mass and earthquake load, this would lead to low base shear increments in the course of the calculation. As a consequence, the correlation factors of the accompanying modes, in particular that of the former base mode, may then tend very strongly towards a value of 1 and thus, analogous to the approach of NORDA (2012), practically represent a complete intermodal correlation. This effect can be seen in Figure 6.19, which shows the correlation factors for different base shear increments of the fundamental and an accompanying mode for the case of a relatively low correlation with $\rho_{B,n} = 0.02$.
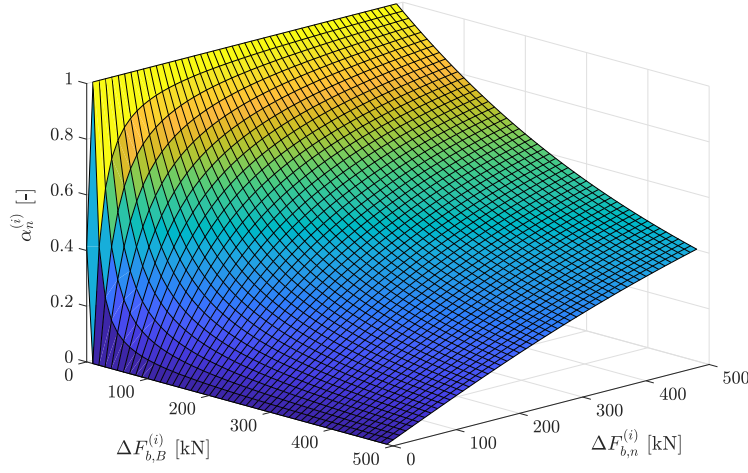
Figure 6.19: $\alpha_n^{(i)}(\Delta F_{b,B}^{(i)}, \Delta F_{b,n}^{(i)})$

For the load combination {-6 1 4} investigated here, however, this problem was still within a reasonable range. The correlation factors for the companion modes 1 and 4 were on average around 0.6 and 0.3. Although these values are significantly higher than the two α_n factors of about 0.35 and 0.15 for the load combination {1 4 -6}, they are still far from the critical limit value of 1.0. In this case, the relation of the initial effective modal mass $M_{eff,6}^{(1)}$ to that of mode 1 is still about 50%.

6.3.5   Analysis of mode changes and the associated load patterns

Finally, the developments of both the considered modes and the incremental load patterns in the course of the *mAMI* are analyzed in more detail. On the one hand, this serves to better understand and assess the irregularity of the inelastic seismic behavior and thus to answer the question of whether an adaptive calculation was indeed useful or even necessary for this bridge model. On the other hand, the self-developed *CAAP* algorithm can be checked with regard to mode identification and direction assignment. For the sake of simplicity, the calculation with $\Delta S_{a,B}^{(i)} = 0.05$ m/s^2 and thus considerably fewer adaption steps (25) compared to $\Delta S_{a,B}^{(i)} = 0.01$ m/s^2 (121) is evaluated in order to be able to analyze all *mAMI* steps from the first formation of a plastic hinge. In addition, only the *mAMI* calculation with correlation factors for LC 3 with reference mode 1 is regarded in the following.

Figures 6.20 and 6.21 show the modes 1, 4 and 6 according to the initial modal analysis and also their changes in the respective steps from the first occurrence of a plastic effect to the end. As can be seen, the algorithm assigned mode 3 and then mode 2 to the initial fourth mode in steps 16 and 19, respectively. Since the deck deflection lines show the same qualitative course, this identification appears to be correct. For the initial mode 6, on the other hand, mode 5

was considered in the last two steps 24 and 25, which also appears to be plausible. As the vertical modes of the bridge deck have their zero points at the pier-deck connection points, they are independent of the decrease in pier stiffness. Consequently, their natural frequencies do not change due to the formation of plastic hinges in the columns, while those of the horizontal bending modes decrease so that the latter tend to get a lower number.

In addition, the mode shapes in both figures are shown as they were considered using the sign factor calculated by the *CAAP* algorithm. This programming can also be classified as valid as there were no mirrored mode shapes in individual steps.

(a) Initial mode 1
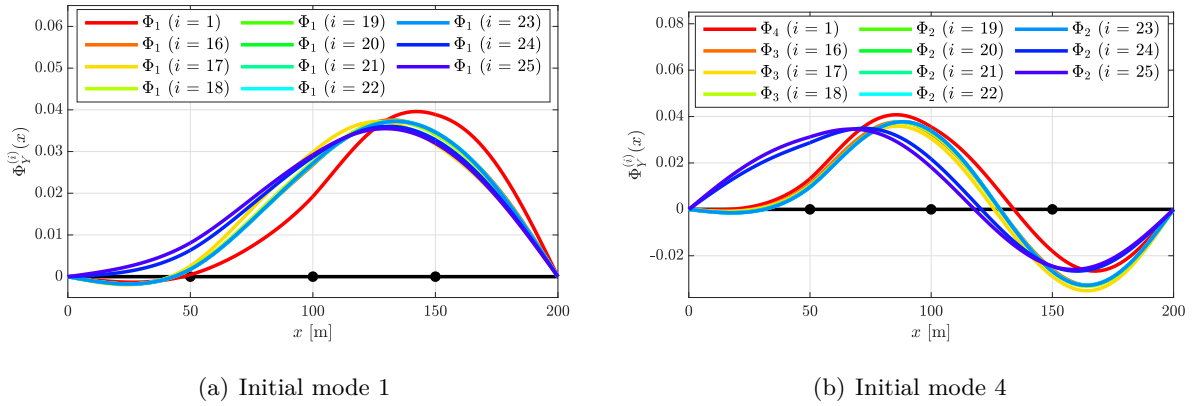
(b) Initial mode 4

Figure 6.20: *Development of initial modes 1 & 4*
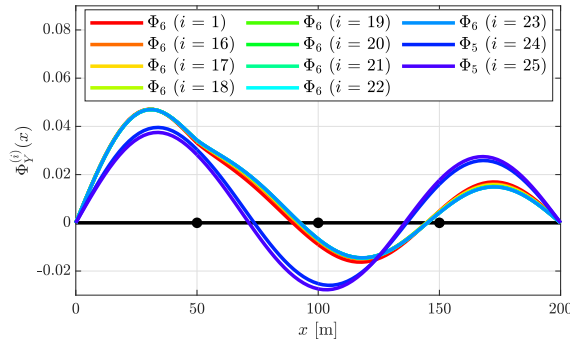
Figure 6.21: *Development of initial mode 6*

Furthermore, Figure 6.20 (a) clearly illustrates that the first mode changes significantly four times, namely in steps 16, 17, 18 and 24. In view of the development of the plastic hinges (cf. Appendix E.2), the first yielding of pier P2 can be assigned to step 16, that of pier P3 to step 18 and the first plastic hinge of P1 to step 24. This provides a very clear explanation for the previously described abrupt changes in the fundamental mode. The initial modes 4 and 6, on the other hand, show a rather small and, in particular, continuous change up to step 23.

Then, however, as the plastic zone at the base of pier P1 begins to form, both accompanying modes change considerably. In particular, the original mode 4, which has now become the second mode, changes its complete curvature characteristics in the left half of the bridge and now exhibits significantly larger deformation components there. Overall, it can therefore be stated that an adaptive pushover analysis is required for this bridge structure due to significant qualitative changes in the relevant transversal mode shapes.

Looking now at the significant changes in the incremental load patterns of the 'interesting' steps 1, 17, 18 and 24 (see Figs. 6.22 & 6.23), the assessment in Section 6.2 that an adaptive load approach is useful for this system is confirmed. While the initial load distribution is strongly dominated by the first mode, it shows significantly increasing loads in the middle and left deck area in step 18. Until the performance state is reached, however, the loads are considerably redistributed and show an increasingly irregular distribution with two changes of direction along the bridge deck in the penultimate *mAMI* step 24, which initially appears questionable. However, this load pattern, which obviously is strongly dominated by mode 6, can be explained on the basis of the intermodal scaling factors $\lambda_n^{(i)}$ and the correlation factors $\alpha_n^{(i)}$. Firstly, the factor $\lambda_5^{(24)}$ of the initial mode 6 (current mode 5) is about 1.5 times the factor for the initial mode 4 and even 8.6 times the factor $\lambda_1^{(24)}$. Secondly, the correlation factor of this mode increases from 0.3 at the beginning to more than 0.6 due to an increasing proportionally contribution of mode 4 to the total base shear. On the one hand, it is true that the mass participation factor $\mu_{eff,6}^{(i)}$ of the 6th initial mode drops by half from 29% to 14%, while $\mu_{eff,1}^{(i)}$ even slightly increases. On the other hand, however, due to the quadratic relationship $(\beta_n^{(i)})^2 = M_{eff,n}^{(i)}$, the modal participation factor β_n only decreases by about 30% (as $\sqrt{0.5} \approx 0.71$). Overall, the substantial increase in the factors $\lambda_n^{(i)}$ and $\alpha_n^{(i)}$ of companion mode 5 (formerly 6) described above therefore outweighs this. Thus the third lateral bending mode gains significantly in influence. This is confirmed by the incremental load distribution in step 24.

(a) Step 1

(b) Step 17
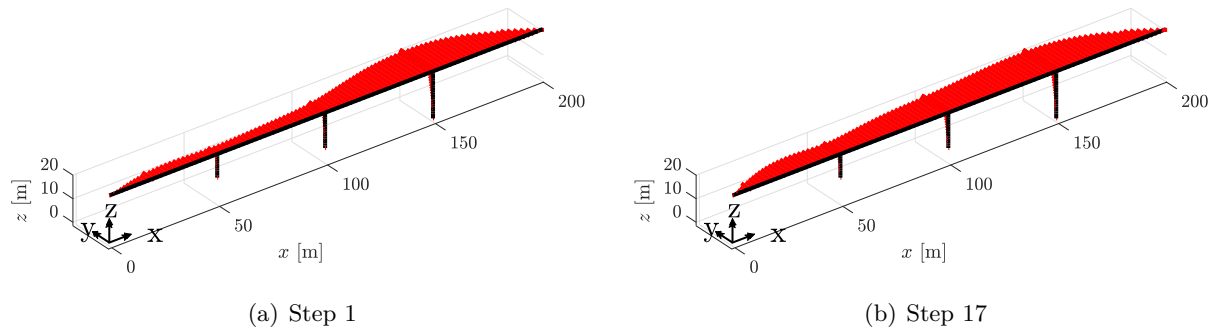
Figure 6.22: *Incremental load pattern - mAMI steps 1 & 17*

(a) Step 18

(b) Step 24
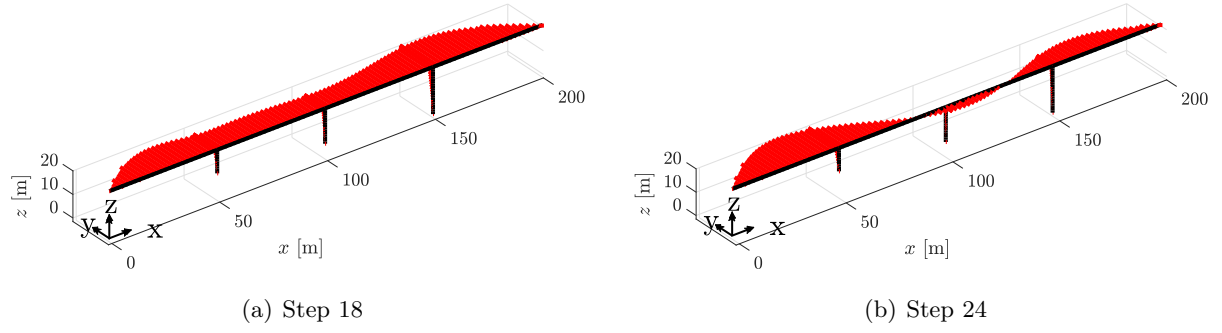
Figure 6.23: *Incremental load pattern - mAMI steps 18 & 24*

Overall, the automatic assignments made by the *CAAP* tool appear to be plausible. The bridge structure studied here also exhibits a very strong change in the mode shapes and the weighting of these in the resulting load distribution, so that the adaptive load approach appears more than justified in the context of a nonlinear-static seismic analysis of this bridge structure.

6.4   Comparison of constant and optimized spectral acceleration increments $\Delta S_{a,B}^{(i)}$

In Section 6.3.4 it was already stated that the *mAMI* with correlation factors achieves the best possible overall agreement with the averaged maxima and minima of the 50 nonlinear time history calculations. In this case, the constant step size $\Delta S_{a,B}^{(i)}$ had to be reduced from 0.05 to 0.01 m/s² in order to ensure sufficient accuracy. However, this calculation required a total of 121 adaption steps for the overall good performing LC 3 (as an example), which resulted in a total computing time of more than 11 hours. This was far longer than the time required for the 50 *NLTHAs*, which lasted around 2 hours in total, although the computational time for post-processing, i.e. reading out the maxima and minima as well as the subequent averaging, was added to this. In view of the pushover curve with the individual adaption step-related segments displayed in different colors according to Figure 6.24, it becomes clear that numerous linear branches were covered with many individual *mAMI* steps, which would not have been necessary. In particular, the initial linear-elastic branch up to a base shear of almost 1000 kN could have been calculated in one single adaption step instead of 72 (as in this case), since the relevant natural frequencies of the system change for the first time in *mAMI* step 73.
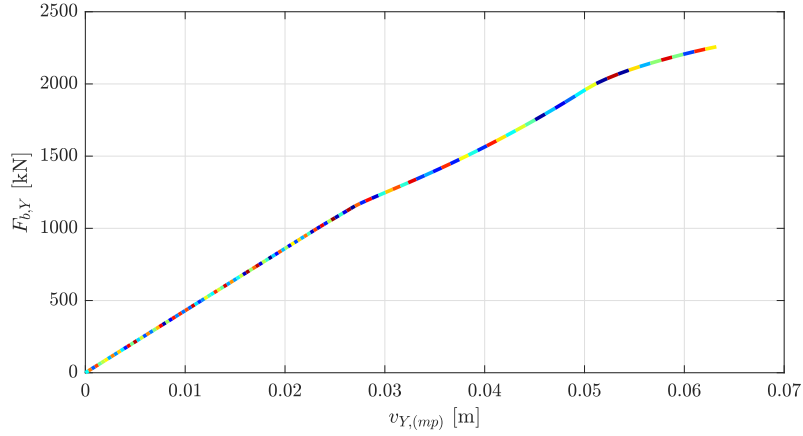
Figure 6.24: *mAMI (pc) calculation with $\Delta S_{a,B}^{(i)} = 0.01$ m/s^2*

Against this background, the application of optimized spectral acceleration increments of the reference mode is now investigated, which is based on a pushover curve analysis in each adaption step according to Section 3.1.4. For this purpose, four different *mAMI* calculations with the limiting criteria $k_{loc} = k_{glob} = 0.5$, 0.8, 0.9 and 0.95 are performed. The following Figures 6.25 and 6.26 visualize the deck deflection lines and the representative force variables already considered in the respective performance state.
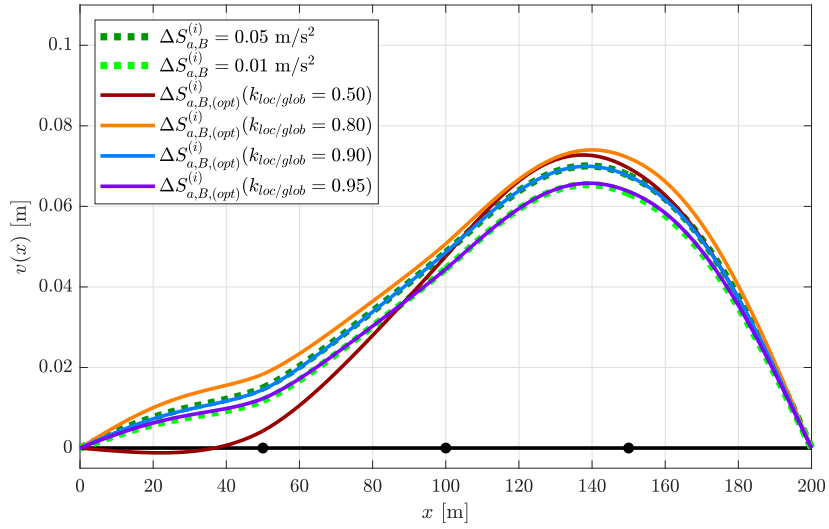
Figure 6.25: *Deck displacements of mAMI calculations with different constant or optimized $\Delta S_{a,B}^{(i)}$*
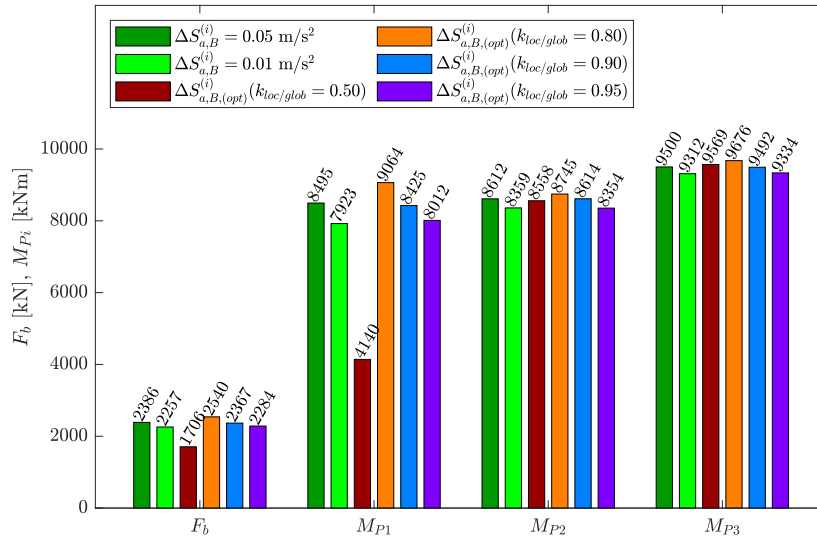
Figure 6.26: *Force variables of mAMI calculations with different constant or optimized* $\Delta S_{a,B}^{(i)}$

Based on the transversal displacements of the bridge deck depicted in Figure 6.25, it can be seen that the calculation with the relatively small k_{loc} and k_{glob} factor of 0.5 leads to significant deviations from the *mAMI* reference calculation considered here with a constant acceleration increment of $\Delta S_{a,B}^{(i)} = 0.01$ m/s^2, especially in the left half of the superstructure. The calculation with $k_{loc} = k_{glob} = 0.8$ already approximates the reference solution considerably better, but still not to a satisfactory degree. The approach of a global and local limiting ratio of 0.9 finally provides an almost complete agreement with the deflection line of the calculation with $\Delta S_{a,B}^{(i)} = 0.05$ m/s^2. Analogously, the limit ratio of 0.95 leads to a deflection line that also corresponds to the course of the *mAMI* calculation with a constant acceleration increment of the reference mode of 0.01 m/s^2, almost without any error. Since only the latter constant acceleration increment was classified as sufficiently accurate in the previous investigations, this applies equally for $k_{loc} = k_{glob} = 0.95$ in case of the *mAMI* with optimized acceleration increments.

Also in view of the analyzed force quantities, a good agreement with the results of the *mAMI* calculation with constant $\Delta S_{a,B}^{(i)} = 0.01$ m/s^2 can be stated for a k value of 0.9 for both the local and global analysis of the pushover curve and even a very good agreement for $k_{loc/glob} = 0.95$.

According to Table 6.1, the calculation with this strict limiting criterion nevertheless requires only just under 7% of the computing time for the calculation with a constant $\Delta S_{a,B}^{(i)}$ of 0.01 m/s^2, with practically identical results, as previously shown. The fact that the computational effort slightly decreased when increasing $k_{loc/glob}$ from 0.5 to 0.8 is due to the fact that negative spectral acceleration increments were determined in the last adaption step of the first calculation, which

was followed by five steps with constant $\Delta S_{a,B}^{(i)} = 0.01$ m/s^2 (cf. explanation at the end of Section 3.1.4).

Table 6.1: *Comparison of computational times*

mAMI calculation	computing time t_c [h]	relative computing time $\frac{t_c}{t_c(\Delta S_{a,B}^{(i)} = 0.01 \text{ m/s}^2)}$ [%]
$\Delta S_{a,B}^{(i)} = 0.01 \text{m/s}^2$	11.03	100.00
$\Delta S_{a,B,(opt)}^{(i)}(k_{loc/glob} = 0.50)$	0.48	4.38
$\Delta S_{a,B,(opt)}^{(i)}(k_{loc/glob} = 0.80)$	0.42	3.78
$\Delta S_{a,B,(opt)}^{(i)}(k_{loc/glob} = 0.90)$	0.55	4.98
$\Delta S_{a,B,(opt)}^{(i)}(k_{loc/glob} = 0.95)$	0.77	6.95

Finally, the following Figure 6.27 depicts the pushover curve of the *mAMI* calculation with the best optimization of the $\Delta S_{a,B}^{(i)}$ values (for $k_{loc/glob} = 0.95$), whereby the individual adaption step-related branches are again shown in varying colours for visual differentiation. The dashed line, on the other hand, represents the initial pushover curve corresponding to the first 'Max computation' based on the incremental load vector $\Delta \mathbf{P}_{max}^{(1)}\left(\Delta S_{a,n,max}^{(1)}\right)$. It can be seen that the entire *mAMI* calculation was performed with 13 instead of the previous 121 adaption steps and, in particular, that the linear-elastic initial branch was mapped in a single *mAMI* step.
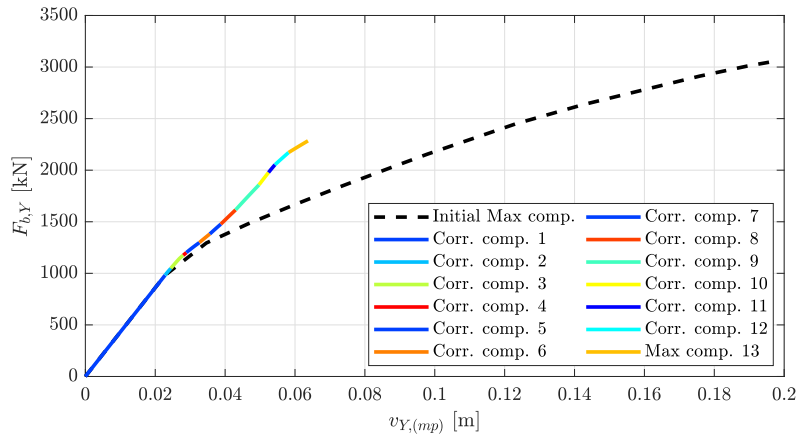
Figure 6.27: *mAMI calculation with optimized* $\Delta S_{a,B}^{(i)}(k_{loc/glob} = 0.95)$

Conclusions

Overall it could be observed that the spectral acceleration increments $\Delta S_{a,B}^{(i)}$ of the reference mode should not be set constant, but varied on the basis of an optimized approach, so that the update of maximum modal spectral accelerations and the adaption of the load pattern is only

carried out in the event of relevant system changes. The latter, resulting from the formation of plastic zones relevant for the global load-bearing behavior, can be identified by correspondingly strict k_{loc} and k_{glob} values of about 0.9 to 0.95. Thereby, the calculation time can be considerably reduced compared to the calculation with sufficiently small constant increments $\Delta S_{a,B}^{(i)}$ (e.g. 0.01 m/s^2), in this case even to just under 7%, with approximately identical calculation results.

6.5   General performance assessment of the *mAMI* on different bridge structures

6.5.1   Preliminary remarks

As already explained in Section 6.1, the monodirectional seismic investigations are concluded with a general assessment of the *mAMI* based on the application to various bridge systems with different complexity in the nonlinear seismic behavior. On the one hand, the influence of higher modes is varied by considering two different mass-stiffness ratios of the bridge deck. In addition to the EI/μ ratio of Calculation I, a further calculation (Calc. II) takes into account an increased bending stiffness by a factor of 10 and additionally the previous linear mass of 5 t/m is no longer applied. This results in an overall EI/μ ratio of the bridge deck that is 16.8 times higher, which increases the dominance of the base mode (e.g. $\mu_{eff,1,Y,(II,\ Model\ 11)} = 71\% \gg \mu_{eff,1,Y,(I,\ Model\ 11)} = 52\%$).

In addition, as already mentioned in Section 6.1, a total of 11 different bridge structures with varying pier lengths are considered. While models 1 and 11 correspond to the models A and B described in Section 6.2 with regular (A) or irregular (B) seismic load-bearing behavior, models 2 to 10 are 'intermediate models' with correspondingly interpolated pier lengths. These are documented in Table E.2 of Appendix E. The variation of the pier lengths and thus of the horizontal stiffness distribution leads to a different degree of change in the relevant mode shapes with increasing load intensity, so that the adaption of the load patterns has a lesser or greater influence.

The previous studies aimed at varifying the numerical procedure. Now the focus is on the applicability of the *mAMI* for mapping the seismic behavior of realistic structures so that all relevant dynamic effects should be considered correctly. For this reason, the micro model (based on fiber hinges, cf. Sec. 4.1) is used to describe the physically nonlinear behavior. The significance of this is briefly explained below.

6.5.2   Importance of applying the micro model

Even at the end of the *mAMI* (pc) calculations for base mode 1 (LC 1-4), the previously investigated bridge model B does not exhibit any vertical components in the lateral modes under consideration (initial numbers 1, 4 and 6). However, if the same *mAMI* analysis (e.g. for LC 3) is performed on the corresponding fiber hinge model of the otherwise identical bridge structure, there are spatial variations of these modes with both horizontal and vertical components at the end of the calculation. This is illustrated in the figure below for the example of the third horizontal mode with the initial mode number 6, which has the number 5 in the performance state of both investigations, of the macro as well as of the micro model (other mode developments: see Figs. E.10 to E.15 in Appendix E). The vertical deformations are highlighted in color. Thus it is clearly visible that significant vertical displacements have only developed in the case of the fiber hinge (micro) model.

The reason for this is the decrease in the tangential axial stiffness, which is shown by the exemplary evaluation of the entry of the initial and the final tangent stiffness matrix corresponding to the degree of freedom (DOF no. 425) associated with the vertical displacement of node 2002. This node is located one meter above the base of the central column P2:

$$\mathbf{K}_{el}(425, 425) = 87593756 \; \frac{\text{kN}}{\text{m}} \; \left(= \frac{2EA}{L^e} \right) \tag{6.4}$$

$$\mathbf{K}_T^{(end)}(425, 425) = 35186836 \; \frac{\text{kN}}{\text{m}} \; . \tag{6.5}$$

(a) $\mathbf{\Phi}_5^{(end)}(f_5 = 1.67 \text{ Hz})$ - Macro model   (b) $\mathbf{\Phi}_5^{(end)}(f_5 = 1.80 \text{ Hz})$ - Micro model
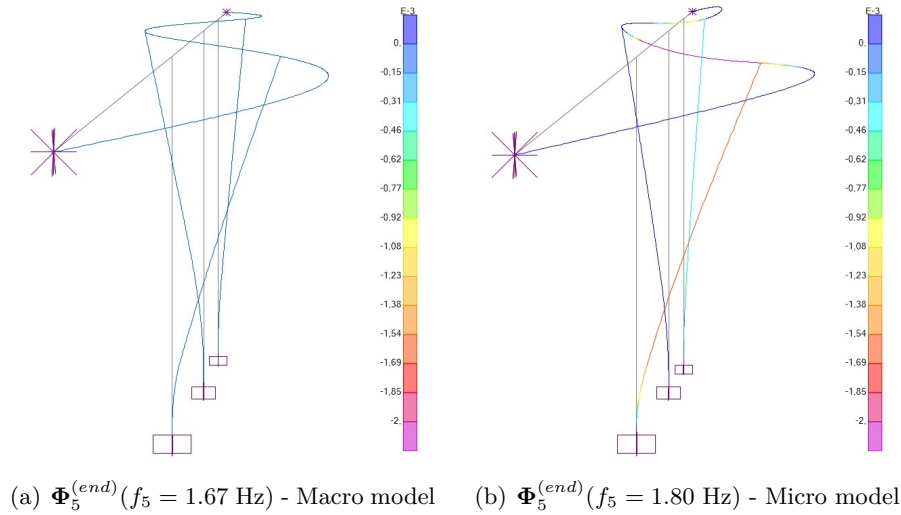
Figure 6.28: *Comparison of the final mode 5 for the macro and micro model B*

The axial stiffness at the base of pier P2 has therefore decreased by 60% by the end of the calculation. In the micro model, this is caused by the yielding of individual fibers as a result of a primary bending load. In the macro model based on plastic hinges, on the other hand, an *M-N* interaction can be taken into account, but this only affects the course of the *M-κ* curve due to the existing normal force. For additional modeling of an *N-ε* hinge, however, which can actually represent a decrease in tangential axial stiffness, *SAP2000* requires a constant bending moment. Thus, the described effect can only be captured with fiber hinges in this case.

The effect of decreasing axial stiffnesses in highly stressed pier areas leads, on the one hand, to noticeable differences in the equivalent forces of a load distribution proportional to mass and mode shape and, on the other hand, to significantly different natural frequencies in later modal analyses, which amount to up to 13% in the previous comparison of the macro and the micro model. Against this background, it is considered advisable or even necessary to use the more realistic micro model in the following investigations.

6.5.3   Realization of this study

In addition to the *NLHTA*, which again represents the reference solution with the analysis of 50 ground motions, a single-mode non-adaptive pushover calculation is first carried out for each bridge model based on the *CSM*. Subsequently, a so-called 'Variation Index' (*VI*) is determined, which generally describes how much the mode shape of the base mode *B* has changed in the course of the calculation, i.e. between the initial and final modal analysis. After normalizing both eigenvectors to their maximum cross-directional displacement, *VI* results as follows:

$$VI = \frac{\sum_j | \, \boldsymbol{\Phi}_B^{(end)}(j) - \boldsymbol{\Phi}_B^{(1)}(j) \, |}{\sum_j | \, \boldsymbol{\Phi}_B^{(1)}(j) \, |} \cdot 100 \; [\%] \; . \tag{6.6}$$

Following the 'Irregularity Index' (*IRI*) by Fischinger & Isakovic (2003), which however refers to the change in the deflection line for the first two iteration steps of a pushover analysis using the *N2 method*, the irregularity of the inelastic seismic behavior is also to be assessed here. With a correspondingly large *VI* (analogous to the *IRI*), a more complex pushover calculation than a *CSM* or *N2* analysis becomes increasingly advisable. Based on this basic idea, an attempt is therefore made to use the *VI* in order to check whether an increasing irregularity of the bridge structures can be recognized by the variation of the pier lengths from Model 1 to 11. In this case, the index could indeed be used subsequent to a *CSM* analysis to decide whether a more complex pushover calculation is necessary or not. The key motivation behind this is, that in many cases the classification of the inelastic seismic behavior of the structure may be unknown in advance.

Since the pier lengths of the investigated bridge structures are very different, it would not make sense to use the same monitoring point at the head of a particular pier for all *CSM* calculations. Instead, a varying *mp* is selected at the respective location of the maximum deformation of the fundamental mode (with $\mu_{eff,Y,max}$) in the corresponding initial form.

For the application of the *mAMI*, the load combination is considered for each bridge model in which all modes with an effective modal mass fraction $\mu_{eff,Y}$ of at least 5% are applied in such a way that the resulting base shear of the associated modal loads points in the same direction. On the basis of the previous findings (cf. Figs. 6.12 & 6.13), this leads to the decisive and most realistic lateral deck displacements. The load combinations based on this are documented for both 'EI/μ' approaches (I & II) in Tables E.3 and E.4 of Appendix E. Furthermore, in view of the conclusions of the previous Section 6.4, optimized spectral acceleration increments $\Delta S_{a,B}^{(i)}$ are applied on the basis of $k_{loc/glob} = 0.9$, since this limiting criterion has proven to be sufficiently accurate in the context of a previous convergence study. In addition, the preliminary investigation of varying monitoring points showed that the latter have a negligible influence on the *mAMI*, so that the center node of the bridge deck can be selected.

In order to achieve a pronounced inelastic seismic behavior, the first calculations (I) are based on the previously considered horizontal ground acceleration of $a_g = 0.1g$. In calculations II an increased design acceleration of $0.3g$ is applied to achieve similar pier loads for the significantly lower mass of the superstructure.

6.5.4   Evaluation of results

Calculation I:
Analogous to the previous investigations, the horizontal deck displacements as well as the base shear and base moments of the piers are studied. The graphical evaluations are shown below as examples for models 1, 6 and 11; the deflection lines for all models can be found in Appendix E.2. These illustrations clearly show that the *mAMI* is in very good agreement with the results of the *NLTHA* with regard to the deformations for models 1-6 and at least in sufficient agreement for models 7-11 with a more comlex nonlinear seismic behavior. Regarding the force quantities, the results can even be classified as unreservedly statisfactory. The *CSM* calculation, on the other hand, has to be described as inadequate for all models. The reason for this is the significant influence of higher modal contributions in this calculation I with the corresponding lower stiffness-mass ratio of the bridge deck. Nevertheless, higher mode effects are not taken into account in the single-mode *CSM* calculation, although the largest effective modal mass of an accompanying mode in the case of model 11 is just under 30% of the effective total mass.

(a) Model 1

(b) Model 6
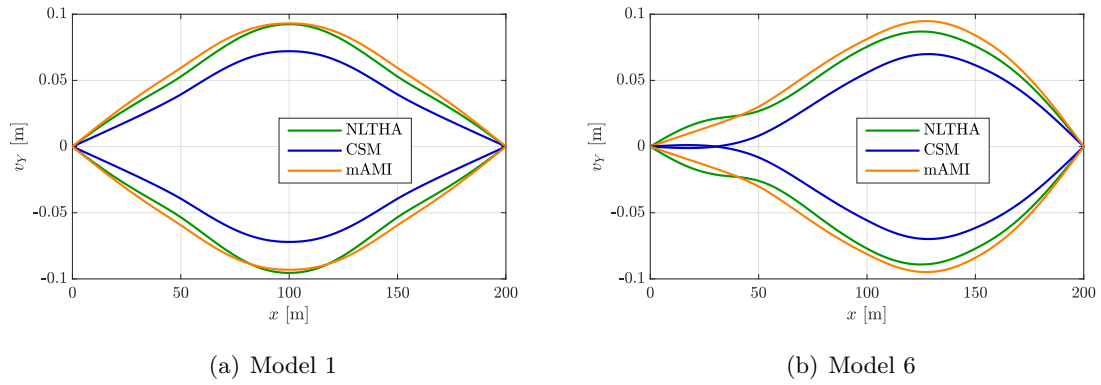
Figure 6.29: *Lateral deck displacements - Calc. I, Model 1 & 6*
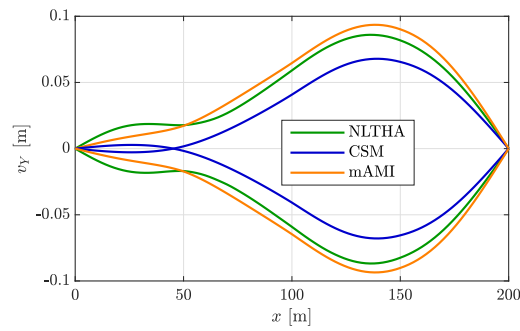
Figure 6.30: *Lateral deck displacements - Calc. I, Model 11*

(a) Model 1

(b) Model 6
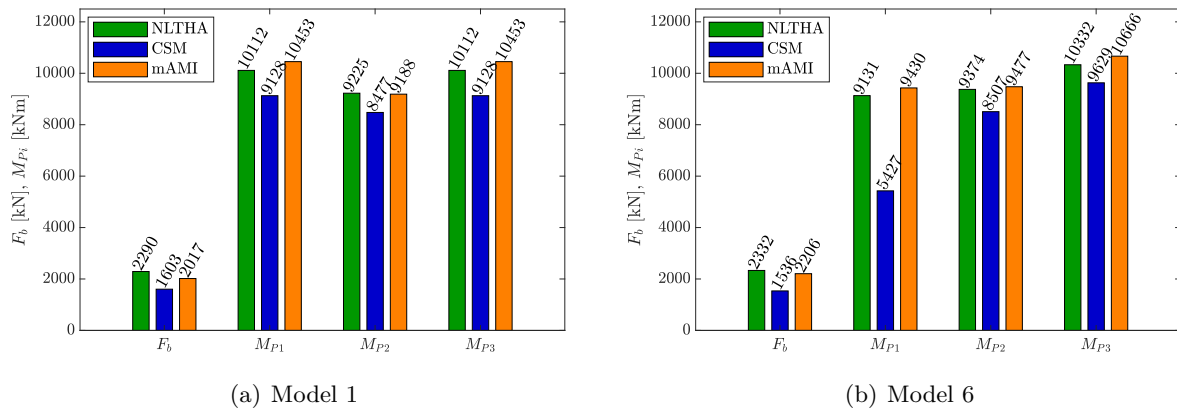
Figure 6.31: *Representative force quantities - Calc. I, Model 1 & 6*
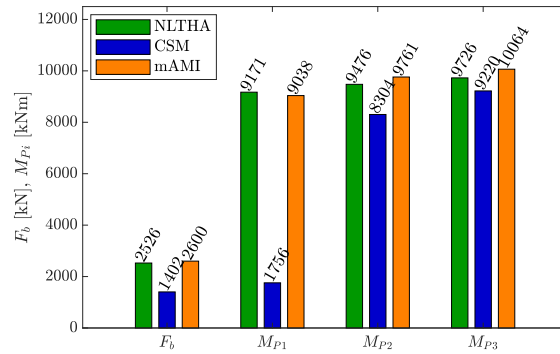
Figure 6.32: *Representative force quantities - Calc. I, Model 11*

Calculation II:

Analogous to the evaluation of Calculation I, only the results of models 1, 6 and 11 are shown as examples and the deflection lines of all models investigated are presented in Appendix E.2. First, it can be stated that in calculation II the *mAMI* provides a good approximation of the *NLTHA* results for Models 1 to 8, while the *CSM* only shows a similar approximation level from Model 6 onwards and performs at least slightly worse for Models 1 to 5. However, regarding the following models, especially from Model 9 onwards, the *mAMI* calculation shows significant deviations from the *NLTHA* results regarding all deformation and force response quantities considered. With respect to these models, the *CSM* calculation appears to deliver significantly better results here, which in fact is a fallacy, especially in the case of deformations, as will be explained in more detail below.

(a) Model 1

(b) Model 6
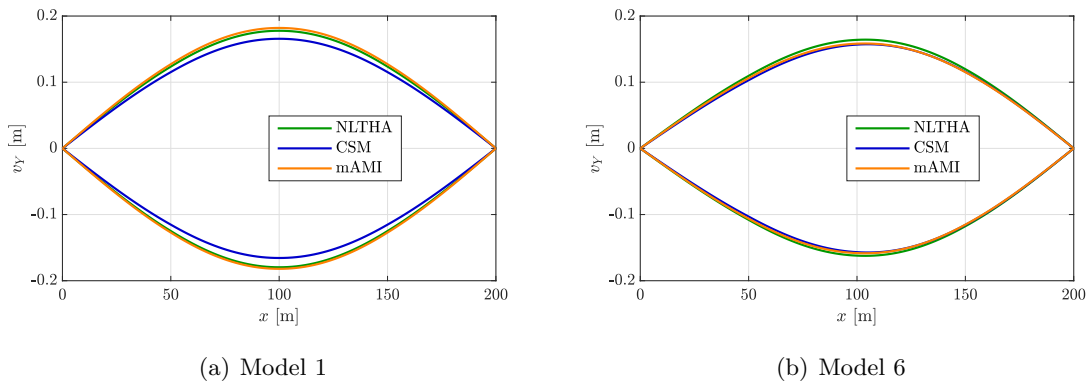
Figure 6.33: *Lateral deck displacements - Calc. II, Model 1 & 6*
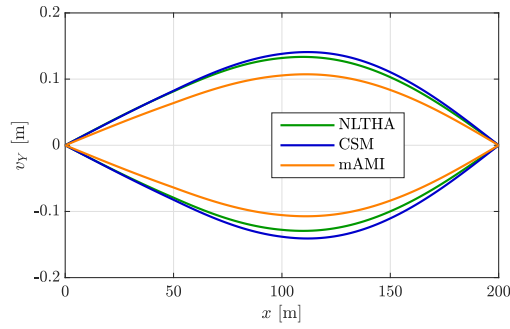
Figure 6.34: *Lateral deck displacements - Calc. II, Model 11*

(a) Model 1

(b) Model 6
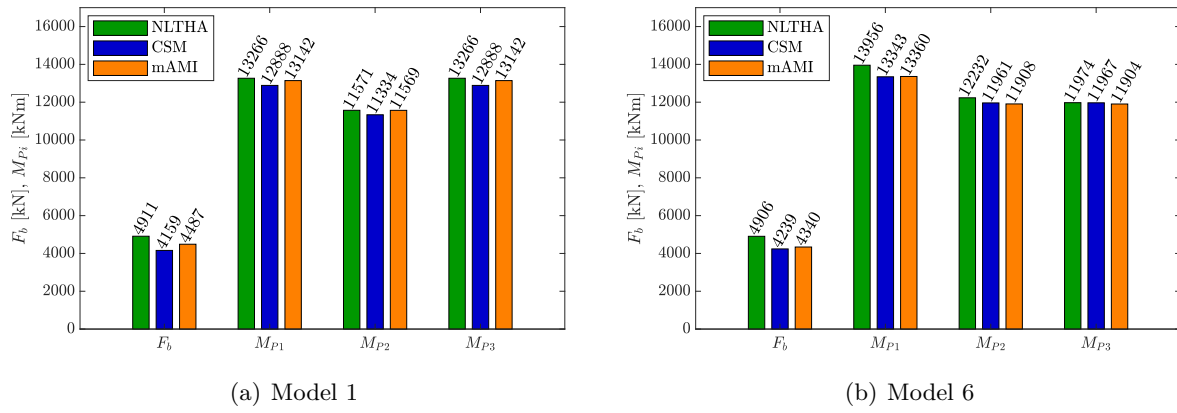
Figure 6.35: *Representative force quantities - Calc. II, Model 1 & 6*
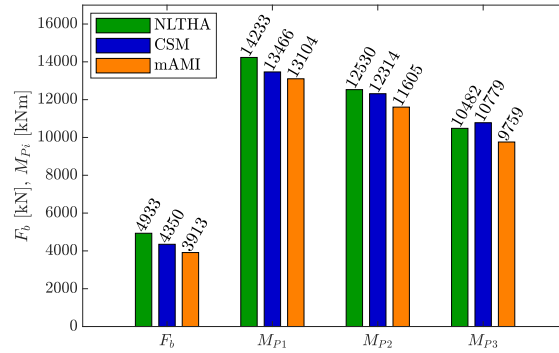
Figure 6.36: *Representative force quantities - Calc. II, Model 11*

A closer analysis reveals that the results of Models 9 to 11 can only be used to a limited extent, as they refer to a structural performance immediately before the failure of pier P1 due to the increased a_g of $0.3g$. As the performance point in the *CSM* calculation of model 11 shows (see Fig. 6.37 (a)), no further seismic load can be absorbed in the system. The final steel strains in

the outermost rebars of the fiber hinge '1H1' (*i*H*j*: *j*-th hinge of beam element *i*) at the base of pier P1 are exactly 25 mm/m, which corresponds to the normative limiting value defined as the limit of the σ-ε diagram. The previous deformation-controlled pushover analysis up to the *mp* displacement of 25 cm finally leads to the actual formation of a moment hinge at the base of the edge pier P1. This can be recognized by the lateral deformations of this pier: the deflection line remains straight and shows a large rotation about the plastic hinge at the base. This local failure corresponds to the abrupt first base shear drop in the pushover curve and thus also in the capacity spectrum (cf. Fig. 6.37 (a)).

For a better understanding of the inelastic load-bearing behavior, the hinge results of fiber hinge '1H1' at the foot of pier P1 are investigated for the *CSM* and *mAMI* calculation as well as the *NLTHA* (see Fig. 6.37 (b)). With respect to the latter calculation, one specific load case of the total of 50 has to be evaluated, as the hysteresis loops cannot be averaged in a meaningful way. For this reason, load case '$a_{g,9}$', based on the ninth accelerogram, is selected as a representative load case, since it contains approximately the same maximum deck displacement as the value of the averaged maxima of all 50 calculations. The same applies to the base moment of pier P1, which plays a central role in the following interpretations (on the next page). In addition, a 'target curve' determined with *INCA2* (PFEIFFER , 2006) was plotted for the constant compression normal force of P1 due to gravity loads as a reference.

(a) S_a-S_d diagram of the *CSM*

(b) Hinge results at the base of P1
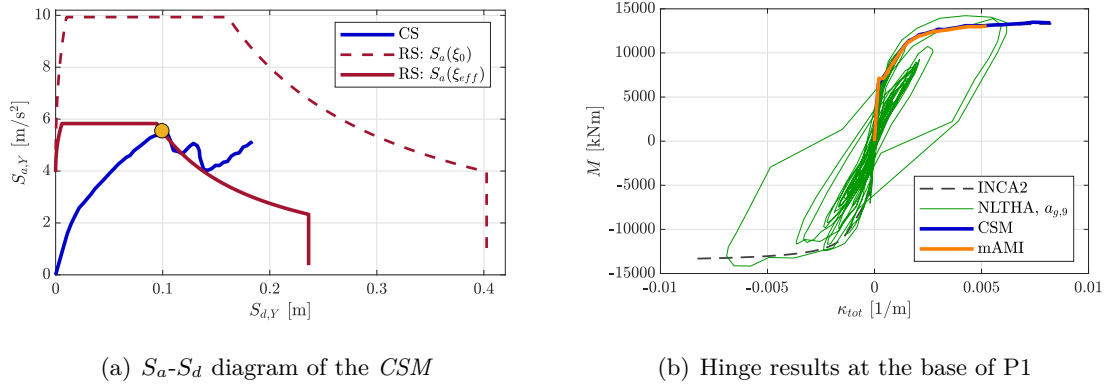
Figure 6.37: *More detailed responses of Model 11*

In the first place, the results confirm the aforementioned fact that the equilibrium state of model 11 is close to the failure of the cross-section at the base of pier P1. In the fixed tensile zone of the box girder cross-section in the static calculations (*CSM* and *mAMI*), the concrete fibers have long since failed completely by tearing and the steel fibers are also near the end of their load-bearing capacity due to the reached ultimate strain of 25 mm/m. This results in two central aspects:

1. Even slightly different bending moments lead to enormous differences in the corresponding curvatures (cf. Fig. 6.37 (b)) due to the low gradient of the final M-κ branch and thus ultimately concerning the base point rotations. In turn, this leads to significant differences in the deck displacements due to the length of the pier. As a consequence, the overall greater curvature in fiber hinge '1H1' in the case of the *CSM* (acc. to Fig. 6.37 (b)) could explain why there are considerably larger deformations in the *CSM* calculation (cf. Fig. 6.34), despite the similar base moments in the performance state of the *CSM* and *mAMI* calculation.

2. An analysis of the *NLTHA* loops shows that a bending moment even higher than the one of the *CSM* calculation has been achieved by a significantly lower curvature (cf. Fig. 6.37 (b)). Against this background, the well-matching deformations of the pushover calculation according to the *Capacity Spectrum Method* are presumably based on the compensation of several errors. A better agreement with the maximum curvatures in the time domain, however, can be attested for the *mAMI* results.

Overall, it must be noted at this point that the load-bearing behavior of Models 9 to 11 near the local failure of the edge column P1 can only be reproduced to a limited extent with the nonlinear-static methods due to the highly plastic behavior in the fiber hinge with an almost flat inelastic M-κ branch.

6.5.5   Final overall evaluation

In order to obtain a better overview of the overall results of calculations I and II with regard to all 11 models, the deviations of the deflection lines resulting from the *CSM* and *NLTHA* calculations, respectively, as well as from *mAMI* and *NLTHA* analyses are each represented by the following scalar 'error' value and then compared with each other:

$$error = \frac{\sum_j \mid \mathbf{v}_{CSM/mAMI}^{(end)}(j) - \mathbf{v}_{NLTHA}^{(decisive)}(j) \mid}{\sum_j \mid \mathbf{v}_{NLTHA}^{(decisive)}(j) \mid} \cdot 100 \; [\%], \tag{6.7}$$

with $\mathbf{v}_{NLTHA}^{(decisive)}(j) = max\{\mathbf{v}_{NLTHA}^{(average,max)}(j), \mid \mathbf{v}_{NLTHA}^{(average,min)}(j) \mid\}$ for each node j.

Following FISCHINGER & ISAKOVIC (2003), this error is first plotted over the self-developed *VI* (see Fig. 6.38 (a)). However, as there is no clear correlation between *VI* and the displacement error, Figure 6.38 (b) contains an alternative representation on the basis of the model numbers.

(a) Error as a function of *VI*

(b) Error as a function of model number
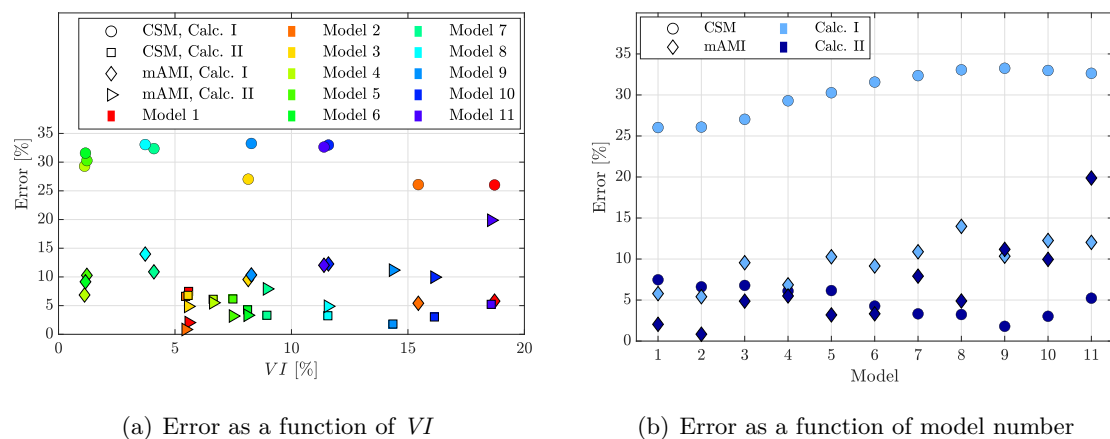
Figure 6.38: *Error of CSM and mAMI with respect to the NLTHA results*

Overall, the two figures show that the *CSM* calculations I lead to obviously unusable results. The calculations II, i.e. the investigations of a much stiffer bridge deck with less influence of higher modes, approximate the *NLTHA* results better with increasing complexity of the inelastic seismic behavior. However, as already explained in Section 6.5.4, the latter effect is probably not trustworthy due to the fact that there is almost a structural failure with a disproportionate increase in plastic deformations due to minimally larger bending moments.

With regard to the *mAMI* results, some models in case of calculations I and the last three in calculations II also show large errors, whereby the latter is related to the mentioned reaching of the inelastic bearing capacity due to the increased seismic intensity ($a_g = 0.3g$).

Furthermore, it should be noted that the 'Variation Index' (*VI*), which relates to the change in the base mode shape (cf. Eq. 6.6), is not able to reliably describe whether a single- or multi-mode as well as an adaptive or non-adaptive nonlinear-static seismic analysis can be expected to produce sufficiently good results (cf. Fig. 6.38 (a)). This is due in particular to the fact that Index *VI* does not take into account the extent to which the overall behavior of the structure is dominated by the basic mode.

6.5.6 Conclusion

In the literature (see i.a. Kappos et al (2012) & Isakovic et al (2003)) there are various publications on when non-adaptive or single-mode pushover methods can be usefully applied for the seismic analysis of bridge structures. Depending on the arrangement of short or long piers and the restraint conditions of the deck at the abutments, the inelastic seismic behavior is classified as more or less complex, so that strong simplifications may or may not be justified. It

must be explicitly assessed whether higher modes significantly influence the structural response and whether or not the mode shapes change significantly in the course of the calculation.

However, it should be questioned whether the simplest possible seismic analysis should always be aimed for at any price. As already mentioned in Chapter 1, a relatively comprehensive calculation may be advisable both in view of the possible economic damage and, above all, the potential danger to life and limb in the event of a collapse due to high earthquake intensities as well as for an economic design in the case of lower earthquake loads. Similar to the jurisprudence, the basic principle of proportionality of means should always be at the forefront here, instead of striving for the greatest possible simplification of the calculation approach at all costs. In particular, a combination of at least a sufficiently complex static analysis, to exploit the good evaluability and assessment of the inelastic seismic behavior, and an additional *NLTHA* as a validation calculation can be useful in some cases. Since only very specific results from the time domain solution are then required to check the static calculation, some of the main disadvantages of *NLTHA*, which relate to the time-consuming evaluation and assessment of results, can thus be avoided. Particularly in view of the overall costs of building a new bridge and the general objective of a high level of safety, this can be entirely reasonable. On the other hand, such elaborate investigations are not suitable for a preliminary design if any system adjustments are to be optimized on the basis of a calculation, but should be replaced by the application of a simplified procedure in the sense of an estimate.

In the investigations documented in this chapter, the *mAMI* application with sensibly chosen parameters, i.e. taking into account the decisive load combination and application of the correlation factors, was mainly unable to achieve satisfactory agreement with the reference results of the *NLTHA* when the inelastic structural capacity was reached or almost exceeded. However, since a complete utilization of the plastic reserve capacity should be avoided in reality anyway, this dissertation did not uncover any practice-relevant cases so far in which the *mAMI* would have delivered unusable results. Nonetheless, this is precisely what needs to be critically investigated, particularly in the subsequent investigations of multidirectional earthquake excitations.

7 Extended *mAMI* calculations of multidirectional earthquake excitations

7.1 Introduction

7.1.1 Current state of science concerning multidirectional pushover concepts

The consideration of orthogonal earthquake components has increasingly become the focus of scientific investigations in the recent past. For this reason, various multidirectional pushover concepts have been developed since the beginning of the last decade, the main features of some of which are presented below. This presentation is initially limited to those methods that are based on a predetermined seismic incident angle (*sia*). Methods with variation of the *sia*, as is relevant for significantly irregular and in particular horizontally curved bridge structures, are discussed in more detail in Section 7.5.1 when investigating an in-plan curved bridge.

Three-dimensional Modal Pushover Analysis (*3D MPA*) by REYES & CHOPRA (2011)

The *Three-dimensional Modal Pushover Analysis* (*3D MPA*) by Reyes & Chopra (2011a) (and Reyes & Chopra (2011b)) is based on separate *MPA* calculations (see Sec. 2.2) for the respective seismic excitations with a subsequent *SRSS* combination of the directional results which are linearly superimposed with the results r_g due to gravity loads:

$$r = \sqrt{r_X^2 + r_Y^2} \quad \rightsquigarrow r_{tot} = r_g \pm r \ . \tag{7.1}$$

Reyes & Chopra (2011a) also present a rather complex extension of this method, in which the combination of the two earthquake components is investigated by simultaneously applying previously determined target displacements in the X and Y directions. Considering all four possible sign combinations, the internal forces are calculated separately, depending on whether they are elastic or already inelastic. In particular due to the fact that this approach assumes the maximum a_g value in both directions, although the corresponding maximum excitations will not occur simultaneously, this extension is not considered in more detail below.

Multidirectional pushover procedure by FUJII (2014)

The multidirectional pushover procedure by FUJII (2014) is based on the consideration of two orthogonal earthquake excitations in the U and V directions, where the number of modes considered is limited to two, i.e. one mode per direction. For both directions, a separate adaptive pushover analysis is first used to determine a pushover curve with a mode proportional load approach. In the next step, the maximum structural response for the respective direction is calculated, for example using a damped response spectrum.

The two directional structural responses are then combined into four possible load combinations:

$$\mathbf{P}_U^\pm = \mathbf{M} \cdot (\beta_{1,U} \cdot \mathbf{\Phi}_1 \cdot S_{a,1} \pm 0.5 \cdot \beta_{2,V} \cdot \mathbf{\Phi}_2 \cdot S_{a,2}) \tag{7.2}$$

$$\mathbf{P}_V^\pm = \mathbf{M} \cdot (\pm\, 0.5 \cdot \beta_{1,U} \cdot \mathbf{\Phi}_1 \cdot S_{a,1} + \beta_{2,V} \cdot \mathbf{\Phi}_2 \cdot S_{a,2}) \;, \tag{7.3}$$

where it is assumed that mode 1 acts mainly in the U and mode 2 in the V direction and the time-delayed occurrence of the maximum excitation in both directions is covered by a constant combination factor of 0.5.

Subsequently, static calculations are carried out on the basis of the load combinations according to Equation 7.2 for the displacements in the U direction and Equation 7.3 for the V direction. The decisive design-relevant structural response is then obtained for each response quantity as the envelope of the four results in the primary or secondary earthquake direction.

In this regard, however, FUJII (2014) himself criticizes the fact that he assumed uncorrelated horizontal components of ground motion. According to his own statement, this is only valid when the direction of incidence of the major principal component of ground motion coincides exactly with the principal direction of the first mode. In addition, his numerical comparative calculations show that the influence of higher modes can certainly be relevant and is therefore lost when determining the structural response. However, even the extension presented in FUJII (2020) only provides for one accompanying mode per direction and is already relatively complex anyway.

***Bidirectional Pushover Analysis* (*BPA*) by CIMELLARO ET AL (2014)**

The so-called *Bidirectional Pushover Analysis* (*BPA*) by CIMELLARO ET AL (2014) also considers the combined earthquake excitation in two horizontal directions. Analogous to the approach presented by FUJII (2014), only one base mode can be considered per direction. In contrast to the previously discussed method however, in which two monodirectional pushover analyses were initially carried out, the load approach is based on a direct combination of the two earthquake components. It is assumed that the principle seismic excitation acts in the X direction and the orthogonal accompanying excitation in the Y direction. Against the background of a partial

correlation of the two components of ground acceleration, the following lateral force pattern is applied in the pushover analysis:

$$P = P_X + P_Y = \mathbf{M}\mathbf{\Phi}_n + \gamma \cdot \mathbf{M}\mathbf{\Phi}_m \quad (0 \leq \gamma \leq 1) \, . \tag{7.4}$$

Although the combination factor γ was initially kept variable, Cimellaro et al ultimately emphasize on the basis of their numerical investigations that the value of $\gamma = 0.6$ is the most suitable. They attribute the significant exceeding of the combination factor of 0.3 provided for in Eurocode 8 - Part 1 (2010) to the pronounced nonlinear load-bearing behavior. For this combined load distribution (acc. to Eq. 7.4), a pushover curve for the primary seismic direction (X) is generated. A maximum spectral response of the structure at the performance point is determined using an inelastic response spectrum, based on a reduction factor R_μ taking nonlinearities into account. The associated *mp* displacement is back-transformed afterwards. With this displacement, the associated displacements in the orthogonal Y direction can be calculated using the bidirectional pushover curve resulting from the MDOF model.

The application of this method, which was initially validated on conventional multi-storey buildings, to bridge structures must also be viewed critically, as only one reference mode can be used for each earthquake direction and it is also a non-adaptive method. Furthermore, it should be critically noted that Cimellaro et al do not take into account any variation of the primary earthquake direction or the direction of the secondary load vector. However, this will be additionally investigated in the later application of the *BPA* in Section 7.4.

Multidirectional *Adaptive Interaction Analysis* (3D *AMI*) by NORDA (2012)

In Section 2.2, the monodirectional basic concept of the *AMI* was already presented. This was extended by Norda (2012) for multidirectional investigations by determining the deformations for each earthquake direction separately via the modal combination (acc. to Eq. 2.20) and then combining them linearly. For this directional linear combination, Norda selects the '1.0-0.3' rule also proposed in Eurocode 8 - Part 1 (2010), so that the following relationship results for the displacement increments of the multidirectional *AMI* (in **p**rimary and **s**econdary **d**irection):

$$\Delta \mathbf{V}^{(i,k)} = \sum_{n(pd)} \alpha_n^{(k)} \cdot \beta_{n,pd}^{(i)} \cdot \mathbf{\Phi}_n^{(i)} \cdot \Delta S_{d,n}^{(i)} \, '+' \, 0.3 \cdot \sum_{n(sd)} \alpha_n^{(k)} \cdot \beta_{n,sd}^{(i)} \cdot \mathbf{\Phi}_n^{(i)} \cdot \Delta S_{d,n}^{(i)} \, . \tag{7.5}$$

However, Norda does not examine the above multidirectional approach herself in more detail or validate it sufficiently. Since the '1.0-0-3' rule was actually derived and comprehensively investigated for the subsequent combination of specific response quantities, its application at load level must be questioned in principle according to the current state of research. Such a critical analysis is therefore implemented with regard to the self-developed *modified AMI* (*mAMI*) in Section 7.2.

Concluding remarks

In addition to the methods presented, there are further multidirectional pushover approaches that have been published in the recent past. The *Coupled Nonlinear Static Pushover* (*CNSP*) procedure by Camara (2011) and Camara & Astiz (2012) should be emphasized here which, however, is also based on a single-mode approach per earthquake direction and on an *SRSS* combination of directional pushover curves. As this is complex on the one hand and represents a very restrictive simplification on the other, this method will not be discussed in more detail. The same applies to the method proposed by Acharjya & Roy (2023) for near-fault motions with fling-step signature as well as for other less common publications (e.g. listed in Cantagallo et al (2022), Chap. 2).

7.1.2   Key issues concerning the bidirectional *mAMI* application

In general, the damage and reduction in stiffness of reinforced concrete columns or piers is significantly increased by a biaxial horizontal load (Rodrigues et al , 2012). However, the question arises to what specific extent a bidirectional earthquake excitation causes these effects, as the maximum seismic excitations in orthogonal directions occur with a time delay in reality. Therefore, the idea of the *AMI* method according to Norda , as shown in Section 7.1.1, is to combine the contributions of the different earthquake excitations already at load level via the '1.0-0.3' rule. Since the constant factor of 0.3, which is not validated in this context, is to be critically questioned, it is replaced here by a general factor ψ (with $0 \leq \psi \leq 1$), which is referred to as the general *percentage rule*, as part of the optimization of the *AMI* method. The following questions need to be answered against this background:

- Is there a specific factor ψ for which the *mAMI* provides good overall agreement with the results of nonlinear time history calculations, regardless of the type of response quantity of interest evaluated? Or, if this is not the case, does such a fixed value at least exist for certain bridge structures, depending on the complexity of the inelastic seismic behavior?

- *If so*: Is this identical for all structures or, alternatively, can it at least be reliably estimated for specific structures in advance on the basis of a simple preliminary investigation?

- *If not*: What other approach is suitable for mapping multidirectional earthquake excitations for applications of the *mAMI* to bridge structures?

7.1.3   Comparative multidirectional time history calculations

For bidirectional seismic analyses in the time domain, neglecting the vertical excitation due to low seismicity (acc. to Eurocode 8 - Part 2 (2011), Sec. 4.1.7(1)), 50 ground acceleration

time histories acting simultaneously in both horizontal directions are applied. These ground motions are considered to belong to the same response spectrum and must obviously be independent of each other, since identical functions would again result in a monodirectional excitation at an angle of 45°, scaled only by the factor $\sqrt{2}$. Furthermore, both accelerograms are applied without reduction, as scaling by a factor of 0.3, for example, reflects the effect that $a_{g,X}$ and $a_{g,Y}$ do not reach their maximum at the same time. However, this circumstance is automatically covered in an *NLTHA*, unlike in a static calculation. It is also important to emphasize in this context that the second horizontal component is not intended to cover an unknown decisive seismic incident angle (*sia*). Rather, the interaction of different wave types in the direction of propagation and orthogonal to it is thus taken into account.

In order to ensure the independence of the two functions $a_{g,X}(t)$ and $a_{g,Y}(t)$ in each *NLHTA* calculation, a specific accelerogram i acting in the X direction is combined in each case with the $(i+1)$-th in the Y direction.

7.2 Investigation on the applicability of the *percentage rule* for determining multidirectional *mAMI* load patterns

7.2.1 Introductory remarks

In the following, results of bidirectional *mAMI* calculations with relevant modal sign combinations and, in particular, varying ψ values are compared with those of corresponding *NLTHAs* with two simultaneous orthogonal base excitations. The two respective monodirectional ground accelerations in the X and Y directions are also studied. An additional comparison with other bidirectional pushover methods is provided in Section 7.4.

For the following studies, it is crucial to generate a measurable influence of the additional earthquake excitation in the X direction. For this purpose, the bridge deck is no longer pinned at one abutment, but is slidably supported at both abutments in the longitudinal direction. However, preliminary investigations have shown that the previously investigated bridge models A and B (cf. Sec. 6.2) cannot sustain the double-axis bending corresponding to the previous earthquake level. Therefore elastomeric bearings with a longitudinal stiffness of 1000 kN/m are applied at the ends of the bridge deck. Furthermore, in order to avoid reducing the already relatively low ground acceleration of $a_g = 0.1g$ by more than a factor of 0.5, a permanent load of 130 kN/m is applied along the bridge deck. Even though this leads to a larger resonant mass of about 13.25 t/m instead of the previous 5 t/m, it especially causes a significant increase in the favorable compressive stresses in the piers, thus leading to a measurable larger flexural strength. As the bending stiffness of the deck is not changed, this additional mass also further

increases the influence of higher modes. In order to be able to correctly map the interaction between the two bending moments and the normal force in the piers, fiber hinges are again used to describe the material nonlinearity. Furthermore, a preliminary study verified that the combined earthquake excitation in the longitudinal and transverse directions of the bridge, i.e. with a *sia* of 0°, is sufficient for these two bridge models, as the results change by less than 1% when the *sia* is varied between 0° and 90° in steps of 10°.

7.2.2 Preliminary study in time domain

The extent to which a bidirectional earthquake excitation affects the base shear and the internal forces in the Y and X directions is initially examined in the time domain, compared with a corresponding monodirectional excitation. The complete tabular evaluation, contained in Appendix F (Tabs. F.1 & F.2), shows that the examined force quantities mostly differ by up to 6%, but in the case of the base moment of pier P1 of model B by almost 24%. It is important to emphasize that, without exception, lower force quantities are present in the case of bidirectional excitation. This is due to the fact that a support node acceleration in the longitudinal direction does not increase the bending moment around the global X-axis, but additionally weakens the cross-section and thus ultimately activates more ductility, which allows the structure to reduce the effective seismic impact to a greater extent. However, since the combination of both earthquake excitations leads to an increased extent of damage due to the larger nonlinear normal stresses in the piers, this excitation is decisive overall and also more realistic.

Figure 7.1 (a) illustrates the normal stress distribution over the cross-section at the base of pier P2 of model A for $t = 6.28$ s of the first bidirectional *NLTHA* calculation, at which the concrete compressive stresses reached their maximum. Here it can be seen that in this state only a small part of the concrete surface still transmits compressive stresses and a considerable part is in tension due to the biaxial bending. About 2/3 of the cross-sectional area is cracked and can therefore no longer transmit tensile stresses. However, the fact that the corresponding fibers can subsequently transmit compressive stresses again, when the load direction changes, can be seen from the σ-ε history of the same calculation depicted in Figure 7.1 (b) with the later time $t = 6.72$ s marked by the yellow marker. Furthermore, it is verified that on the basis of the *Concrete Hysteresis Model* used, cracked concrete fibers cannot absorb any new tensile stresses after the tensile strength has been exceeded once.
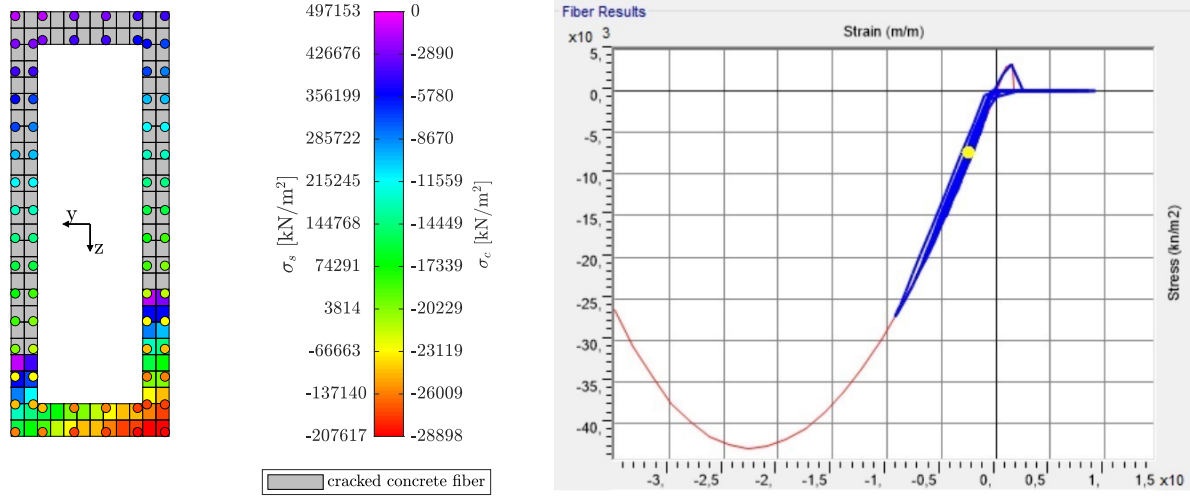
(a) σ_c- & σ_s-distribution ($t = 6.28$ s)   (b) σ-ε history (Fiber 58 in the top left corner)

Figure 7.1: *Hinge results at the base of P2 (multidir. NLTHA 1)*

7.2.3   Investigation of model A

In case of the modified bridge model A, the natural modes 1, 2 and 6 (see Figs. 7.2 & 7.3) are relevant in the X and Y directions, respectively. In the multidirectional *mAMI* calculation, unlike in the time domain, one earthquake direction must always be set as primary and the orthogonal one as secondary. The reason for this is that it would otherwise be assumed that the maximum excitations occur simultaneously in the X and Y directions. The following ψ-values are examined once for primary earthquake in the X direction and once in the Y direction: 0 (monodirectional comparative calculation), 0.1, 0.2, 0.3, 0.35, 0.4, 0.6. For all calculations with a main earthquake in the longitudinal direction ($pd = X$), mode 1 is taken into account in the primary direction and modes 2 and 6 in the secondary direction (Y). The first two are used as reference modes for the corresponding directions. In the calculations with $pd = Y$, additional modes that become relevant in the course of the calculations are considered in the Y direction, which therefore only show significant transversal displacements with increasing loads. Node 3 at the head of the center pier in the symmetry axis is selected as the monitoring point for all calculations. As before, the optimized spectral acceleration increments $\Delta S_{a,B}^{(i)}$ are applied on the basis of $k_{loc/glob} = 0.9$.
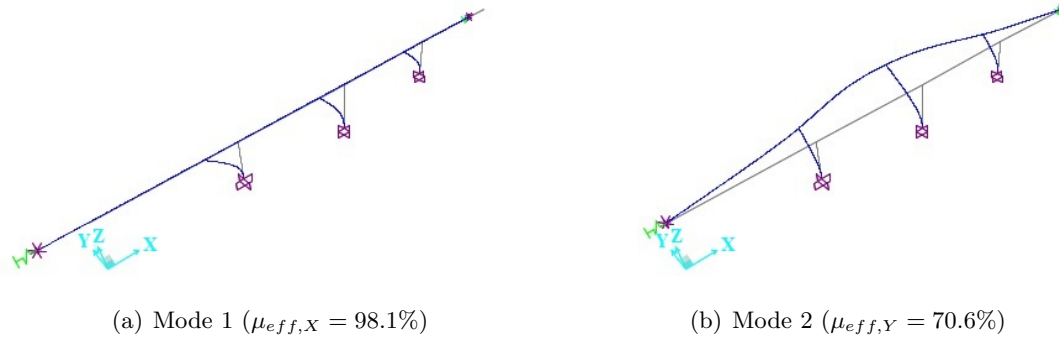
(a) Mode 1 ($\mu_{eff,X} = 98.1\%$)   (b) Mode 2 ($\mu_{eff,Y} = 70.6\%$)

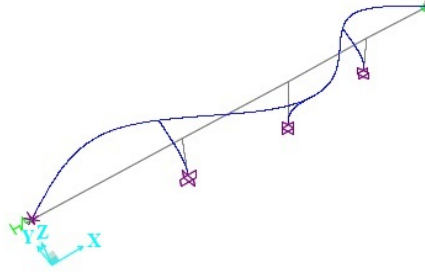***Figure 7.2:*** *Modes 1 & 2 of the modified bridge model A*

Figure 7.3: *Mode 6 ($\mu_{eff,Y} = 20.4\%$) of the modified bridge model A*

The following Figure 7.4 depicts, separately for the main seismic excitation in the X and Y directions, the results for the relevant base moments (M_2 and M_3) of the various multidirectional *mAMI* calculations, plotted against the direction factor ψ, additionally compared with the results of the respective mono- and multidirectional *NLTHAs*. The latter serves to get an impression of the overall influence of bidirectional ground motions in the time domain.

Here it can be seen for the moment M_2 as a result of the *mAMI* calculations with a primary earthquake in the X direction and an additional secondary one in the Y direction that the smallest positive deviation (thus being on the safe side) from the results of the multidirectional *NLTHA* for the edge piers is at $\psi_{opt} = 0.3$ and for the center pier P2 at 0.35 (≈ 0.3). With regard to the base moment M_3 of the *mAMI* calculations with $pd = Y$ and $sd = X$ the ψ_{opt} value for the edge columns is either 0.35 (≈ 0.3) or 0.6, so there is no definitive value for ψ_{opt}. Moreover, with regard to the results at the base of the center column P2 ψ_{opt} is even exactly zero. In the latter case all bidirectional *mAMI* calculations are on the unsafe side when compared with the likewise bidirectional time history calculation, from $\psi > 0.1$ even to a great extent.
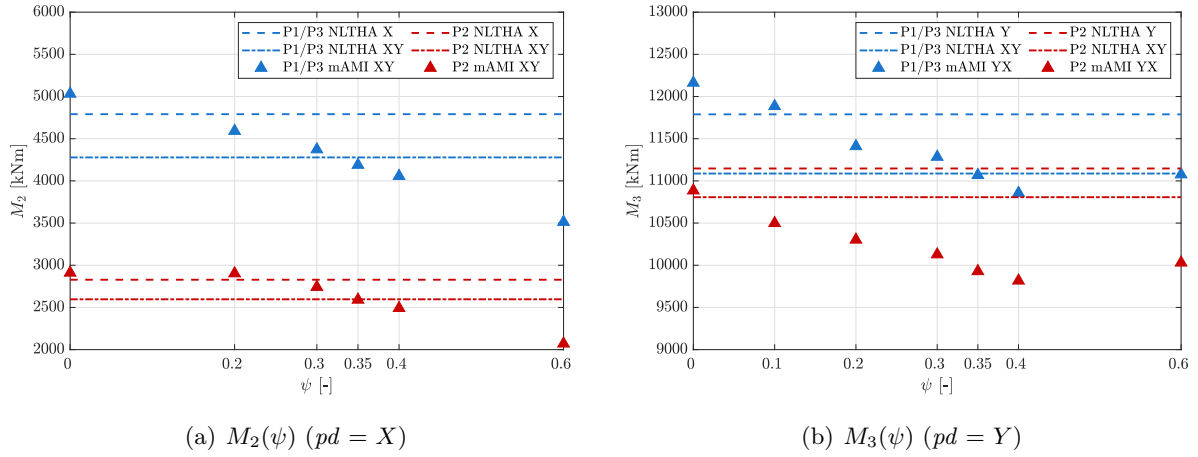
(a) $M_2(\psi)$ $(pd = X)$ (b) $M_3(\psi)$ $(pd = Y)$

Figure 7.4: *Base moments $M_{2/3}(\psi)$ $(pd = X/Y)$, Bridge model A*

The initial question of whether there is a specific ψ_{opt} value that provides the best approximation to the time history results independent of the investigated force quantity and leads to results being on the safe side in any case, could strictly speaking already be answered in the negative at this point. Any further investigation of bridge model B could theoretically be omitted. However, since such a central finding for the optimized *mAMI* method should not be made on the basis of only one bridge model, the results of the asymmetric bridge model B are nevertheless evaluated in more detail below and an independent ψ_{opt} determination is analogously carried out.

7.2.4 Investigation of model B

In the following section, bridge model B is examined, which can be classified as asymmetric. The asymmetry is caused by piers with different lengths yet identical cross-sections, leading to an asymmetric stiffness distribution. All *mAMI* calculations are based on the consideration of mode 1 in the X direction and modes 2, 5 and 7 in the Y direction (see Figs. 7.5 & 7.6), modes 1 and 2 being the reference modes in the corresponding directions at first. Furthermore, node 4 at the top of the longest pier P3 is selected as *mp* and, as before, the optimized acceleration increments $\Delta S_{a,B}^{(i)}$ are computed for the limit criteria $k_{loc} = k_{glob} = 0.9$. Based on the first M_3 results for the calculation with 1.0-fold load vector in the Y direction and with ψ reduced loads in the orthogonal X direction, it was stated that ψ values greater than 0.35 lead to increasingly poorer results. The analysis of M_3 $(pd = Y)$ was therefore limited to this area.

Analogous to the previous evaluation of model A, Figure 7.7 shows the results for the relevant base moments M_2 $(pd = X)$ and M_3 $(pd = Y)$, plotted against the directional factor ψ. As before, the most optimal ψ value can thus be read off with respect to the reference solution of the multidirectional *NLTHAs*.

(a) Mode 1 ($\mu_{eff,X} = 98.3\%$)
      (b) Mode 2 ($\mu_{eff,Y} = 53.5\%$)
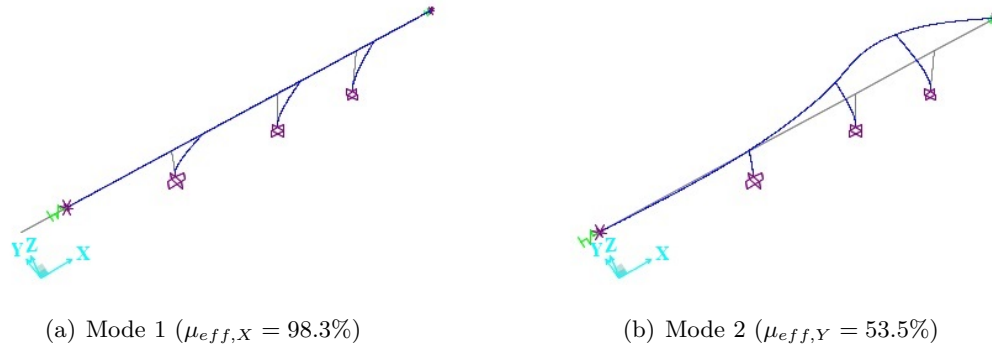
Figure 7.5: *Modes 1 & 2 of the modified bridge model B*

(a) Mode 5 ($\mu_{eff,Y} = 9.0\%$)
      (b) Mode 7 ($\mu_{eff,Y} = 29.4\%$)
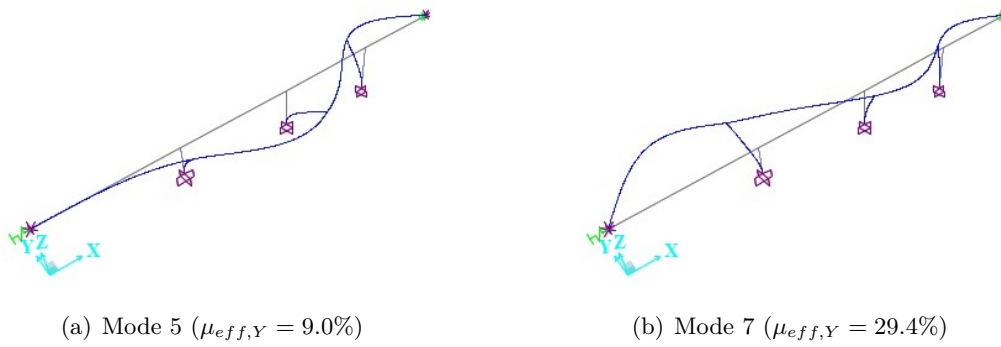
Figure 7.6: *Modes 5 & 7 of the modified bridge model B*

(a) $M_2(\psi)$ ($pd = X$)
      (b) $M_3(\psi)$ ($pd = Y$)

Figure 7.7: *Base moments $M_{2/3}(\psi)$ ($pd = X/Y$)*

The evaluation concerning the base moment M_2 as a result of the *mAMI* calculations with a primary earthquake load in the X direction and an additional secondary load in the Y direction

provides a ψ_{opt} value of 0.1 for both edge piers and a value of 0.2 for the central pier. With regard to M_3 of the *mAMI* with $pd = Y$ and $sd = X$, the ψ_{opt} value for piers P2 and P3 is 0.15 and thus also between 0.1 and 0.2, but all mono- and multidirectional *mAMI* calculations are on the unsafe side with regard to the base moment of edge pier P1. In view of the findings documented in Section 6.3.3, this is d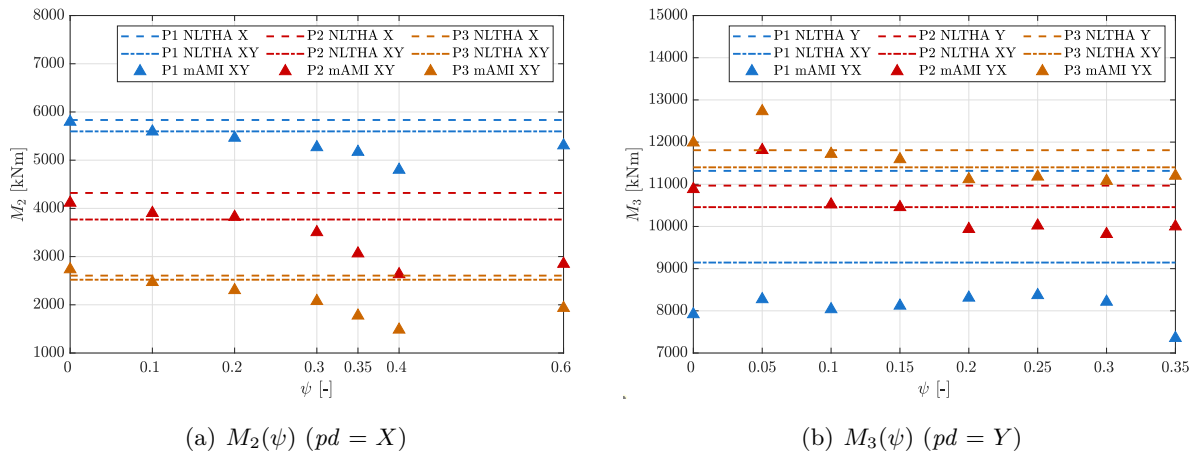ue to the fact that the fundamental mode 2, which has almost no displacement components in pier P1, does not excite the latter sufficiently. Since the accompanying modes are significantly reduced by the correlation factors, the bending moments are significantly underestimated in this pier. This effect will be investigated in more detail in subsequent studies by selecting modes 2, 5 and 7 as varying reference modes in combination with an additional variation of the monitoring point (nodes 2, 3 & 4 at the top of all three piers, respectively).

Beforehand, however, the influence of a negative sign of mode 1 in the secondary X direction on this asymmetric structure is briefly analyzed. The evaluation of the corresponding analysis is shown in Figure 7.8.
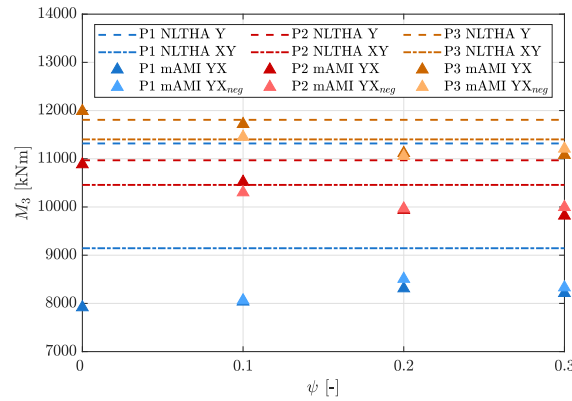
Figure 7.8: *Base moment* $M_3(\psi)$ *(sd = X & −X)*

It can be concluded from this study that the differences in the moments due to the variation in the sign of the longitudinal mode are only of the order of a few percent, which in the case of nonlinear-static *mAMI* calculations could even result from minimally different relevant adaption points within the analysis of the pushover curve anyway. This effect is therefore negligible.

In view of the above, the focus is now on the influence of different reference modes and monitoring points. For this purpose, the following Figures 7.9 and 7.10 show the base moments M_3 due to monodirectional earthquake in the Y direction (i.e. $\psi = 0$) for varying base modes (*BM*) 2, 5 and 7 as well as different monitoring points (*mp*) 2, 3 and 4 in comparison with the respective corresponding *NLTHA* results.

(a) P1

(b) P2

Figure 7.9: *Base moments* $M_{3,P1/P2}(\psi = 0)$ *(pd = Y)*
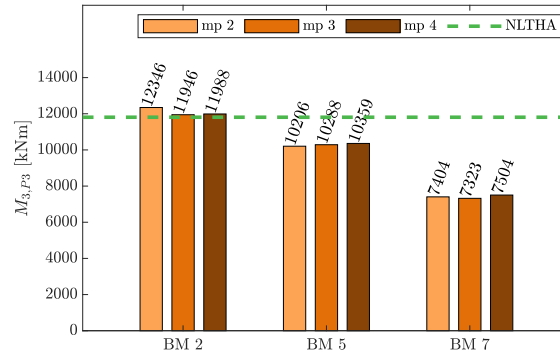
Figure 7.10: *Base moment* $M_{3,P3}(\psi = 0)$ *(pd = Y)*

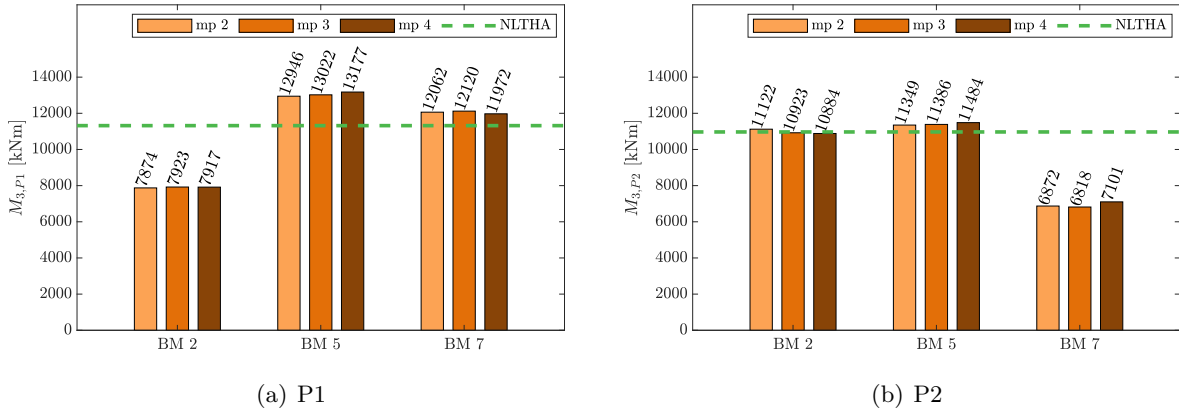With regard to the choice of the respective base mode, these results confirm the finding already elaborated in Section 6.3.3 that all piers relevant for the inelastic seismic behavior should be sufficiently excited by the corresponding reference mode in at least one *mAMI* calculation. In this specific case, good results are only achieved for pier P1 by selecting mode 7 as the base mode, while calculations with reference mode 2 significantly underestimate the actual values and with reference mode 5 overestimate them somewhat more than with mode 7. For the two other piers, however, the choice of the second mode is suitable; base mode 5 leads to similarly good results in relation to the center pier P2.

Furthermore, with regard to the varying *mp* approaches, it can again be stated that these merely have a minor influence on the results in case of the *mAMI*. Only in the case of edge pier P3 the choice of node 2 as *mp* at the top of pier P1 produces a noticeably larger value than the corresponding *NLTHA* calculation. The deviation, however, is small.

On the basis of the last detailed investigations, a more precise and thus, above all, valid analysis of the optimal ψ value for the base moment M_3 of pier P1 can now be carried out. For this purpose, Figure 7.11 illustrates the base moments of different bidirectional *mAMI* calculations with the varying monitoring points 2, 3 and 4 and fundamental mode 2 as well as for the base modes 5 and 7, each in combination with *mp* 2. The findings of the monodirectional *mAMI* analyses, which have just been presented, are once again confirmed: for the shortest and thus stiffest edge pier P1, the smallest possible deviations from the 'NLTHA XY' results are achieved with reference mode 7, being on the safe side. With regard to the main issue of an optimal combination value ψ, it can be seen for the bending moment M_3 of pier P1 that this is even represented by the ψ_{opt} value of 0.2 in this case with a clear overestimation of about 20%.
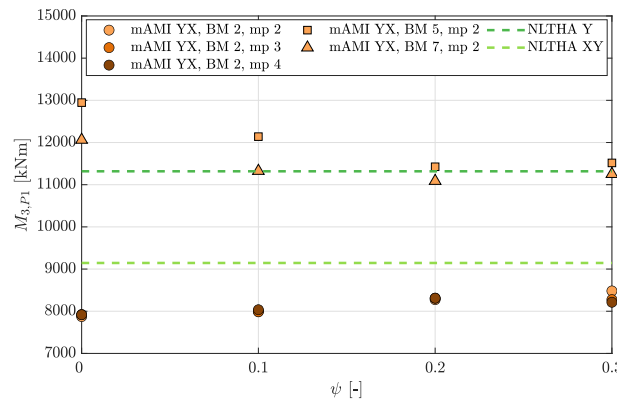
Figure 7.11: *Base moment $M_{3,P1}(\psi)$ ($pd = Y$)*

7.2.5   Conclusion on the ψ_{opt} study

Overall, the initial question of whether there is a specific ψ_{opt} value that provides the best possible approximation to the *NLTHA* results, independent of the respective force quantity of interest, and which despite leads to results being on the safe side in any case must be answered in the negative.

On the one hand, for model A ψ_{opt} values of 0.3 to 0.35 can be identified for three of the four moments considered (M_2 of the edge and center piers & M_3 of the edge piers) and for model B values between 0.1 and 0.15 for most base moments and only for one bending moment of about 0.2; here $\psi = 0.1$ would only lead to a slightly greater overestimation. At this stage, the widely scattered ψ_{opt} values can only be observed; the reason for these significant deviations however remains to be investigated. The same applies to the question whether a suitable ψ value can be reliably estimated in advance for further bridge models.

On the other hand, it has also been shown that a general ψ value > 0, i.e. the *mAMI* calculation with a multidirectional load distribution, can lead to a considerable underestimation of the bending moments. In contrast to model B, where this was due to the unsuitable reference mode 2 for pier P1, it was not the reason with regard to the moment M_3 in pier P2 of model A. In addition, in some cases the diagrams show very discontinuous developments of the moments depending on the respective ψ values, so that the identification of any ψ_{opt} value may only be reliable to a limited extent anyway. In one case, for example, the evaluation provided two different possible ψ_{opt} values of 0.35 and 0.6 with an almost identical result quality.

Against this background, the *mAMI* based on a bidirectional load distribution weighted with 1.0 and ψ appears to be fraught with too much uncertainty overall. Even the generalization of the approach proposed by NORDA (2012) in the sense of the *percentage rule* is therefore not considered a valid concept for multidirectional *mAMI* calculations.

7.3   Elaboration of an alternative multidirectional concept

7.3.1   Subsequent overlaying techniques – state of research

In principle, separately determined structural responses $E_{ed,X}$ and $E_{ed,Y}$ due to orthogonal earthquake excitations in the X and Y directions can be superposed either using the *SRSS* combination rule or on the basis of the *percentage rule*. The *SRSS* approach by NEWMARK & ROSENBLUETH (1971) assumes that each component is a Gaussian stochastic process. Analogous to a modal combination, this superposition method is also based on the assumption of a decorrelation of both components.

As an alternative, NEWMARK (1975) and ROSENBLUETH & CONTRERAS (1977) introduce the *percentage rule* that evaluates E as the sum of 1.0 $E_{ed,pd}$ plus a percentage ψ of the response $E_{ed,sd}$ due to the orthogonal earthquake component in the secondary direction (*sd*). While NEWMARK proposes a combination factor of 0.3 and ROSENBLUETH & CONTRERAS a significantly higher value of 0.4, WILSON ET AL (1995) emphasize that the *percentage rule* can generally lead to an underestimation of the design forces. HUSSAIN & DUTTA (2020) and HUSSAIN ET AL (2022) come to the same conclusion and concretize it to the effect that inelastic structural responses are particularly affected by this. While CANTAGALLO ET AL (2022) again work out that even a factor of 0.3 can lead to a significant overestimation of the results, KHALED ET AL (2010) show in an extensive parameter study that the often-used percentage factor of 0.3 is not generally valid, but depends, on the one hand, on the earthquake itself and, on the other hand, on the investigated bridge structure. BURTON ET AL (2018) come to a comparable conclusion by superimposing normal forces resulting from two monodirectional seismic analyses in the time

domain with varying ψ values and reading out the ψ value corresponding to a probability of exceedance of 10% compared to the result of the bidirectional investigation. This results in a fluctuation of up to 40%, which, according to BURTON ET AL (2018), depends on differences in the structures investigated, the peak ground acceleration (*PGA*) and the response quantity of interest. In conclusion, it can therefore be summarized that, according to the current state of research, the percentage factor poses a problem with regard to the reliability of the final results. However, most publications only point out the problem mentioned and at best give a recommendation for specific structures in certain regions, such as in KHALED ET AL (2010) for reinforced concrete bridges in Canada.

VALDÉS-GONZÁLEZ ET AL (2015) present a single generally valid approach for determining a case-related percentage factor. They include the coherence of the orthogonal earthquake excitations themselves and distinguish between collinear (c) and orthogonal (o) response quantities. While the former directly result from both excitations, such as normal forces or stresses in columns or piers, the latter are, for example, bending moments that are only activated by either $a_{g,X}$ or $a_{g,Y}$. For both categories, VALDÉS-GONZÁLEZ ET AL introduce a specific equation for determining the combination factor, which is denoted here as $\alpha_{c/o}$ (for **c**ollinear and **o**rthogonal response components, respectively, ω_g being the predominant frequency of the ground motion):

$$\alpha_c = \frac{\pm\sqrt{1 + \beta^2 + 2\beta real[\varphi(\omega_g)]} - 1}{\beta} \tag{7.6}$$

$$\alpha_o = \pm\sqrt{\frac{\pm\sqrt{1 + \beta^4 + 2\beta^2 real^2[\varphi(\omega_g)]} - 1}{\beta^2}} \ , \tag{7.7}$$

where $\varphi(\omega)$ is the complex coherency function between the horizontal orthogonal components of the ground acceleration. With the two deterministic functions $g_1(\omega)$ and $g_2(\omega)$, depending on the particular response components on the basis of the structural characteristics (such as stiffness, damping and mass), and the correlation factor k (acc. to Eq. 7.9), β can be calculated as:

$$\beta = \frac{kg_2(\omega_g)}{g_1(\omega_g)} \ , \tag{7.8}$$

$$\text{with } k = \frac{|a_{g,Y}|}{|a_{g,X}|} \ . \tag{7.9}$$

7.3.2 Selection of a suitable subsequent superposition rule based on the available calculation results

In the previous investigations of Section 7.2 it has already been worked out that a simultaneous consideration of orthogonal earthquake components in the *mAMI* at load level does not provide

satisfactory results. Consequently, a superposition must be carried out subsequently as in many other multidirectional pushover procedures. However, a distinction should be made between orthogonal response components, such as orthogonal bending moments M_y and M_z, and collinear quantities, such as normal stresses. The former only depend on a further orthogonal earthquake load to the extent that, for example, certain concrete fibers can additionally crack that would not have been under tension or at least to a lesser extent under monodirectional loading. Overall, the nonlinear seismic behavior itself therefore differs and thus also for example the bending moment in transverse direction due to a longitudinal seismic excitation, even if such an earthquake would not cause this moment itself. However, collinear quantities, such as normal stresses, behave cumulatively so that they are caused directly by both orthogonal ground motion components.

Both on the basis of the previous *mAMI* calculations and based on the preliminary investigation in the time domain, it can be concluded that monodirectional pushover analyses are on the safe side with regard to orthogonal response quantities and in most cases with acceptable deviations from the *NLTHA* results. In this respect, the decisive values of the two monodirectional *mAMI* calculations are considered to be a sensible alternative to combining the earthquake contributions at load level for orthogonal response components.

With regard to collinear variables, however, a reasonable subsequent combination approach must be defined. According to the previous Section 7.3.1, either the *SRSS* or the *percentage rule* with different ψ factors can be considered. This is examined in more detail below using the maximum compressive stresses in the concrete fibers as well as the maximum tensile stresses in the reinforcing steel fibers for bridge model A and B. Specifically, stress demands are examined in the four corner fibers of each pier base which result from both 'mAMI X' and 'mAMI Y' calculations. Subsequently, the two values for each fiber are combined using the *SRSS* and the *percentage rule* with varying ψ values (of 0, 0.1, ... 0.6). For each combination approach, the maximum final result of the four corner fibers is then taken as the decisive design value and compared with the time history solution. It is important to note that the normal stresses must be reduced by the value resulting from gravity loads before the superposition, which is then added back with the correct sign. Due to the inelastic load-bearing behavior, the calculation, on the other hand, should not be carried out entirely without taking the self-weight into account.

Investigation of bridge model A

The decisive maximum compressive stresses of the concrete and tensile stresses of the reinforcement fibers based on the *SRSS* and *percentage rule* superposition are shown below, which are graphically compared with the corresponding results of the nonlinear time history analyses.
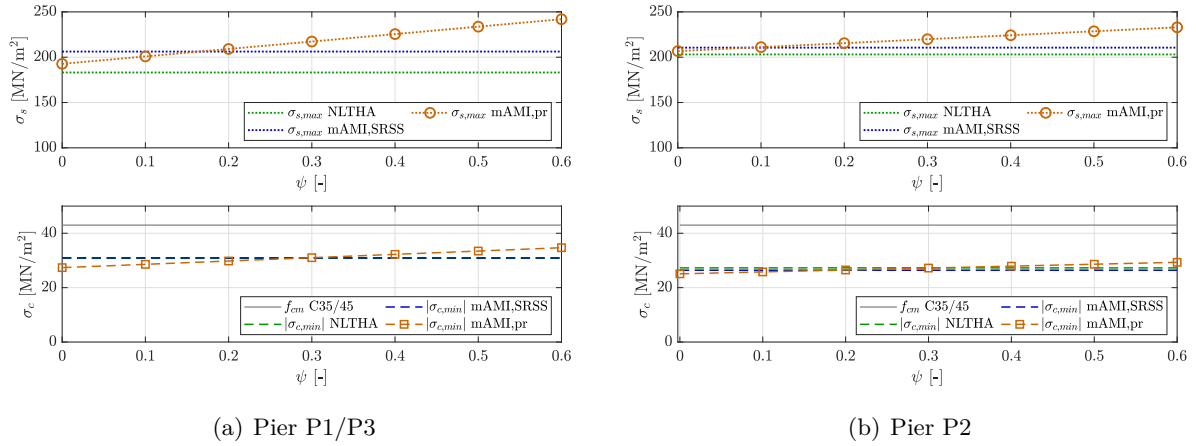
Figure 7.12: *Subsequently combined normal stresses (P1-P3), Bridge model A*

Here it can be seen that the *SRSS* superposition is always conservative with regard to the steel stresses, whereby the deviations from the *NLTHA* values are 12% and 3%, respectively. For the concrete compressive stresses, this combination rule provides an almost complete agreement with the nonlinear time history results.

With regard to the application of the *percentage rule* (pr) it can be stated that a ψ factor of 0.3 provides the best approximation to the concrete compressive stresses in the time domain for all piers. For the steel stresses, however, the optimum combination value for both pier types (edge and center pier) is 0.

Investigation of bridge model B

Next, the maximum compressive stresses of the concrete and tensile stresses of the reinforcement fibers are considered for the asymmetric bridge model B. It should be noted that the monodirectional *mAMI* calculation with reference mode 7 (and *mp* 2) is evaluated for pier P1 and earthquake in the Y direction and the calculation with reference mode 2 (and *mp* 4) in all other cases (i.e. '*mAMI X*' for the evaluation of P1-P3 as well as '*mAMI Y*' regarding P2 & P3).

Once again, it turns out that the *SRSS* superposition of the monodirectional *mAMI* calculation results with regard to the concrete compressive stresses provides values that are almost identical to the decisive results from the time domain solution. Furthermore, the steel tensile stresses from the *SRSS*-combined *mAMI* results are again on the safe side. The deviations from the *NLTHA* are now significantly greater for the short edge pier P1 and remain low for the other piers.

The application of the *percentage rule* now provides ψ_{opt} values of 0.4 (P1 & P2) or 0.2 (P3) for the concrete and 0 (P1 & P3) or 0.2 (P2) for the steel stresses with regard to this model.
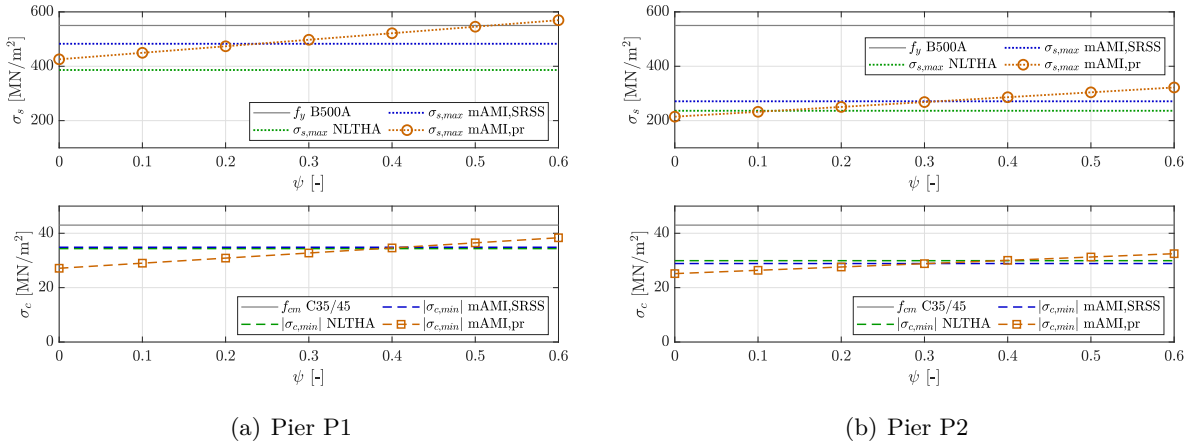
Figure 7.13: *Subsequently combined normal stresses (P1 & P2), Bridge model B*
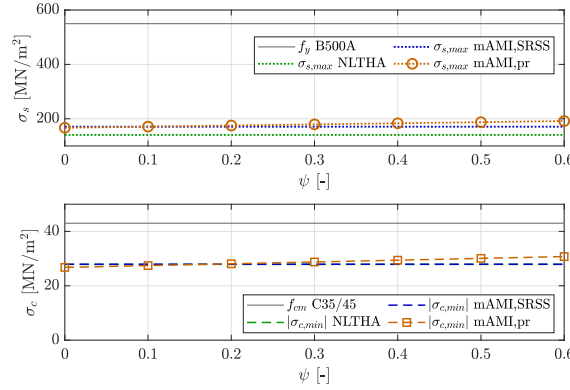

Figure 7.14: *Subsequently combined normal stresses (P3), Bridge model B*

Conclusions

Overall, the previous investigations of normal stresses lead to the conclusion that the *SRSS* combination yields a very good representation of the concrete compressive stresses and steel stresses that are on the safe side with largely acceptable deviations from the time history solutions.

The *percentage rule*, on the other hand, provides very different results for the investigated stress components depending on the combination factor ψ. The optimum ψ values are between 0 and 0.4 for the evaluations considered here in order to represent the best possible approximation of the *NLTHA*. In order to apply this superposition rule meaningfully in the context of the *mAMI*, taking into account bidirectional effects, the ψ value would have to be selected separately for each stress variable to be considered. This would be time-consuming and, apart from that, only possible with a valid equation for determining ψ_{opt}, if corresponding time history results – unlike in this case – are not available. Such a prior calculation could, for example, be based

on Equation 7.6 according to VALDÉS-GONZÁLEZ ET AL (2015), which was carried out for the present models using the concrete compressive stress components of the *mAMI* calculations for earthquakes in the Y and X directions as an example. However, the resulting α_c values were between 0.47 and 0.54 for the results of bridge model A and 0.62, 0.54 and 0.46 for piers P1 to P3 of model B. Thus, the realistic estimation of suitable percentage factors for the reasonable applicability of the *percentage rule* remains unresolved at this point.

Due to the satisfactory results for the *SRSS* combination and the more complex and uncertain application of the *percentage rule* with regard to ψ_{opt}, the multidirectional application of the *mAMI* will therefore be implemented on the basis of the *SRSS* rule for collinear variables.

7.4 Comparison of multidirectional seismic calculation concepts

7.4.1 Relevant background information

Finally, the results of the *mAMI* calculation under the previously elaborated consideration of multidirectional effects are compared once again with the results of the *NLTHA* and also with those of the bidirectional application of the widely used *RSM* as well as the *BPA* and *3D MPA* (cf. Sec. 7.1.1) as further multidirectional pushover concepts. First, however, some framework conditions and, in part, interim results of the multidirectional *RSM*, *BPA* and *3D MPA* calculation are presented in order to better understand their final results discussed below.

Multimodal, multidirectional *Response Spectrum Method* (*RSM*) according to Eurocode 8 - Part 1 (2010)
The multimodal *RSM* calculation, taking into account orthogonal earthquake excitations in the longitudinal and transverse directions, is carried out for two different behavior coefficients (acc. to EUROCODE 8 - PART 2 (2011), Table 4.1): $q = 1.5$ (limited ductile) and $q = 3.5 \lambda$ (ductile). For the second approach, λ is 1.0 in each case (for a detailed derivation, see App. F.2). Modes 1, 2 and 6 (cf. Figs. 7.2 & 7.3) are taken into consideration for the modified bridge model A as well as modes 1, 2, 5 and 7 (cf. Figs. 7.5 & 7.6) for model B.

***Bidirectional Pushover Analysis* (*BPA*) according to Cimellaro et al (2014)**
The *BPA* is applied separately for primary seismic excitation in the X direction and secondary earthquake in the Y direction (with $P = P_X + 0.6\,P_Y$) as well as for the complementary case ($P = P_Y + 0.6\,P_X$), with the governing longitudinal and transverse modes 1 and 2 being used as the base modes for both models. In case of model A, the center of mass (node 3) is selected as *mp*, while for model B essentially the top of pier P3 (node 4) is chosen, supplemented by the additional choice of node 3 only for comparison purposes in the Y direction.

The reduction factors R_μ used to determine the inelastic acceleration response spectra are 1.37 (*pd*: X) and 3.04 (*pd*: Y) for bridge model A and 2.32 (*pd*: X), 2.64 (*pd*: Y, *mp* 4) and 1.99 (*pd*: Y, *mp* 3) for model B. The final inelastic displacements of the monitoring point, which are obtained from the respective performance state, are also listed in tabular form below.

Table 7.1: *BPA:* $\Delta_{mp,inel.}$ *in m*

Bridge model	*pd*: X	*pd*: Y	
		mp: 3	*mp*: 4
A	0.049	0.023	-
B	0.029	0.015	0.023

The linearized pushover curve and the superposition of the corresponding capacity spectrum with the inelastic response spectrum are also shown as examples for the calculation with $pd = Y$ of model A. It is noticeable here that the two linear segments of the idealized pushover curve are approximately the same length, whereby the elastic target displacement is about 6 cm. However, the final inelastic displacement in the performance state is only 2.3 cm (see Tab. 7.1) and thus just beyond the effective yield point (cf. Fig. 7.15 (a)). This means that the ductility μ and consequently the reduction factor R_μ significantly overestimate the effective inelastic part of the total structural response, which leads to an excessive reduction of the response spectrum. This assumption is confirmed in view of Figure 7.15 (b), where a large difference between the elastic and inelastic response spectrum can be seen. The later comparison of methods will show the consequences of this effect.
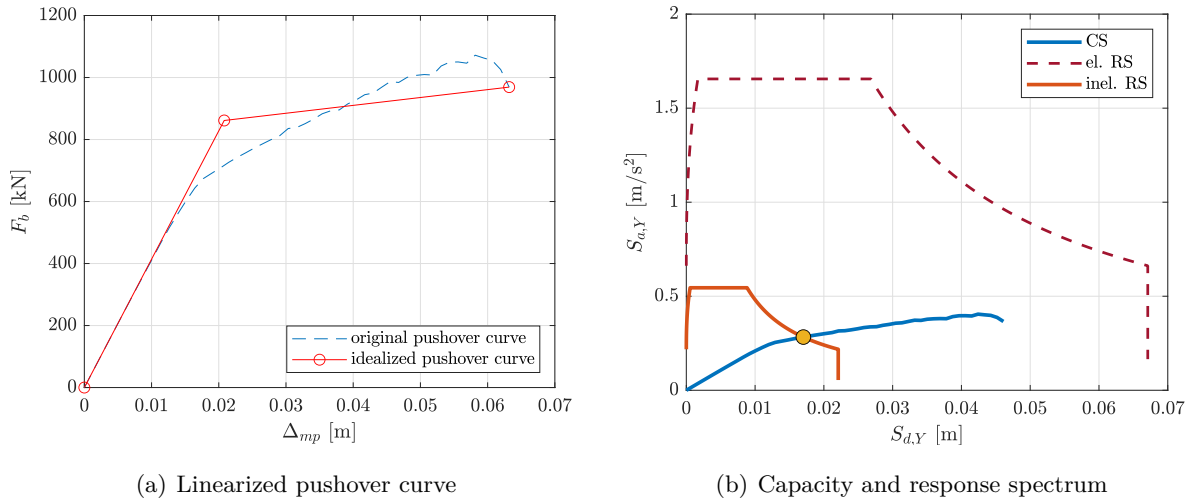

(a) Linearized pushover curve

(b) Capacity and response spectrum

Figure 7.15: *BPA: Pushover curve and capacity spectrum, bridge model A, pd: Y*

3D Modal Pushover Analysis (*3D MPA*) according to Reyes & Chopra (2011a)

For the application of the *3D MPA*, analogous to the *RSM*, mode 1 is taken into account in the *X* direction for both models and modes 2 and 6 for model A as well as modes 2, 5 and 7 in the case of model B in the *Y* direction, respectively. With regard to the monitoring point, for the symmetric model A the center node 3 was chosen and for model B once node 4 at the head of the longest bridge pier P3 and once (analogous to the *MPA* according to Sec. 6.3) different monitoring points (4, 4, 3 and 2 for modes 1, 2, 5 and 7).

The modal base shear and base moment components for the calculations of both models are listed below in order to be able to estimate the influence of the respective modes on the various force variables when comparing the methods later. For the asymmetric model B, only the results for the fixed *mp* 4 are shown as an example.

Table 7.2: *3D MPA: Force quantities - modal contributions, model A*

Modal contribution	$F_{b,Y}$ [kN]	$M_{3,P1/P3}$ [kNm]	$M_{3,P2}$ [kNm]
2	1701	9355	10007
6	1268	5014	-3013
CQC (*pd*: *Y*)	2209	10996	10702
Modal contribution	$F_{b,X}$ [kN]	$M_{2,P1/P3}$ [kNm]	$M_{2,P2}$ [kNm]
1	784	4650	2965

Table 7.3: *3D MPA: Force quantities - modal contributions, model B (mp: 4)*

Modal contribution	$F_{b,Y}$ [kN]	$M_{3,P1}$ [kNm]	$M_{3,P2}$ [kNm]	$M_{3,P3}$ [kNm]
2	1379	599	9204	10492
5	535	-4829	-6016	1830
7	2152	13232	-1295	495
CQC (*pd*: *Y*)	2730	14548	11756	10902
Modal contribution	$F_{b,X}$ [kN]	$M_{2,P1}$ [kNm]	$M_{2,P2}$ [kNm]	$M_{2,P3}$ [kNm]
1	859	5332	3403	1895

7.4.2   Procedure comparison on the basis of pier base moments (orthogonal)

As a first step, the results for the base moments of the three bridge piers are compared separately for both models (see Figs. 7.16 to 7.18).

With regard to the *mAMI*, only the calculation results that have already proven to be useful in previous investigations are evaluated, such as the selection of reference mode 7 for the base

moment $M_{3,P1}$ of model B. Table F.3 in Appendix F summarizes the general conditions of all calculations performed, including the previously described *RSM*, *BPA* and *3D MPA* applications.
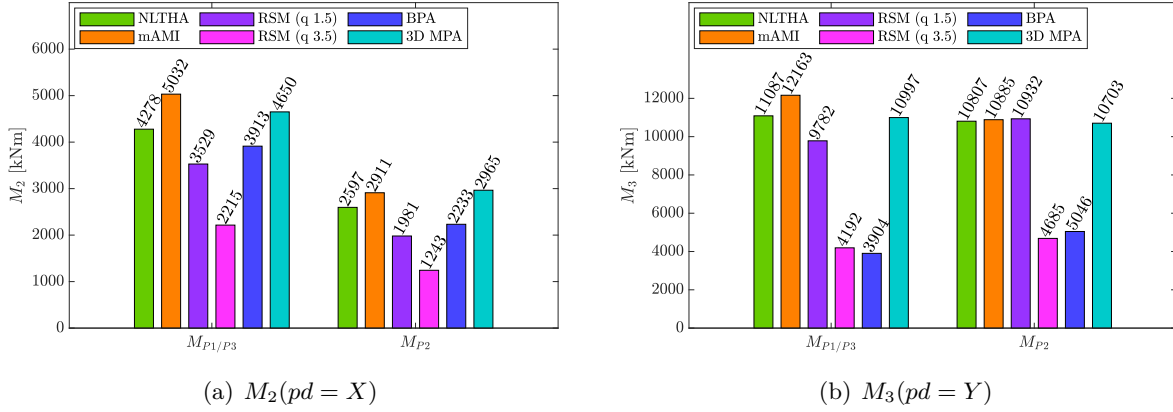
Investigation of bridge model A

(a) $M_2(pd = X)$ (b) $M_3(pd = Y)$

Figure 7.16: *Pier base moments, bridge model A*

While the *BPA* underestimates M_2 slightly, but M_3 strongly by more than 200%, the *mAMI* and *3D MPA* calculations provide a good overall agreement with the *NLTHA*. The *mAMI* is on the safe side in each case. The results of the three-dimensional *MPA*, however, underestimate the *NLTHA* results to a very small but negligible extent in some cases, but deviate significantly less upwards, so that they present the most accurate results overall in this calculation. The *RSM*, on the other hand, assuming limited ductility, sometimes significantly underestimates the bending loads, apart from M_3, while the *q* factor of 3.5 for ductile behavior leads to completely unacceptable underestimations of well over 200%.

Investigation of bridge model B

For bridge model B, the *BPA* also shows an unacceptably large underestimation of all bending moments. This is presumably due to the previously mentioned aspect (cf. Sec. 7.4.1) that the reduction factor R_μ based on the ductility is obviously significantly overestimated and the response spectrum thus has far too low ordinates. The question should therefore be asked as to whether an iterative approach (similar to the concept of reduced response spectra in the context of the *CSM*) would not be more appropriate for determining the inelastic response spectrum. The *mAMI* is still on the safe side in all cases, whereby only the base moment M_3 of the stiff edge pier P1, which is difficult to map (see previous analyses), presents an unsatisfactory exceeding of the time domain solution, while all other bending moments are well mapped.
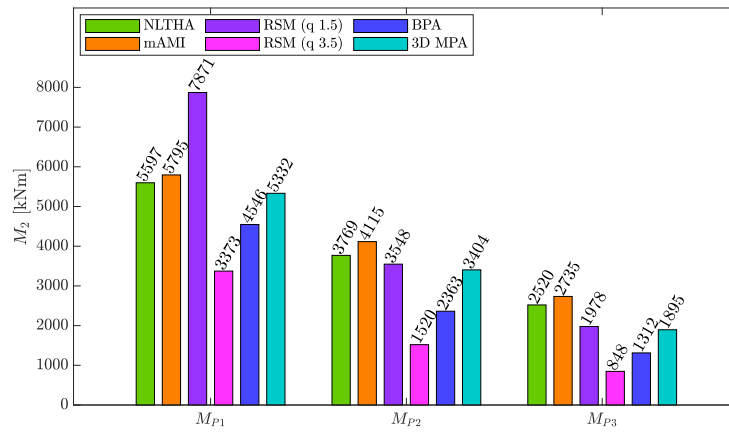
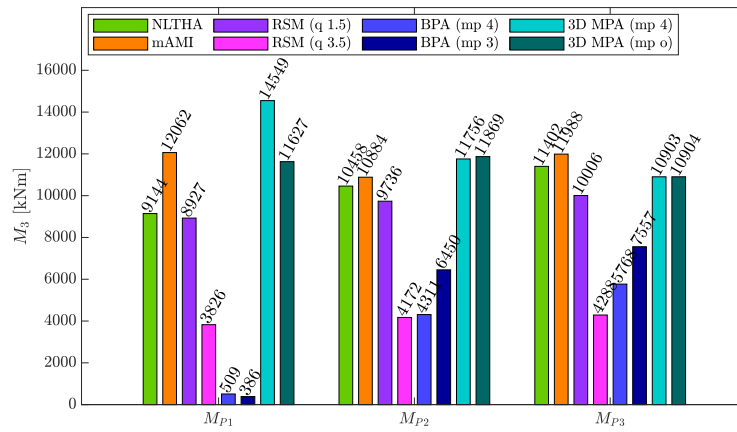**Figure 7.17:** *Pier base moments $M_2(pd = X)$, bridge model B*

Figure 7.18: *Pier base moments $M_3(pd = Y)$, bridge model B*

In contrast to model A, the *3D MPA* with both *mp* approaches sometimes leads to significantly larger errors than the *mAMI*, which in most cases are even on the unsafe side. As expected, methods with stronger simplifying assumptions (*3D MPA* compared to *mAMI*), such as the assumption of invariable mode shapes and the lack of consideration of accumulating damage of individual modal contributions, are no longer able to map an increasingly complex seismic behavior (model B compared to A) with sufficient accuracy. In case of this model, the *RSM* provides even greater deviations from the results of the nonlinear time history calculations. Only in one case ($M_{2,P1}(q = 1.5)$) the *RSM* leads to a significant exceedance of the real base moment, whereas in all other cases an undershooting of the *NLTHA* results is to be observed, partly by a large margin.

7.4.3 Procedure comparison on the basis of normal stresses (collinear)

For the nonlinear procedures, the comparison of the normal stresses in the concrete and the reinforcement is carried out separately for both models (see Figs. 7.19 & 7.20). For this purpose, the decisive normal stresses of the relevant corner fibers for all fiber hinges at the pier base points are analyzed, some of which are directly available (*NLTHA*, *BPA*) and some of which are subsequently calculated by superposition (*mAMI*, *3D MPA*). Based on the results of the previous investigation, for the *BPA* only *mp* 3 in the *Y* direction and for the *3D MPA* the optimized *mp* approach (*mp* 'o') are examined in the following. Table F.4 in Appendix F summarizes the general conditions of all calculations evaluated here.
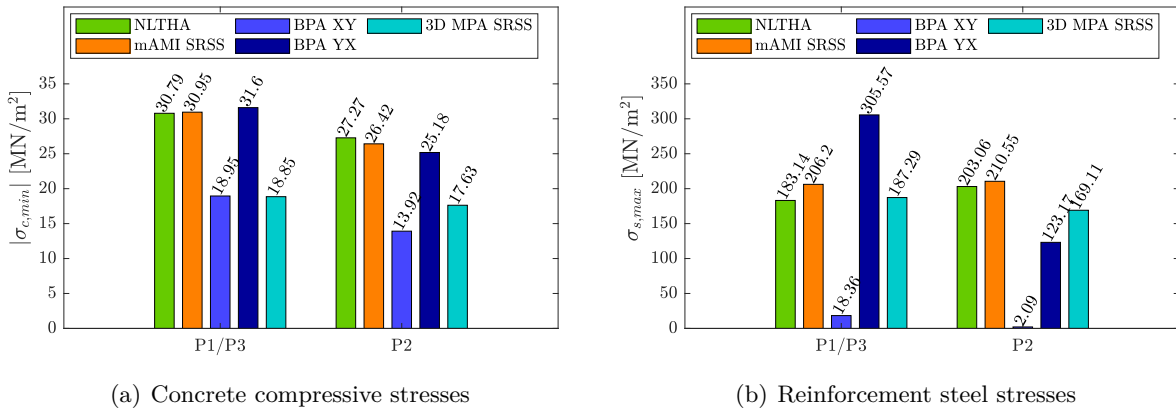
Investigation of bridge model A

(a) Concrete compressive stresses

(b) Reinforcement steel stresses

Figure 7.19: *Concrete and reinforcement steel stresses, bridge model A*

It can firstly be noted that the *mAMI* overall represents the stresses of the *NLTHA* in a satisfactory manner. With the *BPA*, the concrete compressive stresses, at least for the primary earthquake in *Y* direction, are relatively close to the time domain solution, although the moments M_3 in particular, as previously explained, massively underestimate the real bending moments. The stresses in the decisive reinforcement bars, on the other hand, are significantly overestimated in the edge piers and underestimated in the central pier. Further, it can be stated that the *3D MPA*, which led to realistic bending moments in this model, captures the steel stresses relatively well, but strongly underestimates the concrete compressive stresses. One possible explanation for the overall significantly poorer representation of the stresses in contrast to the internal forces by the *3D MPA* would be that nonlinear stress distributions are more strongly influenced by the damage accumulation of higher modes than the overall seismic behavior (e.g. restraining moments). Higher modes are taken into account in the *mAMI*, but are neglected in

the *3D MPA*. This aspect appears to be more relevant than the mutual influence of the stress components due to the orthogonal earthquake excitations, which is neglected in both methods.
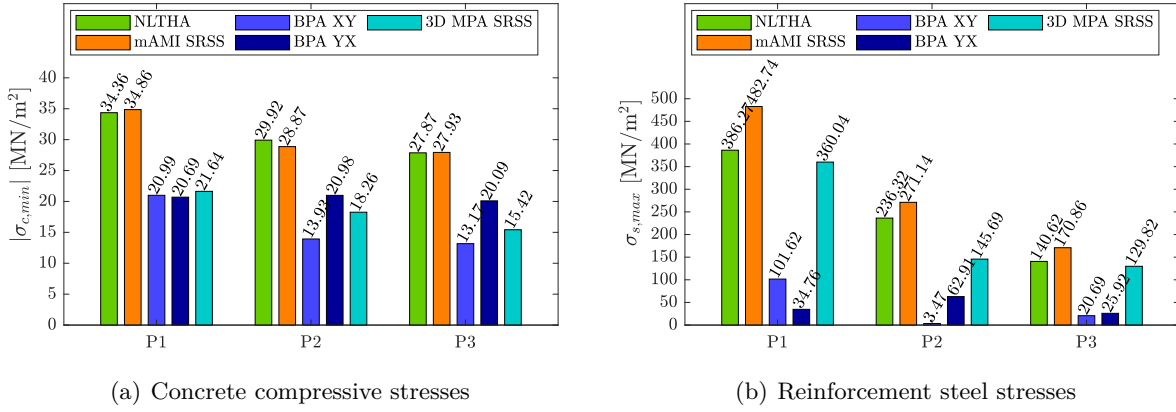
Investigation of bridge model B

(a) Concrete compressive stresses

(b) Reinforcement steel stresses

Figure 7.20: *Concrete and reinforcement steel stresses, bridge model B*

Overall, the stress results of model B show a picture very similar to model A. The concrete compressive stresses of the *mAMI* still present a very good approximation of the time history results. Only the steel stresses are now more on the safe side, sometimes to an inadequate extent as in the case of pier P1, which is difficult to model anyway (cf. evaluations of the moments). Furthermore, the *BPA* again does not lead to a remotely satisfactory result for any of the stresses investigated, where in this case all values lie on the unsafe side. In some cases, the internal seismic forces are underestimated to such an extend that the cross-sections, as a manual check in *SAP2000* showed, are nearly completely under pressure and the tensile stresses in all reinforcing bars are thus approximately 0 (the same also applies to model A). Analogous to model A, the *3D MPA* underestimates the concrete compressive stresses to a considerable extent, while the stresses in the reinforcement are also represented better, but overall still insufficiently.

7.4.4   Procedure comparison based on lateral deck displacements

Finally, the lateral deck displacements for a primary earthquake in the Y direction are compared as an example for the bridge model B with a more complex inelastic seismic behavior (see Fig. 7.21). The same calculations as in the previous analysis of normal stresses are evaluated (cf. Tab. F.5).
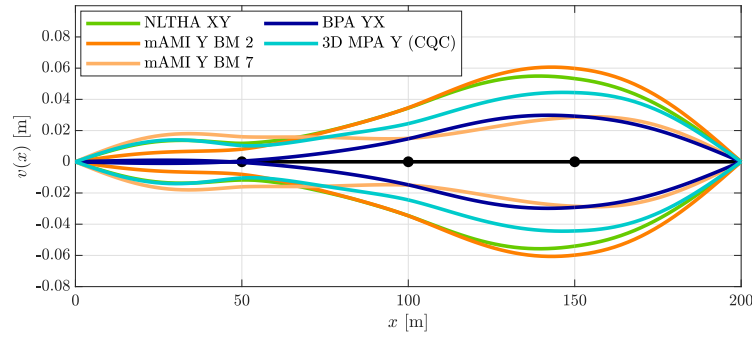
Figure 7.21: *Lateral deck displacements (pd = Y), bridge model B*

The deflection lines of the individual methods confirm the findings obtained from the previously evaluated force quantities. Again, the *mAMI* as a whole, with the two varying reference modes 2 and 7, is on the safe side at every point x and also deviates only slightly from the averaged maximum and minimum deformations of the 50 time history calculations. The *3D MPA* sometimes significantly underestimates the deformations in the middle and especially in the right part of the bridge deck, while it even shows almost exact agreement with the *NLTHA* curve in the left part. The deflection line of the *BPA*, however, is far below the real deformations at every location of the bridge deck, which, according to the previous findings in connection with the studied force variables, is due to the aforementioned effect of an overestimated ductility (and thus R_μ).

7.4.5   Conclusion

Overall, two different approaches of a multidirectional *mAMI* have been developed and reviewed. Approach 1 is based on the idea of applying the combination of directions (as in the '1.0-0.3' rule) at load level. For this purpose, an attempt was made to work out a generally valid combination factor ψ that provides satisfactory results for any evaluation variable. However, as no such factor was found, this approach must be considered a failed attempt.

Approach 2 consists of performing only monodirectional analyses, their results being combined in a suitable manner. Here, orthogonal and collinear responses are treated differently. Orthogonal quantities, such as the base shear and orthogonal bending moments, are taken without any superposition, which yields safe results. Collinear quantities, such as normal stresses, on the other hand, should be subsequently combined using the *SRSS* rule, which leads to satisfactory overall results, not least in comparison with other multidirectional nonlinear-static seismic procedures.

7.5   Final validation of the multidirectional *mAMI* concept based on the application to more complex bridge structures

7.5.1   Investigation of an in-plane curved bridge with asymmetric stiffness distribution

Similar to irregular multi-storey buildings, skewed bridges as well as curved bridges with rotated piers are structures for which the most critical seismic incident angle (*sia*) is not known in advance (see i.a. NOORI ET AL (2019) & ARAÚJO ET AL (2014)). In contrast to straight bridges, where the seismic response is governed by the transverse direction in most cases, varying directions of the orthogonal ground motion input must therefore be investigated, which is followed by the evaluation of the maximum demand for each structural member. The literature already contains specific approaches for considering varying excitation angles in the context of pushover analyses, two of which are briefly presented below.

Pushover procedures with varying *sia*
Approach by ARAÚJO ET AL (2014)
ARAÚJO ET AL (2014) present a simple method that takes into account the variation of the excitation angle, but is otherwise based on the 'standard' pushover method (acc. to EC 8). It essentially consists of the following steps:

1. Select the lateral load pattern. According to EUROCODE 8 - PART 1 (2010), two load distributions are taken into account: one load pattern uniform along the deck and the other proportional to the transversal base mode shape ($F_j = m_j \cdot \Phi_j$). Furthermore, an additional load pattern in longitudinal direction has to be defined, either also uniform or proportional to the longitudinal base mode shape.

2. Definition of the directions of analysis (e.g. 0°, 22.5°, 45°, 67.5° & 90°, cf. Fig. 7.22).

3. Determination of the individual pushover curves for the various directions of analysis and subsequent retransformation to the global axis system:
$E_{y`} = E_{Yy`} - E_{Xy`} = E_Y cos(\theta) - E_X sin(\theta)$
$E_{x`} = E_{Yx`} - E_{Xx`} = E_Y sin(\theta) - E_X cos(\theta)$.

4. For each considered direction of analysis: Determination of the seismic displacement demands by means of the *N2 method*, followed by an *SRSS* combination of both components of the individual structural responses (due to $a_{g,x`}$ & $a_{g,y`}$).
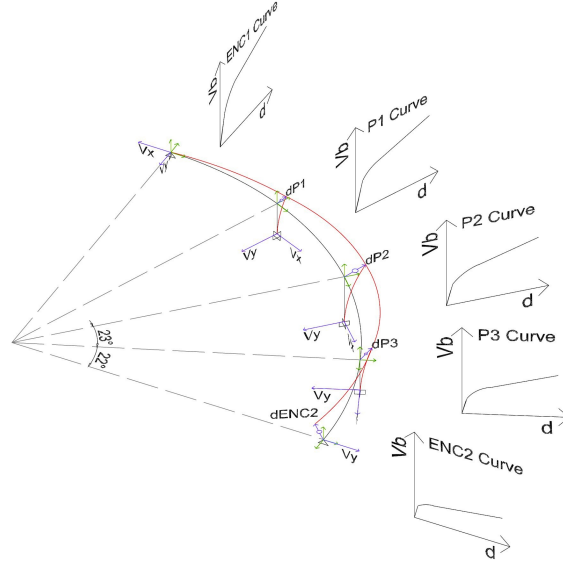
Figure 7.22: *Representative scheme of the pushover procedure proposed by* Araújo et al (2014)

Multidirectional nonlinear static procedure by Cantagallo et al (2023)

Cantagallo et al (2023) provide another method that includes a more comprehensive consideration of the most critical earthquake direction and consists of the following steps:

1. A set of pushover analyses are sequentially carried out by applying mass proportional and triangular load patterns at 24 different incident angles θ (thus with 15° increments).

2. For each θ, two pushover curves are obtained in the X and Y directions.

3. Also for each θ, the pushover curve that reaches a local maximum is selected as the reference pushover curve. If both curves contain a peak response, the one with the larger peak maximum displacement is the corresponding reference curve.

4. For each load pattern and seismic incident angle investigated, the structural demand is computed using the *N2 method*.

Although this method examines the relevance of oblique earthquake loads, it does not superimpose two simultaneously acting orthogonal components of ground motion. For each angle, the load only acts in one direction so that no bidirectional damage accumulation is considered.

Overall, apart from the consideration of different excitation angles, both methods are based on an otherwise highly simplified pushover concept according to the *N2 method*, which neither provides for the consideration of higher mode effects nor an adaptive adjustment of a mode proportional load distribution. For this reason, the methods described are not used below, as they are not sufficiently comparable with the multidirectional *mAMI* concept.

Application of the *mAMI* with varying *sia*

If the decisive excitation angle is unknown, the application of the *mAMI* requires separate calculations to be carried out for different angles of the two orthogonal excitations but, apart from this fact, to be evaluated as before. That means: no superposition is carried out for orthogonal response quantities, whereas the *SRSS* rule is used for collinear components. Finally, the maximum of all *sia*-dependent calculations must be determined for each response quantity of interest.

In the following investigations of the curved bridge studied, the entire FE model is rotated in 10° steps between 0° and 90° for the *sia* variation as part of the *mAMI* calculations in *SAP2000*, where exemplary comparative calculations with larger rotation angles showed deviations of less than 1% from the respective counterparts with $0° \leq \theta \leq 90°$. The rotation of the numerical model has the advantage that the node-related point loads can still be defined in the global X and Y directions, which considerably simplifies the algorithmic implementation. It is only important that the support conditions are related to the local, rotated coordinate systems, which is realized via mass-free and thus unloaded coupled additional nodes whose local x-axis is oriented parallel to the secant of the bridge deck. However, all other joint coordinate systems must still be referenced to the global coordinates for the automated assignment of point loads via the *CAAP* tool.

For the *NLTHAs*, however, the FE model in *SAP2000* does not have to be rotated, but the orthogonal $a_{g,X}$ and $a_{g,Y}$ time history functions are subjected to a rotation angle that corresponds to the respective *sia*. CANTAGALLO ET AL (2023), however, point out that no variation of θ for orthogonal excitations is necessary when examining a sufficient number of accelerograms. They attribute this to the fact that the random superposition of the two ground motion components in the time domain already includes a similarly random effective excitation angle. However, it is precisely this aspect that is to be confirmed again in the following investigations, so that rotated time histories are analyzed.

Investigated curved bridge structure

The calculations are performed on a bridge model that is a curved modification of the previously analyzed model B (cf. Fig. 7.23). Specifically, the deck of model B is curved with a constant radius of curvature of 260 m so that the two nodes at the abutments remain unchanged and the center node 3 at the head of pier P2 is shifted 20 m in the positive Y direction. In addition, piers P1 and P3 are rotated so that their strong cross-sectional axis is still oriented orthogonally to the bridge deck. Apart from the choice of the relevant modes, which are depicted for the case $\theta = 0°$ in Figures 7.24 and 7.25, all other parameters (earthquake intensity, calculation parameters of the *mAMI* etc.) are identical to the previous investigations.
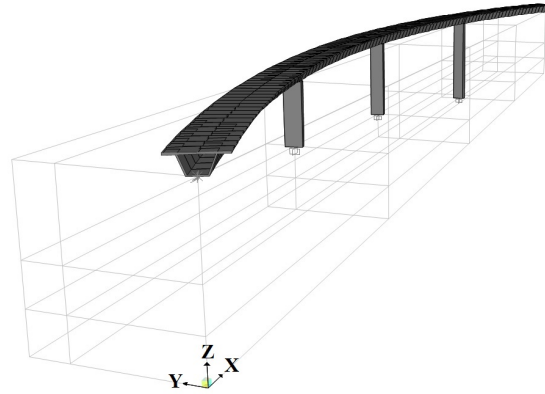
Figure 7.23: *Investigated in-plane curved bridge model*

For $\theta = 0°$, modes 2, 6 and 8 are applied in the Y direction and mode 1 in the X direction; for 90°, the exact complementary assignment applies. In the transverse direction, one calculation is carried out with mode 2 as the reference mode and the deck mass center is chosen as the mp, and another with mode 8 and the mp at the head of the pier P1. Here, the modal sign combination (-2, 6, -8) (acc. to Figs. 7.24 & 7.25) is sufficient, as even the influence of the contrary mode 6 on M_{P3} is negligible. For the intermediate states ($0° < \theta < 90°$), all four relevant modes are applied in both directions, since the effective modal masses change continuously in the global X and Y directions (cf. Fig. 7.26). Up to the bisecting angle of 45°, mode 1 is chosen as the reference mode in the X direction and modes 2 and 8 alternately in the Y direction. From 50° to 80°, the assignment is exactly reversed. This results in a total number of calculations of 30.
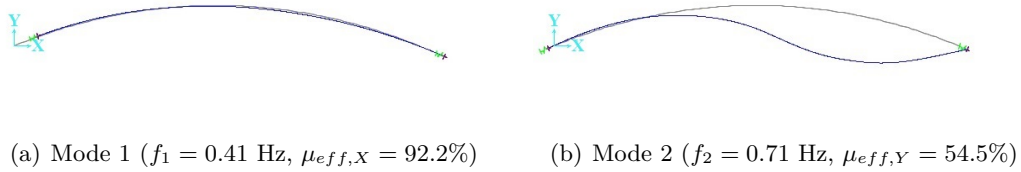

(a) Mode 1 ($f_1 = 0.41$ Hz, $\mu_{eff,X} = 92.2\%$)   (b) Mode 2 ($f_2 = 0.71$ Hz, $\mu_{eff,Y} = 54.5\%$)

Figure 7.24: *Relevant modes 1 & 2 of the curved bridge ($\theta = 0°$)*

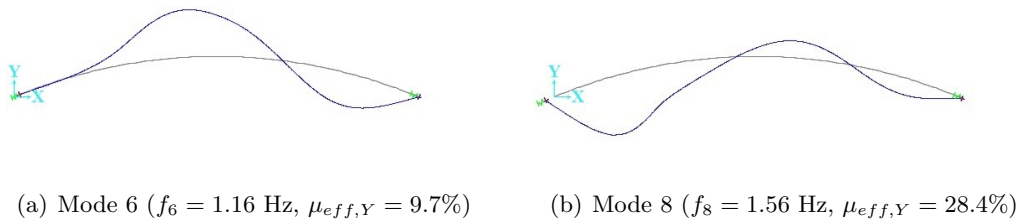(a) Mode 6 ($f_6 = 1.16$ Hz, $\mu_{eff,Y} = 9.7\%$)   (b) Mode 8 ($f_8 = 1.56$ Hz, $\mu_{eff,Y} = 28.4\%$)

Figure 7.25: *Relevant modes 6 & 8 of the curved bridge ($\theta = 0°$)*

Additional analyses, where the base mode switch was considered for angles near 45°, showed that the assumption of a 45°-switch angle was correct (REINERT , 2023). It is also important to mention that in some cases mode 6 becomes mode 5 due to an almost identical natural frequency and numerical inaccuracies as a result of the rotation of the FE model, and mode 8 sometimes becomes mode 7 for the same reason.
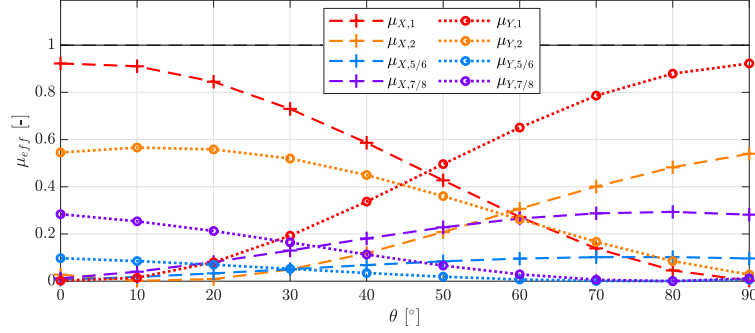

Figure 7.26: *Effective modal masses $\mu_{eff,X/Y,n}(\theta)$ - Curved bridge*

Results

Pier base moments

As already explained, the local joint coordinate systems must correspond to the respective global coordinate system for algorithmic reasons, since all point loads using the *CAAP* tool are related to global coordinates. For this reason, however, restraint nodes without any active DOF can also have rotated joint coordinate systems, as these do not receive any point loads. For the sake of simplicity, the joint coordinate systems of the three pier bases are therefore oriented so that their x-axis is parallel to the secant between the abutment points and the y-axis in the global X-Y plane is orthogonal to it and thus orthogonal to the tangent of the bridge deck at node 3. As a result, the base moments in the restraint node of P2 already correspond to the desired values, whereas the bending moments M_2 and M_3 of P1 and P3 are still related to the tangential and radial directions via a corresponding decomposition with the angle of $\Delta\gamma = \pm 11.0875°$ ($= arcsin(50/260)$) (cf. Fig. 7.27). By varying the *sia*, the respective orthogonal moments are no longer only dependent on one ground motion component, so that these are also determined via the following *SRSS* combination, taking into account the previously mentioned decompositions:

$$M_{2,Pi} = \sqrt{\begin{aligned}&(M_{y_{loc},Pi}(mAMI_{X,glob}) \cdot cos(\gamma_i) + M_{x_{loc},Pi}(mAMI_{X,glob}) \cdot sin(\gamma_i))^2 \\ &+ (M_{y_{loc},Pi}(mAMI_{Y,glob}) \cdot cos(\gamma_i) + M_{x_{loc},Pi}(mAMI_{Y,glob}) \cdot sin(\gamma_i))^2\end{aligned}} \quad (7.10)$$

$$M_{3,Pi} = \sqrt{\begin{aligned}&(M_{x_{loc},Pi}(mAMI_{X,glob}) \cdot cos(\gamma_i) + M_{y_{loc},Pi}(mAMI_{X,glob}) \cdot sin(\gamma_i))^2 \\ &+ (M_{x_{loc},Pi}(mAMI_{Y,glob}) \cdot cos(\gamma_i) + M_{y_{loc},Pi}(mAMI_{Y,glob}) \cdot sin(\gamma_i))^2\end{aligned}} \,. \quad (7.11)$$

Figure 7.27: *Local joint coordinate systems at the pier foot points*

The base moments M_2 and M_3 of the three bridge piers are shown in Figures 7.28 and 7.29, which are plotted against the seismic incident angle (*sia*) both for the bidirectional *NLTHA* and for the combined results of the *mAMI* (acc. to Eqs. 7.10 & 7.11).

(a) P1

(b) P2

Figure 7.28: *Base moments $M_{2/3}(\theta)$ - P1 & P2*

Figure 7.29: *Base moments $M_{2/3}(\theta)$ - P3*

To begin with, the assertion formulated by Cantagallo et al (2023) that different excitation angles in bidirectional time history calculations are covered by a sufficient number of time records (here: 50) is confirmed. Thus, no significant fluctuations as a function of θ are recognizable for all three bridge piers. Furthermore, similar to the previously investigated uncurved model B, the monodirectional *mAMI* for pier P1 with the third horizontal mode shape as the reference mode (mode 7 or 8) provides the largest and thus decisive seismic demand due to a transverse excitation and for the two remaining piers with the governing transverse mode (mode 2) as the reference mode.

The envelope of the *SRSS*-combined *mAMI* results with different reference modes yields the design-relevant base moments for this procedure. The results for $M_3(\theta)$ show that the excitation angles of 0° and 70° are decisive for pier P1, which is dominated by modes 1 and 8, while the excitation angle of 20° causes the greatest internal forces for piers P2 and P3, which are significantly influenced by modes 1 and 2. For column P1, whose bending moments are difficult to capture, the value is approximately 20% on the safe side, whereas for the other two piers the overestimation is much lower.

For M_2, a *sia* of 0° or 90° is decisive for P1, which only exceeds the maximum moment in the time domain by 9%. The percentage exceedance is significantly greater for the central pier with a critical excitation angle of 80°, where the absolute values are low overall, which quickly results in a large relative deviation. Finally, the largest moment M_2 of the edge pier P3 occurs again at 0°, but with a relatively small exceedance of the *NLTHA* result.

Normal stresses at the pier base points
Finally, the collinear normal stresses in the concrete and the reinforcement are examined (see Figs. 7.30 & 7.31). With regard to the maximum concrete compressive stresses, a satisfactory agreement with the time history results is shown for every pier and all excitation angles. However, there are significant fluctuations in the tensile stresses of the reinforcement, which are significant due to the larger overall values. The maximum values are significantly higher than those of the *NLHTA*, which is unacceptable for an economical seismic design.

In the time domain, when examining a sufficient number of accelerograms, it is not necessary to use the absolute maxima for design, but only the mean value of the maxima of the respective calculations. Since, as already mentioned, numerous *NLTHAs* obviously also cover different excitation angles in the bidirectional excitation case, this basic idea could also be transferred to the different *mAMI* results with varying *sia*, provided that a sufficient number of excitation angles were considered. For this reason, the arithmetic mean values of the respective *sia*-related maxima are also depicted in the three figures below.
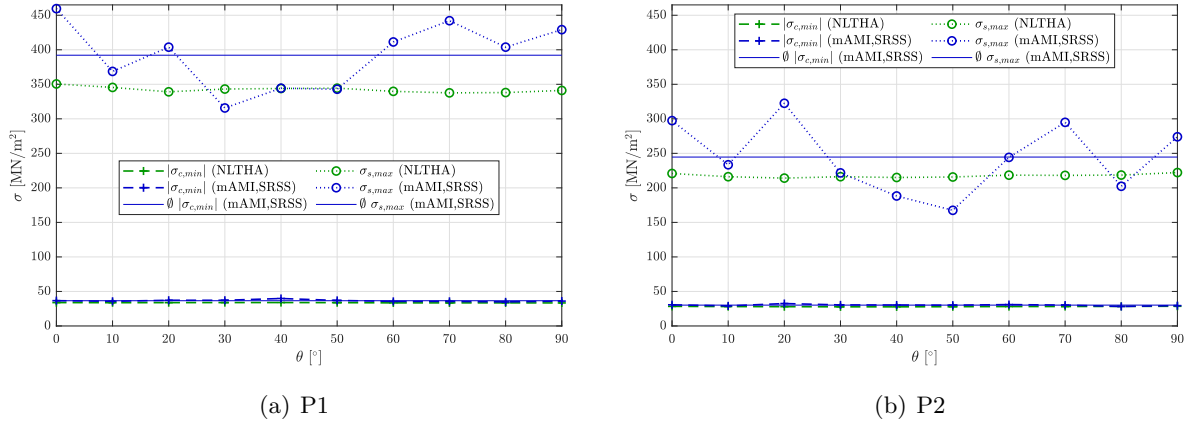
(a) P1

(b) P2

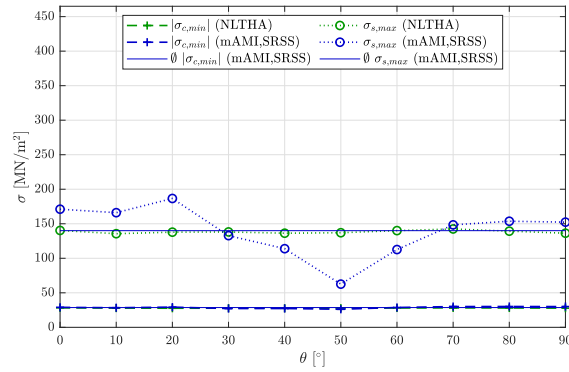**Figure 7.30:** *Normal stresses $\sigma_{c/s}(\theta)$ - P1 & P2*

Figure 7.31: *Normal stresses $\sigma_{c/s}(\theta)$ - P3*

Overall, these show considerably smaller deviations from the *NLTHA*; only in pier P1, whose nonlinear seismic behavior is difficult to model, the mean value of the steel stresses is still clearly overconservative. The same averaging scheme could also be applied to the bending moments, for example, although the deviations here were not that significant overall. However, since all values are on the safe side, this would automatically apply to the mean value as well.

For this new averaged approach, however, it would have to be verified on the basis of numerous further investigations that the mean value is also still on the safe side in each case and thus – due to the smaller deviation from the *NLTHA* solution compared to the absolute maximum – represents an improvement of the still conservative results.

Conclusion

Overall, the analyses of the bending moments lead to the conclusion that the *SRSS* combination delivers conservative results with mostly acceptable deviations from the time history solutions.

In the case of the stresses investigated, the deviations of the overall maxima are also all on the safe side, although in some cases the *NLTHA* results are enormously exceeded with regard to the steel stresses. If the mean value of the respective maxima were taken as the design basis here – analogous to the consideration of a sufficient number of ground motions in time history calculations – there would be significantly smaller deviations overall from the results in the time domain, which would still be on the safe side without exception, at least for the structure examined here. However, this is not necessarily transferable to a wide range of structure-excitation combinations and would therefore have to be verified by further comprehensive studies.

7.5.2   Investigation of a cable-stayed bridge

In the course of the final validation, the *mAMI* is applied together with an *NLTHA* to a realistic cable-stayed bridge with asymmetric stiffness distribution. Since cable-stayed bridges have a slightly different seismic behavior than the bridge structures considered so far, the performance of the *mAMI* should also be analyzed for such kind of systems. Without being able to go into the inelastic seismic behavior of cable-stayed bridges in detail at this point, only size effects due to the usually larger spans and cross-sectional dimensions and coupling effects between deck, cables, the towers and their foundation are mentioned here. For more detailed discussions, however, reference is made to VALDEBENITO & APARICIO (2006), CAMARA (2011) or CAMARA (2018), CAMARA & ASTIZ (2014) and ZHOU (2016).
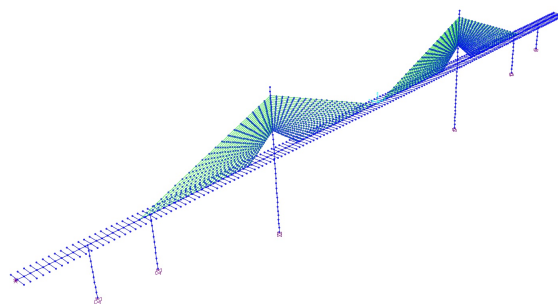
Investigated bridge structure

The investigated bridge model is an idealized model of the *Pont de Brotonne* crossing the *Seine* between *Rouen* and *Le Havre* on the north coast of France (see Fig. 7.32 (a), further detailed views and sections of the bridge construction are listed in Appendix F.3). A comprehensive preliminary investigation of the entire bridge structure with a total length of about 1278 m (cf. Fig. F.1) showed that only the main span with 320 m and the three secondary spans on both sides (with 1 x 143.5 & 2 x 58.5 m) are susceptible to vibrations. The outer spans exhibit practically no considerable vibration components. Thus, only the dynamically relevant area is mapped numerically, simplified with lateral displacement restraints at both ends of the deck (cf. Fig. 7.32 (b)). The cable forces and further details regarding the deck, pier and pylon cross-sections are taken from FREYSSINET (1976) and in particular HERZOG (1999) (Sec. 2.10). The previously mentioned idealization of the FE model mainly refers, among other details, to the highly idealized cross-sections of the two central (main) piers and pylons by means of circular approximations (with equal areas) of the actual cross-sections (cf. Fig. F.2). Due to the different pier lengths in the analyzed part of the bridge, this system also has an asymmetric stiffness distribution in the longitudinal direction. The inelastic behavior is again taken into account by arranging distributed fiber hinges along the bottom areas of all main, side and edge

piers and the two pylons. Specifically, these are placed on the lowest 10 m of the central main piers and on the lowest 5 m of the side and edge piers with a respective spacing of about 25 cm. In addition, almost the entire lower area of the pylons, which are significantly tapered in contrast to the main piers, was modeled with distributed fiber hinges with similar spacing up to the point of application of the stay cables (almost 16 m). A standard value of 5% is again used as the basic damping for this system.

Figures 7.33 to 7.38 show the relevant eigenmodes considered in the X, Y and Z directions, respectively. Since the vertical earthquake component has a minor, but not negligible influence on this structure, it is additionally considered.

(a) Brotonne bridge (picture)   (b) Numerical model in *SAP2000*

Figure 7.32: *Brotonne bridge (France): Picture[5] and FE model*
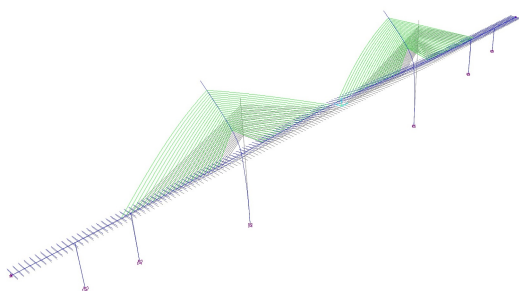
(a) Mode 1 ($f_1 = 0.26$ Hz, $\mu_{eff,Y} = 18.4\%$)   (b) Mode 3 ($f_3 = 0.42$ Hz, $\mu_{eff,Y} = 7.7\%$)
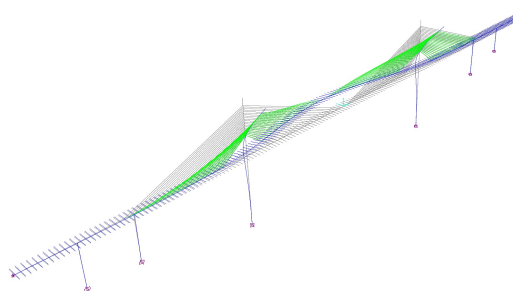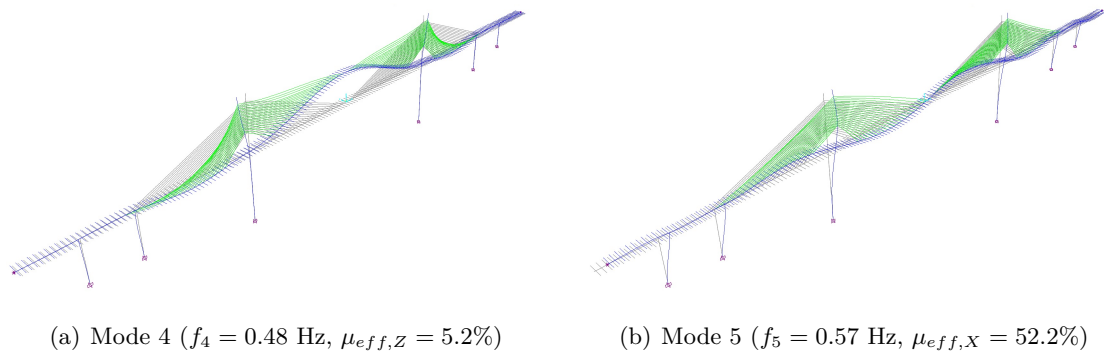
Figure 7.33: *Brotonne bridge: Relevant modes 1 & 3*

---

[5] `https://structurae.net/en/media/68926-brotonne-bridge`, call: 09/2023

(a) Mode 4 ($f_4 = 0.48$ Hz, $\mu_{eff,Z} = 5.2\%$)

(b) Mode 5 ($f_5 = 0.57$ Hz, $\mu_{eff,X} = 52.2\%$)

Figure 7.34: *Brotonne bridge: Relevant modes 4 & 5*

(a) Mode 6 ($f_6 = 0.64$ Hz, $\mu_{eff,Y} = 5.5\%$)

(b) Mode 23 ($f_{23} = 0.71$ Hz, $\mu_{eff,Y} = 3.3\%$)
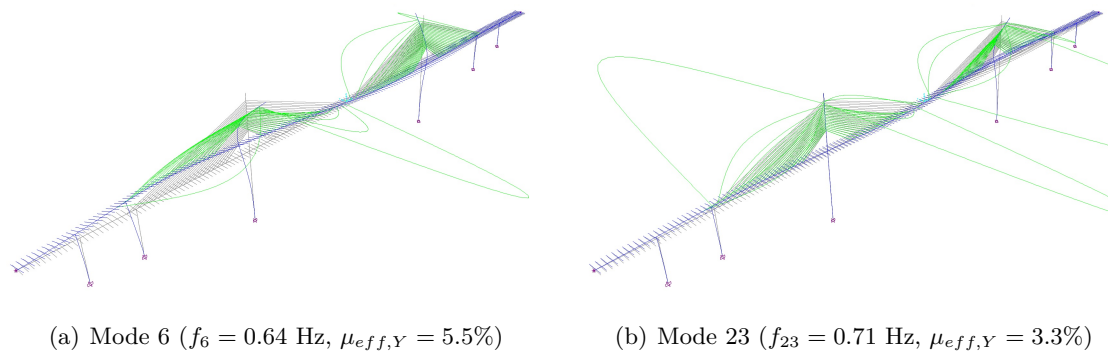
Figure 7.35: *Brotonne bridge: Relevant modes 6 & 23*

(a) Mode 31 ($f_{31} = 0.73$ Hz, $\mu_{eff,Y} = 6.0\%$)

(b) Mode 36 ($f_{36} = 0.75$ Hz, $\mu_{eff,Y} = 6.7\%$)
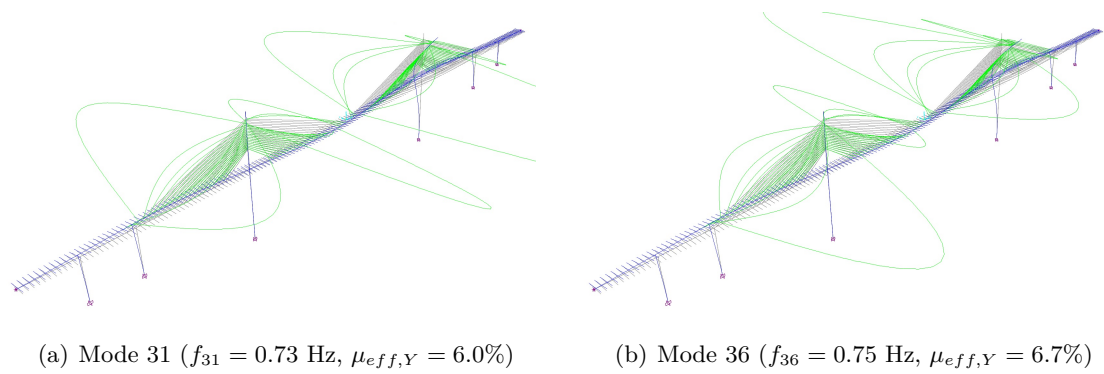
Figure 7.36: *Brotonne bridge: Relevant modes 31 & 36*

(a) Mode 40 ($f_{40} = 0.78$ Hz, $\mu_{eff,X} = 5.6\%$)   (b) Mode 48 ($f_{48} = 0.80$ Hz, $\mu_{eff,X} = 3.3\%$)
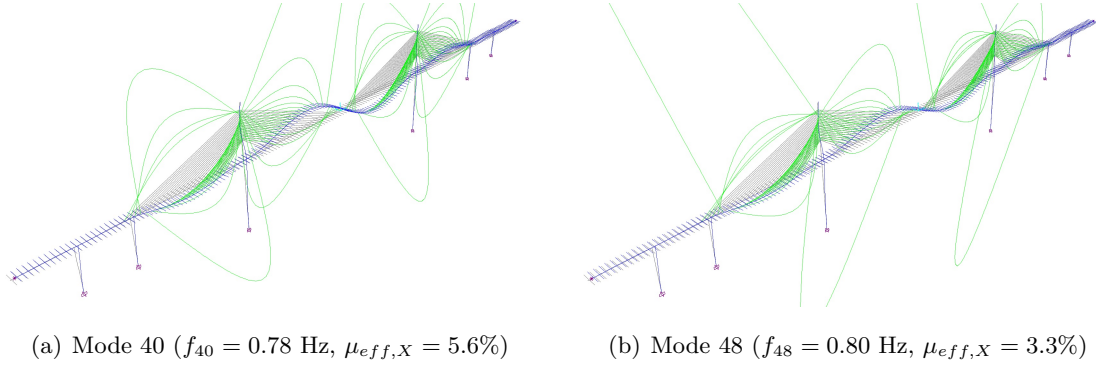
Figure 7.37: *Brotonne bridge: Relevant modes 40 & 48*
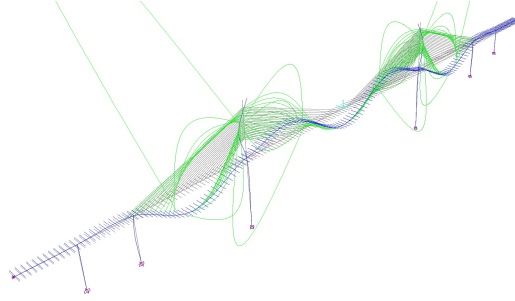
Figure 7.38: *Brotonne bridge: Relevant mode 98 ($f_{98} = 1.08$ Hz, $\mu_{eff,Z} = 3.0\%$)*

Calculations performed

In principle, the same calculations are performed as for the previously analyzed curved bridge: a multidirectional *NLHTA* as well as monodirectional *mAMI* calculations, now, however, not only for seismic excitation in the X and Y directions, but also for the vertical earthquake component. Due to the fact that in the piers and pylons of this bridge structure a seismic excitation in transverse direction also causes minor moments about the weak axis and ground motions in longitudinal direction about the strong axis, the orthogonal bending moments are determined by means of the *SRSS* rule. On the basis of comprehensive preliminary investigations with varying earthquake intensities, a_g is set to $0.3g$, which activates a significantly inelastic seismic behavior without coming close to reaching the ultimate limit state. Moreover, the vertical design excitation is set to $a_{g,z} = 0.9a_g = 0.27g$.

For the time history calculation, the Rayleigh parameters α_M and α_K are determined using the two fundamental natural frequencies in the X and Y directions (modes 5 & 1) with $\xi_1 = \xi_5 = 5\%$. Furthermore, a time increment of 0.04 s was chosen, which is lower than the limit criterion of $\Delta t < T_{min,decisive}/20$ of $T_{98}/20 = 0.046$ s in this case.

The *mAMI* calculation for seismic excitation in the longitudinal direction is based on the selection of mode 5 as reference mode and modes 40 and 48 as accompanying modes, with node 4 at the head of the left main pier as the monitoring point. In addition, two different monodirectional *mAMI* calculations are carried out for earthquake in the transverse direction of the bridge, each based on the modal contributions 1, 3, 6, 23, 31 and 36. In the first case, mode 1 is chosen as the base mode, again combined with node 4 as the *mp*. As this calculation can presumably not sufficiently activate the edge piers, which are also relevant with regard to the global inelastic seismic behavior, a second calculation is carried out with the 36th mode as the reference mode, since the corresponding mode shape has significantly larger relative deformation components in the area of the edge piers on both sides of the bridge. Node 7 at the top of the right main pier (MP2) is selected as the *mp* in this case, which is located approximately at the main peak of the reference mode (cf. 7.36 (b)). Analogous to the previously examined curved bridge, the sole consideration of the modal sign combination is also sufficient here in the transverse direction, in which all modal base shear components act in the positive Y direction. Only for MP2 and SP2 a mirrored mode 6 (acc. to Fig. 7.35 (a)) would theoretically be decisive, which is negligible however. Finally, the *mAMI* calculation for vertical seismic excitation considers modes 4 and 98, where the first is chosen as the reference mode and the deck mass center as the *mp*.

Results

In the following, the base moments of all 6 piers are depicted chronologically along the bridge deck from edge pier EP1, via side pier SP1 to main pier MP1 and vice versa for the right side. It should be noted that the local coordinate systems are oriented in such a way that M_2 now results mainly from earthquakes in the transverse direction. In each case, the result of the nonlinear three-directional time history calculation is compared with the *SRSS* combinations of the monodirectional *mAMI* calculations in the X, Y and Z directions.
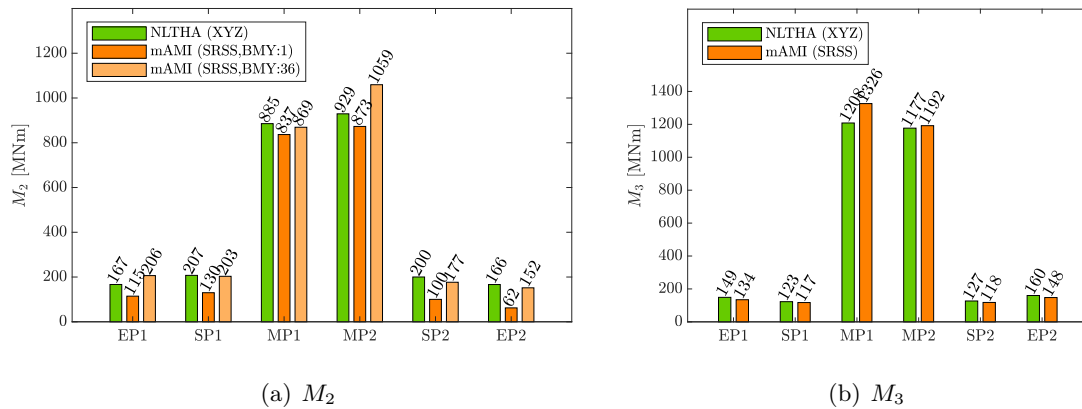

(a) M_2

(b) M_3

Figure 7.39: *Base moments $M_{2/3}$ - Cable-stayed bridge*

Overall, the moments are still relatively well captured by the *mAMI*, with only M_2 of side pier SP2 and M_3 of edge pier EP1 being slightly underestimated by 13% and 10%, respectively. With regard to the moment M_2 due to a primary transverse excitation, it is noticeable that a calculation with the first fundamental mode in the Y direction leads to an underestimation of the real responses in all piers. As expected, this applies in particular to the edge and side piers, on which mode 1 does not have much impact. However, contrary to expectations, the calculation based on the reference mode 36 also provides larger and therefore decisive moments in the main piers.

Next, analogous to the previous investigations, the maximum concrete compression and steel tensile stresses in the reinforcement at the pier bases are compared (see Fig. 7.40).
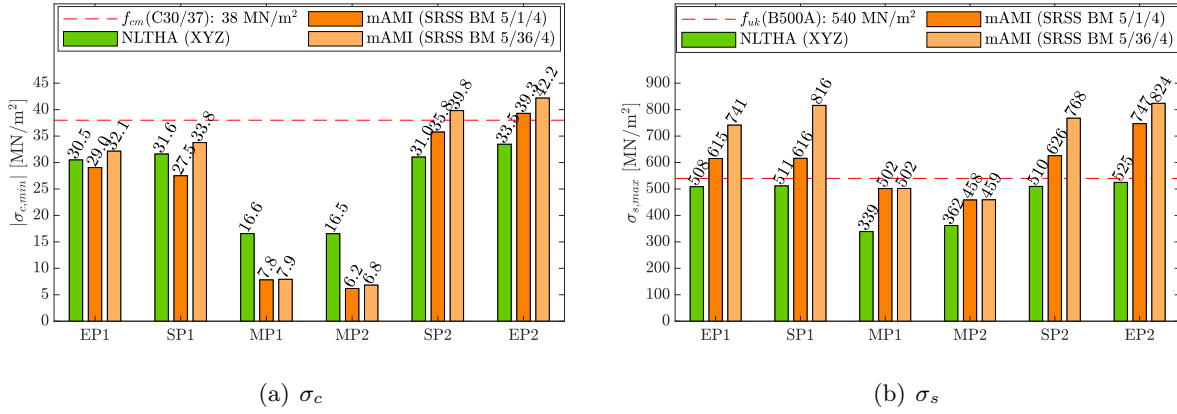

(a) σ_c \hspace{4cm} (b) σ_s

Figure 7.40: *Normal stresses $\sigma_{c/s}$ - Cable-stayed bridge*

The investigated stresses reveal the first considerable application limit of the *mAMI* method. Concerning the steel stresses, the *NLTHA* results are strongly overestimated (up to 60%) and sometimes even the characteristic tensile strength of the reinforcement is exceeded. The concrete stresses show a varied picture. While the maximum concrete compressive stresses at the base of EP1 and SP1 are fairly well met, in the main piers they are underestimated by a factor of almost 3 and in SP2 and EP2 they are overestimated by almost 30%, partly exceeding the mean compressive strength of the concrete. A more detailed analysis of the individual '*mAMI X*' and '*mAMI Y*' calculations reveals that maximum stresses are reached in certain piers that are only just below f_{cm} and f_{uk} respectively. The subsequent *SRSS* superposition thus leads to stress values in the decisive corner fibers that are significantly above the respective strength. Although the bending moments, which are primarily dominated by the respective monodirectional excitations, can still be adequately mapped, this does not apply in any way to the collinear normal stresses. Since the maximum stresses are close to the corresponding material strengths, the lack

of consideration of damage accumulation due to orthogonal earthquake excitations leads to a massive overestimation of the load-bearing capacity of the individual material points.

Furthermore, it should be noted that the normal stresses are appreciably influenced by the vertical components of the cable forces. In this context, various aspects could be named as additional reasons for this inadequate representation of the real normal stresses. One important aspect is the modal coupling as a characteristic feature of cable-stayed bridges. This means that an earthquake in longitudinal direction can itself excite vertical eigenmodes due to coupling effects (cf. CAMARA (2011), Sec. 2.2.1), which cannot be taken into account in the 'mAMI X' calculation according to the current state of development. In order to investigate this aspect in more detail, seven more precise *NLTHAs* (with a smaller step size of 0.01 s) were carried out deliberately neglecting vertical ground motions in order to detect the influence of self-induced vertical vibrations caused by a purely horizontal earthquake. For this purpose, the corresponding time histories of the normal force at the base of the main pier MP1 were transformed into the frequency domain. A higher frequency resolution could be generated due to the more precise time sampling. The corresponding *FFT* spectra (*Fast FOURIER Transformation*) are shown in Figure 7.41 (a). It is noticeable that in addition to a central peak at about 0.55-0.60 Hz, there is another significant peak at a frequency of about 1 Hz. Since earthquakes pose a broadband excitation, this could be due to natural modes 82 to 89, all of which have at least an initial natural frequency close to 1 Hz. However, a closer look at the associated modes reveals that the 85th natural mode is a pure vertical mode in which both edge spans and the main span of the bridge deck oscillate vertically in synchronization (cf. Fig. 7.41 (b)). Hence, exactly the previously described effect of a self-induced vertical oscillation by corresponding vertical components of coupling modes, excited in the X direction, could have occured with a significant effect on the normal force and thus on the normal stresses at the base of the main pier MP1. This effect is not currently represented by the *mAMI*.
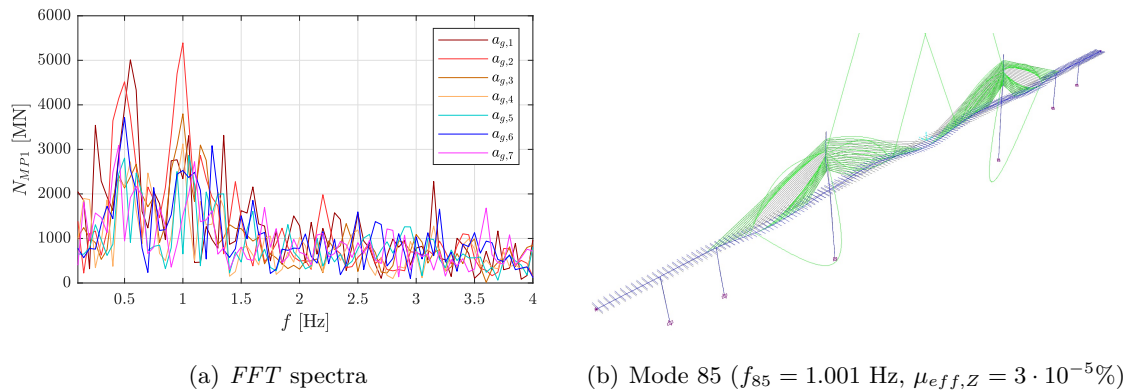

(a) *FFT* spectra

(b) Mode 85 ($f_{85} = 1.001$ Hz, $\mu_{eff,Z} = 3 \cdot 10^{-5}\%$)

Figure 7.41: *FFT spectra of $N_{MP1}(t)$ & mode 85 - Cable-stayed bridge*

Concluding remarks

Overall, it has been shown that the multidirectional *mAMI* is also capable of realistically capturing the bending moments in the piers of this complex cable-stayed bridge structure with a reasonable effort of four calculations. However, as in some previous calculations, it is necessary to identify which piers cannot be excited by the governing mode in the transverse direction and which mode should be selected as the reference mode instead.

On the other hand, the calculations also revealed that the normal stresses in the piers are completely inadequately captured here, as the monodirectional calculations already cause stress components close to the strength level and the *SRSS*-combined values would thus lead in part to a theoretical exceeding of f_{cm} or f_{uk}. If, in contrast to the previously investigated curved bridge, normal stresses occur that are in the range of the respective material strength, the subsequent superposition of the results due to orthogonal earthquake excitations will generally not provide realistic results. The background to this is that – unlike the simultaneous consideration of different modal contributions at load level – no damage accumulation can be taken into account with regard to multidirectional ground motion components. In addition, normal stresses in the piers of cable-stayed bridges are influenced by coupling effects of X and Z vibrations due to the vertical components of the cable forces. It was worked out that this could also excite vertical modes, which, however, would have no influence even in the course of the '*mAMI Z*' calculation due to an effective modal mass of almost zero (here e.g. mode 85). Rather, such modes are activated in the time domain by oblique cable forces from natural modes that are seismically excited in the longitudinal direction, which cannot currently be modeled in the course of the *mAMI*.

With regard to the computing times for this extensive numerical model, it can be stated that all 50 *NLTHAs* required a total computing time of about 37 h, although this enormous number of load cases would certainly not be used in practice. The *mAMI* calculations required 16 h in the case of the '*mAMI X*' calculation, 1.5 h plus 21.5 h in the case of the two '*mAMI Y*' calculations with reference modes 1 and 36, respectively, due to the complex load-bearing behavior and the associated large differences concerning the mode shapes in the adaption steps. The analysis of the vertical excitation, however, only required 35 minutes.

Finally, it should also be mentioned that, even more than in case of the previously analyzed curved bridge, the automated mode assignment reached its limits with this structure. As the cable vibrations (in contrast to those of the bridge deck) of the individual modes considerably changed in some cases and, in addition, some deck eigenmodes with similar mode shapes partly exhibited almost identical frequencies, certain modes could not be clearly assigned in various steps, so that this had to be done by the user.

8 Summary and outlook

8.1 Summary and conclusions

Seismic design of bridges is of great importance in many cases. Depending on the expected earthquake intensity, relatively complex earthquake calculations may be useful or even necessary to ensure a sufficient level of safety while maintaining an economical design.

In general, different concepts of varying complexity are available for seismic analyses of structures. For example, nonlinear time history calculations can be carried out. These are generally classified as demanding and time as well as memory intensive and are also characterized by a laborious post-processing, essentially complicating the evaluation and interpretation of the results. In contrast, there are various static approaches, which are divided into linear and nonlinear concepts. While the strong simplifications of the linear *Response Spectrum Method* (*RSM*) are not justified in some cases, there are numerous generally more accurate nonlinear procedures with varying degrees of simplification. However, even with relatively complex approaches, the vast majority of methods is still based on significantly simplifying assumptions, which in some cases lead to considerable limitations. The *Adaptive Multimodal Interaction Analysis* (*AMI*) by Norda (2012) is considered here as the best available option. Its advantages are a continuous adaption of the load distribution plus continuous updates of the spectral demand values and, in particular, a simultaneous combination of the modal contributions at load level. The latter aspect even allows a damage accumulation of the relevant modes, which can be quite significant in case of a pronounced inelastic behavior.

Nevertheless, the following weaknesses of the *AMI* were identified in this PhD dissertation:

1. The *AMI* does not include an initial calculation for dead loads under consideration of P-Delta effects.

2. The determination of the maximum modal spectral displacements or accelerations is based on an unnecessary simplification: the extrapolation of the elastic branch of the idealized capacity curve and the subsequent application of the *equal displacement rule.*

3. The determination of the incremental load vector is initially based on joint displacements, which must be determined via pseudo-displacement spectra and then converted into nodal loads via the tangent stiffness relationchip.

4. In most cases, the use of constant spectral increments of the base mode leads to a considerable number of superfluous, time-consuming adaption steps that are not accompanied by any noticeable system changes.

5. The modal load combination is based on the assumption of fully correlated modes, which cannot be accurately corrected by introducing an additional modal participation factor.

As part of this PhD dissertation, the *AMI* was therefore optimized and extended to eliminate the existing deficits (*modified AMI*: *mAMI*). The focus of these adjustments was, among other aspects, the accumulation of damage from different modal components while simultaneously taking into account a realistic correlation via correlation factors $\alpha_n^{(i)}$ as well as a reasonable combination of multidirectional earthquake excitations. While the introduction of the $\alpha_n^{(i)}$ factors led to a significant improvement in the results overall, the parameter study on differently weighted directional linear combinations showed that the previous multidirectional approach of the *AMI* at load level is unreliable even if the combination factor is generalized. An alternative superposition concept was therefore developed, separately for orthogonal and collinear response quantities. Furthermore, the method was adapted so that no constant spectral increments of the reference mode are assumed. Instead, individual adaption steps of the *mAMI* are always related to the occurrence of new relevant plastic effects, which significantly reduces the required number of steps and thus the numerical effort. In addition, the *AMI* concept was supplemented by an initial calculation of the dead loads, taking into account P-Delta effects. The load approach was adapted so that inertia forces are now determined directly from spectral accelerations. In contrast to NORDA (2012), these spectral values are calculated via a more precise tangential extrapolation of the current idealized capacity spectrum.

A self-developed algorithm (*Complete Automated Adaptive Pushover*: *CAAP*) enables the fully automated application of the *mAMI* using the FE calculation kernel of *SAP2000*. The source code has been put into public domain for further communication exchange in earthquake engineering science.

Corresponding mono- and multidirectional earthquake investigations of various bridge structures finally provided the following central conclusions:

- The *mAMI* is able to consider higher mode effects combined with a realistic assessment of the intermodal correlation. It updates mode proportional load patterns as well as maximum spectral target accelerations based on the current inelastic system properties.

- It requires only a few adaption steps due to the automated identification of relevant plastic effects.

- The signs of the considered modes should be varied at least to the extent that the relevant combinations for the maximum loading of all structural members and response quantities of interest are taken into account.

- All relevant members (in terms of the inelastic seismic behavior) should be activated by a selected reference mode.

- In case of multidirectional seismic excitation, orthogonal response components (e.g. bending moments) can be conservatively evaluated from monodirectional analyses with mostly justifiable inaccuracies, while collinear response quantities (e.g. normal stresses) have to be subsequently combined by means of the *SRSS* rule.

Under these basic conditions, displacements and force variables could overall be satisfactorily determined, even in case of complex inelastic seismic behavior (e.g. asymmetric pier lengths, curved or cable-stayed-bridges,...). Exceptions to this are mainly the responses of stiff (short) bridge piers in combination with an asymmetric stiffness distribution. Furthermore, also normal stresses could be calculated with sufficient accuracy in most cases. Only in the case of the cable-stayed bridge investigated, where the maximum stresses were in the range of the material strengths, the subsequent *SRSS* combination of directional components had to be classified as inaccurate. In addition to the neglection of modal couplings by the stay cables, possibly leading to self-induced vertical modes, this represents the only content-related application limit of the *mAMI* that has been identified within the scope of this PhD dissertation.

Overall, the *mAMI* can therefore be used as a special form of the pushover calculations permitted in common standards for earthquake design, e.g. applied to bridge structures. In particular, it provides a comprehensive picture of the inelastic load-bearing behavior in the event of an earthquake, allowing the structure to be evaluated more precisely and possibly optimized in this respect. Due to the previously described adjustments, the *mAMI* fundamentally represents an improvement on existing static methods for seismic analyses of complex structures. In most cases, the calculation effort for this method is manageable due to the exclusive consideration of only a few relevant modal load combinations with varying base modes or modal signs.

8.2   Outlook: Further need for research

During the development of the *mAMI* and the *CAAP* algorithm and in the analyses carried out, two essential aspects were neglected, as they would have gone beyond the scope of this PhD dissertation: varying ground motions at different pier base points for long-span bridges and soil-structure interaction (*SSI*) effects. In this regard, further research is needed to investigate how these two effects can be accurately considered within the framework of the *mAMI* with reasonable modeling and numerical effort.

In the calculations carried out, an asymmetric stiffness distribution as a rule led to the requirement of including different reference modes for a specific earthquake direction with the associated selection of suitable monitoring points. This was the only way to determine the correct bending moments in all bridge piers. Although in this context the mere variation of the monitoring points has generally not shown any major effects, it is conceivable that relevant plastic effects may not all be identified by a single *mp* for a fixed reference mode. If this unlikely, but not completely ruled out, special case should occur, the analysis of the pushover curve would have to be extended so that, for example, two pushover curves are evaluated for different monitoring points, whereby the smaller base shear increment of the two would then be decisive.

Furthermore, as part of the investigation of the in-plane curved bridge with an a priori unknown critical seismic incident angle (*sia*), it was worked out that averaged maximum values of the *sia*-dependent normal stresses would represent more economical, but still conservative results of the design stresses. The idea behind this averaging scheme came from the fact that a sufficiently large number of time histories encompasses the variation of the *sia*. Then an averaging of the *mAMI* results over all *sia* should be equivalent to the averaged time history solution, provided the number of angles considered is sufficiently high. However, it has already been explicitly pointed out that this cannot be classified as valid on the basis of the available results alone and must therefore be confirmed by further comprehensive studies on systems with an unknown critical direction of ground motion.

In the case of the investigated cable-stayed bridge, it has been shown that the normal stresses calculated using the *mAMI*, which lie in the range of the material strengths, show unacceptably large deviations from the *NLTHA* results. A further step here could be to analyze how the results improve for a lower earthquake intensity, thus leading to reduced stresses. In the evaluations carried out, it was also determined that an additional problem could lie in self-induced vertical modes that have not yet been taken into account. A corresponding consideration of this effect within the *mAMI* would thus have to be developed theoretically and then validated in comprehensive studies.

Finally, the $CAAP$ algorithm reached its limits with regard to mode identification in case of the curved bridge and especially the cable-stayed bridge. It is true that no incorrect assignments were made in these investigations either. However, the algorithm was unable to automatically identify and thus assign mode shapes with sufficient certainty in various cases, which resulted in numerous necessary user inputs. For the convenient $mAMI$ calculation of such bridge structures, the $CAAP$ tool would therefore have to be extended by several more detailed checks, which would also enable reliable assignments in the case of more complex mode changes.

Bibliography

ACHARJYA, A., ROY, R. (2023)

Estimating seismic response to bidirectional excitation per unidirectional analysis: A reevaluation for motions with fling-step using SDOF systems, Soil Dynamics and Earthquake Engineering, Vol. 164, No. 2, 1-21, 2023

ADHIKARI, G., PETRINI, L., CALVI, G. M. (2008)

Is direct displacement based design valid for long span bridges?, Proceedings of the 14th World Conference on Earthquake Engineering, Beijing (China), October 12-17, 2008

ADHIKARI, G., PETRINI, L., CALVI, G. M. (2010)

Application of direct displacement based design to long span bridges, Bulletin of Earthquake Engineering, Vol. 8, No. 4, 897-919, 2010

ALBANESI, T., BIONDI, S., PETRANGELI, M. (2002)

Pushover analysis: An energy based approach, Proceedings of the 12th European Conference on Earthquake Engineering, London (UK), September 9-13, 2002

ALLEMANG, R. J., BROWN, D. L. (1982)

A Correlation Coefficient for Modal Vector Analysis, Proceedings of the 1st International Modal Analysis Conference, Orlando (USA), November 8-10, 1982

ANTONIOU, S., PINHO, R. (2004A)

Advantages and Limitations of adaptive and non-adaptive Force-based Pushover Procedures, Journal of Earthquake Engineering, Vol. 8, No. 4, 497-522, 2004

ANTONIOU, S., PINHO, R. (2004B)

Development and Verification of a Displacement-based adaptive Pushover Procedure, Journal of Earthquake Engineering, Vol. 8, No. 5, 643-661, 2004

ARAÚJO, M., MARQUES, M., DELGADO, R. (2014)

Multidirectional pushover analysis for seismic assessment of irregular-in-plan bridges, Engineering Structures, Vol. 79, 375-389, 2014

ASSARZADEH, H. (2016)
Displacement-based seismic design of concrete continue bridges, International Journal of Bridge Engineering, Vol. 4, No. 2, 29-44, 2016

ATC-40 (1996)
Seismic Evaluation and Retrofit of Concrete Buildings, Applied Technology Council, Vol. 1, 1996

AYDINOGLU, N. (2003)
An Incremental Response Spectrum Analysis Procedure Based on Inelastic Spectral Displacement for Multi-Mode Seismic Performance Evaluation, Bulletin of Earthquake Engineering, Vol. 1, No. 1, 3-36, 2003

AZIMINEJAD, A., ZARE, M., MOGHADAM, A. S. (2014)
Improvement of adaptive pushover procedure in performance assessment of steel structures, Proceedings of the 2nd European Conference on Earthquake Engineering and Seismology, Istanbul (Turkey), August 25-29, 2014

BERGAMI, A. V., NUTI, C., LAVAROTO, D., FIORENTINO, G., BRISEGHELLA, B. (2020)
IMPAβ: Incremental Modal Pushover Analysis for Bridges, Applied Sciences, Vol. 10, No. 12, 4287, 2020

BRACCI, J. M., KUNNATH, S. K., REINHORN, A. M. (1997)
Seismic performance and retrofit evaluation of reinforced concrete structures, Journal of Structural Engineering, Vol. 123, No. 1, 3-10, 1997

BURTON, H. V., DOORANDISH, N., SHOKRABADI, M. (2018)
Probabilistic evaluation of combination rules for seismic force demands from orthogonal ground motion components, Engineering Structures, Vol. 177, No. 15, 234-243, 2018

CALVI, G. M., KINGSLEY, G. R. (1995)
Displacement-based seismic design of multi-degree-of-freedom bridge structures, Earthquake Engineering and Structural Dynamics, Vol. 24, No. 9, 1247-1266, 1995

CALVI, G. M., PRIESTLEY, M. J. N. (2007)
Design and Assessment of Bridges, In: Pecker, A. (eds) Advanced Earthquake Engineering Analysis, CISM International Centre for Mechanical Sciences, Vol. 494, Springer, Vienna (Austria), 2007

CALVI, G. M., PRIESTLEY, M. J. N., KOWALSKY, M. J. (2013)
Displacement-Based Seismic Design of Bridges, Structural Engineering International, Vol. 23, No. 2, 112-121, 2013

CAMARA, A. (2011)

Seismic Behaviour of Cable-Stayed Bridges: Design, Analysis and Seismic Devices, PhD dissertation, Universidad Politécnica de Madrid (Spain), 2011

CAMARA, A. (2018)

Seismic behavior of cable–stayed bridges: a review, MOJ Civil Engineering, Vol. 4, No. 3, 161-169, 2018

CAMARA, A., ASTIZ, M. A. (2012)

Pushover analysis for the seismic response prediction of cable-stayed bridges under multi-directional excitation, Engineering Structures, Vol. 41, 444-455, 2012

CAMARA, A., ASTIZ, M. A. (2014)

Analysis and control of cable-stayed bridges subjected to seismic action, Structural Engineering International, Vol. 24, No. 1, 27-36, 2014

CANTAGALLO, C., PELLEGRINI, F. A., SPACONE, E., CAMATA, G. (2022)

Multidirectional Lateral Loads and Combination Rules in Pushover Analysis, Seismic Behaviour and Design of Irregular and Complex Civil Structures IV. Geotechnical, Geological and Earthquake Engineering, Vol. 50, 249–259, 2022

CANTAGALLO, C., TERRENZI, M.;,SPACONE, E., CAMATA, G. (2023)

Effects of Multi-Directional Seismic Input on Non-Linear Static Analysis of Existing Reinforced Concrete Structures, buildings, Vol. 13, No. 7, 1656, 2023

CARVALHO, G., BENTO, R., BHATT, C. (2013)

Nonlinear static and dynamic analyses of reinforced concrete buildings – comparison of different modelling approaches, buildings, Vol. 4, No. 5, 451-470, 2013

CATACOLI, S. S. (2014)

Displacement demands for performance based design of skewed bridges with seat type abutments, PhD dissertation, University of British Columbia (Canada), 2014

CHIOREAN, C. G. (2003)

Application of Pushover Analysis on Reinforced Concrete Bridge Model, Part I - Numerical Models, Technical Report (PROJECT POCTI/36019/99), Cluj-Napoca (Romania), 2003

CHIOU, J. S., YANG, H. H., CHEN, C. H. (2008)

Plastic hinge setting for nonlinear pushover analysis of pile foundations, Proceedings of the 14th World Conference on Earthquake Engineering, Beijing (China), October 12-17, 2008

Chopra, A. K., Goel, R. K. (2002)

A modal pushover analysis procedure for estimating seismic demands for buildings, Earthquake Engineering and Structural Dynamics, Vol. 31, No. 3, 561-582, 2002

Chopra, A. K., Goel, R. K. (2004)

A modal pushover analysis procedure to estimate seismic demands for unsymmetric-plan buildings, Earthquake Engineering and Structural Dynamics, Vol. 33, No. 8, 903–927, 2004

Cimellaro, G. P., Giovine, T., Lopez-Garcia, D. (2014)

Bidirectional Pushover Analysis of Irregular Structures, Journal of Structural Engineering, Vol. 140, No. 9, 04014059, 2014

COMPUTERS & STRUCTURES, INC. (2016)

CSi Analysis Reference Manual – For SAP2000, ETABS, SAFE and CSiBridge, 2016

Dhakal, R. P., Mander, J. B., Mashiko, N. (2007)

Bidirectional Pseudodynamic Tests of Bridge Piers Designed to Different Standards, Journal of Bridge Engineering, Vol. 12, No. 3, 284-295, 2007

DIN EN 1998-1/NA:2021-07

German National Annex (G.N.A.) – Nationally defined parameters – Eurocode 8: Design of structures for earthquake resistance – Part 1: General rules, seismic actions and rules for buildings, DIN: Berlin (Germany), 2021

Dowell, R. K., Seible, F., Wilson, E. L. (1998)

Pivot Hysteresis Model for Reinforced Concrete Members, ACI Structural Journal, Vol. 95, No. 5, 607-617, 1998

Dwairi, H., Kowalsky, M. (2006)

Implementation of Inelastic Displacement Patterns in Direct Displacement-Based Design of Continuous Bridge Structures, Earthquake Spectra, Vol. 22, No. 3, 631–662, 2006

EN 1990:2010-12

Eurocode 0: Basis of structural design, CEN: Brussels (Belgium), 2010

EN 1992-1-1:2011-01

Eurocode 2: Design of concrete structures – Part 1-1: General rules and rules for buildings, CEN: Brussels (Belgium), 2011

EN 1998-1:2010-12

Eurocode 8: Design of structures for earthquake resistance – Part 1: General rules, seismic actions and rules for buildings, CEN: Brussels (Belgium), 2010

EN 1998-2:2011-12

Eurocode 8: Design of structures for earthquake resistance – Part 2: Bridges, CEN: Brussels (Belgium), 2011

FAJFAR, P. (2000)

A nonlinear analysis method for performance based seismic design, Earthquake Spectra, Vol. 16, No. 3, 573-592, 2000

FEMA 356 (2000)

Prestandard and Commentary for the seismic rehabilitation of buildings, American Society of Civil Engineers (ASCE), Reston (USA), 2000

FIB MODEL CODE FOR CONCRETE 2010

Model Code for Concrete for Concrete Structures, Ernst & Sohn, Berlin (Germany), 2010

FISCHINGER, M., ISAKOVIC, T. (2003)

Inelastic Seismic Analysis of Reinforced Concrete Viaducts, Structural Engineering International, Vol. 13, No. 2, 111-118, 2003

FREEMAN, S. A. (1998)

Development and use of capacity spectrum method, Proceedings of the 6th U.S. National Conference on Earthquake Engineering, Seattle (USA), May 31-June 4, 1998

FREEMAN, S. A., NICOLETTI, J. P., TYRRELL, J. V. (1975)

Evaluation of existing buildings for seismic risk, Proceedings of the 1st U.S. National Conference on Earthquake Engineering, Ann Arbor (USA), June 18, 1975

FREYSSINET INTERNATIONAL (1976)

Brotonne Bridge, Technical Report FI.1013A/08.76, Freyssinet International, 1976

FUJII, K. (2014)

Prediction of the largest peak nonlinear seismic response of asymmetric buildings under bidirectional excitation using pushover analyses, Bulletin of Earthquake Engineering, Vol. 12, No. 2, 909-938, 2014

FUJII, K. (2020)

Modified mode-adaptive bi-directional pushover analysis considering higher mode for asymmetric buildings, Seismic Behaviour and Design of Irregular and Complex Civil Structures III, Springer, ISBN: 978-3-030-33531-1, 83-95, 2020

GASPARINI, D. A., VANMARCKE, E. H. (1976)

Simulated Earthquake Motions Compatible with Prescribed Response Spectra, MIT Civil Engineering, Research Report R76-4, Massachussets Institute of Technology, Cambridge (UK), 1976

GUPTA, B., KUNNATH, S. K. (2000)

Adaptive spectra-based pushover procedure for seismic evaluation of structures, Earthquake Spectra, Vol. 16, No. 2, 367–391, 2000

HERZOG, M. A. M. (1999)

Elementare Berechnung von Seilbrücken: Geschichte, Statik, Schwingungen, Werner, ISBN: 3-8041-2083-0, Sec. 2.10, 16-28, 1999

HILBER, H. M., HUGHES, T. J. R., TAYLOR, R. L. (1977)

Improved numerical dissipation for time integration algorithms in structural dynamics, Earthquake Engineering and Structural Dynamics, Vol. 5, No. 3, 283-292, 1977

HOLTSCHOPPEN, B. (2009)

Beitrag zur Auslegung von Industrieanlagen auf seismische Belastungen, PhD dissertation, RWTH Aachen University (Germany), 2009

HUSSAIN, M. A., DUTTA, S. C. (2020)

Inelastic seismic behavior of asymmetric structures under bidirectional ground motion: An effort to incorporate the effect of bidirectional interaction in load resisting elements, Structures, Vol. 25, 241-255, 2020

HUSSAIN, M. A., DUTTA, S. C., DAS, S. (2022)

Effect of bidirectional ground shaking on structures in the elastic and post-elastic range: Adequacy of design provisions, Journal of Building Engineering, Vol. 45, 103656, 2022

ISAKOVIC, T., FISCHINGER, M. (2014)

Seismic Analysis and Design of Bridges with an Emphasis to Eurocode Standards, Geotechnical, Geological and Earthquake Engineering, Vol. 34, No. 6, 195-225, 2014

ISAKOVIC, T., FISCHINGER, M. (2011)

Applicability of Pushover Methods to the Seismic Analyses of an RC Bridge, Experimentally Tested on Three Shake Tables, Journal of Earthquake Engineering, Vol. 15, No. 2, 303-320, 2011

ISAKOVIC, T., FISCHINGER, M., KANTE, P. (2003)

Bridges: when is single mode seismic analysis adequate?, Structures & Buildings, Vol. 156, No. 2, 165-173, 2003

KÄMPER, D. M., OSTERKAMP, M. (2024)

CAAP (Complete Automated Adaptive Pushover) – Users Manual, `https://github.com/DMKaemper/CAAP-Complete-Automated-Adaptive-Pushover-`, University of Wuppertal (Germany), 2024

KALKAN, E., KUNNATH, S. K. (2004)

Method of modal combinations for pushover analysis of buildings, Proceedings of the 13th World Conference on Earthquake Engineering, Vancouver (Canada), August 1-6, 2004

KALKAN, E., KUNNATH, S. K. (2006)

Adaptive modal combination procedure for nonlinear static analysis of building structures, Journal of Structural Engineering, Vol. 132, No. 11, 1721-1731, 2006

KAPPOS, A. J. (2015)

Performance-Based Seismic Design and Assessment of Bridges, Perspectives on European Earthquake Engineering and Seismology, Vol. 2, No. 7, 163-205, 2015

KAPPOS, A. J., GOUTZIKA, E. D., STEFANIDOU, S. P., SEXTOS, A. G. (2011)

Problems in Pushover Analysis of Bridges Sensitive to Torsion, Computational Methods in Earthquake Engineering, Springer, ISBN: 978-94-007-0053-6, 99-122, 2011

KAPPOS, A. J., PARASKEVA T. S., SEXTOS, A. G. (2005)

Modal pushover analysis as a means for the seismic assessment of bridge structures, Proceedings of the 4th European Workshop on the Seismic Behaviour of Irregular and Complex Structures, Thessaloniki (Greece), August 26-27, 2005

KAPPOS, A. J., SAIIDI, M. S., AYDINOGLU, M. N., ISAKOVIC, T. (2012)

Seismic Design and Assessment of Bridges – Inelastic Methods of Analysis and Case Studies, Springer, ISBN: 978-94-007-3942-0, 2012

KHALED, A., MASSICOTTE, B., TREMBLAY, R. (2010)

Seismic Behaviour of Rectangular R/C Bridge Columns under Bidirectional Earthquake Components, Proceedings of the 9th U.S. National and 10th Canadian Conference on Earthquake Engineering, Toronto (Canada), July 25-29, 2010

KHAN, E., SULLIVAN, T. J., KOWALSKY, M. J. (2014)

Direct Displacement–Based Seismic Design of Reinforced Concrete Arch Bridges, Journal of Bridge Engineering, Vol. 19, No. 1, 44-58, 2014

KOWALSKY, M. J. (2002)

A displacement-based approach for the seismic design of continuous concrete bridges, Earthquake Engineering and Structural Dynamics, Vol. 31, No. 3, 719–747, 2002

KRAWINKLER, H., SENEVIRATNA, G. D. P. K. (1998)

Pros and cons of a pushover analysis of seismic performance evaluation, Engineering Structures, Vol. 20, Nos. 4-6, 452-464, 1998

LEFORT, T. (2000)

Advanced pushover analysis of RC multi-storey buildings, MSc dissertation, Imperial College London (UK), 2000

MARJANOVIC, M., PETRONIJEVIC, M. (2018)

Pushover analysis of bridges including soil-strcuture interaction effects, Inproceedings, ASES - Association of Structural Engineers of Serbia, 2018

MESKOURIS, K., HINZEN, K-G., BUTENWEG, C., MISTLER, M. (2011)

Bauwerke und Erdbeben, Vieweg und Teubner, 3. Aufl., ISBN: 978-3-8348-0779-3, 2011

MOGHADAM, A. S., TSO, W. K. (2002)

A puhover procedure for tall buildings, Proceedings of the 12th European Conference on Earthquake Engineering, London (UK), September 9-13, 2002

NEWMARK, N. M., ROSENBLUETH, E. (1971)

Fundamentals of Earthquake Engineering, Prentice-Hall: Hoboken, ISBN: 978-0-1333-6206-0, New Jersey (USA), 1971

NEWMARK, N. M. (1975)

Seismic design criteria for structures and facilities, Trans-Alaska pipeline system, Proceedings of the U.S. National Conference on Earthquake Engineering (pp. 94-103), Michigan (USA), 1975

NGO-HUU, C., KIM, S.-E. (2012)

Practical nonlinear analysis of steel-concrete composite frames using fiber-hinge method, Journal of Constructional Steel Research, Vol. 74, 90-97, 2012

NOORI, H. R., MEMARPOUR, M. M., YAKHCHALIAN, M., SOLTANIEH, S. (2019)

Effects of ground motion directionality on seismic behavior of skewed bridges considering SSI, Soil Dynamics and Earthquake Engineering, Vol. 127, 105820, 2019

NORDA, H. (2012)

Beitrag zum statischen nichtlinearen Erdbebennachweis von unbewehrten Mauerwerksbauten unter Berücksichtigung einer und höherer Modalformen, PhD dissertation, RWTH Aachen University (Germany), 2012

PAOLACCI F., GIANNINI R., ALESSANDRI S., DI SARNO L., ERDIK M., YENIDOGAN C. (2013)
Pseudo-dynamic test of an old R.C. highway bridge with plain steel bars - part I: Assessment of the "as-built" configuration, 2nd Conference on Smart Monitoring, Assessment and Rehabilitation of Civil Structures (SMAR 2013), Istanbul (Turkey), September 9-11, 2013

PARASKEVA, T. S., KAPPOS, A. J. (2010)
Further development of a multimodal pushover analysis procedure for seismic assessment of bridges, Earthquake Engineering and Structural Dynamics, Vol. 39, No. 2, 211-222, 2010

PARASKEVA, T. S., KAPPOS, A. J., SEXTOS, A. G. (2006)
Extension of modal pushover analysis to seismic assessment of bridges, Earthquake Engineering and Structural Dynamics, Vol. 35, No. 10, 1269-1293, 2006

PARET, T. F., SASAKI, K. K., EILBECK, D. H., FREEMAN, S. A. (1996)
Approximate inelastic procedures to identify failure mechanisms from higher mode effects, Proceedings of the 11th World Conference on Earthquake Engineering, Acapulco (Mexico), June 23-28, 1996

PEGON, P., PINTO, A. V. (2000)
Pseudo-dynamic testing with substructuring at the ELSA Laboratory, Earthquake Engineering and Structural Dynamics, Vol. 29, No. 7, 905-925, 2000

PETRONIJEVIC, M., MARJANOVIC, M., MILOJEVIC, D. (2018)
Pushover Analysis for Seismic Assessment of RC Nisava Bridge, 16th European Conference on Earthquake Engineering, Thessaloniki (Greece), June 18-21, 2018

PFEIFFER, U. (2006)
INCA 2 (Users Manual) – Berechnung beliebiger Massivbauquerschnitte, TUHH, Hamburg (Germany), 2006

PINHO, R., ANTONIOU, S., CASAROTTI, C., LÓPEZ, M. (2005)
A Displacement-Based Adaptive Pushover for Assessment of Buildings and Bridges, NATO International Workshop on Advances in Earthquake Engineering for Urban Risk Reduction, Istanbul (Turkey), May 30-June 1, 2005

PINHO, R., CASAROTTI, C., ANTONIOU, S. (2007)
A comparison of single-run pushover analysis techniques for seismic assessment of bridges, Earthquake Engineering and Structural Dynamics, Vol. 36, No. 10, 1347-1362, 2007

PINKAWA, M. (2022)

Erdbebenbemessung in Deutschland – aktueller Stand und zukünftige Entwicklung, 1. Fachkongress Konstruktiver Ingenieurbau, 171-182, Technical Academy Esslingen (Germany), May 10-11, 2022

PINTO, A., MOLINA, J., TSIONIS, G. (2001)

Cyclic Test on a Large-Scale Model of an Existing Short Bridge Pier (Warth Bridge - Pier A70), Institute for the Protection and Security of the Citizen, European Laboratory for Structural Assessment (ELSA), Ispra (Italy), 2001

PINTO, A., PEGON, G., MAGONETTE, G., MOLINA, J., BUCHET, P., TSIONIS, G. (2002)

Pseudodynamic tests on a large-scale model of an existing RC bridge using non-linear substructuring and asynchronous motion, Institute for the Protection and Security of the Citizen, European Laboratory for Structural Assessment (ELSA), Ispra (Italy), 2002

PRIESTLEY, M. J. N., CALVI, G. M. (2003)

Direct displacement based seismic design of concrete bridges, Proceedings of the 5th International Conference of Seismic Bridge Design and Retrofit for Earthquake Resistance (ACI International Conference), San Diego (USA), September 27-October 1, 2003

PRIESTLEY, M. J. N., CALVI, G. M., KOWALSKY, M. J. (2007)

Displacement-Based Seismic Design of Structures, IUSS PRESS, Pavia (Italy), ISBN: 978-88-6198-000-6, 2007

REINERT, D. S. (2023)

Adaptive multimodale Pushover-Berechnung von Brückentragwerken unter simultaner Berücksichtigung multidirektionaler Bodenbeschleunigungen, MSc dissertation, University of Wuppertal (Germany), 2023

REQUENA, M., AYALA, G. (2000)

Evaluation of a simplified method for the determination of the nonlinear seismic response of RC frames, Proceedings of the 12th World Conference on Earthquake Engineering, Auckland (New Zeeland), January 30-February 4, 2000

REYES, J. C., CHOPRA, A. K. (2011a)

Three-dimensional modal pushover analysis of buildings subjected to two components of ground motion, including its evaluation for tall buildings, Earthquake Engineering and Structural Dynamics, Vol. 40, No. 7, 789-806, 2011

Reyes, J. C., Chopra, A. K. (2011b)

Evaluation of three-dimensional modal pushover analysis for unsymmetric-plan buildings subjected to two components of ground motion, Earthquake Engineering and Structural Dynamics, Vol. 40, No. 13, 1475-1494, 2011

Rodrigues, H., Varum, H., Arede, A., Costa, A. (2012)

Comparative efficiency analysis of different nonlinear modelling strategies to simulate the biaxial response of RC columns, Earthquake Engineering and Engineering Vibration, Vol. 11, No. 4, 553-566, 2012

Rosenblueth, E., Contreras, H. (1977)

Approximate design for multicomponent earthquakes, Journal of the Engineering Mechanics Division, Vol. 103, No. 5, 881-893, 1977

Salihovic, A., Ademovic, N. (2017)

Nonlinear analysis of reinforced concrete frame under lateral load, Coupled Systems Mechanics, Vol. 6, No. 4, 523-537, 2017

Suarez, V. A., Kowalsky, M. J. (2011)

A Stability-Based Target Displacement for Direct Displacement-Based Design of Bridge Piers, Journal of Earthquake Engineering, Vol. 15, No. 5, 754-774, 2011

Sürmeli, M., Yüksel, E. (2015)

A variant of modal pushover analyses (VMPA) based on a non-incremental procedure, Bulletin of Earthquake Engineering, Vol. 13, No. 11, 3353-3379, 2015

Sürmeli, M., Yüksel, E. (2018)

An adaptive modal pushover analysis procedure (VMPAA) for buildings subjected to bi-directional ground motions, Bulletin of Earthquake Engineering, Vol. 16, No. 4, 5257–5277, 2018

Themelis, S. (2008)

Pushover Analysis for Seismic Assessment and Design of Structures, PhD dissertation, Heriot-Watt University Edinburgh (UK), 2008

Valdebenito, G. E., Aparicio, A. C. (2006)

Seismic Behaviour of Cable-Stayed Bridges: A State-of-the-Art Review, Proceedings of the 4th International Conference on Earthquake Engineering, Taipei (Taiwan), October 12-13, 2006

Valdés-González, J., Ordaz Schroeder, M., De-la-Colina Martínez, J. (2015)
    Combination rule for critical structural response in soft soil, Engineering Structures, Vol. 82,
    No. 1, 2015

Vidic, T., Fajfar, P., Fischinger, M. (1994)
    Consistent inelastic design spectra: strength and displacement, Earthquake Engineering and
    Structural Dynamics, Vol. 23, No. 5, 507-521, 1994

Wei, B., Zeng, Q., Liu, W. (2011)
    Applicability of Modal Pushover Analysis on Bridges, Advanced Materials Research, Vol.
    255-260, 806-810, 2011

Wilson, E. L., Der Kiureghian, A., Bayo, E. P. (1981)
    Short Communications - A Replacement for the SRSS Method in Seismic Analysis, Earthquake
    Engineering and Structural Dynamics, Vol. 9, No. 2, 187-194, 1981

Wilson, E. L., Suharwardy, I., Habibullah, A. (1995)
    A clarification of the orthogonal effects in a three-dimensional seismic analysis, Earthquake
    Spectra, Vol. 11, No. 4, 659-666, 1995

Zhou, Y. (2016)
    *Dynamic Assessment of the Long-Span Cable-Stayed Bridge and Traffic System Subjected to
    Multiple Hazards*, PhD dissertation, Colorado State University (USA), 2016

APPENDIX

A Derivation of spatial load distribution based on Equation 3.8

Equation 3.8 in Section 3.1.2 is widely used in literature and numerous standards for load distributions proportional to mass and mode shape. However, in Section 3.1.2 it was pointed out that this formula is based on the assumption of a sole occurrence of eigenvector or load components in the direction of ground motion under consideration. Therefore the question arises if this Equation can be adapted to a spatial load distribution. This can be easily derived from two obvious requirements, which are:

1. The sum of the load components in the earthquake direction, which is referred to as the primary direction (pd), must still correspond to the base shear:

$$\sum_j F_{(pd),j} = F_b \left(= F_{b,(pd)} \right) \ .$$
(A.1)

2. Any load component in a secondary direction (sd) must have the same magnitude as the load in the earthquake direction (pd) at the same node (j) and thus with the same nodal mass m_j if the accelerations are identical:

$$F_{n,(pd),j} = m_j \cdot \ddot{v}_{n,(pd),j} \stackrel{!}{=} F_{n,(sd),j} = m_j \cdot \ddot{v}_{n,(sd),j} \ .$$
(A.2)

The obvious fulfillment of Equation A.2 with identical nodal accelerations can also be related to the general (nontrivial) equality of the eigenvector components:

$$\ddot{v}_{n,(pd),j} \stackrel{!}{=} \ddot{v}_{n,(sd),j}$$
(A.3)

$$\Leftrightarrow \omega_n^2 \cdot \Phi_{n,(pd),j} \cdot sin\left(\omega_n t - \varphi_n\right) \stackrel{!}{=} \omega_n^2 \cdot \Phi_{n,(sd),j} \cdot sin\left(\omega_n t - \varphi_n\right)$$
(A.4)

$$\Leftrightarrow \Phi_{n,(pd),j} \stackrel{!}{=} \Phi_{n,(sd),j} \ .$$
(A.5)

With regard to Equation 3.8, however, the second requirement is only fulfilled if $m_j \Phi_{n,(pd),j}$ and $m_j \Phi_{n,(sd),j}$ not only have the same eigenvector component $\Phi_{n,(pd),j} = \Phi_{n,(sd),j}$, but are also related to the same denominator. According to requirement 1, this must be the sum of the forces in the primary direction (pd), resulting in the following equation for the spatial load pattern proportional to mass and mode shape (ad = arbitrary direction):

$$F_{n,(ad),j} = F_{b,(pd)} \cdot \frac{m_j \Phi_{n,(ad),j}}{\sum_n m_j \Phi_{n,(pd),j}} \ . \tag{A.6}$$

B Derivation of effective yield points in the *mAMI*
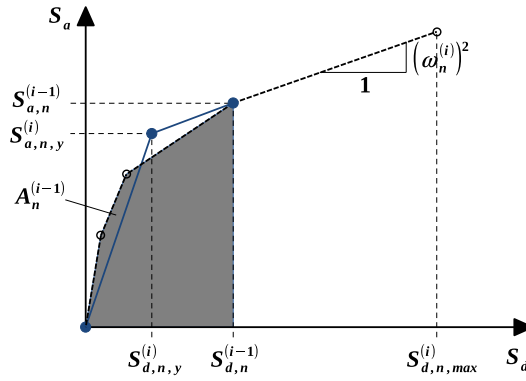
Figure B.1: *Idealization of the capacity spectrum in the IRSA acc. to* AYDINOGLU *(2003)*

With respect to Figure B.1, there are two basic equations that can be formulated in order to determine the effective yield point:

$$\frac{S_{d,n,y}^{(i)} \cdot S_{a,n,y}^{(i)}}{2} + \frac{\left(S_{d,n}^{(i-1)} - S_{d,n,y}^{(i)}\right) \cdot \left(S_{a,n}^{(i-1)} + S_{a,n,y}^{(i)}\right)}{2} \overset{!}{=} A_n^{(i-1)} \tag{B.1}$$

$$\frac{S_{a,n}^{(i-1)} - S_{a,n,y}^{(i)}}{S_{d,n}^{(i-1)} - S_{d,n,y}^{(i)}} \overset{!}{=} \left(\omega_n^{(i)}\right)^2 \quad . \tag{B.2}$$

From Eq. B.2 follows:

$$\leadsto S_{d,n}^{(i-1)} - S_{d,n,y}^{(i)} = \frac{S_{a,n}^{(i-1)} - S_{a,n,y}^{(i)}}{\left(\omega_n^{(i)}\right)^2} \tag{B.3}$$

$$\leadsto S_{d,n,y}^{(i)} = S_{d,n}^{(i-1)} - \frac{S_{a,n}^{(i-1)} - S_{a,n,y}^{(i)}}{\left(\omega_n^{(i)}\right)^2} \quad . \tag{B.4}$$

Insertion of Eq. B.3 into Eq. B.1 yields:

$$\frac{S_{d,n,y}^{(i)} \cdot S_{a,n,y}^{(i)}}{2} + \frac{\left(\frac{S_{a,n}^{(i-1)} - S_{a,n,y}^{(i)}}{\left(\omega_n^{(i)}\right)^2}\right) \cdot \left(S_{a,n}^{(i-1)} + S_{a,n,y}^{(i)}\right)}{2} \stackrel{!}{=} A_n^{(i-1)}$$

(B.5)

$$\Leftrightarrow S_{d,n,y}^{(i)} \cdot S_{a,n,y}^{(i)} + \frac{\left(S_{a,n}^{(i-1)}\right)^2 - \left(S_{a,n,y}^{(i)}\right)^2}{\left(\omega_n^{(i)}\right)^2} \stackrel{!}{=} 2 \cdot A_n^{(i-1)} \ ,$$

with $\left(S_{a,n}^{(i-1)} - S_{a,n,y}^{(i)}\right) \cdot \left(S_{a,n}^{(i-1)} + S_{a,n,y}^{(i)}\right) = \left(S_{a,n}^{(i-1)}\right)^2 - \left(S_{a,n,y}^{(i)}\right)^2$ (3rd binomial formula).

Furthermore, the unknown yield displacement $S_{d,n,y}^{(i)}$ can be eliminated from this equation, thus reducing the number of unknowns to one (only $S_{a,n,y}^{(i)}$ still unknown), by insterting Eq. B.4:

$$\left(S_{d,n}^{(i-1)} - \frac{S_{a,n}^{(i-1)} - S_{a,n,y}^{(i)}}{\left(\omega_n^{(i)}\right)^2}\right) \cdot S_{a,n,y}^{(i)} + \frac{\left(S_{a,n}^{(i-1)}\right)^2 - \left(S_{a,n,y}^{(i)}\right)^2}{\left(\omega_n^{(i)}\right)^2} \stackrel{!}{=} 2 \cdot A_n^{(i-1)}$$

$$\Leftrightarrow S_{d,n}^{(i-1)} \cdot S_{a,n,y}^{(i)} - \frac{S_{a,n}^{(i-1)} \cdot S_{a,n,y}^{(i)}}{\left(\omega_n^{(i)}\right)^2} + \frac{\left(S_{a,n,y}^{(i)}\right)^2}{\left(\omega_n^{(i)}\right)^2} + \frac{\left(S_{a,n}^{(i-1)}\right)^2}{\left(\omega_n^{(i)}\right)^2} - \frac{\left(S_{a,n,y}^{(i)}\right)^2}{\left(\omega_n^{(i)}\right)^2} \stackrel{!}{=} 2 \cdot A_n^{(i-1)}$$

(B.6)

$$\Leftrightarrow \left(\frac{S_{a,n}^{(i-1)}}{\omega_n^{(i)}}\right)^2 + \left(S_{d,n}^{(i-1)} - \frac{S_{a,n}^{(i-1)}}{\left(\omega_n^{(i)}\right)^2}\right) \cdot S_{a,n,y}^{(i)} \stackrel{!}{=} 2 \cdot A_n^{(i-1)}$$

$$\Rightarrow S_{a,n,y}^{(i)} = \frac{2 \cdot A_n^{(i-1)} - \left(\frac{S_{a,n}^{(i-1)}}{\omega_n^{(i)}}\right)^2}{S_{d,n}^{(i-1)} - \frac{S_{a,n}^{(i-1)}}{\left(\omega_n^{(i)}\right)^2}} \ .$$

(B.7)

After solving Eq. B.7, $S_{a,n,y}^{(i)}$ can be inserted into Eq. B.4 in order to finally calculate the corresponding yield displacement:

$$\Rightarrow S_{d,n,y}^{(i)} = S_{d,n}^{(i-1)} - \frac{S_{a,n}^{(i-1)} - S_{a,n,y}^{(i)}}{\left(\omega_n^{(i)}\right)^2} \ .$$

(B.8)

C Further background information about the post-experimental study of the *ELSA PSD tests*

C.1 α *operator splitting scheme* (Pegon & Pinto , 2000)

The starting point is the well-known system of nonlinear equations of motion for seismic excitations, whereby $\mathbf{a}$, $\mathbf{v}$ and $\mathbf{d}$ represent the acceleration, velocity and deformation vectors, respectively:

$$\mathbf{Ma} + \mathbf{Cv} + \mathbf{r}(\mathbf{d}) = \mathbf{f} = -\mathbf{MI}^{base}a \ . \tag{C.1}$$

The α *operator splitting scheme* for each point in time consists of the following four steps (Pegon & Pinto , 2000):

1. Compute estimates for the current displacements and velocities (prediction phase):

$$\tilde{\mathbf{d}}^{n+1} = d^n + \Delta t \mathbf{v}^n + \frac{\Delta t^2}{2} \left(1 - 2\beta\right) \mathbf{a}^n \ , \tag{C.2}$$

$$\tilde{\mathbf{v}}^{n+1} = \mathbf{v}^n + \Delta t \left(1 - \gamma\right) \mathbf{a}^n \ , \tag{C.3}$$

with $\beta = \frac{(1-\alpha)^2}{4}$, $\gamma = \frac{(1-2\alpha)}{2}$, $\alpha \in [-\frac{1}{3}, 0]$.

2. Apply the displacements $\tilde{d}_j^{n+1}$ of all FE nodes j to the numerical model and the displacements at the top of the tested piers to the latter (control phase) in order to get the static restoring force vector $\tilde{\mathbf{r}}^{n+1}$ (measuring phase).

3. Solve the following system of linear equations for $\mathbf{a}^{n+1}$ (calculating phase):

$$\hat{\mathbf{M}} \mathbf{a}^{n+1} = \hat{\mathbf{f}}^{n+1+\alpha} \ , \tag{C.4}$$

where the pseudo-mass matrix $\hat{\mathbf{M}}$ and the pseudo-force vector $\hat{\mathbf{f}}^{n+1+\alpha}$ are given by

$$\hat{\mathbf{M}} = \mathbf{M} + \gamma \Delta t \left(1 + \alpha\right) \mathbf{C} + \beta \Delta t^2 \left(1 + \alpha\right) \mathbf{K}^I \text{ and} \tag{C.5}$$

$$\hat{\mathbf{f}}^{n+1+\alpha} = \left(1 + \alpha\right) \mathbf{f}^{n+1} - \alpha \mathbf{f}^n + \alpha \tilde{\mathbf{r}}^n - \left(1 + \alpha\right) \tilde{\mathbf{r}}^{n+1} + \alpha \mathbf{C} \tilde{\mathbf{v}}^n - \left(1 + \alpha\right) \mathbf{C} \tilde{\mathbf{v}}^{n+1}$$
$$+ \alpha \left(\gamma \Delta t \mathbf{C} + \beta \Delta t^2 \mathbf{K}^I\right) \mathbf{a}^n . \tag{C.6}$$

Here, $\mathbf{K}^I$ is a stiffness matrix, which is chosen as close as possible to the elastic matrix $\mathbf{K}^e$, but, for the sake of stability, higher or equal to the current tangent siffness matrix $\mathbf{K}^t(\mathbf{d})$.

4. Compute the actual displacements and velocities for the current state (correction phase) according to:

$$\mathbf{d}^{n+1} = \tilde{\mathbf{d}}^{n+1} + \Delta t^2 \beta \mathbf{a}^{n+1} \text{ and} \tag{C.7}$$

$$\mathbf{v}^{n+1} = \tilde{\mathbf{v}}^{n+1} + \Delta t \gamma \mathbf{a}^{n+1} . \tag{C.8}$$

C.2   Applied material parameters according to Pinto et al (2002)

Table C.1: *Material parameters of pier A40 according to* PINTO ET AL *(2002)*

Parameter	Value	Unit	Tested value
E_{cm}	33500	MN/m^2	no
f_c	51.6	MN/m^2	yes
ρ_c	2.349	t/m^3	yes
E_{st}	200000	MN/m^2	no
f_y	546.4	MN/m^2	yes
f_u	660.2	MN/m^2	yes
ε_u	65	mm/m	yes
ρ_{st}	7.849	t/m^3	no

C.3 Arrangement of the longitudinal reinforcement
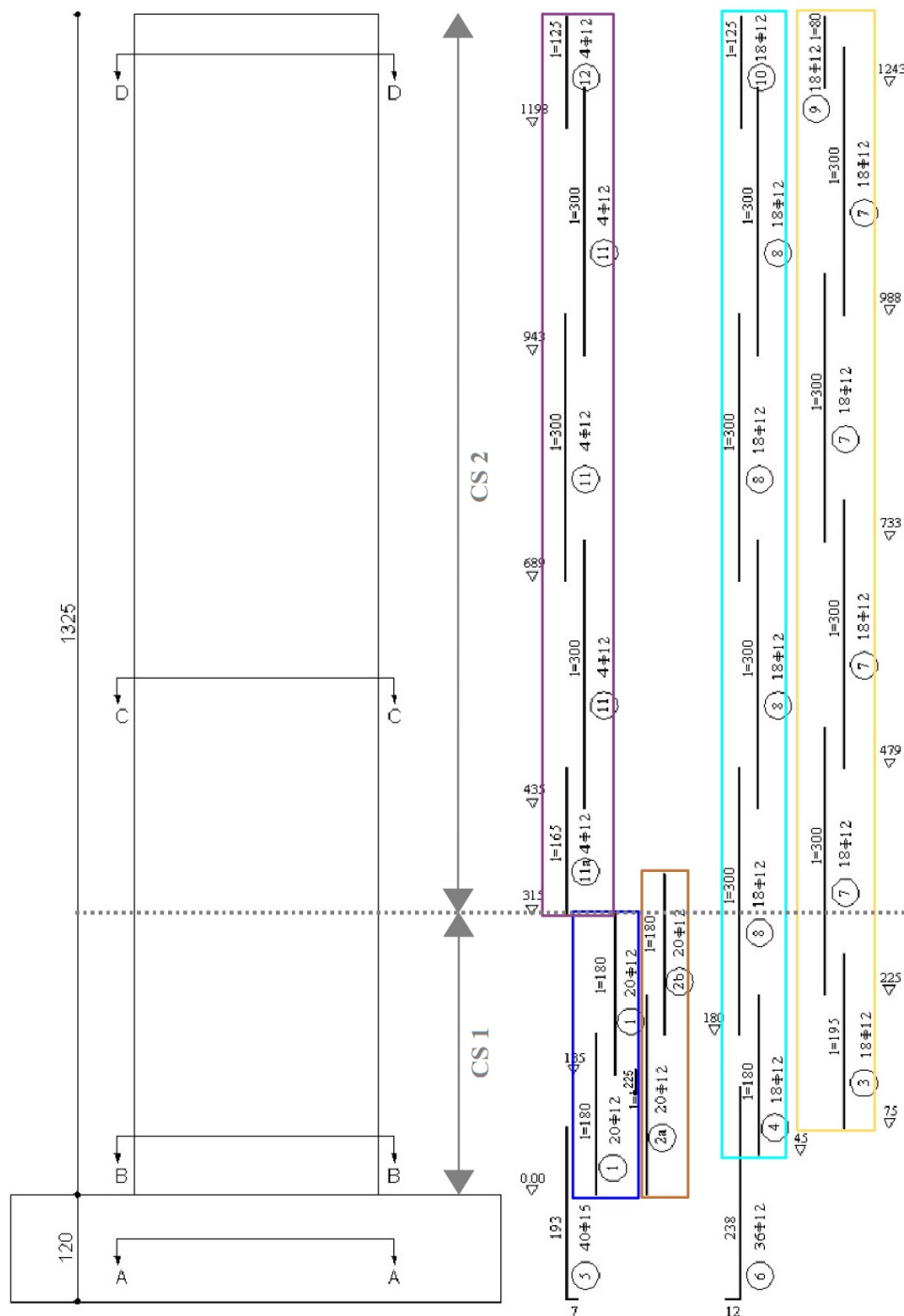
Figure C.1: *Vertical arrangement of the longitudinal bars of pier A40 according to* Pinto et al *(2002)*

As reinforcement item 1 ends at 3.15 m from the top of the footing and item 2b also has a certain (not specifically calculated) anchoring length, cross-section 1 is simplistically only applied up to 3.15 m instead of 3.5 m. On the other hand, the fact that item 3 (unlike items 1 and 2a) is not overlapped by the insertion stirrups anchored in the foundation block, but actually only starts at 75 cm, is also neglected for reasons of simplification. According to Pinto et al (2002), the concrete cover is uniformly 1.5 cm.
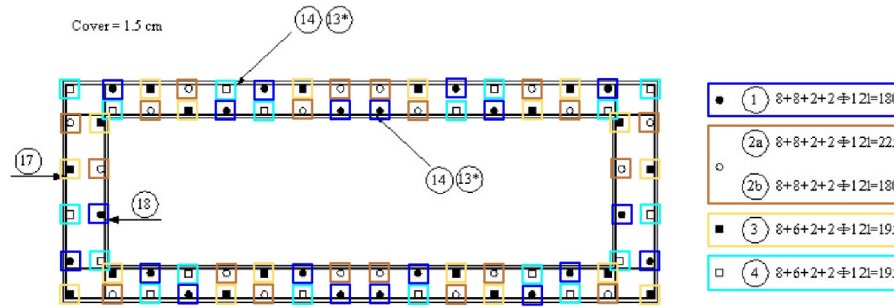
Figure C.2: *Longitudinal bars in cross-section 1 of pier A40 according to Pinto et al (2002)*
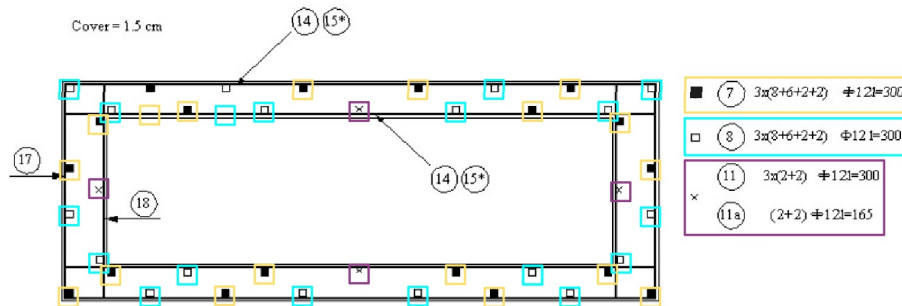
Figure C.3: *Longitudinal bars in cross-section 2 of pier A40 according to Pinto et al (2002)*

C.4 Derivation of the two scaling factors SF_m for the membrane and SF_{pb} for the plate bending effect

These factors are calculated on the basis of the quotient of the respective ideal and the corresponding gross cross-section value as follows (with n_{bars} = number of longitudinal bars with a diameter of ϕ_l):

$$
\begin{aligned}
A_{id} &= A_c + \left(\frac{E_{st}}{E_{cm}} - 1 \right) \cdot n_{bars} \cdot \left(\frac{\pi \phi_l^2}{4} \right) \\[2mm]
&= 250 \cdot 120 + \left(\frac{200000}{19833} - 1 \right) \cdot 20 \cdot \left(\frac{\pi 2^2}{4} \right) \\[2mm]
&= 30571 \text{ cm}^2
\end{aligned}
\tag{C.9}
$$

$$
\rightsquigarrow SF_m = \frac{A_{id}}{A_c} = 1.02 \ [-]
$$

$$
\text{and}
$$

$$
\begin{aligned}
I_{yy,id} &= I_{yy,c} + \left(\frac{E_{st}}{E_{cm}} - 1 \right) \cdot n_{bars} \cdot \left(\frac{\pi \phi_l^2}{4} \right) \cdot z_l^2 \\[2mm]
&= \frac{1}{12} \cdot 250 \cdot 120^3 + \left(\frac{200000}{19833} - 1 \right) \cdot 20 \cdot \left(\frac{\pi 2^2}{4} \right) \cdot 53.75^2 \\[2mm]
&= 37649011 \text{ cm}^4
\end{aligned}
\tag{C.10}
$$

$$
\rightsquigarrow SF_{pb} = \frac{I_{yy,id}}{I_{yy,c}} = 1.045 \ [-] \ .
$$

C.5   Arrangement of potential plastic or fiber hinges
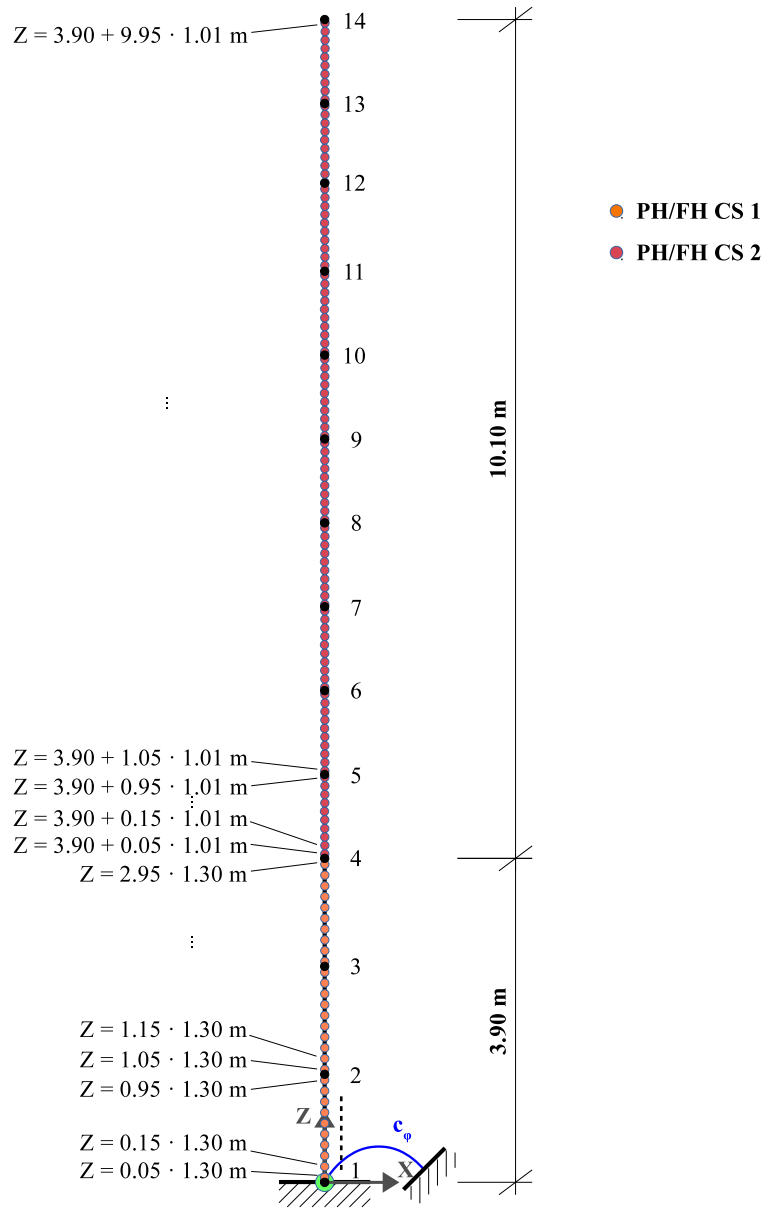
Figure C.4: *FE model of pier A40: Vertical arrangement of the plastic or fiber hinges*

C.6   Further calculation results
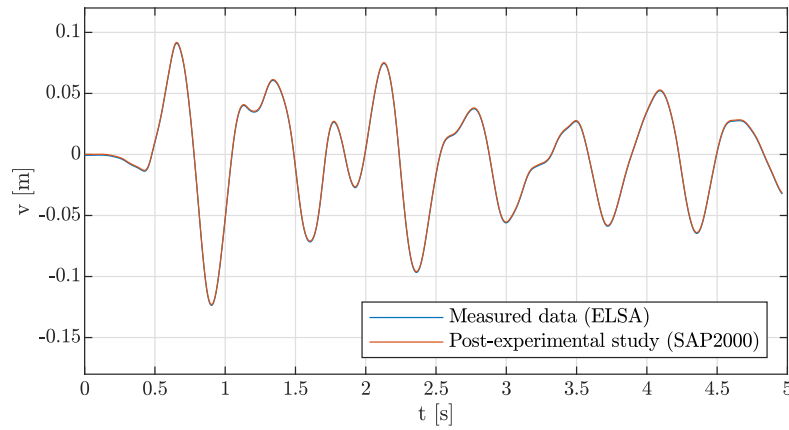
Figure C.5: *Plausibility check of pier head displacements (pier A40)*
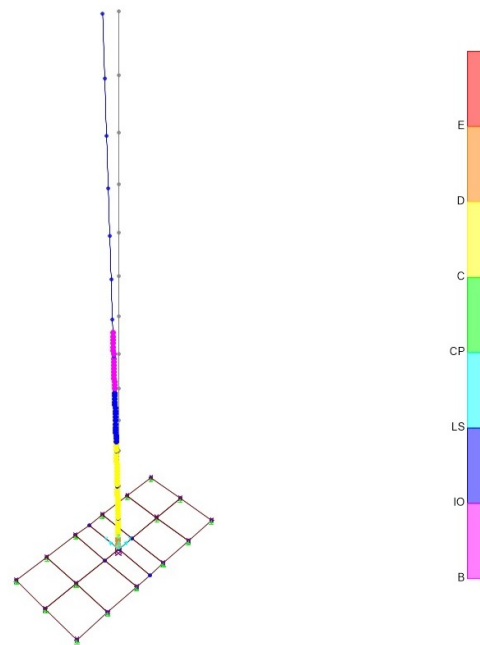
Figure C.6: *Distribution of plastic hinge states (pier A40, PSD step 228)*

D Examplary *MATLAB* script for the *CAAP* application

```matlab
%% Program and data specifications
% Path of SAP2000
arg.info.sap_path = 'C:\Program Files\Computers and Structures\
   SAP2000 20\SAP2000.exe';
% Path of $2k file
arg.info.sap_file = 'C:\Users\Admin\Documents\Computations SAP\
   Rp_Y__BMode_2__mp_3\STBB_00003A_V343P_mAMI__monodir_earthquake
   .$2k';
% Name of export file (xml)
arg.info.export_file_name = 'Auto_Export';
% Details for automated mail notifications
arg.info.mail_notification.mailadress = 'blogg@uni-wuppertal.de';
arg.info.mail_notification.name = 'blogg';
arg.info.mail_notification.password = 'password';
arg.info.mail_notification.smtp_server = 'mail.uni-wuppertal.de';

%% General computational details
% Name of nonlinear loadcase for gravity loads
arg.info.name_vert = 'Dead';
% Name of initial modal analysis
arg.info.name_modal = 'Modal';
% Name of initial pushover analysis
arg.info.name_pushover = 'Push_Y';
% Choice of procedure
arg.info.procedure = 'ami_o'; % mAMI procedure with optimized
   spectral acceleration increments of the base mode
```

```matlab
% Detailed program output in command window requested?
arg.info.console_output = 1;
% Sound requested (e.g. in order to indicate the end of the
   computation)?
arg.info.sound = 1;


%% Specific computational details
% Nonlinear steps of the pushover analysis
arg.comp.nl_steps = [100 150]; % [min max]
% If no convergence could be found: increase fault tolerance by '
   d_tol'
arg.comp.d_tol = 1.000E-03; % [-]
% Adaptive computation? (only way in case of mAMI)
arg.comp.adaptive = 1;
% Define k_loc & k_glob:
arg.comp.k_loc = 0.9; % [-]
arg.comp.k_glob = 0.9; % [-]
% For the event that negative spectral acceleration increments
   occur during
% the calculation and the method changes from 'ami_o' to 'ami_c':
% -> Define constant acceleration increment of the base mode:
arg.comp.delta_s_a_b = 0.01; % [m/s^2]
% In the case of an adaptive procedure: Fully automated
   computation?
% (only way in case of mAMI)
arg.comp.auto_run = 1;
% Should the algorithm have the decision-making power for
   critical mode
% self-assignments within the 'ultima ratio' in '
   caap_check_eigenmodes'
% (this option is recommended for calculations that you do not
   keep an eye
% on all the time; however, this harbors the risk that the
   calculation has
% to be repeated with 'arg.ber.algodec = 0' if the previous run
   contains
```

```matlab
% wrong self-assignments)
arg.comp.algodec = 1;


%% Load combinations (here: only one decisive modal load
   combination investigated)
% Definition of the main earthquake direction!
arg.comp.d_earthquake = 'Y';
% Define, which modes should be taken into account in which
   direction and whith which sign.
modes_y = [2 6 -1 5];
% Hysteretic behavior
arg.ber.hb = 'A'; % Case A: stable hysteresis loops (high energy
   dissipation level)


%% Response spectrum details
% Normative source
arg.rs.source = 'ec8-1';
% Direction
% -> The question, if the response spectrium corresponds to
   horizontal or vertical accelerations is automaticly answered
   within the "caap_pushover_pointloads" program routine
% (in case of the earthquake direction 'X' or 'Y': 'horizontal';
   in case of 'Z': 'vertical')
% a_g (horizontal acceleration)
arg.rs.a_g = 0.05*9.81; % [m/s^2]
% a_vg (vertical acceleration)
arg.rs.a_vg = 0.9*arg.rs.a_g; % [m/s^2] (acc. to DIN EN 1998-1,
   Tab. 3.4 for "type 1")
% Soil parameter S (Foundation soil class D & response spectrum
   type 1)
arg.rs.S = 1.35; % [-]
% Control periods T_B, T_C & T_D (in case of foundation soil
   class D & response spectrum type 1)
arg.rs.T_BCD = [0.2 0.8 2.0]; % [s] ((1x3)-array)
% Resolution of the T axis
arg.rs.dT = 0.01; % [s] (= default value)
```

```matlab
% Upper and lower limit values for the T axis
arg.rs.T_max = 5; % [s]
arg.rs.T_min = 0; % [s]


%% MAIN
% Save console output
% Delete txt file with console output, if already existing
if exist('Console_output.txt','file')==2
        diary off
        delete('Console_output.txt');
end
% Prepare a new file and start to record the console output
diary Console_output.txt
% Output starting time
disp(' '); % blank line
disp('Begin: Investigation of all load combinations k')
time = clock;
time_str = cell(1,5);
for i_value = 1:5
        if length(num2str(time(i_value))) == 1
                time_str{i_value} = ['0',num2str(time(i_value))];
        else
                time_str{i_value} = num2str(time(i_value));
        end
end
disp(['Time: ',time_str{3},'.',time_str{2},'.',time_str{1},' - ',
   time_str{4},':',time_str{5},' Uhr']) % output date and time
disp(' '); % blank line
% Build up "tic-toc"-relation
t_start = tic;
% Investigation of all requested load combinations k
for k = 1:size(modes_y,1)
        % Short console output
        disp(' ') % blank line
        disp(['Start with computation of load combination ',
           num2str(k),'!'])
```

```matlab
        disp(' ') % blank line
        % Save output variable "arg" with the above settings
            firstly as
        % temporary variable 'arg_tmp'
        arg_tmp = arg;
        % Save model file in folder that corresponds to the
            current load combination
        % a) Create subfolder
        mkdir(['load_combi__',num2str(k)])
        % b) Create new path for the SAP2000 model
        [sap_filepath,sap_name,sap_ext] = fileparts(arg.info.
            sap_file);
        arg_tmp.info.sap_file = [sap_filepath '\load_combi__'
            num2str(k) '\' sap_name '-load_combi__' num2str(k)
            sap_ext];
        % c) Place model file in new subfolder
        copyfile(arg.info.sap_file,arg_tmp.info.sap_file)
        % Evaluate arg.comp.modes.y
        arg_tmp.comp.modes.y = modes_y(k,:);
        % Function call here for fully automated procedure and
            thus without
        % previous model file (-> [])
        MAIN_CAAP([],arg_tmp);
end
% Output end time of the computation
disp(' '); % blank line
disp(['End: Computation of (all) load combination(s) ',num2str(k)
    ])
time = clock;
time_str = cell(1,5);
for i_value = 1:5
        if length(num2str(time(i_value))) == 1
                time_str{i_value} = ['0',num2str(time(i_value))];
        else
                time_str{i_value} = num2str(time(i_value));
        end
```

```matlab
end
disp(['Time: ',time_str{3},'.',time_str{2},'.',time_str{1},' - ',
    time_str{4},':',time_str{5},' Uhr']) % output date and time
disp(' '); % blank line
% Output total computing time
sec = toc(t_start); % [s]
disp(['The entire computation for (all) ',num2str(k),' load
    combination(s) took ',num2str(sec),' seconds!'])
hms = [floor(sec/3600),floor(rem(sec,3600)/60),floor(rem(rem(sec
    ,3600),60))];
disp(['This corresponds to ',num2str(hms(1)),' h, ',num2str(hms
    (2)),' m and ',num2str(hms(3)),' s.'])
% Stop recording the console and save the output txt file
diary off
```

E Further information on the monodirectional earthquake investigations

E.1 Information concerning the analyzed models

M-κ curves for the plastic hinges of bridge models A & B:

(a) Pier P1 & P3

(b) Pier P2

Figure E.1: M-κ curves for bridge model A

(a) Pier P1

(b) Pier P2
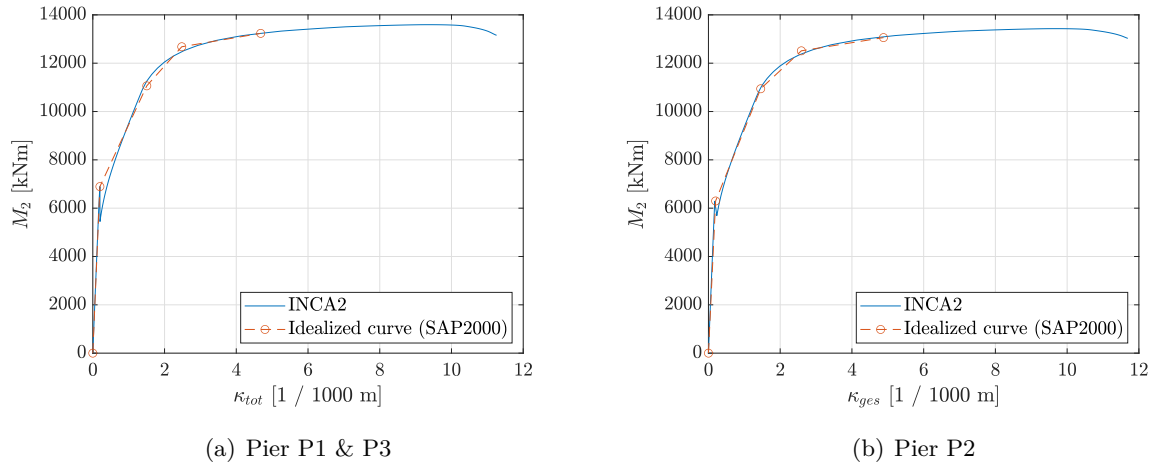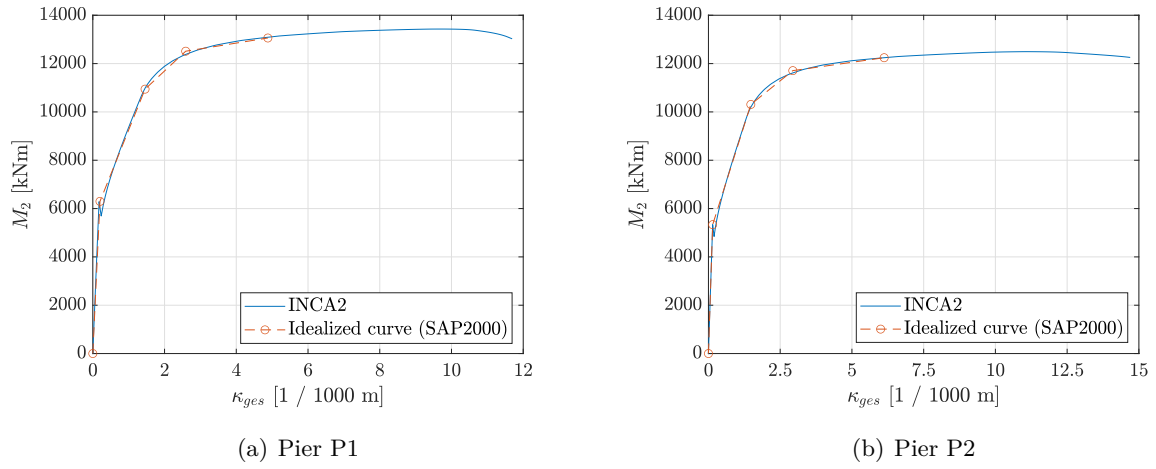
Figure E.2: *M-κ curves for bridge model B (1): Piers P1 & P2*
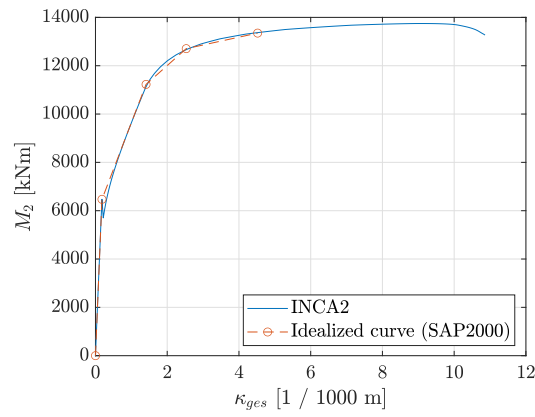
Figure E.3: *M-κ curves for bridge model B (2): Pier P3*

Material parameters and σ-ε curves for both materials considered (acc. to Eurocode 2 - Part 1-1 (2011)):

Table E.1: *Material parameters of bridge models A & B*

Parameter	Value	Unit	Source
E_{cm}	34000	MN/m^2	DIN EN 1992-1-1, Tab. 3.1
f_{cm}	43	MN/m^2	DIN EN 1992-1-1, Tab. 3.1
ε_{c1}	2.25	mm/m	DIN EN 1992-1-1, Tab. 3.1
ε_{cu1}	3.5	mm/m	DIN EN 1992-1-1, Tab. 3.1
f_{ctm}	3.2	MN/m^2	DIN EN 1992-1-1, Tab. 3.1
E_S	200000	MN/m^2	DIN EN 1992-1-1, 3.2.7(4)
f_{yk}	500	MN/m^2	Proportional limit acc. to designation
f_{yR}	550	MN/m^2	$(1.1 \cdot f_{yk})$
k	1.05	-	DIN EN 1992-1-1, Tab. C.1
ε_y	2.75	mm/m	$(\frac{f_y}{E_S})$
ε_{uk}	25	mm/m	DIN EN 1992-1-1, Tab. C.1

According to DIN EN 1992-1-1, 3.1.5(1), this results in the following plasticizing parameter k for concrete:

$$k = 1.05 \cdot E_{cm} \cdot \frac{\varepsilon_{c1}}{f_{cm}} = 1.87 \; [\text{-}] \; . \tag{E.1}$$

Furthermore, the course of the σ-ε curves for both materials is required. The concrete compressive stresses are calculated according to Eq. 3.14 of DIN EN 1992-1-1:

$$\sigma_c = f_{cm} \cdot \frac{k\eta - \eta^2}{1 + (k-2)\eta} \; , \tag{E.2}$$

with $\eta = \frac{\varepsilon_c}{\varepsilon_{c1}}$. For the concrete tensile stresses, whose nonlinear σ-ε curve is not specified in DIN EN 1992, Equations (5.1-29) & (5.1-30) of the FIB MODEL CODE (2010) are used:

$$\sigma_{ct} = \begin{cases} E_{cm} \cdot \varepsilon_{ct} & \text{, for } \sigma_{ct} \leq 0.9 f_{ctm} \\ f_{ctm} \cdot \left(1 - 0.1 \cdot \frac{0.00015 - \varepsilon_{ct}}{0.00015 - \frac{0.9 \cdot f_{ctm}}{E_{cm}}} \right) & \text{, for } 0.9 f_{ctm} < \sigma_{ct} \leq f_{ctm} \; . \end{cases} \tag{E.3}$$

For the steel stresses, the widely used linearized representation is used, which is based on two segments: an elastic and a plastic branch. This curve is fully described by the above parameters.

The resulting two σ-ε curves are shown in the figure below.

(a) Concrete

(b) Reinforcement steel
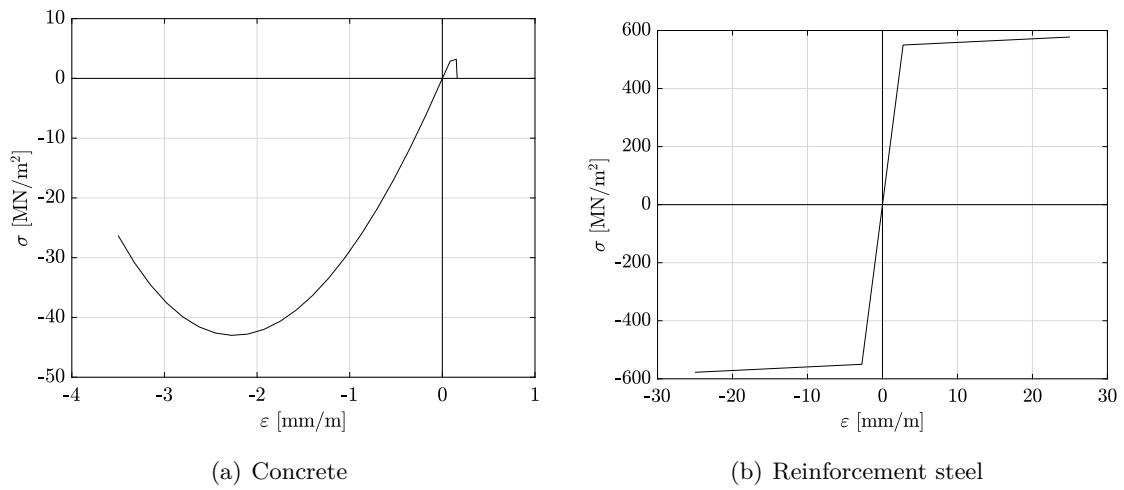
Figure E.4: *σ-ε curves used*

Vertical arrangement of the potential plastic or fiber hinges:
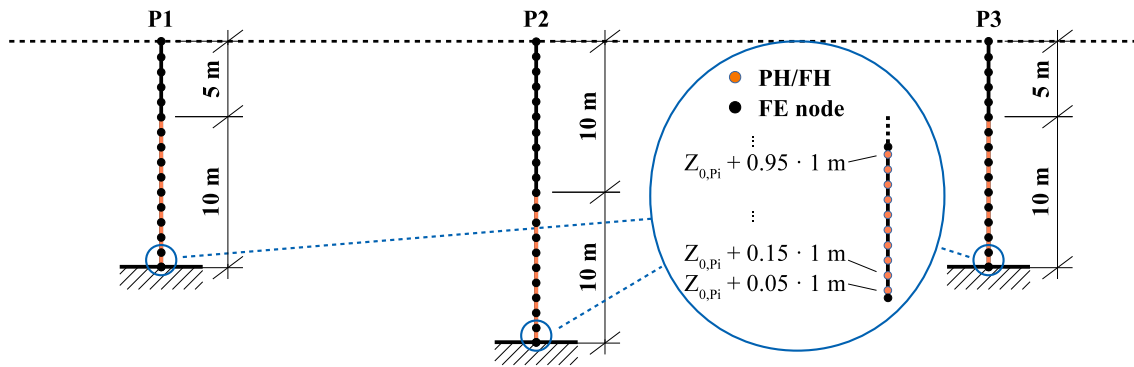
Figure E.5: *Bridge model A: Vertical arrangement of the plastic or fiber hinges*
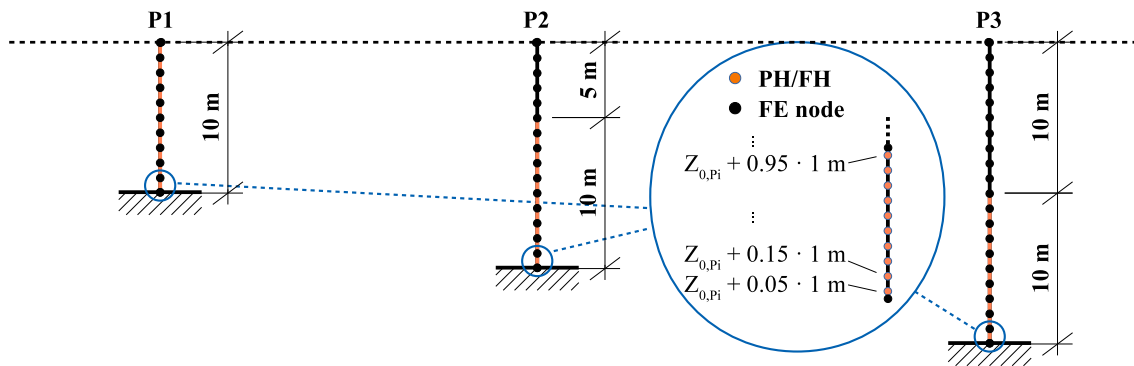
Figure E.6: *Bridge model B: Vertical arrangement of the plastic or fiber hinges*

E.2 Information concerning the *mAMI* calculations

Successive development of plastic hinges:

The plastic hinge (PH) states at the end of adaption steps 16, 18 and 24 of the *mAMI* calculation with $\Delta S_{a,B}^{(i)} = 0.05$ m/s^2, LC 3, in which relevant system changes were identified in accordance with the mode development examined in Section 6.3, are shown below.
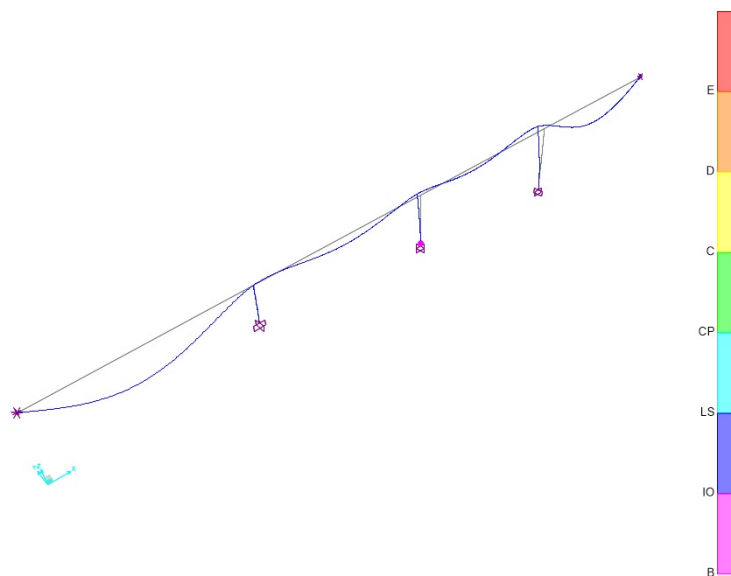
Figure E.7: *mAMI calculation with $\Delta S_{a,B}^{(i)} = 0.05$ m/s^2 (LC 3): PH states in step 16*
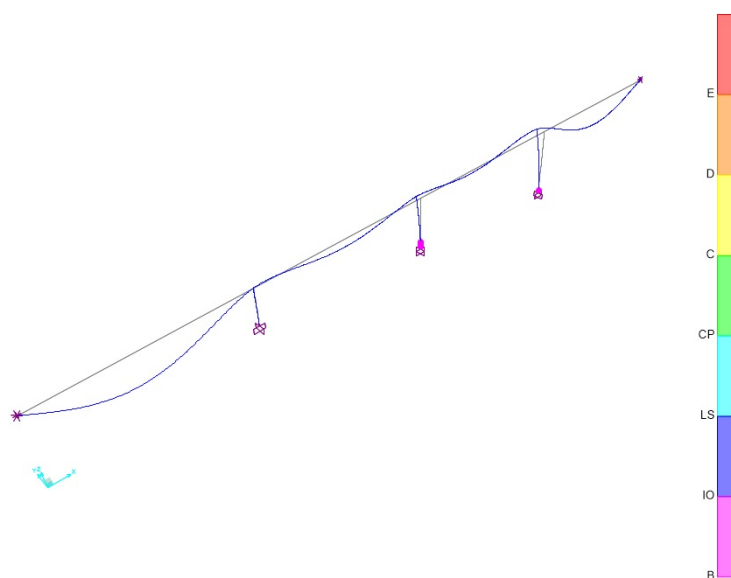
Figure E.8: *mAMI calculation with $\Delta S_{a,B}^{(i)} = 0.05$ m/s^2 (LC 3): PH states in step 18*
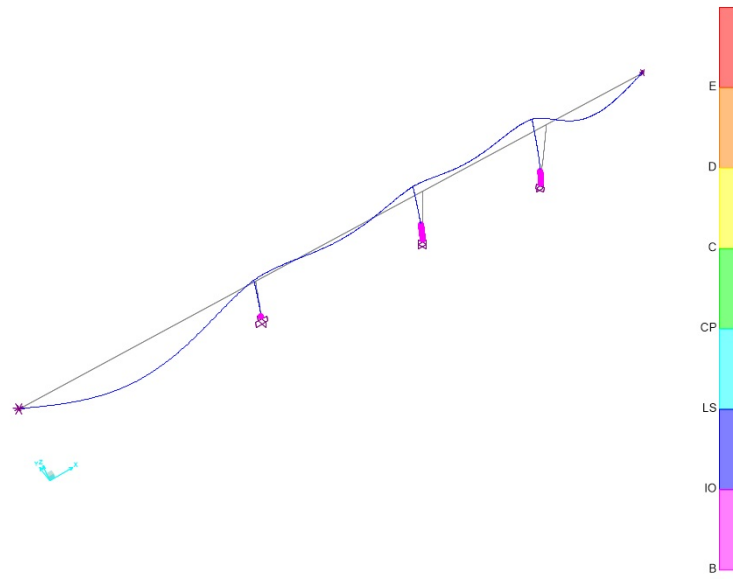
Figure E.9: *mAMI calculation with $\Delta S_{a,B}^{(i)} = 0.05$ m/s^2 (LC 3): PH states in step 24*

Comparison of mode developments for both the PH and the FH model:

(a) $\boldsymbol{\Phi}_1^{(1)}(f_1 = 1.01$ Hz) - PH model   (b) $\boldsymbol{\Phi}_1^{(end)}(f_1 = 0.52$ Hz) - PH model
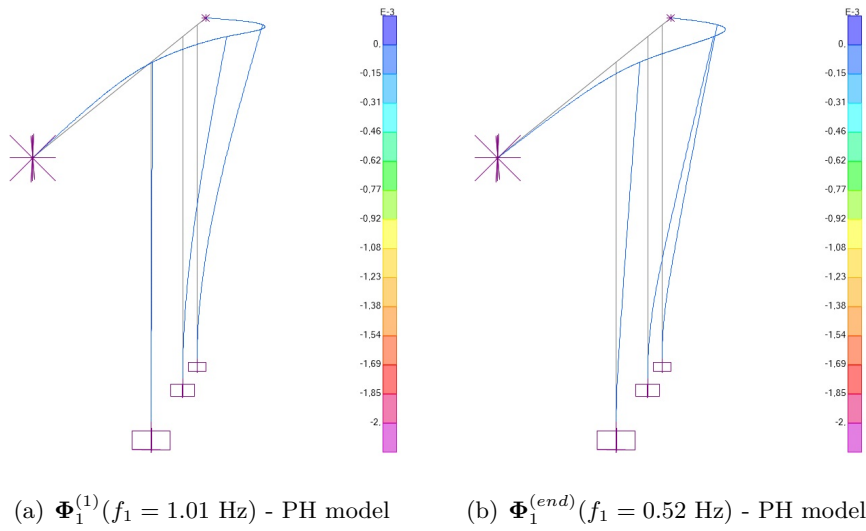
Figure E.10: *Development of initial mode 1 - PH model 11*

(a) $\mathbf{\Phi}_1^{(1)}(f_1 = 1.02$ Hz$)$ - FH model

(b) $\mathbf{\Phi}_1^{(end)}(f_1 = 0.57$ Hz$)$ - FH model
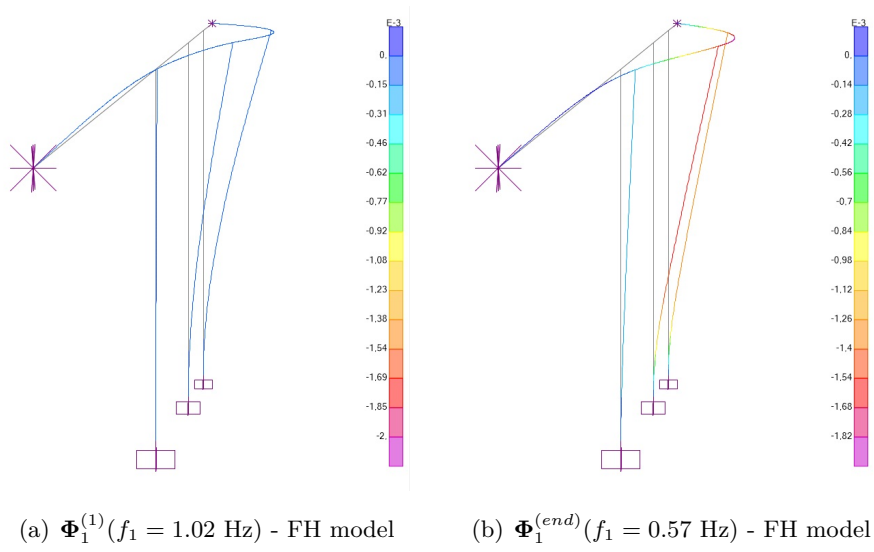
Figure E.11: *Development of initial mode 1 - FH model 11*

(a) $\mathbf{\Phi}_4^{(1)}(f_4 = 1.63$ Hz$)$ - PH model

(b) $\mathbf{\Phi}_2^{(end)}(f_2 = 1.06$ Hz$)$ - PH model
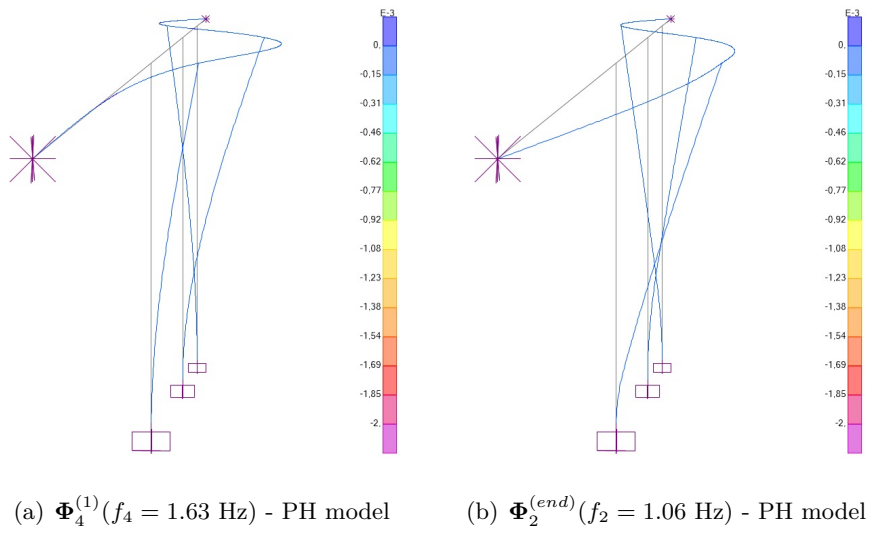
Figure E.12: *Development of initial mode 4 - PH model 11*

(a) $\mathbf{\Phi}_4^{(1)}(f_4 = 1.66 \text{ Hz})$ - FH model   (b) $\mathbf{\Phi}_2^{(end)}(f_2 = 1.20 \text{ Hz})$ - FH model
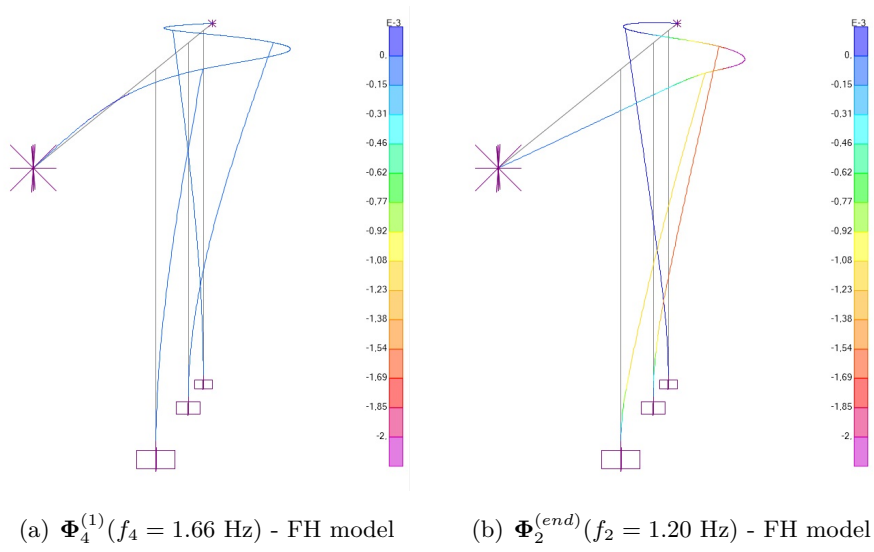
Figure E.13: *Development of initial mode 4 - FH model 11*

(a) $\mathbf{\Phi}_6^{(1)}(f_6 = 2.25 \text{ Hz})$ - PH model   (b) $\mathbf{\Phi}_5^{(end)}(f_5 = 1.67 \text{ Hz})$ - PH model
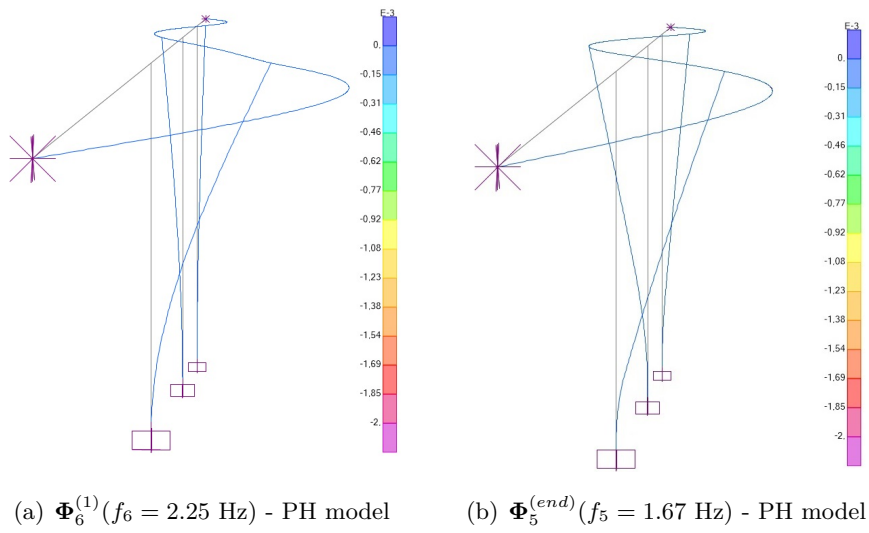
Figure E.14: *Development of initial mode 6 - PH model 11*

(a) $\boldsymbol{\Phi}_6^{(1)}(f_6 = 2.28$ Hz$)$ - FH model
(b) $\boldsymbol{\Phi}_5^{(end)}(f_5 = 1.80$ Hz$)$ - FH model
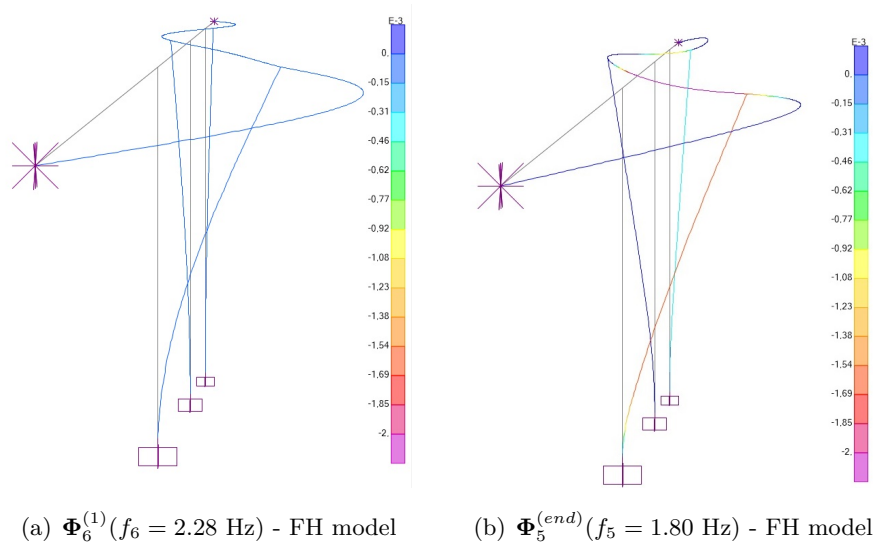
Figure E.15: *Development of initial mode 6 - FH model 11*

Parameter study documented in Section 6.5:

Table E.2: *Overview of the 11 bridge models examined as part of the parameter study*

Bridge model	Pier lengths [m]		
	H_1	H_2	H_3
1	15.0	20.0	15.0
2	14.5	19.5	15.5
3	14.0	19.0	16.0
4	13.5	18.5	16.5
5	13.0	18.0	17.0
6	12.5	17.5	17.5
7	12.0	17.0	18.0
8	11.5	16.5	18.5
9	11.0	16.0	19.0
10	10.5	15.5	19.5
11	10.0	15.0	20.0

Table E.3: *mAMI load combinations for the 11 bridge models studied - Calc. I*

Bridge model	Modal load combination	$\sum \mu_{eff,Y}^{(1)}$ [%]
1	{-1,4,5}	90.0
2	{-1,4,-5}	89.8
3	{1,-3,-5}	89.1
4	{1,5}	88.1
5	{-1,-3,-5}	90.2
6	{1,-3,5}	90.2
7	{-1,-3,-5}	90.3
8	{1,3,-5}	90.4
9	{-1,3,-6}	90.6
10	{1,-4,6}	90.8
11	{1,4,6}	91.0

Table E.4: *mAMI load combinations for the 11 bridge models studied - Calc. II*

Bridge model	Modal load combination	$\sum \mu_{eff,Y}^{(1)}$ [%]
1	{-1,5}	86.2
2	{-1,-5}	86.3
3	{1,-5}	86.2
4	{1,5}	86.0
5	{-1,-5}	85.7
6	{1,5}	85.3
7	{-1,-5}	84.7
8	{1,-5}	84.1
9	{-1,-5}	83.3
10	{1,5}	82.4
11	{1,2,5}	87.1
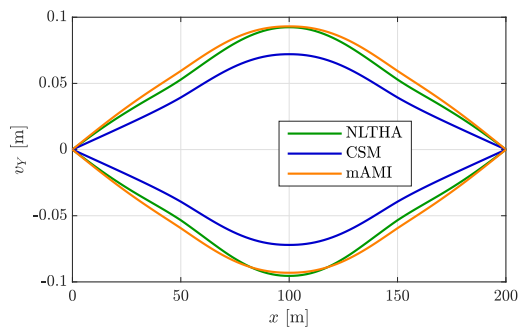
(a) Model 1
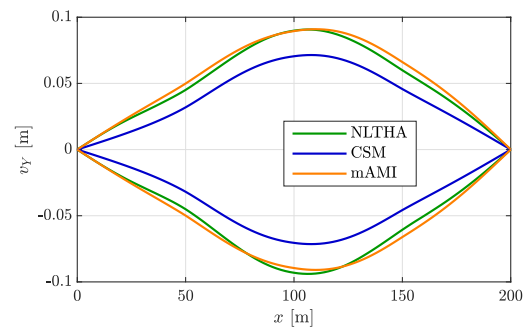
(b) Model 2

Figure E.16: *Lateral deck displacements - Calc. I, Model 1 & 2*
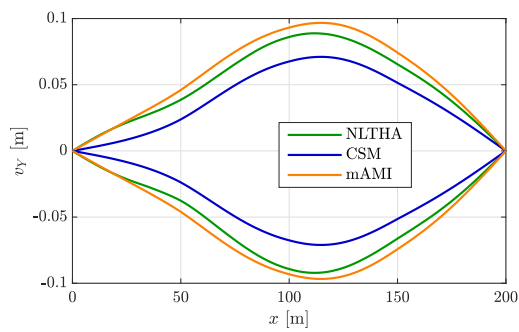
(a) Model 3
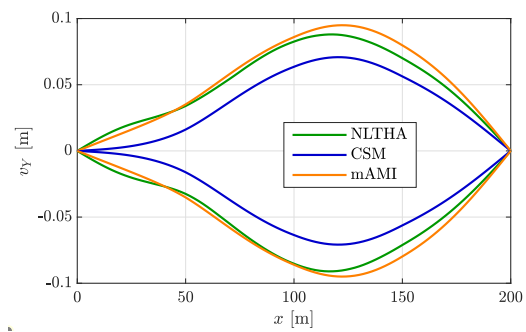
(b) Model 4

Figure E.17: *Lateral deck displacements - Calc. I, Model 3 & 4*
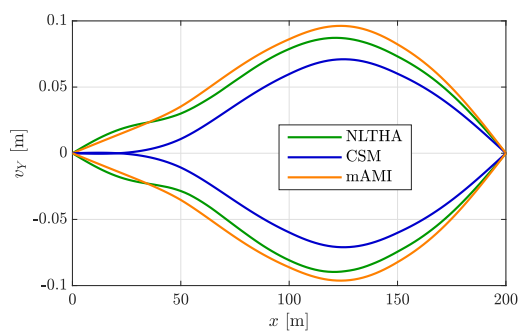
(a) Model 5
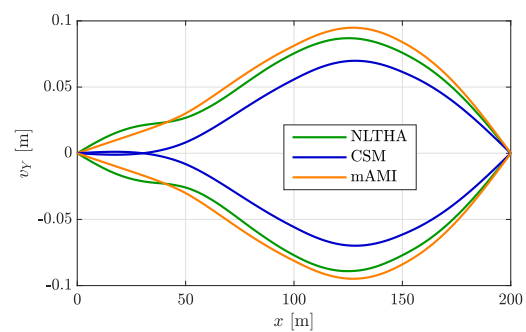
(b) Model 6

Figure E.18: *Lateral deck displacements - Calc. I, Model 5 & 6*
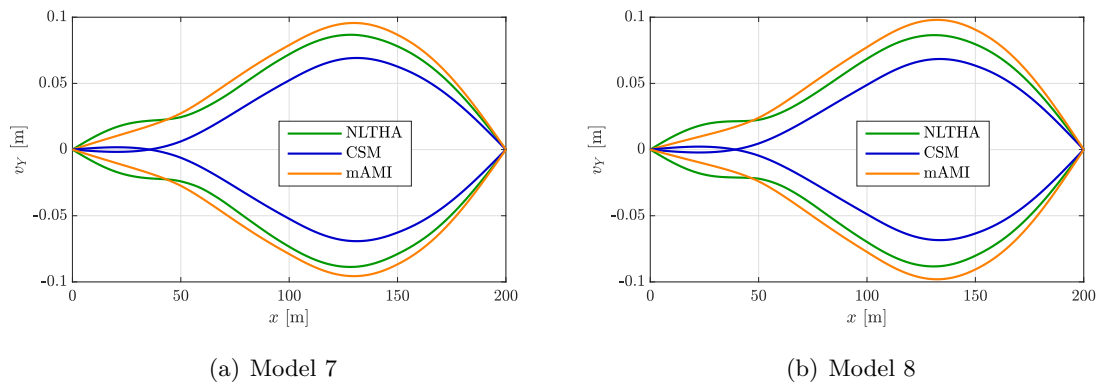
(a) Model 7

(b) Model 8

Figure E.19: *Lateral deck displacements - Calc. I, Model 7 & 8*
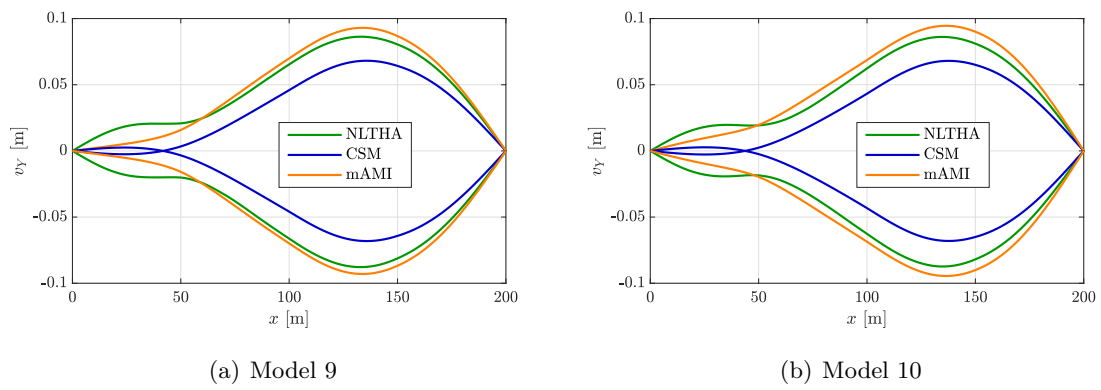
(a) Model 9

(b) Model 10

Figure E.20: *Lateral deck displacements - Calc. I, Model 9 & 10*
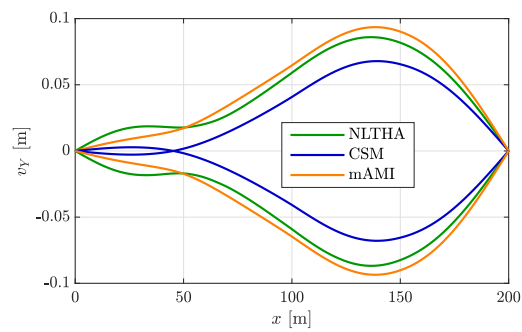
Figure E.21: *Lateral deck displacements - Calc. I, Model 11*
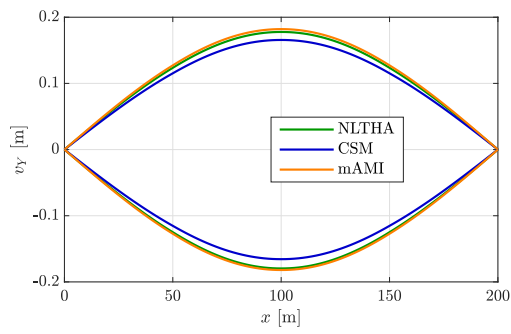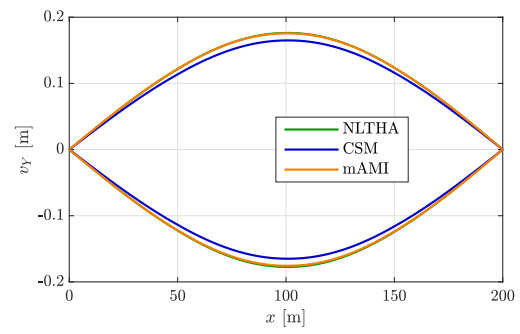
(a) Model 1

(b) Model 2

Figure E.22: *Lateral deck displacements - Calc. II, Model 1 & 2*
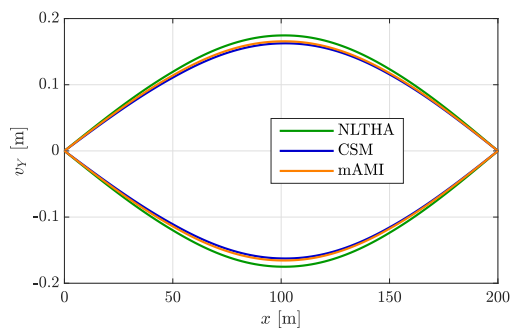
(a) Model 3
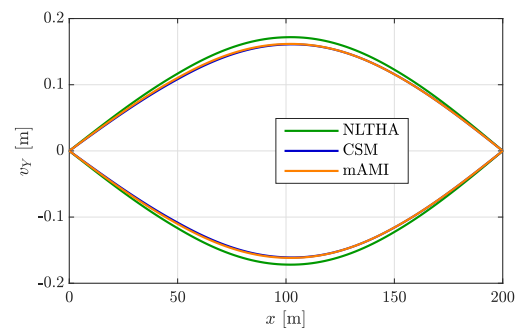
(b) Model 4

Figure E.23: *Lateral deck displacements - Calc. II, Model 3 & 4*
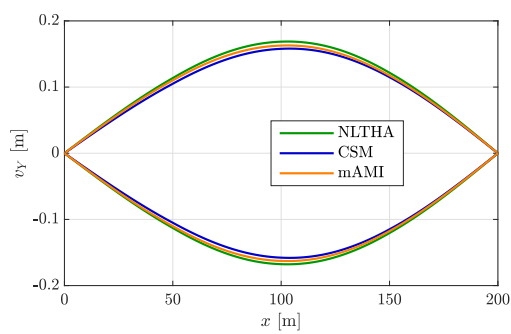
(a) Model 5
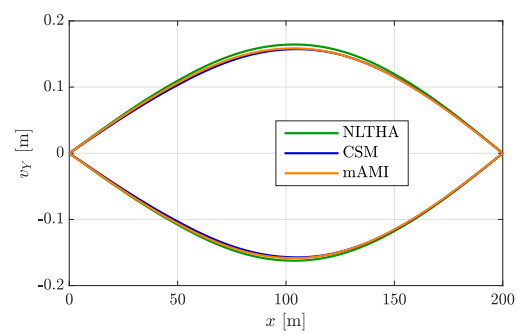
(b) Model 6

Figure E.24: *Lateral deck displacements - Calc. II, Model 5 & 6*
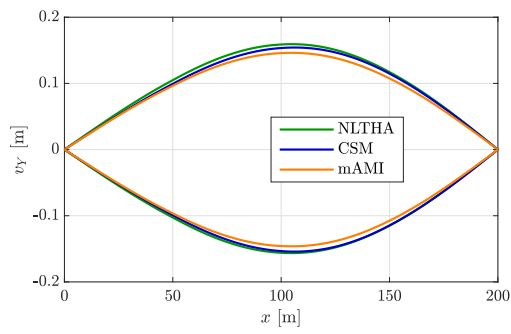
(a) Model 7
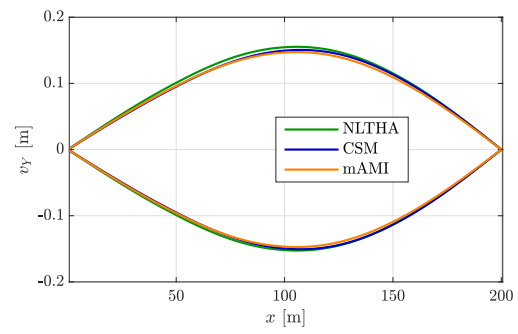
(b) Model 8

Figure E.25: *Lateral deck displacements - Calc. II, Model 7 & 8*
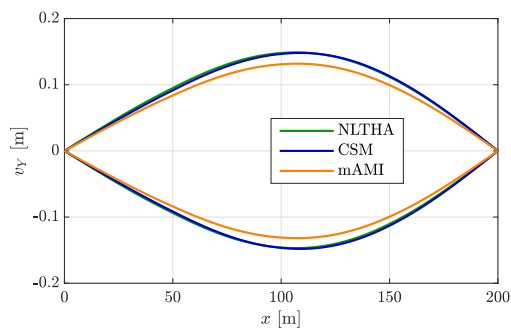
(a) Model 9
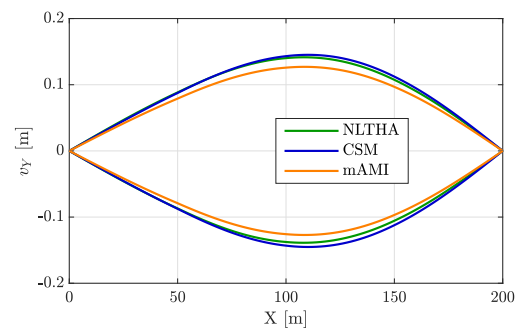
(b) Model 10

Figure E.26: *Lateral deck displacements - Calc. II, Model 9 & 10*
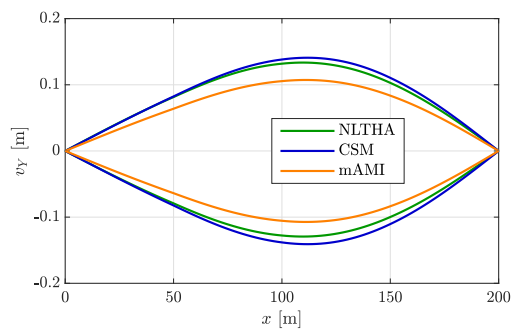
Figure E.27: *Lateral deck displacements - Calc. II, Model 11*

F Further information on the multidirectional earthquake investigations

F.1 Preliminary study in the time domain

Representative force quantities of bridge models A & B:

Table F.1: Force quantities - model A (mono- & bidir. NLTHA)

Excitation	$F_{b,Y}$ [kN]	$M_{3,P1/P3}$ [kNm]	$M_{3,P2}$ [kNm]
Monodirectional Y	2417	11789	11147
Bidirectional XY	2293	11087	10807
Deviation [%]	5.41	6.33	3.15
Excitation	$F_{b,X}$ [kN]	$M_{2,P1/P3}$ [kNm]	$M_{2,P2}$ [kNm]
Monodirectional X	798	4791	2829
Bidirectional XY	718	4278	2597
Deviation [%]	11.14	11.99	8.93

Table F.2: Force quantities - model B (mono- & bidir. NLTHA)

Excitation	$F_{b,Y}$ [kN]	$M_{3,P1}$ [kNm]	$M_{3,P2}$ [kNm]	$M_{3,P3}$ [kNm]
Monodirectional Y	2637	11318	10968	11808
Bidirectional XY	2318	9144	10458	11402
Deviation [%]	13.76	23.78	4.88	3.56
Excitation	$F_{b,X}$ [kN]	$M_{2,P1}$ [kNm]	$M_{2,P2}$ [kNm]	$M_{2,P3}$ [kNm]
Monodirectional X	1025	5834	4320	2606
Bidirectional XY	950	5597	3769	2520
Deviation [%]	7.90	4.23	14.62	3.41

F.2 Comparison of multidirectional seismic calculation concepts

Multimodal *RSM* under consideration of a bidirectional seismic excitation:

For the *RSM* calculation based on ductile behavior, the factor λ must be determined separately for both directions (X & Y). Assuming that the shortest pier P1 in both bridge models (A & B) will first develop a plastic zone in the lower third of the pier (plastic hinge idealized in the middle of this zone), the following results for λ according to EUROCODE 8 - PART 2 (2011), Tab. 4.1:

$$L_s = 15 \text{ m} \cdot \frac{5}{6} = 12.5 \text{ m} \quad \text{(model A)} \tag{F.1}$$

$$L_s = 10 \text{ m} \cdot \frac{5}{6} = 8.33 \text{ m} \quad \text{(model B)} . \tag{F.2}$$

Transverse direction:

$$H = 2.74 \text{ m} \quad \rightsquigarrow \alpha_s = \frac{12.5 \text{ m}}{2.74 \text{ m}} = 4.56 \geq 3.0 \quad \rightsquigarrow \lambda = 1.0 \quad \text{(model A)} \tag{F.3}$$

$$H = 2.74 \text{ m} \quad \rightsquigarrow \alpha_s = \frac{8.33 \text{ m}}{2.74 \text{ m}} = 3.04 \geq 3.0 \quad \rightsquigarrow \lambda = 1.0 \quad \text{(model B)} . \tag{F.4}$$

Longitudinal direction:

$$H = 1.02 \text{ m} \quad \rightsquigarrow \alpha_s = \frac{12.5 \text{ m}}{1.02 \text{ m}} = 12.25 \geq 3.0 \quad \rightsquigarrow \lambda = 1.0 \quad \text{(model A)} \tag{F.5}$$

$$H = 1.02 \text{ m} \quad \rightsquigarrow \alpha_s = \frac{8.33 \text{ m}}{1.02 \text{ m}} = 8.17 \geq 3.0 \quad \rightsquigarrow \lambda = 1.0 \quad \text{(model B)} . \tag{F.6}$$

Furthermore, according to EUROCODE 8 - PART 2 (2011), Sec. 4.1.6 (5)P, it is checked whether the q factor of 3.5 must be reduced due to the normalized longitudinal force:

$$\eta_k = \frac{N_{Ed}}{A_c \cdot f_{ck}} = \frac{10.625 \text{ MN}}{1.2172 \text{ m}^2 \cdot 35 \text{ MN/m}^2} = 0.25 \leq 0.3 \quad \rightsquigarrow q = 3.5 \quad \text{(model A)} \tag{F.7}$$

$$\eta_k = \frac{N_{Ed}}{A_c \cdot f_{ck}} = \frac{10.472 \text{ MN}}{1.2172 \text{ m}^2 \cdot 35 \text{ MN/m}^2} = 0.25 \leq 0.3 \quad \rightsquigarrow q = 3.5 \quad \text{(model B)} . \tag{F.8}$$

General conditions of the calculations performed:

Table F.3: *Calculations used to analyze the representative force quantities*

Procedure	Bride model A	Bride model B
NLTHA	50 bidirectional *NLTHAs*	50 bidirectional *NLTHAs*
mAMI	*pd X*: BM 1 & *mp* 3	*pd X*: BM 1 & *mp* 4
	pd Y: BM 2 & *mp* 3	*pd Y*: BM 2 & *mp* 4 (P2, P3, $F_{b,Y}$) and BM 7 & *mp* 2 (P1)
RSM	*CQC*-combined modal results for $q = 1.5$ & $q = 3.5$	
BPA	*pd X*: $P = P_1 + 0.6P_2$ (*mp* 3)	*pd X*: $P = P_1 + 0.6P_2$ (*mp* 4)
	pd Y: $P = P_2 + 0.6P_1$ (*mp* 3)	*pd Y*: $P = P_2 + 0.6P_1$ (*mp* 4 & 3)
3D MPA	*CQC*-combined modal results for	
	pd X: mode 1 and *mp* 3	*pd X*: mode 1 and *mp* 4
	pd Y: modes 2 & 6 and *mp* 3	*pd Y*: modes 2, 5 & 7 and *mp* 4 & 'o' (4/3/2)

Table F.4: *Calculations used to analyze the representative normal stresses*

Procedure	Bride model A	Bride model B
NLTHA	50 bidirectional *NLTHAs*	50 bidirectional *NLTHAs*
mAMI	*SRSS*-combined directional results of	
	pd X: BM 1 & *mp* 3	*pd X*: BM 1 & *mp* 4
	pd Y: BM 2 & *mp* 3	*pd Y*: BM 2 & *mp* 4 (P2, P3, $F_{b,Y}$) and BM 7 & *mp* 2 (P1)
BPA	*pd X*: $P = P_1 + 0.6P_2$ (*mp* 3)	*pd X*: $P = P_1 + 0.6P_2$ (*mp* 4)
	pd Y: $P = P_2 + 0.6P_1$ (*mp* 3)	*pd Y*: $P = P_2 + 0.6P_1$ (*mp* 3)
3D MPA	*CQC*-combined modal results for	
	pd X: mode 1 and *mp* 3	*pd X*: mode 1 and *mp* 4
	pd Y: modes 2 & 6 and *mp* 3	*pd Y*: modes 2, 5 & 7 and *mp* 'o' (4/3/2)

Table F.5: *Calculations used to analyze the lateral deck displacements*

Procedure	Bride model B
NLTHA	50 bidirectional *NLTHAs*
mAMI	*pd Y*: BM 2 & *mp* 4 and BM 7 & *mp* 2
BPA	*pd Y*: $P = P_2 + 0.6P_1$ (*mp* 3)
3D MPA	*CQC*-combined modal results of modes 2, 5 & 7 with *mp* 4, 3 & 2 ('o')

F.3   Final validation: Investigation of a cable-stayed bridge
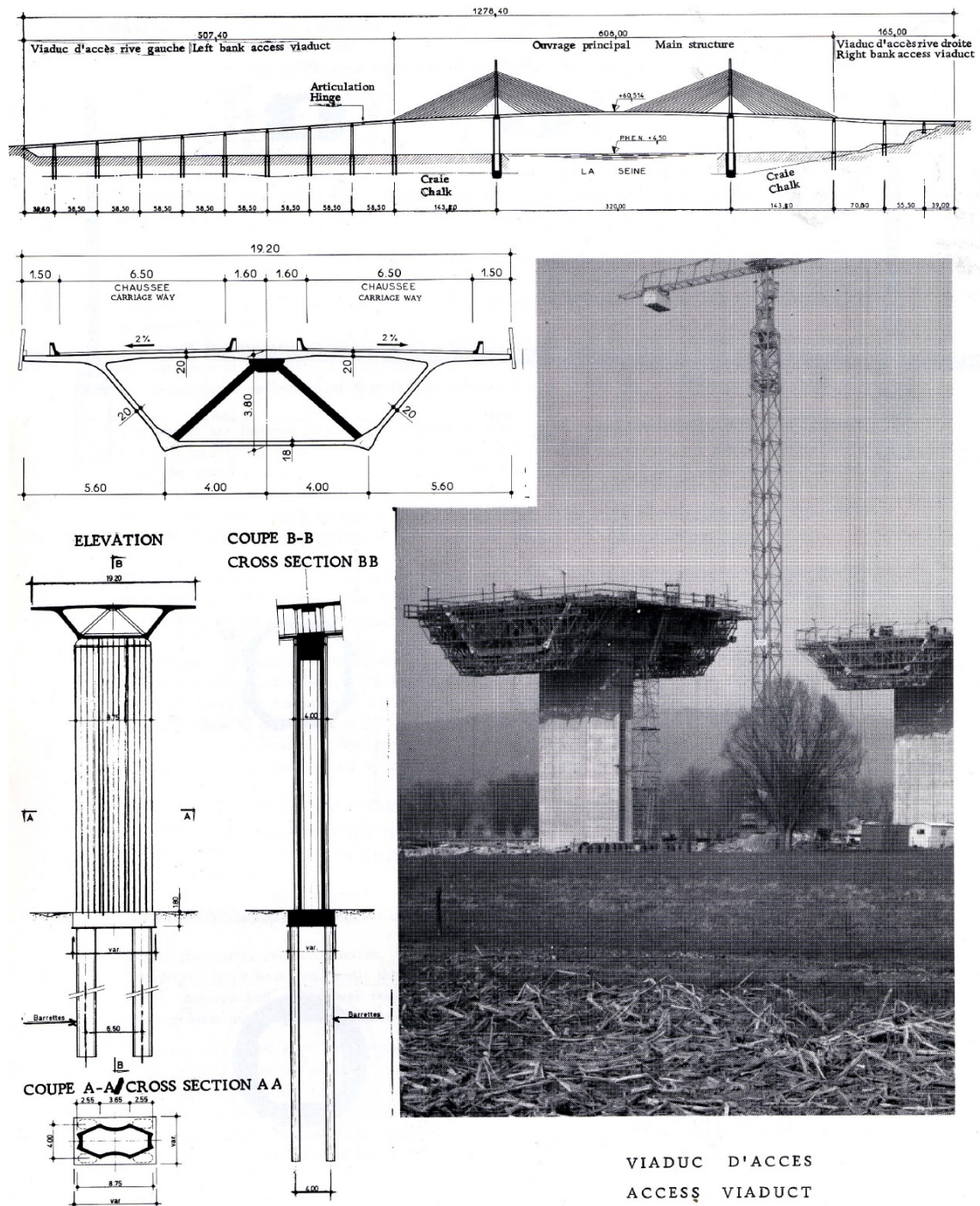
Figure F.1: *Brotonne bridge - Further illustrations (1) (*FREYSSINET *(1976))*
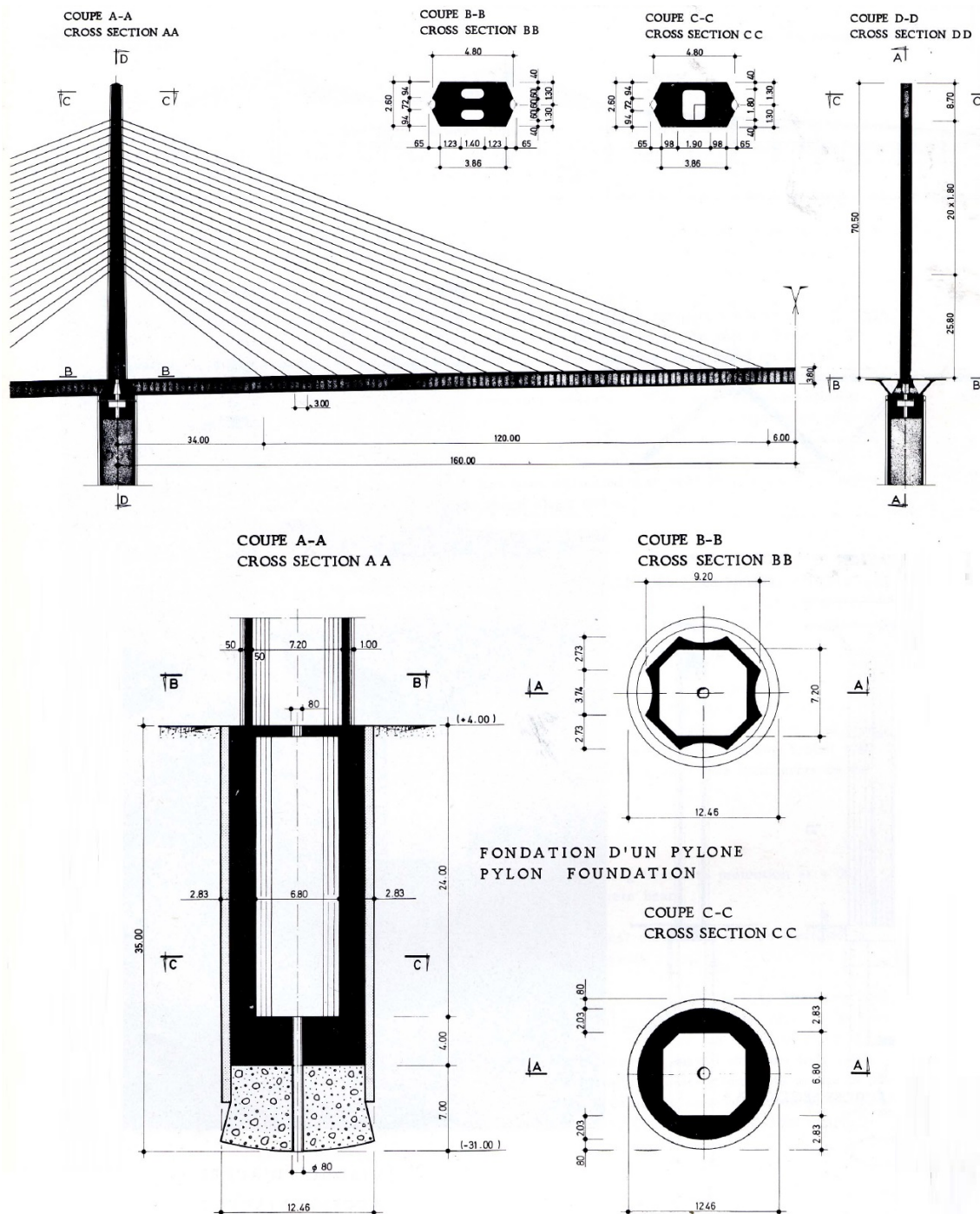
Figure F.2: *Brotonne bridge - Further illustrations (2) (*Freyssinet *(1976))*

Lebenslauf

Dominik Matthias Kämper   Geburtsdatum/-ort: 09.04.1993, Essen
Staatsangehörigkeit: deutsch

WISSENSCHAFTLICHER WERDEGANG

12/2017 – 03/2024	**Promotionsstudium im Bauingenieurwesen an der Bergischen Universität Wuppertal**
10/2015 – 11/2017	**Masterstudium im Bauingenieurwesen an der Bergischen Universität Wuppertal**

Abschluss:	Master of Science
Vertiefung:	Konstruktiver Ingenieurbau
Note:	1.3
Thesis:	*Spektralbereichssimulation stochastisch erregter Strukturen im Modalraum*

10/2012 – 11/2015	**Bachelorstudium im Bauingenieurwesen an der Bergischen Universität Wuppertal**

Abschluss:	Bachelor of Science
Note:	1.6
Thesis:	*Durchstanzbewehrungssysteme und deren theoretische Modelle*

06/2012	Abitur, Gymnasium-Essen-Überruhr (Durchschnitt: 1.5)

AKADEMISCHE UND SONSTIGE TÄTIGKEITEN IM BAUINGENIEURWESEN

Seit 04/2024	**Bauingenieur, GERB Engineering GmbH (Essen)**
01/2019 – 08/2021	**Freier Mitarbeiter, Ingenieurbüro EZI – Ingenieure GmbH (Solingen)**
12/2017 – 03/2024	**Wissenschaftlicher Mitarbeiter, Bergische Universität Wuppertal**
(10/2022 – 03/2024)	Computational Applied Mechanics Univ.-Prof. Dr.-Ing. habil. Jaan-Willem Simon
(12/2017 – 09/2022)	Lehrstuhl für Baumechanik und Numerische Methoden Univ.-Prof. Dr.-Ing. habil. Wolfhard Zahlten
03/2015 – 10/2017	**Studienbegleitende Beschäftigung im Ingenieurbüro Pühl und Becker – Ingenieurberatung VBI, Essen**
09/2013 – 10/2017	**Studentische/Wissenschaftliche Hilfskraft, Bergische Universität Wuppertal**
	Lehrstuhl für Baumechanik und Numerische Methoden Univ.-Prof. Dr.-Ing. habil. Wolfhard Zahlten

Bochum, Juli 2025

Berichte aus dem Konstruktiven Ingenieurbau

Bergische Universität Wuppertal

Berichte aus dem Konstruktiven Ingenieurbau

Bergische Universität Wuppertal

Heft 16   Stopp, K.: Trag- und Verformungsverhalten großflächig gegründeter Stahlbetontragwerke unter Berücksichtigung der Boden-Bauwerk-Interaktion, 2010; ISBN 978-3-940795-15-1

Heft 17   Porsch, M.: Modellierung von Schädigungsmechanismen zur Beurteilung der Lebensdauer von Verbundkonstruktionen aus Stahl und Beton, 2010; ISBN 978-3-940795-16-8

Heft 18   Mannsfeld, T.: Tragverhalten von Stahlbetonflächentragwerken unter Berücksichtigung der temperaturbedingten Nichtlinearitäten im Brandfall, 2011; ISBN 978-3-940795-17-5

Heft 19   Gelien, M.: Ein Beitrag zur Bemessung von Stahlbetonstützen im Brandfall, 2011; ISBN 978-3-940795-18-2

Heft 20   Festschrift Gerhard Hanswille, 2011; ISBN 978-3-940795-19-9

Heft 21   Bergmann, M.: Zur Bemessung von Hohlprofilverbundstützen im Brandfall; ISBN 978-3-940795-20-5

Heft 22   Peter, C.: Tragverhalten von Verkehrstunneln im Brandfall mit einer Innenschale aus PP-Faserbeton, ISBN 978-3-940795-21-2

Heft 23   Chanou, M.: Zum Tragverhalten von Hohlprofil-Verbundstützen mit Mehrkernquerschnitten, ISBN 978-3-940795-22-9

Heft 24   Menkenhagen, Philipp: Beitrag zum Tragverhalten des Lasteinleitungsbereichs von Hohlprofil-Verbundstützen unter Berücksichtigung der Verformungseigenschaften von Schubringen, 2016; ISBN 978-3-940795-23-6

Heft 25   Zwolinski, Stefan: Ermittlung der Grünzugfestigkeit erdfeuchter Zementleimgemische als Grundlage für die Optimierung der Produktion von sofort entschalten Betonwaren, 2018; ISBN 978-3-940795-24-3

Heft 26   Dolasse, André: Mikrowellenverfahren zur Untersuchung des Erhärtungs- und Trocknungsverhaltens von zementgebundenen Baustoffen, 2019; ISBN 978-3-940795-25-0

Heft 27   Loh, Lutz: Zum Torsionstragverhalten vorgespannter Segmenttürme - Ein Nachweismodell für überdrückte und klaffende Segmentfugen mit kreisringquerschnitt, 2023; ISBN 978-3-940795-26-7

Heft 28   Blau, Nick: Untersuchungen zur Ermüdungssicherheit von Querrahmenanschlüssen bei Verbundbrücken, 2024; ISBN 978-3-940795-27-4

Berichte aus dem Konstruktiven Ingenieurbau

Bergische Universität Wuppertal